Università degli Studi di Genova
Dipartimento di Fisica
Scuola di Dottorato di Ricerca in Fisica e Nanoscienze

Tesi di Dottorato di Ricerca

Characterization of new solid state particle detectors and measurement of the central exclusive production of $t\bar{t}$ pairs at CMS

Candidato:
Roberto Mulargia

Relatore:
Prof. Enrico Robutti

Relatore:
Prof. Silvano Tosi

XXXIII ciclo

Contents

Introduction

The CERN Large Hadron Collider (LHC) allows particle physics to explore unprecedented regimes and make a huge step forward in the understanding of fundamental interactions. The discovery of the Higgs boson by the ATLAS [1] and CMS [2] collaborations provided an excellent test of the standard model (SM) of particle physics. On the other hand, it is long known that the SM can only be an approximation at low energies of a more general theory, yet to be discovered: therefore, in addition to precision measurements within the SM, searches for signatures of new physics (NP) models beyond the SM represent a key goal of the physics programs of the LHC experiments. Searches are performed analysing a range of experimental signatures as wide as possible. So far, no evidence for deviations from the SM has been reported.

The top quark, owing to its large mass, close to the electroweak (EWK) symmetry breaking scale, has long been seen as a window on NP. Several NP models indeed foresee a privileged role for the top quark sector. The LHC experiments have a huge program of measurements of top quark properties. At the LHC, in proton-proton collisions, the top quark is predominantly produced via quantum chromodynamics (QCD) diagrams that yield top quark-antiquark pairs, or via EWK diagrams in the so called "single top" production. Recently, at the CMS collaboration, the possibility arose to explore a new production mechanism of the top quark, the central exclusive production via gamma-gamma fusion. In fact, beam protons can often interact without disintegrating themselves, rather losing a small fraction of their energy and momentum, by exchanging photons, for example, and continuing their path: the lost 4-momentum can yield a variety of particles, referred to as the X system in the following, giving rise to events of the form $pp \to pXp$; the X system can be top quark-antiquark pairs. CMS installed a new detector, the proton precision spectrometer (PPS), positioned at around $210\,mathrmm$, along the beam line, on either side of the beam interaction point: PPS allows to reconstruct those protons that interacted without disintegrating themselves. The measurement of the proton lost momentum, together with the reconstruction of the decay products of the X system by the central CMS detector, allows the study of events of the form $pp \to pt\bar{t}p$. The cross section for this process has never been measured before. From a theoretical point of view, in the context of the standard model, the cross section is foreseen to be very small, generally below $1\,mathrmfb$: calculations using the Monte Carlo generator FPMC [3] combined with MadGraph5 [4] yield a value of around $0.3\,mathrmfb$. However NP scenarios can enhance it to values that can be tested with the data already collected by the LHC. In my PhD thesis, I participated in the ongoing efforts to measure the cross section of the $pp \to pt\bar{t}p$ process, selecting the so-called semi-leptonic channel, that is events where one

of the two top quarks decays to a fully hadronic final state and the other to a final state containing a charged lepton-neutrino pair.

While in the first run of its operation PPS comprised silicon-strip tracking detectors, a new silicon-pixel-based detector has been designed and built: during my PhD, I participated in all phases of the construction, commissioning and installation of the new pixel detectors. The system is made of several layers of sensitive material arranged in a mechanical structure, called "roman pot", that allows a positioning very close to the beam line: in fact, protons undergo only a tiny deviation after the interaction and, exploiting the LHC optics system, at 210 $mathrmm$ from the interaction point, they are still very close to the beam line. For these reasons, PPS silicon detectors operate under extreme conditions, in a very high radiation environment. Characterising and optimising the behaviour of the new detectors under various levels of radiation exposure played a role of paramount importance during the commissioning phase.

The LHC is in operation since 2008. With the aging of some parts and the evolution of the operating conditions, the experiments have constantly updated and improved all systems along the years, taking advantage of the continuous advancements of the technologies for particle detectors. In 2020, the LHC and the experiments were in a shutdown phase for repairs and upgrades. In 2022, the operations will resume with a higher proton center-of-mass energy and with a larger luminosity. Very high luminosities yield extreme pile-up conditions, that is a large number of multiple interactions during the same beam bunch crossing, a phenomenon that can make event reconstruction problematic for the experiments. To cope with such extreme operating conditions, and at the same time maintain excellent performances, efforts have been devoted to design new generation timing detectors: in addition to spatial information, a precise timing information in fact can help correctly assigning the reconstructed tracks to the interaction that produced them. In my PhD, I joined the TimeSpot collaboration, a team aimed at conceiving new solid-state timing detectors that implement novel configurations of p-n junctions to achieve unprecedented resolutions on the timing measurements.

This thesis is structured as follows:

Part I describes the CMS experiment and in particular the new PPS system;

Part II describes novel solid state detectors technologies;

Part III describes the data analysis for the measurement of the cross section of the process $pp \to pt\bar{t}p$.

Part I

The LHC and the CMS experiment

A part of the work of my PhD concerned the operation and the upgrade studies of the CMS experimental apparatus and, in particular, the PPS subsystem. In addition, the data analysis for the measurement of the cross section for the $pp \to pt\bar{t}p$ process makes use of all the subsystems of CMS to reconstruct the decay products of the $t\bar{t}$ pair, as well as of PPS to reconstruct the protons. Part I of my thesis therefore comprises a series of chapters dedicated to the description of the LHC accelerator, the CMS detector, and in particular the PPS system, the CMS software infrastructure, including the reconstruction of the physics objects of interest for the data analysis, and the upgrade plans of the experiment.

Chapter 1

The Large Hadron Collider

The *Large Hadron Collider* (LHC) machine is the world's largest and most powerful particle accelerator since 2008 and was designed to accelerate protons up the a center-of-mass energy of $\sqrt{s} = 14\,\text{TeV}$ and lead nuclei up to an energy per nucleon $E_{Pb} = 2.76\,\text{TeV}$. It is operated by the European Organization for Nuclear Research, Conseil Européen pour la Recherche Nucléaire, (CERN) and is located in a 26.7 km long circular tunnel approximately 100 m underground at the border between France and Switzerland, in the vicinity of Geneva.
The accelerator consists of two parallel tubes evacuated and kept at ultrahigh vacuum where bunches of $\sim 10^{11}$ protons or fewer lead nuclei circulate in opposite directions. Each bunch trail the previous one after a delay time multiple of 25 ns, hence the machine can contain up to 2080 bunches. The beams are accelerated by 16 radiofrequency cavities and their motion is guided by thousands of electromagnets including 1232 dipole magnets to bend their direction and quadrupole magnets to ensure that the bunches remain squeezed despite the electromagnetic repulsion of the charged beam particles.
Eventually the beams are focused further down to a diameter in the order of $\sim 10\,\mu$m and are made to cross each other in four points around the LHC ring, called Interaction Points or IPs, and the collisions are studied by the four multipurpose detectors: ALICE [5] (IP2), ATLAS [6] (IP1), CMS [7] (IP5), LHCb [8] (IP8).
LHC is the latest addition to the CERN accelerator complex, shown in Fig 1.1 and represents only the last acceleration to 7 TeV step before the hadrons are made to collide.
In the case of protons, the particles are obtained by the ionization of hydrogen molecules in the duoplasmatron proton source. The protons are then gradually accelerated while traveling in the Linac2 up to 50 MeV, then in the four rings of the Proton Synchrotron Booster (PSB) up to 1.4 GeV and in the Proton Synchrotron (PS) up to 26 GeV. The protons will then reach 450 GeV in the Super Proton Synchrotron before being injected in the LHC.

The instantaneous luminosity of a particle collider can be expressed as

$$\mathcal{L} = \frac{N_b N_p^2 f}{S_{eff}} \tag{1.0.1}$$

where N_b denotes the number of colliding bunches, N_p the number of protons per bunch, and f is the revolution frequency around the ring. S_{eff} is the effective

cross section of the beam and depends on the beam focus as well as on the beam crossing angle and the size of the bunches.
In 2018 at the end of Run 2 (2015-2018), the LHC reached an instantaneous luminosity peak of about $2 \cdot 10^{34}\,\mathrm{cm}^{-2}\mathrm{s}^{-1}$ which is a factor of two higher than the LHC design luminosity but is the experimentally confirmed limit to the instantaneous luminosity for the current accelerator.
However, such a high instantaneous luminosity is an excellent result in terms of data production and hence discovery potential. In fact, the rate dN/dt of events of a given physics process can be calculated multiplying the instantaneous luminosity $\mathcal{L}$ by the cross section σ of the process under investigation:

$$\frac{dN}{dt} = \sigma \cdot \mathcal{L} \tag{1.0.2}$$

The integrated luminosity L is obtained integrating the value of the instantaneous luminosity $\mathcal{L}$ as a function of time, and determines the total expected number of events for a certain physics channel.
At the end of Run 2, the total integrated luminosity since the beginning of LHC operation reached $L = 189.3\,\mathrm{fb}^{-1}$ for each of CMS and ATLAS, of which $160\,\mathrm{fb}^{-1}$ were accumulated during Run 2 alone. The ALICE and LHCb experiments aim to a deliberately lower number of collisions per bunch crossing and this peak luminosity is not relevant for their purposes.

At present, the LHC is in Long Shutdown 2 (LS2) during which machine consolidation measures are being implemented in order to enable the accelerator to reach the beam energy of 7 TeV. Due to the global sanitary emergency, the data taking period after the LS2, called Run 3 will start at the beginning of 2022, almost one year later than scheduled, and it will hopefully see pp collisions with an energy of 14 TeV. During Run 3 and before the Long Shutdown 3 (LS3) scheduled for 2024, the LHC aims to reach a total integrated luminosity of $L = 350\,\mathrm{fb}^{-1}$, well above the initial LHC goal of about $300\,\mathrm{fb}^{-1}$.

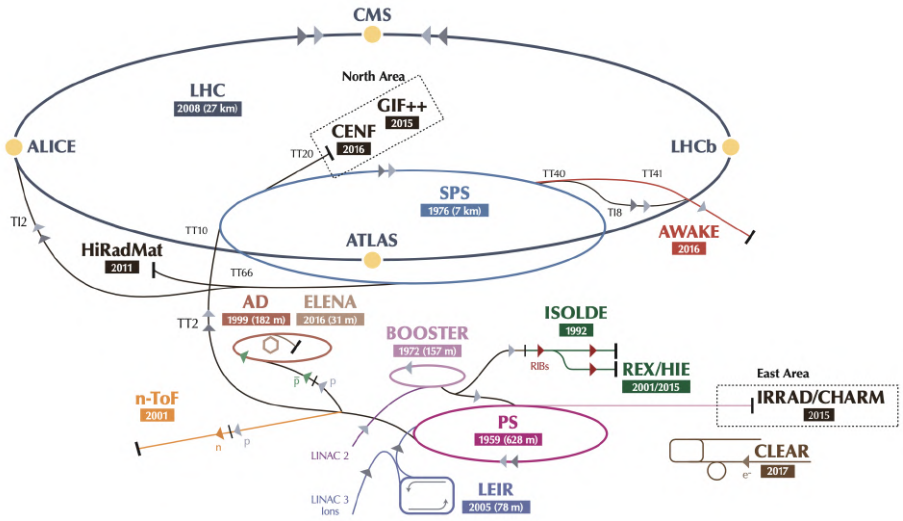

Figure 1.1: The complex of accelerators at CERN [9]

Chapter 2

The Compact Muon Solenoid

The Compact Muon Solenoid (CMS) experiment revolves around the construction, operation and upgrade of the detector of the same name at LHC and the physics analysis of the data produced by it. More than 5000 people from 200 institutes in 50 countries are involved in this effort, making it one of the largest international scientific collaboration in history.
The Compact Muon Solenoid detector is located close to the city of Cessy, France, in a cavern and tunnel approximately 100 m deep underground around the interaction point five of the LHC. It started its operation in 2008 as a large multipurpose detector with a broad physics program, ranging from Standard Model studies and searches for extra dimensions and dark matter particles.
The main focus of the experiment is on proton-proton (pp) collisions provided by LHC at high energies and instantaneous luminosities. The detector also studies lead nuclei ($PbPb$) collisions in a dedicated program, which is not relevant for this thesis and hence it will not be discussed further.

During the Run 2 (2015-2018), the LHC provided an integrated luminosity of $L_{del} = 162.85\,\text{fb}^{-1}$ [10] for pp collisions at $\sqrt{s} = 13\,\text{TeV}$ at the center the CMS experiment, of which $L_{rec} = 150.26\,\text{fb}^{-1}$ was recorded. The data provisioning and recording progress over time is shown in Fig. 2.1.

The CMS detector is designed to accurate measure the trajectory, momentum and energy of the particles produced after the high-energy pp collisions of the LHC, except for neutrinos which interact only very weakly.
This task is performed thanks to different subdetectors such that the ensemble of their measurements allows for a full characterisation of the pp event.
Bunch crossings (or BX) have a frequency of 40 MHz, in other words they are separated by a 25 ns delay. During each bunch crossing multiple collisions occur but most of these interactions are too weak to produce interesting events. The particles produced by these softer interactions are what is referred to as pileup (or PU). Each subdetector is designed to deal with very high level of pileup and the data acquisition must be quicker than the bunch crossing period. For this reason all detectors are characterized by a fast readout together with a fine granularity, which is needed to deal with the huge amount of particles produced in each collision. Another consequence of the high luminosity of the LHC is

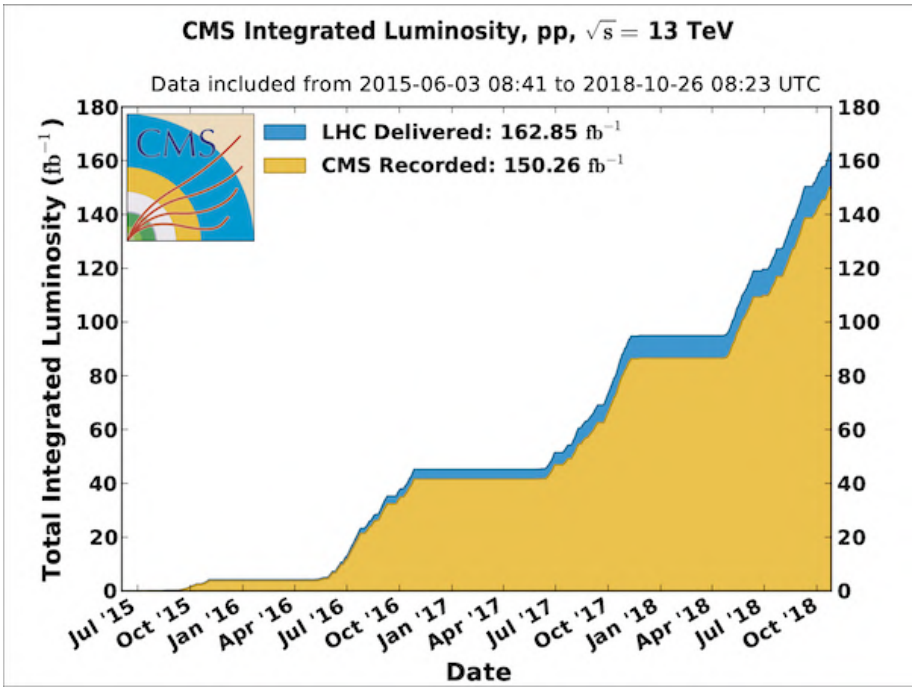

Figure 2.1: Integrated luminosity over time provided by the LHC (blue) and recorded by the CMS experiment (yellow) [10]

that the detectors have been built to face with a high radiation damage.

In the setting of this thesis, the part of the CMS detector which is located in the IP5 cavern will be referred to as the *central detector*. On the other hand, the *Precision Proton Spectrometer* (PPS) is a CMS subsystem which is located hundreds of meters away from the central CMS detector but it has a prominent role in this thesis and hence will also be described in detail in the following chapters.

In order to describe the positions and the directions of the measured objects, the CMS experiment uses the conventional coordinate system depicted in Fig. 2.2. Its origin is placed in the nominal collision point inside the CMS detector (IP5). The x-axis points to the center of the accelerator ring while the y-axis points vertically upwards and the z-axis points along the beam axis to make the coordinate system right-handed.

Since the detector has a cylindrical symmetry around the beam pipe, it is often used a cylindrical or spherical coordinate system. The azimuthal angle φ ($0 < \varphi < 2\pi$) is measured starting from the x-axis in the x-y plane and the polar angle ϑ ($0 < \vartheta < \pi$) from the positive the z-axis. The radial coordinate r is measured from the axis origin.

Instead of using the polar angle ϑ, two other variables are often used: the pseudorapidity η defined as

$$\eta = -\ln\left(\tan\frac{\vartheta}{2}\right) = -\frac{1}{2}\ln\left(\frac{p+p_z}{p-p_z}\right) = \operatorname{artanh}\frac{p_z}{p} \tag{2.0.1}$$

where p is the is the particle momentum and p_z is its z-component; or the

rapidity y, defined as

$$y = \frac{1}{2} \ln \left(\frac{E + p_z}{E - p_z} \right) \tag{2.0.2}$$

where E is the particle energy. Pseudorapidity differences are Lorentz-invariant and hence they do not depend on longitudinal boosts of particular particles, which is important for hadron collision experiments as the interacting partons carry different momenta.
It is also common to use transverse components of energy and momentum, E_T and p_T , respectively. These variables are defined in the x-y plane and are useful since the their initial state (i.e. before the collision) value is zero and it is expected to be the same in the final state, allowing the search for non-detected particles.

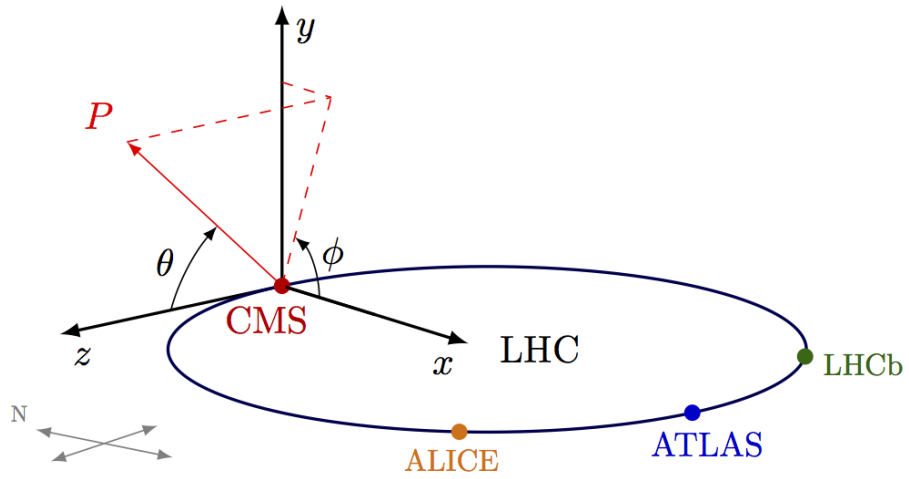

Figure 2.2: The coordinate system used by the CMS experiment. The x-axis points towards the center of the LHC ring, the y-axis is oriented up towards the sky, and the z-axis is defined to be parallel to the beam line in counter-clockwise direction.[11]

In the following sections both the central CMS detector and its PPS subsystem will be described.

2.1 Central Detector

The central detector of the CMS has a cylindrical design with a length of 28.7 m, a diameter of 15 m and a mass of about 14000 tons. The subdetectors are layered around the beam axis, symmetrically to the primary interaction point, as illustrated in Fig. 2.3.

The components can be grouped into four main subsystems, whose short description follows.

- The huge *solenoid magnet* defines the whole architecture of the detector with its inner diameter of 6 m and its length of 12 m. It can generate a magnetic field with a strength of up to 4 T which is used to bend the trajectories of electrically charged particles, hence enabling the measurement of their momenta. It takes the form of a cylindrical coil of superconducting

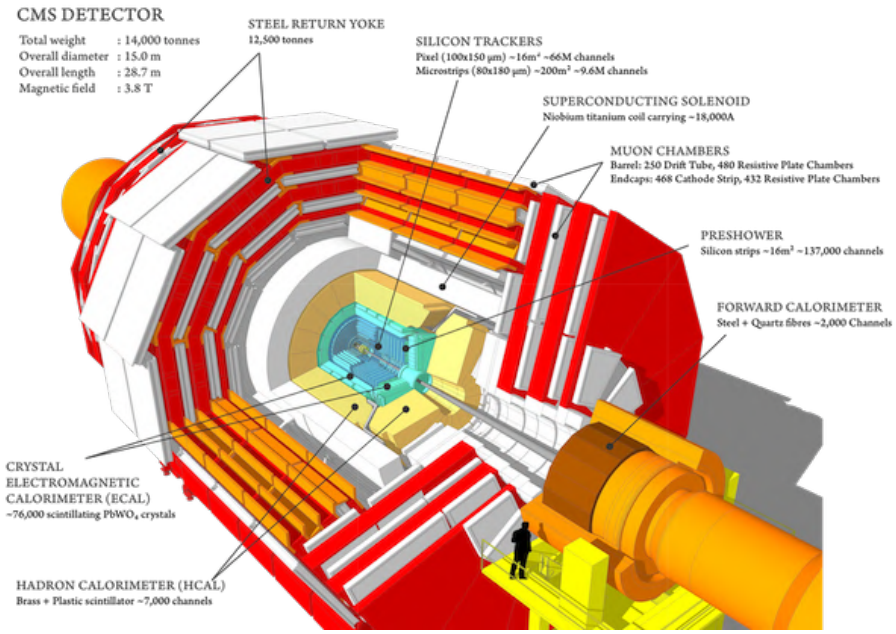

Figure 2.3: A cutaway illustration of the central CMS detector[7]

niobium-titanium (NbTi) cables which operate at a temperature of 4.7 K. The magnetic field is confined into the detector volumes by three layers of massive iron return yoke.

- The *inner tracking system* consists of pixel detectors and silicon strip detectors to identify charged particles and to measure their trajectories. In fact the measured curvature allows the measurements of the particles momenta and charge signs. The two components are installed as close as possible to the interaction point to achieve the best possible spatial resolution.

- The *calorimetry system* aims to measure the energies and directions of traversing particles. It comprises an electromagnetic calorimeter (ECAL), a preshower detector, a hadronic calorimeter (HCAL) and a very-forward calorimeter. The ECAL detects particles that interact electromagnetically, mostly electrons, positrons, and photons, whereas the HCAL is designed for the detection of charged and uncharged hadrons, such as protons, neutrons, pions, and kaons.

- The *muon system* occupies a large peripheral volume of the detector as it is installed between the layers of the iron return yoke, being the muons the only charged particles exiting the detector inner layers. It comprises resistive plate chambers (RPC), drift tubes (DT) and cathode strip chambers and its purpose is the identification of muons and the precise measurement of their momenta and charge signs.

More subsystems and subdetectors contribute to the data taking for the experiment, including the Precision Proton Spectrometer (PPS).

In the following subsections the above mentioned CMS components will be described in more details

2.1.1 Tracking system

The tracking system of the CMS detector is the one installed at the closest distance from the interaction point and it records the transit positions of charged particles, hence enabling very precise 3D measurements along their path. The detection principle is based on silicon semiconductor technology: the transit of a charged particle is able to induce electron-hole formation the volume of a reverse biased silicon pn junction and hence a measurable current that are digitized by the readout electronics. These resulting *hits* can be grouped into tracks using advanced pattern recognition algorithms to reconstruct a trajectory per particle indicating both its origin, or "vertex", and its direction of travel.

The expected particle flux varies greatly at different distances from the interaction point and different silicon detector geometries are necessary in order to resolve the hits of neighboring particles. At small radii, a pixel detector with high granularity is installed while in outer regions with reduced flux a strip detector technology is sufficient. The overall used material, comprising also support structures, cables, and inner cooling constructions, is reduced to minimize its influence on traversing particles. The CMS tracking subdetector, and especially the inner pixel detector, is exposed to extremely high radiation doses and although it is cooled down to a temperature of $-10\,^{\circ}\mathrm{C}$ its lifespan is generally shorter than other outer detectors.

The innermost pixel detector started its operation in 2009 and was designed and optimized for the LHC nominal instantaneous luminosity of $10^{34}\,\mathrm{cm}^{-2}\mathrm{s}^{-1}$ and a maximum level-1 trigger rate of 100 kHz. However, as explained in Chapter 1, LHC has swiftly exceeded its design luminosity and simulation studies showed a severe efficiency drop coming from the pixel detector also due to an increase in pileup up to and exceeding 50. For this reason, an upgraded pixel detector was designed and finally installed during the year-end technical stop of 2016/2017 [12].

A schematic view of the original CMS tracking system, including the pixel detector, is shown in Fig. 2.4. In total, the CMS tracker covers a longitudinal region of $|\eta| < 2.5$, has a length of 0.54 m, a diameter of nearly 1.1 m, and an active area of about $200\,\mathrm{m}^2$. The original pixel detector consisted of three barrel layers (BPIX) at radii of 4.4 cm, 7.3 cm and 10.2 cm, and two endcap disks (FPIX), one at each positive and negative z side. The detector consisted of 1440 silicon sensors modules segmented with a pixel pitch of $100 \times 150\,\mu\mathrm{m}^2$ for a total of approximately 66 M channels. The geometry was carefully chosen to yield optimal spatial resolution: BPIX modules are oriented parallel to the magnetic field, while endcap sensors are tilted by 20°. This allows the electron and holes produced by the charged particle traversing the detector to be distributed over several pixels, either by the Lorentz drift or by the geometrical arrangement, and this charge sharing can improve the resolution up to $10\,\mu$m in $r\phi$ direction and $20-45\,\mu$m along the z-axis, depending on the incidence angle of the particle track [13].

The comparison between the upgraded and original pixel detectors is shown in Fig. 2.5. The new layout has four barrel layers, improving the track quality, and 3 disks for each side, allowing 4 measurements per track up to $\eta < 2.5$. The

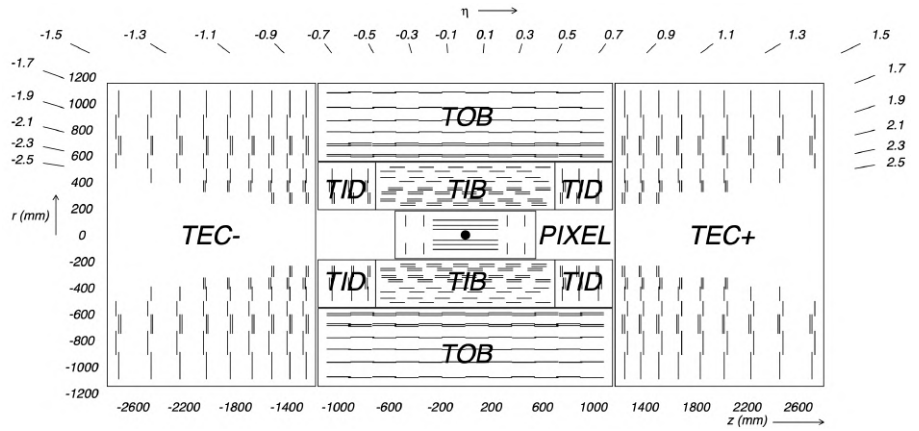

Figure 2.4: Schematic representation of the original (2009-2016) tracking system layout on a radial plane, showing from the center the pixel detector detector, the inner barrel (TIB) and disk (TID) detectors, the outer barrel (TOB) and endcap (TEC) subdetectors. Each line represents a detector module and double lines indicate back-to-back strip detector modules.[12]

upgraded detector shares the silicon pixel sensor geometry with its predecessor but a new ReadOut Chip (ROC) has been developed and installed. The new readout is able to cope with a higher pixel occupancy and has a digital output with higher readout speed. The same ROC is used for the PPS tracking detector.

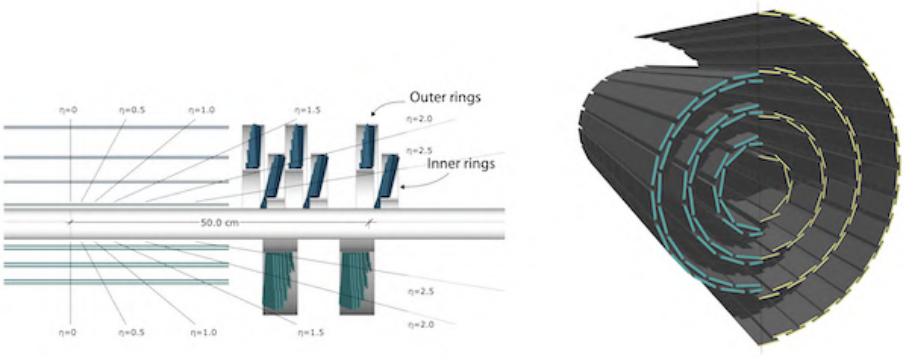

Figure 2.5: Left: Schematic comparison between the original (bottom) and upgraded (top) pixel detector layouts. Right: View comparing the pixel barrel layers in the original (left) and upgraded (right) pixel detector [12].

2.1.2 Calorimeters

The calorimeter system of the CMS detector is installed around the tracking system and is mostly enclosed by the solenoid. Its purpose is the precise energy measurement and full absorption of all particles except for muons and neutrinos. High granularity of its components is required for the accurate localization of energy deposits, which are combined with further subdetector information for the purpose of particle identification. It is divided into two subdetectors with

different detection techniques and its geometry is largely bound by the surrounding solenoid. The electromagnetic calorimeter (ECAL) measures photons and charged particles, mostly electrons and positrons, which primarily interact with the detector material via the electromagnetic force. The hadronic calorimeter (HCAL) on the other hand is constructed for detecting strongly interacting particles such as protons, neutrons, pions, and kaons. In order to provide a reliable measurement of missing transverse energy, the calorimeter system is fully hermetic within a region of $|\eta| < 5$ with a maximized amount of used material to cover also the non-Gaussian tails of expected energy distributions [7]. The geometric calorimeter layout is depicted in Fig. 2.6.

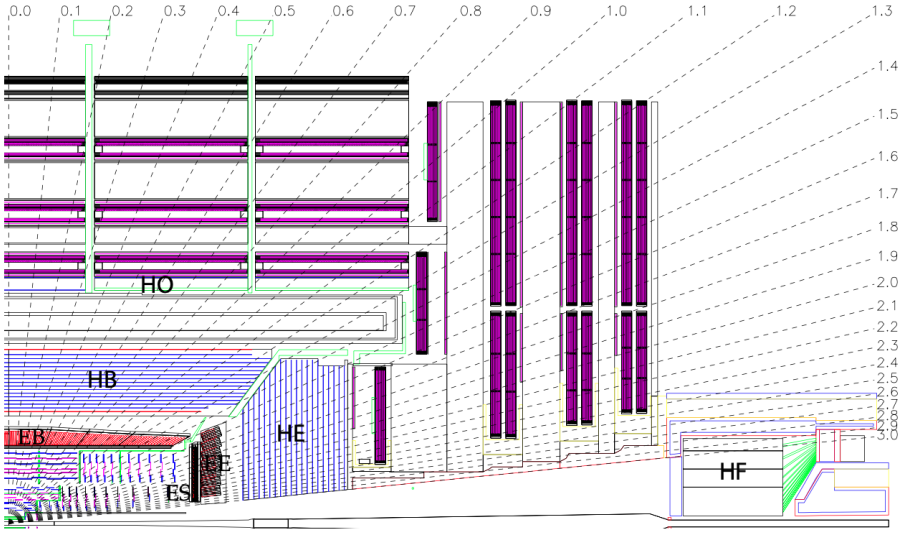

Figure 2.6: Cross section of one quadrant of the CMS calorimeter system [7]. The electromagnetic calorimeter (ECAL) consists of the ECAL Barrel (EB), the ECAL Endcaps (EE), and ECAL preshower (ES) components. The hadronic calorimeter comprises the HCAL Barrel (HB) and the HCAL Endcaps (HE), as well as the HCAL Outer (HO) detector beyond the solenoid and the HCAL Forward (HF) detector focused on measuring objects traveling close to the beam line.

The CMS Electromagnetic Calorimeter (ECAL) [14] is a hermetic detector up to a pseudorapidity of $|\eta| < 3$. It comprises a Barrel (EB) and an Endcap (EE) calorimeter with a preshower (ES) in front of the latter. The ECAL consists of lead tungstate ($PbWO_4$) scintillator crystals, a radiation resistant material whose response time is very fast, both crucial aspects for ECAL. The high density of $8.3\,\mathrm{g\,cm^{-3}}$ allows the construction of a relatively compact calorimeter that still contains most of the electromagnetic shower since the radiation length is only $X_0 = 0.86\,\mathrm{cm}$. With a crystal length of 23 cm in the barrel and 22 cm in the endcaps, ECAL provides therefore a total length of $25.8\,X_0$ of showering material in the barrel and $22\,X_0$ in the endcap. Additional $3\,X_0$ are provided in the pseudorapidity range $1.65 < |\eta| < 2.6$ by the ES, a lead adsorber with silicon strip sensors. The front cross section of the crystal of size $22 \times 22\,\mathrm{mm^2}$ in the barrel detector and $28.6 \times 28.6\,\mathrm{mm^2}$ in the endcaps provide a fine granularity, which allows a precise matching with the tracking information.
The material is transparent for scintillation light, which is produced when tra-

versed by charged particles. Its brightness provides a measure for the energy of the inducing particle. The light output of the crystals is strongly dependent on the temperature and makes necessary temperature stabilization of the ECAL. The scintillation light of each crystal is detected by avalanche photodiodes and vacuum photo-triodes in the EB and EE subdetectors, respectively. Both devices were extensively tested in magnetic field and after high irradiation, ensuring stable operation for more than 10 years.
The energy resolution was originally estimated with test beam data by summing over the energy deposits of the 3×3 grid around a centrally hit crystal and can be expressed as [7]

$$\left(\frac{\sigma_E}{E}\right)^2 = \left(\frac{2.8\%}{\sqrt{E[\text{GeV}]}}\right)^2 + \left(\frac{12\%}{E[\text{GeV}]}\right)^2 + (0.3\%)^2 \tag{2.1.1}$$

and it was reconfirmed by measuring electrons from Z boson decays in proton-proton collision data.

The HCAL is a sampling calorimeter consisting of alternating layers of non-magnetic brass absorber and plastic scintillators tiles. It is designed to the energy measurement of strongly interacting particles that survive the passage through the ECAL and create hadronic showers in the brass layers and induce detectable light in the subsequent scintillators. The produced light is collected by the plastic tiles and is converted by wavelength shifting fibers and measured by hybrid photodetectors (HPD). To improve the detection of early showers, the first scintillator tiles are placed between ECAL and the first absorber layers. Because of the limited remaining volume inside of the enclosing solenoid, the scintillator layers are only 3.7 mm thick in order to maximize the amount of absorber material.
The calorimeter is divided into four main components installed in different regions. Analogously to other subsystems, it is divided into a barrel part comprising the barrel (HB) and tail-catching outer calorimeter (HO) with a pseudorapidity coverage of $|\eta| < 1.3$, and two endcap disks. The endcaps comprise an endcap calorimeter (HE) in the range of $1.3 < |\eta| < 3$ and an additional forward calorimeter (HF) that extends the coverage up to $|\eta| = 5.2$. The division of the barrel detector into HB and HO arises from the limited space available: the HB, located inside the superconductive coil of the magnet, is supplemented by the HO located outside the solenoid, right before the muon chambers with whom shares the ϕ segmentation. The HO extends the effective absorption of the HB to approximately ten interaction lenghts λ_{int} by using the solenoid magnet itself as absorber material.
Since the calorimeter is required to be as hermetic as possible, HCAL Forward (HF) subdetectors are placed on either side of the detector beyond the muon endcap systems. They have a distance of ± 11.2 m to the interaction point, a length of ± 1.65 m, and cover a region of $3.0 < |\eta| < 5.0$.
The design energy resolution of the HCAL is

$$\left(\frac{\sigma_E}{E}\right)^2 = \left(\frac{100\%}{\sqrt{E[\text{GeV}]}}\right)^2 + (4.5\%)^2 \tag{2.1.2}$$

Using *pp* collision data recorded in 2016, the reconstructed energy response is found to be in excellent agreement between simulated and recorded data events [15].

2.1.3 Muon Detectors

Muons at moderate energies go across both the tracker and the calorimetry systems with a minimum loss of energy, and therefore can be measured by a detector installed outside the magnet coil. Ideally the magnet is only traversed by muons and the non measurable neutrinos and for this reason the muon identification has a superior signal-to-noise ratio and is heavily used in both trigger and physics analyses.
The muon system constitutes the outermost component of the CMS detector and is interlaced with the iron return yoke of the magnet system [16]. The measurement principle is based on gaseous detectors, which produce electron avalanches through gas ionization when traversed by charged particles. This detector technology was chosen because it provides cost-efficient coverage of almost the full solid angle even for such a large area coverage.
The architecture of the muon system is divided in two regions and comprises three different detector technologies: Drift Tubes (DT), Resistive Plate Chambers (RPC) or Cathode Strip Chambers (CSC). A schematic illustration of the detector is provided in Fig. 2.7.

The barrel region, $|\eta| < 1.2$, contains four layers of a total of 250 Drift Tube (DT) chambers complemented by five layers of Resistive Plate Chambers (RPC). The first three DT chambers contain twelve planes of aluminum drift tubes of which eight are responsible for measuring coordinates in the transverse

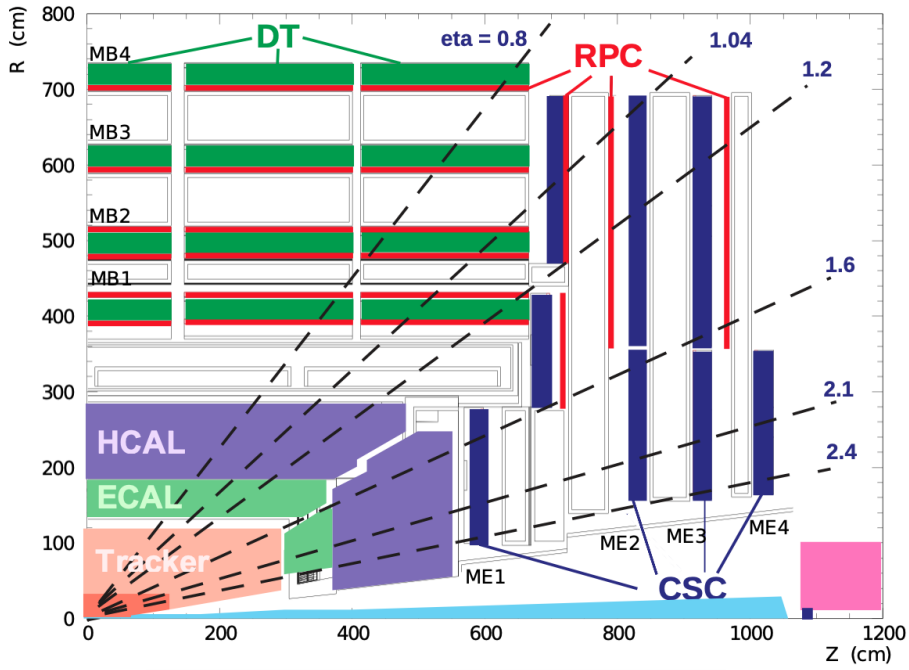

Figure 2.7: A longitudinal view of the muon system [7]. The barrel region uses interlaced gaseous Drift Tube (DT) chambers and Resistive Plate Chambers (RPC), whereas the endcaps rely on a combination of Cathode Strip Chambers (CSC) and RPCs

$r\phi$ plane and the remaining four planes function in the longitudinal rz plane. The outermost chambers only measure in $r\phi$ direction with eight planes of drift tubes each. The RPC technology consists of two high-resistivity plastic planes with readout strips interleaved by a gas chamber and they are operated in avalanche mode.
The endcaps are equipped with 486 Cathode Strip Chambers (CSC) $0.9 < |\eta| < 2.4$ overlapped by three RPC layers up to $|\eta| < 1.6$. The CSCs are characterized by faster drift times and they provide a three-dimensional measurement since their cathode strips are segmented and positioned almost perpendicularly with respect to the anode wires. This design stabilizes the operation in the forward regions, wherea high particle flux a the strong, less homogeneous magnetic field are present.
The muon detector single point resolution varies from $80 - 120\,\mu$m in the DT system, to $40 - 150\,\mu$m in the CSC, and to $0.8 - 1.2\,$cm in the RPC system [17]. While the DT and CSC systems offer a better spatial resolution of the muon tracks, the RPC detectors exhibit a faster response and deliver accurate timing information of the order of 1 ns, which can be utilized for the purpose of triggering. Therefore, the approaches are employed in conjunction in the respective detector regions to achieve an optimal resolution for both time and position measurements. The hit and track segment reconstruction efficiency The hit and track segment reconstruction efficiency for traversing muons was found to be in the range of $95\% - 98\%$ [17].

2.2 Precision Proton Spectrometer

The Precision Proton Spectrometer [18] (PPS) is a CMS subdetector which is not located in the CMS cavern but is installed in the LHC tunnel at a distance of approximately 200 m in both directions from the central CMS detector (Fig. 2.8). This detector aims at the measurements of the protons which interacted in the IP5 but survived the collision and continued their motion slightly deflected from the beam direction. This big distance is therefore necessary in order for the proton to be separated enough from the rest of he beam to be intercepted by a detector.

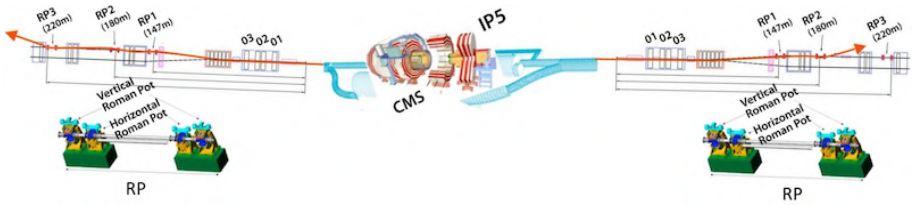

Figure 2.8: Schematic representation of the PPS detector locations with respect to the central CMS detector [18].

The investigated protons are the ones involved in *Central Exclusive Production* (CEP) processes, namely $pp \to pXp$. In these processes the interaction inside of the central detector is not elastic and even though the protons survive the collision, the interaction energy is big enough to make it possible for the central detector to detect a huge variety of produced particles. The PPS detectors

consist of a silicon tracking system to measure the position and direction of the protons, and a system of timing detectors to measure their arrival time. The ensemble of their measurements allows the reconstruction of the mass and momentum of the centrally produced system as well as the z coordinate of the primary vertex. The physics of the CEP processes will be described in detail in Chapter 8 (pag. 99) as the focus of the data analysis in this thesis is the central exclusive production of a $t\bar{t}$ pair decaying semi-leptonically. The PPS detector and its data is therefore crucially important in the scope of this thesis and will be described in detail.

The Precision Proton Spectrometer was designed in 2014 as a joint project CMS-TOTEM[1] and started its operation in 2016. The PPS system has been later integrated in the CMS trigger, data acquisition and detector control systems and has hence become a CMS subdetector.
In order to be able to detect the outgoing protons, the PPS sensors must be placed in the extreme proximity of the LHC beam and therefore they must be inserted into the beam pipe thanks to movable structures called *Roman Pots* (RP). In addition they must be able to operate in an extremely high radiation environment and cope with the very high pile-up of normal LHC running. The PPS sensor occupy a total of 8 Roman Pots, 4 in each arm of the spectrometer, or side in respect to the CMS central detector. In Fig. 2.9 the layout of the beam line in the 200 m region is showed: the PPS stations are indicated in red while the TOTEM ones in green. Two Roman Pots house the tracking detectors while the remnant two house the timing detectors. Downstream the detectors a new collimator magnet (TCL6) was also installed in order to protect subsequent quadrupole magnet (Q6) from shower particles originating in the PPS stations.

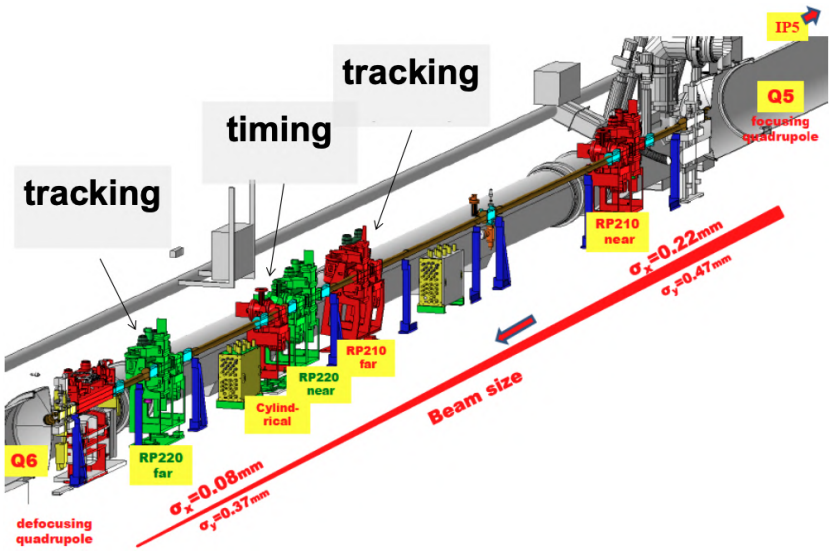

Figure 2.9: Schematic representation of the beam line in the 200 m region [20]

[1]The TOTal Cross Section, Elastic Scattering and Diffraction Dissociation Measurements at the LHC (TOTEM) experiment [19] is dedicated to the precise measurement of the total pp cross section, to the study of the elastic pp scattering and of diffractive processes.

2.2.1 The Roman Pots

The Roman Pots are movable systems required to approach the detectors as close as possible to the beam without preventing stable beam operation. This technology was introduced at the ISR [21] in 1970s and successfully used in later colliders like the SppS, Tevatron, HERA, and RHIC. The Roman Pot geometry and materials were carefully chosen and gradually developed in order to minimize their impact on the beam and allow a normal operation during high-luminosity run. In particular in its closest part to the beam the RPs are equipped with a thin window of thickness 150 μm which is able to withstand the Ultra-High Vacuum (UHV) while keeping a flatness better than 50 μm
The sensors and their front end electronics are placed inside a secondary vacuum vessel and moved into the primary vacuum of the machine through vacuum bellows. In this way, the thin window physically separates the detectors from the primary LHC vacuum, which is preserved against an uncontrolled out-gassing of the detector materials. Fig. 2.10a shows the most recently improved version of the RP which is a box-shaped structure and was installed in 2016 in the tracking stations at 203 and 214 m.
A cylindrical RP geometry was also designed and installed to house the PPS timing detectors. The choice of a cylindrical geometry provides the necessary space for all potential technologies of timing detectors and at the same time reduces the beam coupling impedance by minimizing resonant cavities. As for the box-shaped RP, also the cylindrical one implements a thin window for a closer approach of the detectors to the beam, in this case 300 μm thick. The drawings of the cylindrical vessel are shown in Fig. 2.10b.
The Roman Pot technology has enable the sensors to be as close as 12σ from the beam plus a safety margin of 0.3 mm.

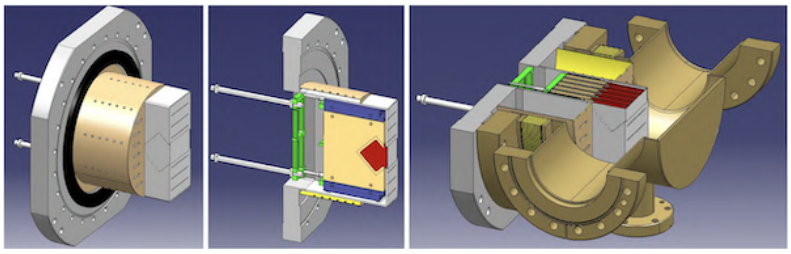

(a) Box-shaped RP housing the PPS tracking system.

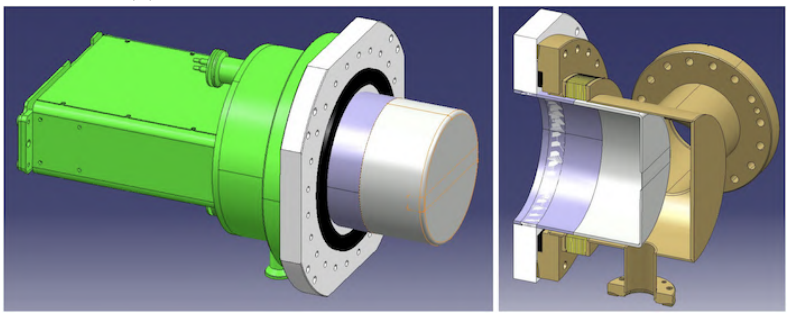

(b) Cylindrical RP housing the PPS timing system

Figure 2.10: Schematic drawing of the two Roman Pot geometries in use by PPS.

2.2.2 Tracking stations

The measurement of the deflection of the proton from the beam direction can be related to the fraction of the momentum they lost during the collision and hence the amount of energy available for the X system in the Central Exclusive Production $pp \to pXp$. More details about these relations will be given in Chapter 8 (pag. 99).
The tracking system in PPS plays a central role in the study of CEP processes and was designed for a position resolution of $\sigma_x \simeq 10\,\mu$m in x direction and $\sigma_y \simeq 30\,\mu$m in y direction [18] (see Fig. 2.2 Pag.11 for the coordinate system definition).
A very important requirement for the measurement of high-momentum protons is the reduction of the insensitive area at the sensor's edge facing the beam as this extends the acceptance for centrally produced systems with lower masses. Such a short distance from the beams entails an extremely high level of radiation. Fig. 2.11 shows an example of the proton fluence in the PPS tracking sensor. For an integrated luminosity of $L = 100\,\text{fb}^{-1}$, a maximum proton fluence of $5 \cdot 10^{15}\,\text{p}\,\text{cm}^{-2}$ is expected, which corresponds to $1 - 3 \cdot 10^{15}\,\text{n}_{\text{eq}}\,\text{cm}^{-2}$ where the uncertainty is due to the lack of measurements of damage in silicon made by

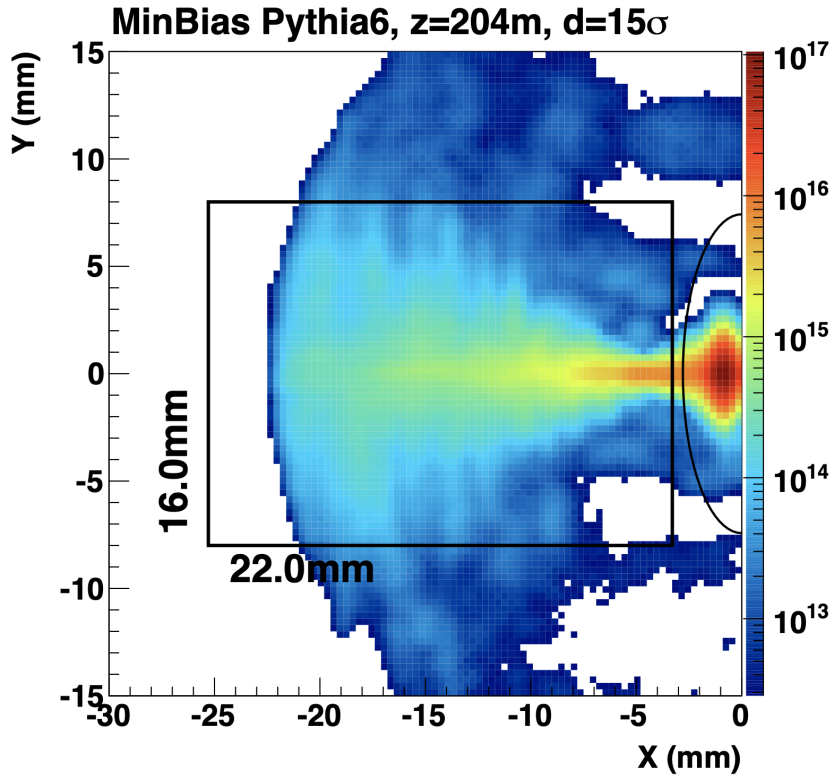

Figure 2.11: Simulated proton fluence in the tracking station at 204 m from the IP for $L = 100\,\text{fb}^{-1}$. The rectangle indicates the detector surface transverse to the beam assuming a detector tilt angle of 20°. The ellipse shows the 15σ beam contour. In the detector edge a value of the order of $5 \cdot 10^{15}$ protons cm^{-2} is obtained. [18].

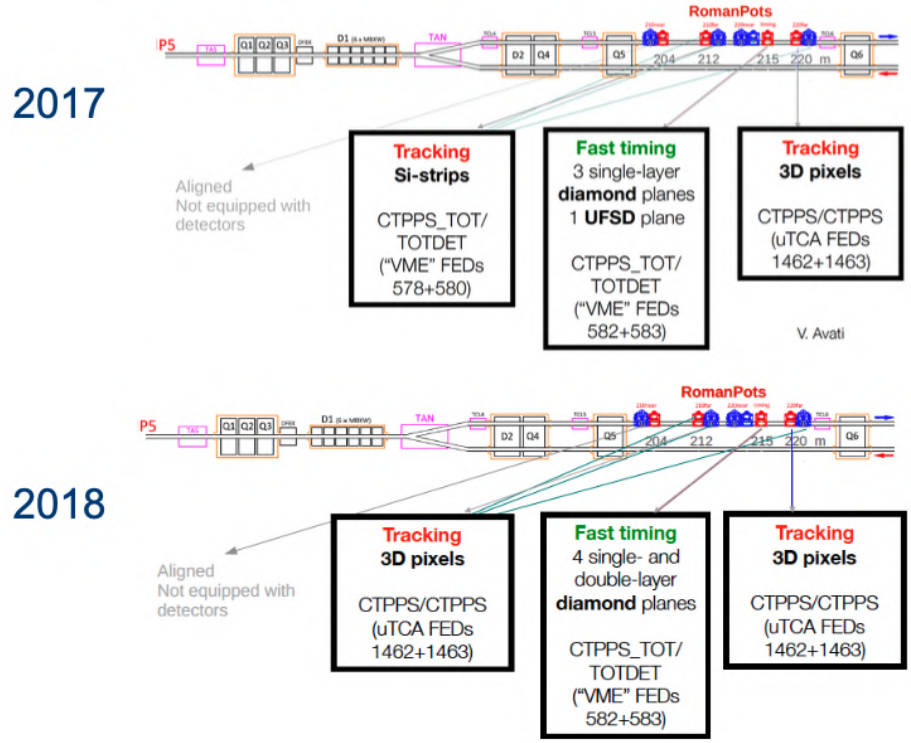

Figure 2.12: Detector technologies adopted by PPS in 2017 and 2018 [20].

protons at the TeV scale. The highly non uniformity of the radiation expected fluence should also be noted as it poses as a problematic environment for the detector readout integrated circuit (ROC, readout chip).

During the 2016 and 2017 data taking, two silicon detector technologies were simultaneously in use in the PPS tracking system: a strip detector in the horizontal Roman Pot 210far and a 3D pixel detector in the 220far RP.
Since 2018, both the tracking stations housed 3D silicon detectors.
Figure 2.12 provides a summary of the evolution of the detector technologies adopted by PPS.

Strip Tracking Detector

The silicon strip detector have always been in use in the vertical Roman Pots dedicated to the TOTEM experiment. They proved the ability to operate detectors in close proximity to the beam line at high luminosity and paved the way for the use of more efficient detector technologies based on pixelated silicon sensors.
Besides the use in 2016 and 2017 in the horizontal Roman Pots for PPS, the TOTEM silicon strip detectors inside of the TOTEM vertical RPs also contributed to the PPS operation for alignment purposes in special, low luminosity, dedicated LHC runs.
In fact, during these special run, the RPs can be pushed as close as $5\,\sigma$ to the beam and a partial overlap between the detectors in horizontal pots and those

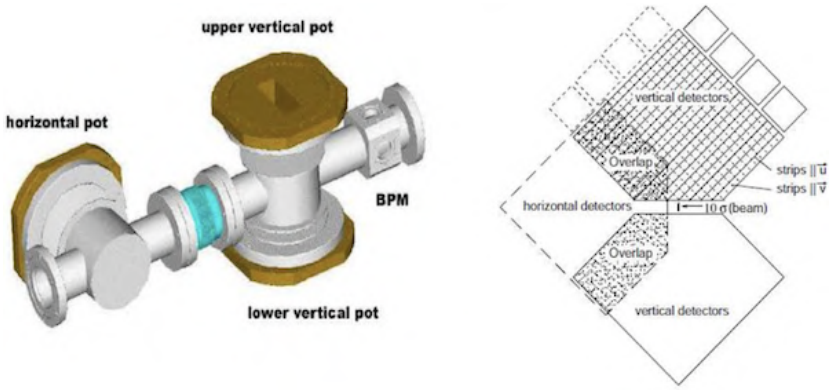

Figure 2.13: Schematic view of the horizontal and vertical Roman Pots and the overlap among the two sensors [23]

.

in vertical pots can be achieved, as shown in Fig. 2.13. Using all hits from this run, the relative alignment between RPs of each station can be obtained. If instead only elastic events are chosen, the alignment with respect to the beam can be derived. This procedure is fundamental for physics reconstruction and rely on the fact that the optics does not change between alignment and physics, high luminosity, runs.

TOTEM strip detectors have been qualified to operate up to fluences of $1.5 \cdot 10^{14}\,\text{protons}\,\text{cm}^{-2}$ [22], however it was decided to use them for the 2016 high-luminosity data taking, during which a substantial efficiency loss in the highest irradiated region was observed.
Moreover, in high pileup conditions, a strip tracking detector is affected by ambiguities due to the pattern matching of hit strips in different orientations. In general, for n simultaneous tracks, n^2 points are reconstructed. Under these conditions, the tracking capability of the PPS detector has been severely impacted by the limits of this technology until it was abandoned in the 2018.

Pixel Tracking Detector

A pixel detector was first installed in the PPS Roman Pots during the 2016-17 extended winter LHC shutdown and in 2018 became the baseline detector technology for the PPS tracking system. Innovative 3D silicon pixel sensor were chosen because of their intrinsic radiation hardness and the possibility to implement slim edges. The main feature of 3D sensors is that, instead of implementing the electrodes on the wafer surfaces, as in the planar technology, they are etched in a column shape perpendicular to the surface.
Although the structure of 3D pixel sensors was proposed as early as in 1997 [24], their production has proven to be very technologically challenging and 3D silicon sensors technology is still considered innovative.
The sensors used in the PPS tracker were produced by the Fondazione Bruno Kessler (FBK) with the 3D Double-side, Double-Type-Column (3D-DDTC) technology [25], described by the schematic cross section in Fig. 2.14a.
The FBK 1E pixel configuration is shown in Fig. 2.14b while the pixel layout in the proximity of the sensor edge is displayed in Fig. 2.14c.

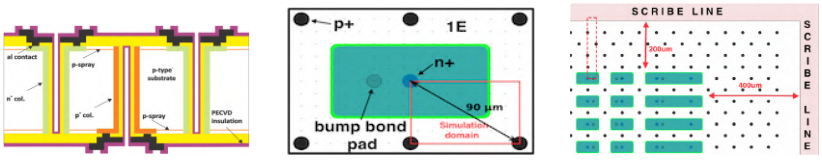

(a) FBK 3D-DDTC cross section. **(b)** Layout of the 6 modules mounted in each RP station. **(c)** FBK 3D sensor edge layout.

Figure 2.14: Cross section, pixel electrode configuration and edge layout of the FBK 3D sensors [25] [26].

Each RP station of the PPS tracking detector consists of one stack of six planes, called RPix modules, where each plane contains a 3D silicon sensor read out by six PSI46dig ReadOut Chips (ROCs). Each ROC reads 52×80 pixels, whose dimensions are $150 \times 100\,\mu\text{m}^2$. Given the small area of the detector, covered by a small number of individual sensors, a generous number of planes was chosen, in order to provide comfortable redundancy and make the system resilient to possible failures. Each plane is tilted by 18.4° to increase the charge sharing and therefore improve the spatial resolution.
The design of the front-end electronics and of the DAQ is based on that developed for the Phase 1 upgrade of the CMS silicon pixel detectors. The complete readout chain of one detector package is shown in Fig. 2.15 (pag.25).
Each RPix module consists of a flexible hybrid circuit hosting: the silicon sensor, six PSI46dig ROCs bump-bonded to the silicon sensor, and one Token Bit Manager (TBM) chip. ROCs are responsible for charge collection, charge discrimination and data buffering, while the TBM reads out the six ROCs of the module using a token ring protocol and serializing the data over a single output line. A view of a module is shown in Fig. 2.16a (pag.25).
The RPix portcard, shown in Fig. 2.16c (pag.25) was designed and produced by INFN-Genova. It shares its geometry with the TOTEM portcard in order to fit inside the Roman pot, but contains most of the components of the Phase I central pixel detector. The board receives the output data from the six RPix modules and transmits them on six optical fibres towards the Pixel Front-End Driver (FED) DAQ module, using a POH7 opto-electrical converter mezzanine card [27]. The portcard also receives fast configuration commands from the Pixel Front-End Controller (FEC) via optical fibers, translates these signals using Detector Optical Receivers (DOH) and dispatches them to the modules. Moreover the RPix portcard integrates other components such as the radiation sensors, part of the TOTEM DCS (Detector Control System) radiation monitoring, and the CMS Tracker Optical Control Link components that are capable of receiving and decoding the commands sent from the Tracker FEC.
For the back-end DAQ and control systems, composed by a FED and two FECs, μTCA crates are used. These boards, developed for the Phase 1 Pixel Upgrade project, replace the VME standard used so far for the CMS and TOTEM DAQ. Crates are located in the service cavern of CMS in order to be also accessible during data taking.

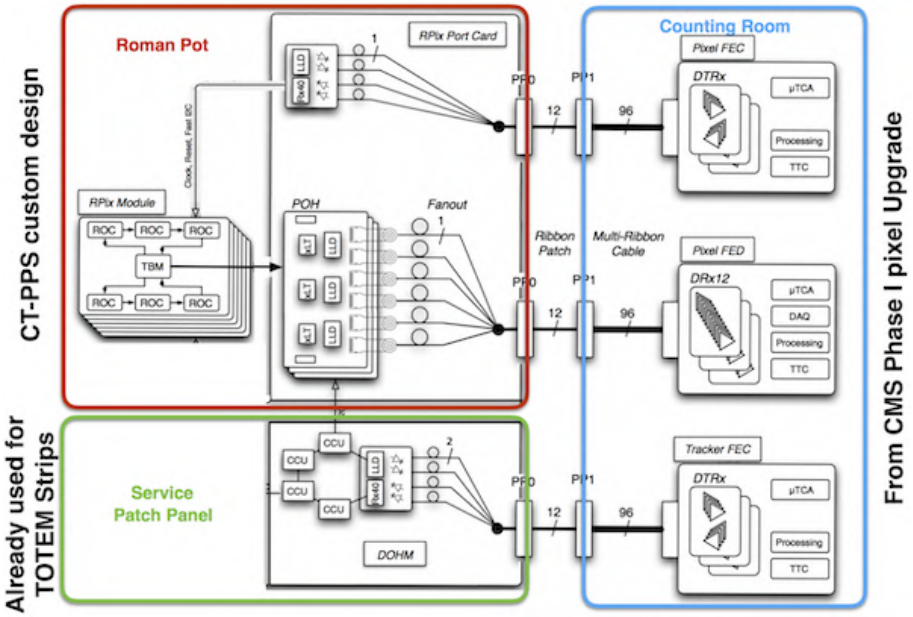

Figure 2.15: Detector readout blocks. The RPix modules and the RPix portcards are located inside the RP, the DOH Mezzanine (DOHM) is installed inside the service patch pannel in the LHC tunnel, and the FEDs and FECs are hosted in the counting room [26].

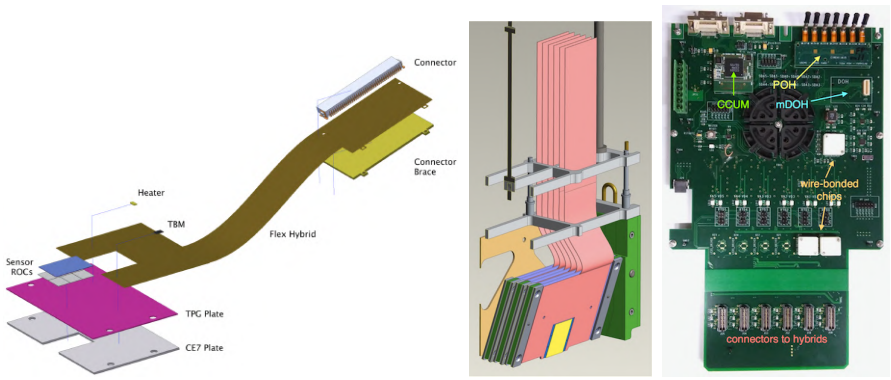

(a) Exploded view of one pixel module.

(b) Layout of the 6 modules mounted in each RP station

(c) RPix portcard

Figure 2.16: Readout electronics for the PPS pixel tracker [18] [26].

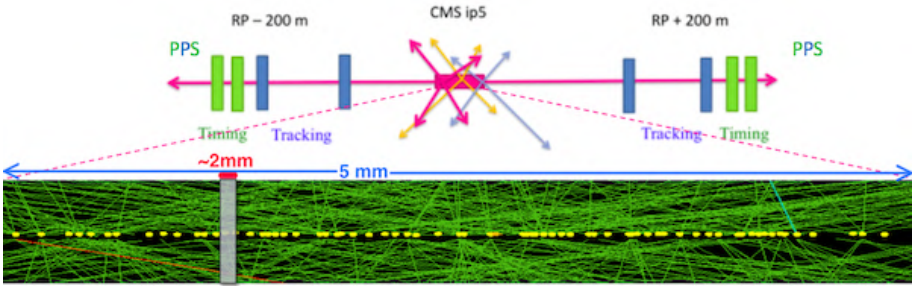

Figure 2.17: Schematic illustration of the determination of the z coordinate of the vertex using timing in PPS.

2.2.3 Timing stations

The measurement of the arrival time of the protons has an important role in PPS since it enables the identification of the correct interaction vertex, reducing the background from pileup at high luminosity. In the current LHC conditions, while the average number of hard collisions per bunch crossing is approximately 50, the number of softer collisions are expected to be orders of magnitude higher. The vertices of these collisions are spread out along the beam (z) direction within few centimetres, as depicted in Fig. 2.17 and the timing information on a pair of protons enables the determination of the vertex position thanks to the simple formula

$$z_{vertex} = c\frac{t_1 - t_2}{2} \quad . \tag{2.2.1}$$

A precision of $\sigma_t = 20\ ps$ on the time of arrival of the protons in each side would determine the vertex position with a precision of $\sigma_z \simeq 4.2\ mm$, and such a resolution on the vertex is enough to avoid the event loss due to the pileup.

The ambitious target for that time resolution, however, is not the only strict operational requirement for the PPS timing detectors and their sensors. As for the PPS trackers, the timing sensors must be as close to the beam as possible, hence the dead region at the edge closer to the beam must be as slim as possible. In addition, since the rate of the protons is highly non uniform, the sensor must be finely segmented in order to reduce the probability of double hits in the same channel. Again, as for the PPS tracker system, also the timing sensors must rely on very radiation hard technologies, as they are required to withstand an expected fluence up to $2 \cdot 10^{13}$ $\mathrm{n_{eq}cm^{-2}}$.
PPS timing detectors are housed in 4 Roman Pots, 2 in each arm. The baseline technology is based on diamonds sensors adapted from the ongoing TOTEM upgrade program [28]. Diamond detectors are characterised by an intrinsic resistance to radiation damage and an excellent performance in timing given by a very low noise thanks to the large energy gap. On the other hand the large energy gap causes a small charge released during the passing of a proton, hence a low noise amplifier is needed to keep the signal to noise (S/N) ratio large enough.
Ultra Fast Silicon Detectors, based on *Low Gain Avalanche Detector*, have also been used as timing detectors in PPS. Their technology improves the time resolution by increasing the signal slew rate thanks to a small internal gain.
Both the sensor technologies allow a fine segmentation and are very thin, allow-

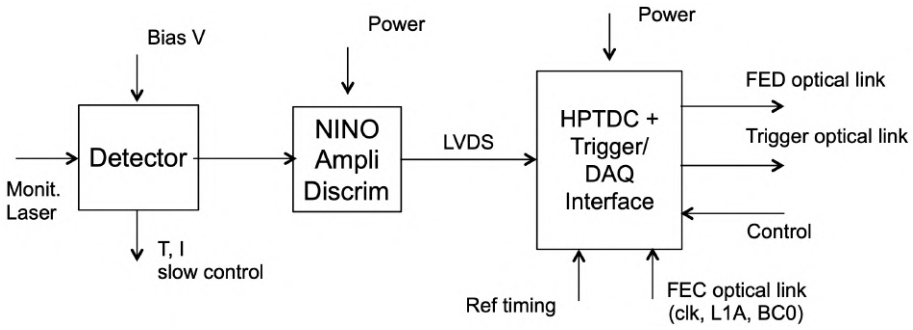

Figure 2.18: Diagram of the timing readout system [18].

ing the stack of multiple sensors. This in turns allows to compensate for the lower timing performances of a single plane with a resolution gain of $1/\sqrt{N}$ using N detector planes. The two detector technologies will be described shortly in the following subsection.

For what concerns the readout electronics, already available components have been chosen: the amplifier-discriminator *NINO* and the time-to-digital converter *HPTDC*, as shown in Fig. 2.18.

NINO is an 8-channel amplifier and discriminator implemented in CMOS 250 nm [29]. Each channel is a fully differential ultra fast (≤ 1 ns peaking time) preamplifier and discriminator. Thanks to the circuit saturation, the NINO output is a voltage pulse. The output pulse width is equal to the time-over-threshold, and therefore is a function of the input pulse amplitude. The intrinsic time resolution of the NINO chip was measured to be below a RMS value of 10 ps.

The LVDS output of the NINO is fed into the High Performance Time to Digital Converter (HPTDC) [30]. The time base for the TDC measurement is a Delay Locked Loop (DLL) with 32 delay elements and a clock synchronous counter, both driven by the same clock reference. The clock reference can be taken directly from the clock input of the TDC chip or can come from an on-chip Phase Locked Loop (PLL). The HPTDC provides the option of dual time measurement: in which both the raising and falling edges of the input pulses are determined. This allows to measure the time-over-threshold and therefore the detector pulse amplitude. The nominal intrinsic time resolution is approximately ~ 20 ps. The interface between the HPTDC and the timing FEC and FED is done by means of an FPGA in the front-end board installed in the tunnel.

The PPS timing measurements require a complementary timing system able to provide a very low jitter (≤ 1 ps) replica of the master clock to the front-end TDCs. In order to achieve sub-picosecond time synchronization, single electronics modules are placed in each arm, synchronized via an RF feedback system, operating at a frequency of about 480 MHz over a single coaxial cable. This scheme is based on a system in use at SLAC for the synchronization of the Linac Coherent Light Source (LCLS) experiments with the electron accelerator beam [31].

Diamond detector

Diamond detectors are the default choice for measuring the protons time of arrival in PPS. These detectors are radiation hard, thanks to the diamond structure, but the charge released by a proton in a diamond sensor can be considered small ($\sim 12000\,e$ for a $500\,\mu$m thick sensor). Because of the small charge collected, the output signal cannot be fed directly into the NINO and needs to be amplified by a discrete components and fine impedance adaptation board.
The PPS timing detector based on diamond technology has been installed in 2016 in the cylindrical Roman Pots, for a total of 4 planes per RP and 12 readout channels per plane, so to preserve the characteristics of the TOTEM upgrade design [28]. Each plane of the timing detector is formed by four $4 \times 4\,\mathrm{mm}^2$ diamond sensor with different pad geometries. The pixel pad shape is just given by the metallization pattern and pixels of different size can be easily implemented on the same diamond crystal. As shown in Fig. 2.19, each plane has different sensor arrangements, which are rotated and swapped while keeping small-size pads near the beam where a higher occupancy is expected. In this configuration, a space resolution of $\sim 150\,,\mu$m can be reached ($\sim 125\,,\mu$m by neglecting 5% of outliers) [28]. The time resolution of this detector measured with beam tests is $\sim 100\,,$ps per plane. The diamond planes were installed in the cylindrical RP during the technical stop in the second week of June 2016 (TS1), but due to an issue that required an access in the LHC tunnel to be solved, the commissioning phase only started after the technical stop in the middle of September (TS2).
For the 2017 data taking, three planes of diamond detectors have been installed in each cylindrical RP, being the fourth substituted by an UFSD.

Ultra Fast Silicon Detectors

Ultra Fast Silicon Detectors (UFSD) are an innovative sensor technology focused on extreme timing performances, based on the Low Gain Avalanche Detector (LGAD) technology [32]. Considering that for improving the timing resolution it is important to have a steep slew rate dV/dt, a thin sensor would be preferable for a fast collection of the charge. However, at the same time a thin sensor means a small produced charge. The solution proposed by the UFSD is to use a thin silicon sensor (diode) and at the same time recover a reasonable amount of charge by means of a small internal gain given by a thin multiplication layer implant, as depicted in Fig. 2.20.
This sensor technology will be described in more detail in Chapter 7.

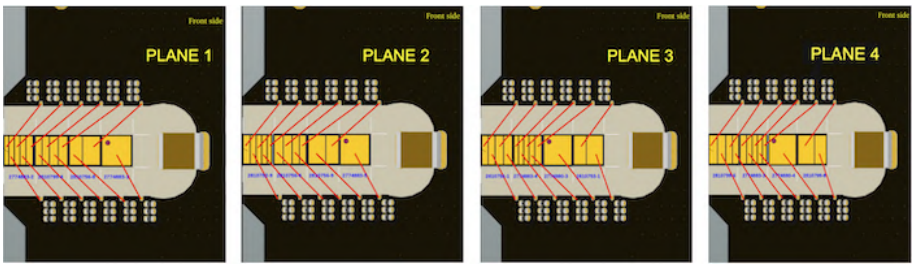

Figure 2.19: Diamond detector plane layout [28]. Diamond sensors with different pad configurations are swapped or rotated in order to maximise the spacial resolution.

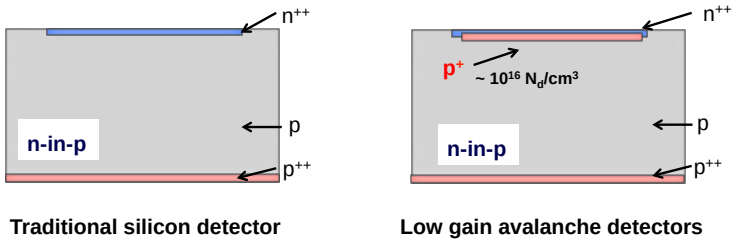

Figure 2.20: Schematic comparison between a traditional pn-junction based Silicon detector and a Low Gain Avalanche Detector.

UFSD Sensors with a layout compatible with the PPS requirements have been produced at Barcelona Institute of Microelectronics (IMB-CNM) in 2016. Each sensor, whose geometry is shown in Fig. 2.21, has an active area of $12 \times 6\,\mathrm{mm}^2$ and a thickness of $50\,\mu\mathrm{m}$. The sensor pads are organized in a matrix of 16 columns and 2 rows. The pixel size varies as a function of the distance from the beam: the 8 pads for each column closer to the RP edge have a dimension $\sim 1.5\,\mathrm{mm}^2$, while the others have an area of $\sim 3\,\mathrm{mm}^2$.
Since regions between two pixels are expected to have bad timing capability, the pixels belonging to the two rows are slightly staggered and the two rows have a different height. This design allows with only one sensor layout to recover low performance regions by arranging detector planes back-flipped one respect to the other. In 2016, the UFSD technology had not yet achieved their expected radiation hardness and this limited their use as timing detectors in PPS.
As the UFSD signal is quite compatible with the one produced by the diamond detectors, it was possible to adapt the prepared readout system and the mechanical housing inside of the RP already studied for the diamond detectors to welcome the UFSD plane. The sensors have been installed in a custom amplification board, shown in Fig. 2.22, specifically designed to provide three stages of amplification with the lowest noise possible. The narrow pixels forming each line of sensors have been bonded in pairs, as the board contains only 12 readout channels. The rest of the readout chain is the same of diamonds (NINO + HPTDC). The setup achieved a time resolution of $\sigma_t = 30\,\mathrm{ps}$ per plane.

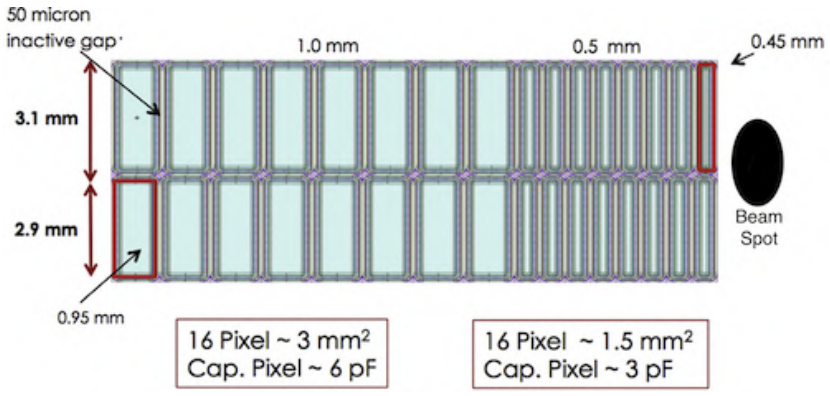

Figure 2.21: UFSD sensor geometry for the PPS timing detectors.

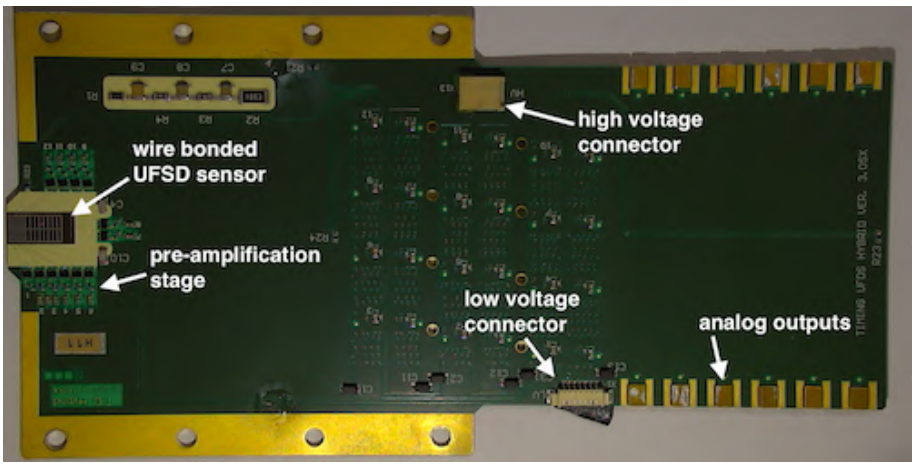

Figure 2.22: UFSD board for the PPS timing detectors.

2.3 Trigger and Data Acquisition

The LHC provides one bunch crossing every $25\,ns$ in the interaction point at the center of the CMS. Since the full detector measurement of a single event corresponds to a storage size in the order of $\sim 1\,\text{MB}$ [7] 10^9 and the LHC provides approximately 10^9 proton-proton collision per second, a data output of $\sim 950\,\text{TB/s}$ would be required to save the totality of the information produced. However, the data acquisition system is not able to reach such a high rate but its throughput is limited to $\sim 100\,\text{MB}$ per second. A selection of the interesting events must be quickly performed in order to reach a sustainable rate of a few hundreds Hertz. The trigger system is designed to do so by saving only the events which exhibit previously specified signatures of interesting processes.
The trigger system is included in some detectors electronics and readout systems but it is also performed on dedicated hardware trigger processors and a computing cluster which runs software-based, slower triggers.
The data rate reduction is implemented in CMS in two steps: the Level-1 (L1) Trigger and High-Level Trigger (HLT) [33].
The L1 trigger is able to receive the signal, take the decision and send back the result in a time shorter than the detector internal buffers latency of $3.2\,\mu\text{s}$, hence decreasing the rate down to a maximum of 100 kHz. In order to do so the L1 trigger is completely hardware-implemented, both in Field Programmable Gate Arrays (FPGAs) and Application Specific Integrated Circuits (ASICs) and the system only uses information from the calorimeter and muon systems in order to roughly recognize good object candidates such as muons, electrons, photons, jets, and global sums of transverse and missing transverse energy. These objects are called *trigger primitives* and their choice determines the trigger logic.
If the L1 trigger is accepted, all the CMS subdetectors send their data belonging to that event to the back-end electronics which transfers it to the HLT for further filtering. Its trigger decision is less time-constrained and can afford to include information from the inner tracker to perform a more sophisticated calculation. The HLT latency is limited to 50 ms in order to keep the final output frequency to values of about $100 - 300\,\text{Hz}$, therefore its algorithm must be carefully struc-

tured in parallel paths that aim to apply different selections on different objects while sharing common information in order to increase performance. The event will be trasferred to the CERN Tier-0 computing center to be stored only if it is accepted by at least one path. In case of high rate channels, depending on the instantaneous luminosity and pileup conditions, a fraction of the triggered events is rejected. This path pre-scaling is mostly used to build *minimum bias* data, that is a collection of underlying events with few constraints are applied.

Chapter 3

CMS software infrastructure and offline reconstruction

The data produced by all the subdetectors of the CMS experiment, described in previous Chapter 2 is the focus of the data analyses efforts to investigate high-energy particle collisions. This processes comprise the study of a vast quantity of recorded and simulated events to find and examine rare processes with sufficient statistical significance to test the physics theory.
The data analysis presented in this thesis aims to the measurement of the cross section of the central exclusive production of a pair of $t\bar{t}$ quarks in their semi-leptonic decay channel and it will be extensively described in Part III.

In order to be able to efficiently and reliably analyse such a big amount of data, sophisticated algorithms are used for the fulfillment of a multitude of tasks, ranging from physics object reconstruction, to signal extraction procedures with multivariate techniques, as well as management of particular analysis workflows and the dependencies between them. For more than a decade, the CMS experiment has been building a considerable amount of software libraries into a common CMS software framework which will be described in this chapter.

3.1 CMS Software Framework

The software framework of the CMS experiment, *CMSSW*, provides an object-oriented tool for a variety of applications for the data production and analysis and most of [34]. It is used in the high-level trigger for the implementation of the trigger paths (see section 2.3) and in the detector operation for calibration and alignment tasks. The framework is the basis of the offline data processing, from the production of simulated collision events, to the physics objects reconstruction routines.

The control and data flow of CMSSW is event-based and in particular revolves around the Event Data Model (EDM) [34]. A CMSSW program is made of configurable modules, written in C++ for the most part, which provide the analysis algorithms for a variety of applications. The modular programming

approach is therefore dominant because allows the creation of a program as a sequence of independent, interchangeable modules, such that each contains everything necessary to execute only one aspect of the desired functionality. In fact, in an event-by-event loop, data is passed between modules and, for example, a module can either stop the processing of an event, analyze existing event content or pass the content to the downstream modules to be analyzed.

All the information related to an event is stored in a *collection* and formatted as tree structures as provided by the ROOT toolkit [35]. These quantities include, for example, hits, tracks, and energy deposits, but also high-level data like trigger decisions and hypotheses of reconstructed particle.
The data elaboration can be executed in a multi-threaded process where some modules operate simultaneously while others run sequentially. The Python programmin language is adopted for the configuration and steering scripts.

3.2 Reconstructed Physics Objects

The data produced by the CMS detector after a collision take the form of binary hit information and calibrated energy deposits in the three-dimensional detector map described using its coordinate system. These measurements are combined to form candidates for stable particles characterized by their energy, momentum and trajectory.
These particle objects are the main characters of any phisics data analysis, as the one described in part III of this thesis. The simplest objects are electrons, muons, neutrinos and various jet types, which originate from the hadronization process of a quark. In this section, the fundamental objects will be described, starting from their identification and reconstruction using the *Particle Flow* algorithm. The reconstruction of the proton object is much more deeply related to the analysis presented in this thesis and will be discussed in Chapter 8.

3.2.1 The Particle Flow Algorithm

The Particle Flow (PF) algorithm is the tool for the identification and reconstruction of particles from the measurements of all CMS subdetectors [36].
A proton-proton interaction during a collision produces an ensemble of particles, called event. These particles include photons, electrons, muons and jets; each of them flies through the CMS detectors and creates electrical signals which carry the information about the particle identity and quantities. A representation of this is shown in Fig. 3.1.
During a bunch crossing many proton-proton collisions occur and while only a small fraction of those produce interesting events, most of them produce visible particles, causing the so-called pileup events. The PF algorithm enables the reconstruction of the primary vertex of the event under study while identifying and rejecting all the particles from pileup events. This process is called pileup mitigation.

The PF algorithm starts elaborating the information from the almost detector level, simpler PF objects (tracks and energy deposits), then links the PF objects in more global candidates and finally reconstructs the particles and primary vertex. These three consecutive steps which will be shortly described in the following paragraphs.

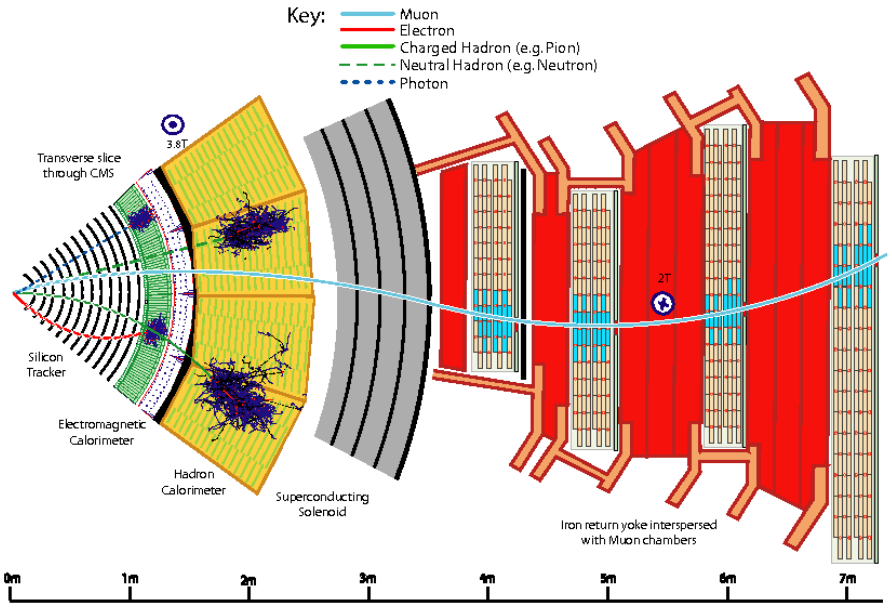

Figure 3.1: Schematic representation of the specific particle interactions in a transverse slice of the CMS detector. [36]

Determination of PF objects

Track candidates are built starting from seeds of pairs or triplets of hits in the inner tracking system, called tracklets. These tracklets are built by iterating a Combinatorial Track Finder [37] and later extrapolated to the outer layers of the trcking system in order to find compatible hits, which are assigned to the track if the fit of the expected flight path is of good quality.
The most prominent tracks such as those from charged particles with large momentum are reconstructed first. Their hits are then removed to decrease the combinatorial complexity for reconstruction of less prominent particles.
Taking a $t\bar{t}$ event subject of the data analysis in this thesis (part III) as example, the computational time on a commercial CPU to reconstruct all the event tracks is about $\sim 0.7\,\mathrm{s}$ and quickly increases with the number of pileup events [37] until the reconstruction fails. The luminosity increase expected for the next LHC upgrade and the consequent pileup increase will require a new reconstruction algorithm, as discussed in Chapter 4, in order to restore the reconstruction efficiency to the current levels.

Energy deposits by particles are measured by the calorimeter system and the fine segmentation these detectors allows the deposit to occur in a cluster of detector cells. The cells whose energy measurement is over a threshold are considered clustering starting points and the neighboring cells are subsequently added if their energy measurement is at least twice their noise level. In order to resolve energy deposits coming from different particles, the energy deposit profile is fitted to a Gaussian-based model. Cluster positions are expressed in the (η, ϕ) plane for barrel of both ECAL and HCAL and in the (x, y) plane for the endcaps and preshower calorimeters.

As the muons are the only charged particle to be observed outside the solenoid magnet in the muon chambers, the reconstruction of their tracks is slightly different. Track segments are formed by clustering hit in the DT or CSC subdetectors (see subsection 2.1.3) and a *standalone muon* tracks are reconstructed from these segments exploiting the full muon system readout.

Link Algorithm

The link algorithm combines the tracks and energy clusters reconstructed in the previous step. The algorithm must always consider the fact that electrically neutral particles are only appear in the detector as energy deposits, hence they do not have any associated track.
If several tracks match the same cluster in the calorimeter, or vice versa, only the combination with the smallest distance is kept. Links between HCAL and ECAL clusters are created in a similar way [37].
As for muons, the standalone muon tracks are linked with the compatible one in the inner tracker system.

Particle and primary vertex reconstruction

The final reconstruction of the particles is performed by an iterative algorithms which identifies the physics objects by combining the information of various PF objects. The reconstruction logic depends on the particles and will be described in the following subsections.
Prominent muons are reconstructed first and their expected energy deposits in the calorimeters are removed from any further reconstruction. Electrons are then reconstructed using tracks that are matched to ECAL clusters. Since electrons lose energy before entering the calorimeter by emitting bremsstrahlung photons, nearby ECAL energy deposits which are compatible with such photons are added to the electron candidate. Charged hadrons are reconstructed from the combination of the remaining tracks and HCAL clusters. A compatibility between the momentum of the particle candidate and the energy deposit is also verified. If their are not compatible but a related activity in the muon system is present, the particles are identified as low quality muons. At last, neutral hadrons and photos are reconstructed solely by calorimeter clusters with no matched tracks; the particle is identified as a neutral hadron if the HCAL reports a higher energy deposit or as a photon as the energy deposit is higher in the ECAL.

When a number of particles are reconstructed, a primary vertex can be located in order to select all the particles originating from it and hence forming the main event, and rejecting the remaining ones which are attributed to pileup collisions. In order to locate the vertex, the z coordinate of the intersection between high quality tracks and the beam direction is computed. Tracks with similar intersection points are grouped together and a number of collision vertices are inferred [37]. Finally, the position of each vertex is determined using a fit method and the vertex associated with the highest sum of scalar transverse momenta is identified as the primary vertex.

3.2.2 Muons

As the CMS name may suggest, muons play an important role in the experiment. In order to be able to reconstruct muon over a large momentum range, two different reconstruction strategies are implemented.
The reconstruction of *tracker muons* starts from tracks with $p > 2.5\,\text{GeV}$ and $p_T > 0.5\,\text{GeV}$ in the inner tracking system which are extrapolated to the outer muon system. After having considered the multiple scattering processes in the detector materials, if a compatible hits in the outer muon system is found, the object is identified as a tracker muon [37]. Its momentum is extracted from the inner track measurement.
In case of higher energy muon, multiple hits in the muon system can occur since the particle is able to penetrate more than one plane. These hits are linked in muon tracks which are extrapolated inwards, as described above, to form a *global muon* track. In this approach, the muon momentum is calculated from the measurements of both the inner tracker and the muon system.
The two reconstruction strategies allow the PF algorithm to identify 99% of all muon which are produced within the acceptance of the CMS detector, as measured in $Z/\gamma^* \to \mu^+\mu^-$ events in 2016 collision data [38].

Once a muon candidate is identified, its isolation is computed using the activity related to other particles nearby the muon track. By requiring a sufficiently isolated muon it is possible to prevent the false identification of an energetic hadron as a muon. The track is confirmed as an isolated muon if the sum of the transverse momenta from objects in a cone whose radius is $\Delta R = \sqrt{\Delta\eta^2 + \Delta\phi^2} = 0.3$ around the muon track does not exceed $\sim 10\%$ of the muon's transverse momentum.

3.2.3 Electrons

The reconstruction and identification of electrons is generally more inefficient and more error prone than the muons one. In fact, electrons are mainly identified using tracks in the inner detector matched with ECAL clusters and both of these measurements also involve other particle types. Additionally, the intense magnetic field causes charged particle to lose energy by emitting bremsstrahlung photons with a total radiating power strongly dependent on the particle energy and inversely dependent on particle mass, $P \propto (E/m)^4$. Additional bremsstrahlung emission is also caused by interaction with the detector material. As a result, the energy loss because of bremsstrahlung is potentially significant and the photon emissions cause the trajectories to exhibit non-Gaussian deviations.
In order to mitigate the effect of the energy loss, a ECAL cluster which appears as caused by an electron is joined with compatible energy deposits in along the ϕ direction to form a super cluster (SC). The SC position is determined by an energy-weighted mean over all associated cells.
In order to accurately reconstruct the electron track, on the other hand, powerful fit techniques are implemented [36].

The electron identification and tracking efficiencies were measured for $Z/\gamma^* \to e^+e^-$ events in 2016 collision data [39]. The track finding efficiency was found to be $\sim 95\%$ in the range $25\,\text{GeV} < p_T < 500\,\text{GeV}$ and $|\eta| < 2.1$.

3.2.4 Jets

A jet is a narrow cone of hadrons and other stable particles produced by the hadronization of a quark or gluon produced by the pp collision. Obtaining information on the produced jets give access to the kinematic quantities of the partons involved in the hard scattering process.
In order to form the particle cluster know as jets, three main algorithms are used: the k_T [40], anti-k_T [41] and the Cambridge-Aachen [42] algorithms.

Jets used in the analysis in part III of this thesis were clustered with the anti-k_T algorithm with a distance parameter of $R = 0.4$ in the (η, ϕ) plane. The CMS implementation of this algorithm relies on the FASTJET package [43].
The anti-k_T algorithm merging of two objects, i and j, is governed by the value of the parameter d_{ij}, calculated for each pair of particles under scrutiny.

$$d_{ij} = \begin{cases} \min\left(p_{T,i}^{-2}, p_{T,j}^{-2}\right) \cdot \frac{\Delta\eta_{ij}^2 + \Delta\phi_{ij}^2}{R^2} & , \text{ if } i \neq j \\ p_{T,i}^{-2} & , \text{ if } i = j. \end{cases} \tag{3.2.1}$$

Particles pairs with a smaller d_{ij} value are merged earlier and one can decide the maximum dimension of the jet with the R parameter. In fact, the d_{ij} value for a hard particle and a soft one will be much smaller than the d_{ij} value for similarly separated hard particles. The anti-k_T algorithm provides a robust reconstruction of the jet axis and a almost circular jet shape in the (η, ϕ) plane.

Both the jet energy scale (JES) and the jet energy resolution (JER) must be calibrated, in read data as well as in simulated events data. The JES correction is the elimination of the energy offset caused by pileup events while the JER correction is the definition of the true energy spread of the jet. An estimation of these errors is computed by comparing simulated di-jets events in the cases of pileup and no pileup modeling and by performing measurements inside of random cones in events recorded with a zero-bias trigger. Jets also contain information about the flavour of the originating quark so jet flavour corrections are necessary and derived from simulations by comparing predictions of complementary event generators, PYTHIA [44] and Herwig++ [45].

The jet energy calibration uncertainties on the full dataset recorded from 2016 to 2018 [46] are reported in Fig.3.2. For central jets with $p_T > 30\,\text{GeV}$, the total uncertainty is below 2% and is dominated by the jet flavour dependence while the pileup offset is of minor importance.
Moreover, the uncertainty is not dependent on the pseudorapidity η in the central region $|\eta| < 2.5$ and amounts to approximately 2.5% for jets with $p_T \simeq 30\,\text{GeV}$. Again, the jet flavour uncertainty is dominant in the central detector while the other uncertainties, including the pileup modeling, gain importance in more forward regions.

b-Tagging

The data analysis of the $pp \to pt\bar{t}p$ process, studied in part III of this thesis, as many other data analyses, includes the reconstruction of two jets originating from the decay of bottom, also called beauty, b quarks, each originating in turn by the decay of a top, also called truth, t quark. Correctly recognizing the jet as a b-jet is process is therefore of great importance for these analysis. This task, called b-tagging is assigned to algorithms based on the distinctive properties of

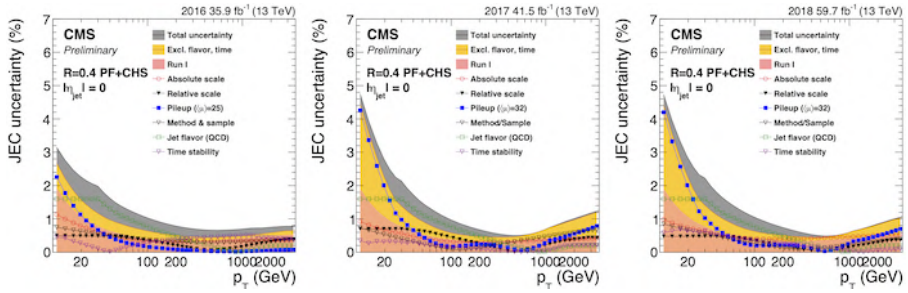

(a) Jet energy calibration uncertainties as a function of p_T.

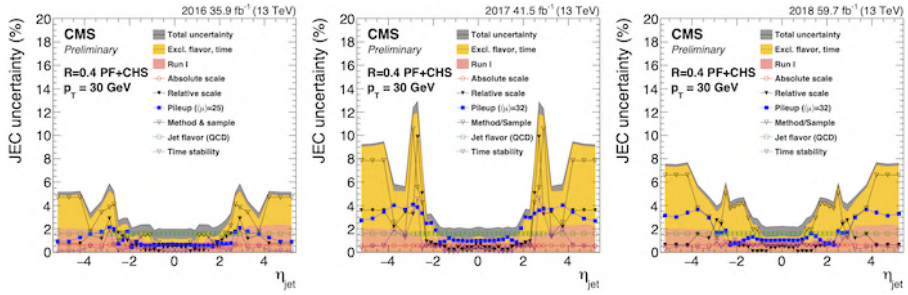

(b) Jet energy calibration uncertainties as a function of η.

Figure 3.2: Jet energy calibration uncertainties for the dataset from 2016 to 2018 for central jets as a function of p_T and for jets with $p_T \simeq 30\,\text{GeV}$ as a function of η [46]

b hadrons. In fact, b quarks have a high mass tend to form hadrons with masses of the order of 5 GeV which have a peculiarly long lifetime of the order of picoseconds. The long-lived b hadrons travel a significant distance in the detector before decaying at a secondary vertex. The displacement with respect to the position of the primary vertex, typically $\sim 1\,\text{cm}$ at a momentum of $\sim 100\,\text{GeV}$, can be resolved by exploiting the high spatial resolution of their decay products, especially in the semileptonic decay channel $b \to l\nu X$. Because of the high b mass, the jets resulting from b-hadrons are generally broader than the ones originating from other lighter quarks and the lepton from the semileptonic b decay is typically soft and not isolated.
Recent b-tagging algorithms implemented in the CMS software framework combine all the information on a jet available from the detectors to determine its b-tag [47]. The performance of such algorithms can be quantified by the probability of correctly identify a jet coming from a b quark as a b-jet and by the probability to mistakenly identify it (mistag). As these probabilities vary from data to simulation, the algorithms need to be calibrated in order for the simulation to be corrected with scale factors.

The *deepCSV* b-tagging method [48] will be briefly described as it is the one used in the analysis in this thesis. This algorithms exploits the advances in the field of deep machine learning to improve the identification of b-jets and it differs from previous algorithms, such as the *CSVv2* tagger, for its more numerous hidden layers and nodes per layers, which allow a simultaneous training for all jet flavours. On the other hand it uses the same algorithm for secondary vertex reconstruction than its predecessor, called *Combined Secondary Vertex* in its

second revision (*CSVv2*) [47].
A jet is identified as a *b*-jet if the discriminator output exceeds a threshold value, called *working point*, which is chosen as a parameter.

The performances of the deepCSV and the other *b*-tagging algorithms were measured in simulation and compared to data from the 2016 dataset.
Fig. 3.3a shows the misidentification probability as a function of the *b*-tagging efficiency in simulated $t\bar{t}$ events. At a misidentification probability of 1% the tagging efficiency against *udsg* jets (produced from gluons and u, d and s quarks) amounts to approximately 68% while the efficiency drops to approximately 43% against *c*-jets.
Fig. 3.3b shows the comparison of the deepCSV discriminator distribution between measured and simulated jets. The agreement between real and simulated data is reasonable in a large transverse momentum range $50\,\text{GeV} < p_T < 250\,\text{GeV}$. The residual differences can be corrected according to the data analysis phase space.

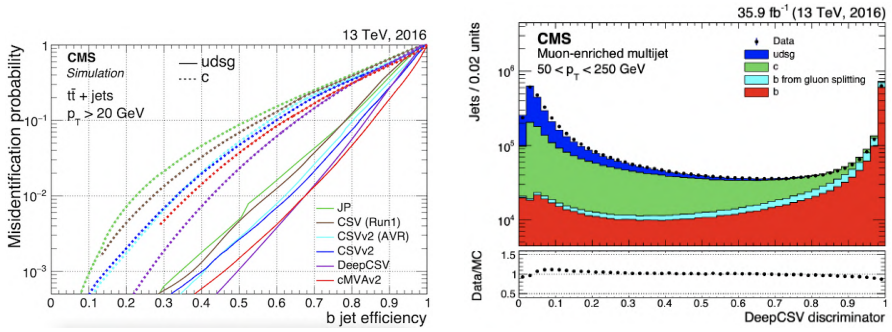

(a) Comparison of misidentification probability versus *b*-tagging efficiency for various tagging algorithms as measured in simulated $t\bar{t}$ events.

(b) Comparison of the discriminator output of the deepCSV algorithm between data and simulation in muon-enriched QCD multijet events.

Figure 3.3: Performances of the deepCSV *b*-tagging algorithm for the 2016 dataset [47].

3.2.5 Missing Transverse Energy

The sum of the transverse momenta of all particles produced in the collision is expected to be zero, as the incoming protons carry a negligible transverse momentum and its sum is conserved during the collision [36]. Since the CMS detector is almost completely hermetic, it is required to reconstruct the transverse momentum of all the measurable event objects. The Missing Transverse Energy (MET) is an important quantity to obtain information about particles that leave the experiment undetected, such as neutrinos and hypothetical BSM particles. For instance, the analysis in part III of this thesis includes the reconstruction of a neutrino originating from the semileptonic decay of one t quark. The MET, also denoted with the symbol $\not{E}_T$, is defined as the magnitude of the negative vectorial sum $\vec{p}_T^{\,miss}$ of the measured $\vec{p}_T$ of all measured objects, as

$$\vec{p}_T^{\,miss} = -\sum_{i}^{particles} \vec{p}_{T,i} \tag{3.2.2}$$

$$\not{E}_T = |\vec{p}_T^{\,miss}| \quad . \tag{3.2.3}$$

The determination of MET is affected by the reconstruction inefficiencies and inaccuracies for all other particles and therefore relies on the good performance of the PF algorithm. The MET description is especially deteriorated by misidentified or misreconstructed muons with large transverse momenta [36], such as the muons from cosmic rays which seldom traverse the CMS detector in coincidence with a bunch crossing. It is possible to reject these particles by requiring the muon trajectories to be within 1 cm from the beam axis, while accounting for the displaced muon tracks originating from the leptonic decay of b hadrons.

An estimation of the performance of MET reconstruction was performed using recorded collision data [49]. The MET scale and resolution were studied in $Z/\gamma^* \to l^+l^-$+jets events where the Z boson was accurately reconstructed without any source of missing transverse momentum. Hence, it is possible to study the MET quality by comparing the momentum of the Z boson to that of the hadronic recoil system, while a separate study was necessary for the transverse and parallel MET components with respect to the Z boson direction.
The measured scale and resolution in data are in agreement with the expectations from simulation [49].

Chapter 4

CMS upgrade for High Luminosity LHC

The Large Hadron Collider operation and its experiments have been providing excellent collision data and physics results for more than a decade. In order to extend the LHC discovery potential an upgrade schedule of the machine and the experiments has been studied and is being implemented in order to keep searching for physics beyond the standard model (BSM) and improving the current measurements on rare processes.
In 2015, the LHC started providing the experiments with *pp* collision with a 13 TeV center of mass energy. The LHC upgrade program will entail a small increase in collision energy but most of its ambition is directed towards a sharp increase in luminosity.
The present LHC baseline plan, as defined at the end of 2020 is schematically shown in Figure 4.1. The upgraded accelerator will start its operation in 2027 and the decade following these upgrades is called *Phase-2* of LHC operation or, most commonly, *High Luminosity LHC* (HL-LHC). The much higher collision rates will exceed the capabilities of the current CMS detector, which is consequently undergoing a significant upgrade to continue to function efficiently. In this chapter, the future of the LHC and CMS will be briefly discussed.

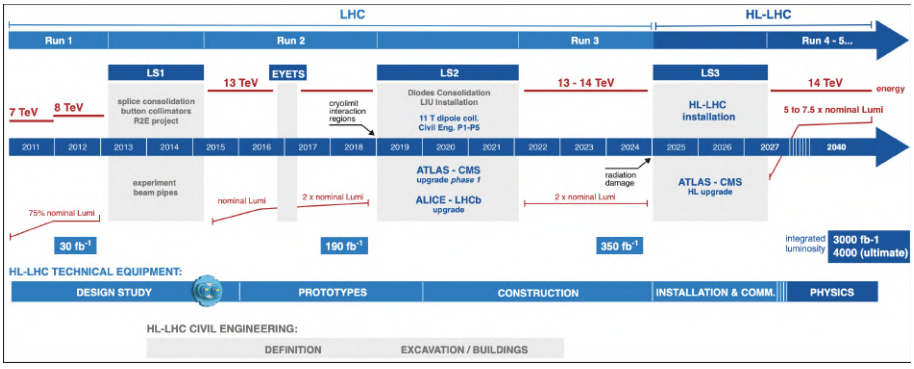

Figure 4.1: Plan for LHC and High Luminosity LHC showing the collision energy (upper line) and luminosity (lower line) [50].

4.1 High Luminosity LHC

The upgrade process for the Large Hadron Collider is already ongoing and has seen the realization during LS2 of some of the major civil works required for the HL-LHC project, schematically shown in Fig. 4.2. Some of the works involve the replacement of existing LHC equipment (in Points 2, 6, 7 and 8). The work at Point 4 involves infrastructure both above and below ground and essentially consists of upgrades to the cryogenic system. More significant work will be necessary at Points 1 (ATLAS) and 5 (CMS), including civil engineering interventions to create the space required for the new technical installations.
Starting in 2024, the Long Shutdown 3 (LS3) will be approximately 2.5 years long and the accelerator machine will be significantly overhauled, with the introduction of a plethora of innovative, yet challenging technologies. These include: novel superconducting magnets able to generate a magnetic field up to 12 T, very compact new superconducting RF cavities, high-current superconducting links with almost zero energy dissipation. The optics in the CMS interaction region will be also upgraded to produce more tightly focused and overlapping beams at collision. At the end of the upgrade process, there will be a total length of more than 1.2 km of modified machine and 1 km of additional technical services [50].

The targets for the new High Luminosity LHC project were established by CERN at the end of 2010 [51]. While the target beam energy is kept at 7 TeV, the target instantaneous luminosity is set to $\mathcal{L}_{lev} = 5 \cdot 10^{34}\,\mathrm{cm}^{-2}\mathrm{s}^{-1}$ although the machine will be able to provide an instantaneous luminosity of $\mathcal{L}_{peak} = 2 \cdot 10^{35}\,\mathrm{cm}^{-2}\mathrm{s}^{-1}$ at the beginning of each fill.

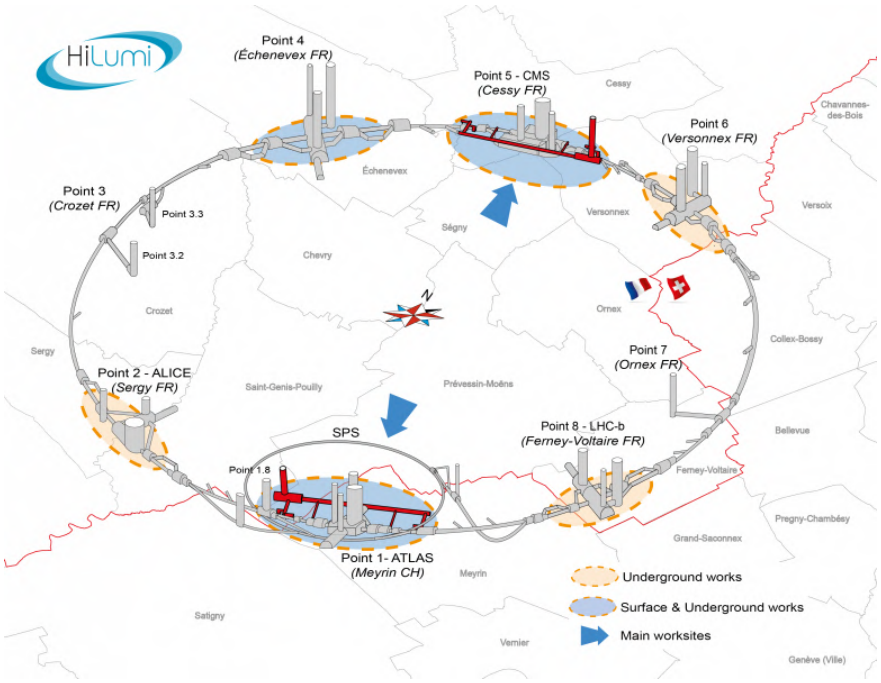

Figure 4.2: Diagram showing the location of the work required for the HL-LHC [50].

HL-LHC is also expected to provide the experiments with an integrated luminosity of $L_{year} = 250\,\text{fb}^{-1}$ per year which would amount to a staggering total of $L_{tot} = 3000\,\text{fb}^{-1} = 3\,\text{ab}^{-1}$. As a comparison, the total integrated luminosity for Run 1, 2 and 3 of LHC is expected to be $L_{LHC} \simeq 350\,\text{fb}^{-1}$.

4.2 CMS upgrade

The astonishing luminosity levels provided by the new accelerator machine will pose as both a thrilling opportunity but also as a cumbersome challenge. The CMS physics program will benefit from the high luminosity for precision measurements, including detailed studies of the new phenomena discovered during Run 1, 2 and 3, and for direct searches for new physics. The study of the Higgs boson will continue to be pivotal to the experiment program but, although no new particles have been observed yet at the TeV scale, there is still the possibility that they exist but the cross sections of their production are lower than expected or they are more difficult to observe experimentally. Improvements in analysis techniques and and large samples of data will likely enable to search for even more rare signals and evidences for dark matter [52].
From the detector point of view, however, the HL-LHC conditions will be extremely challenging. The nominal leveled luminosity of $\mathcal{L}_{lev} = 5 \cdot 10^{34}\,\text{cm}^{-2}\text{s}^{-1}$ will imply an average of 140 *pp* interactions during each bunch crossing. An even more ambitious scenario is to operate at $\mathcal{L}_{lev} = 7.5 \cdot 10^{34}\,\text{cm}^{-2}\text{s}^{-1}$ which would imply a 30% increase in luminosity but an average of 200 *pp* collisions. Only $\sim 1\%$ of those interactions will be of interest to CMS while the rest will be pileup. From the detector and software descriptions in sections 2 and 3, it was already clear that the spatial overlap of tracks and energy deposits from pileup degrade the identification and the reconstruction of the hard interaction. In addition, the higher collision rate, and hence the higher production particles, results in more radiation damage over the life span of the detectors. The upgraded CMS detector will have to survive and function efficiently in the much harsher environment while producing a higher data rate.

The HL-LHC challenge for the CMS detector required the study of a completely innovative approach to the particle detection and event reconstruction. Given the depth of the CMS upgrade project [52], its full description is not in the scope of this thesis. However, the development of innovative detector technologies will be the main topic of part II of this thesis, with a particular focus on radiation hard detector technologies for timing measurement. In fact, the upgrade project set the plan to include a much more precise timing information to the spatial particle tracking, in order to achieve what is now generally known as *4D tracking*.
The new CMS detector for HL-LHC, also called CMS detector Phase-2, will include an utterly new detector, the *MIP Timing Detector* (MTD) [53], which will give timing information for MIPs with a time resolution as low as 30 ps at the beginning of HL-LHC operation in 2027.

In this chapter, a glimpse of the innovative concept of 4D tracking will be given and the project for the new MIP timing detector will be briefly described.

4.2.1 4D tracking

The upgraded CMS detector will use the time information for the purpose of assigning charged tracks to the correct interaction vertex among 200 or more *pp* collisions per each bunch crossing. The ensemble of spatial and temporal information on a track is generally referred as 4D tracking and is a new paradigm in the CMS experiment which is expected to obtain the same reconstruction efficiency of the LHC age in the harsh HL-LHC conditions.

This is possible because within the bunch crossing, the single *pp* collisions do not all occur at the same exact time but are distributed over time interval with a $180 - 200$ ps RMS value. Due to the longitudinal extent to the beams, during the bunch crossing, there will be a region where the two bunches overlap. Aside from the time distribution, the collisions also occur in this overlap volume and are hence spatially spread along the beam axis of about 4.5 cm RMS value. This time and space spread of the collision is also typical in LHC conditions but for LHC luminosity levels, the spatial (3D) tracking was sufficient to separate the vertices, match the tracks from their origin vertex and reject pileup.
Figure 4.3a shows the vertices distribution in HL-LHC along the beam direction for pileup levels ranging from 30 (LHC) to 140 and 200 (HL-LHC). In addition, Fig. 4.3b shows the comparison of the probability density functions for the same scenarios. In high luminosity conditions, the vertices will have the same spatial spread as the ones in LHC conditions but the peak value of the line density dN_V/dz of the number N_V of collision vertices is expected to increase from the $0.4\,\mathrm{mm}^{-1}$ value at LHC condition, to $1.2\,\mathrm{mm}^{-1}$ for 120 pileup collisions and up to $1.9\,\mathrm{mm}^{-1}$ for a HL-LHC scenario with 200 pileup collisions. The upgraded tracking system of the CMS Phase-2 detector will be characterized by a higher spatial granularity but such a high line density is expected to increase the probability of spatial overlaps between hits and consequently a substantial failure rate increase in the PF algorithm for the event reconstruction and pileup rejection.

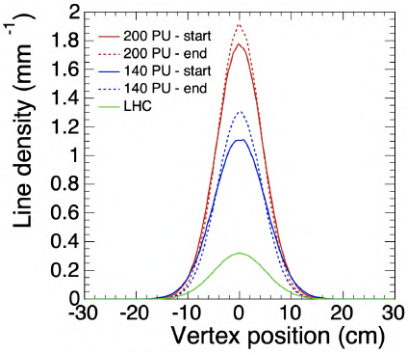

(a) Comparison of the distributions of the vertices along z direction between LHC and HL-LHC conditions. The solid line refers to the start of the fill, the dashed refers to the more focused beam at the end of the fill.

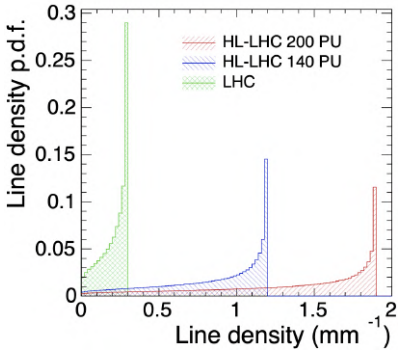

(b) Probability density functions of the line density along the beam axis for LHC and HL-LHC pileup levels. The modes of the distributions are 0.3, 1.2 and $1.9\,\mathrm{mm}^{-1}$, their means are are 0.2, 0.9 and $1.4\,\mathrm{mm}^{-1}$.

Figure 4.3: Comparison of the characteristics of the vertices between pileup levels at LHC conditions ($\simeq 30$) and at two scenarios for HL-LHC (140 and 200 pileup) [53].

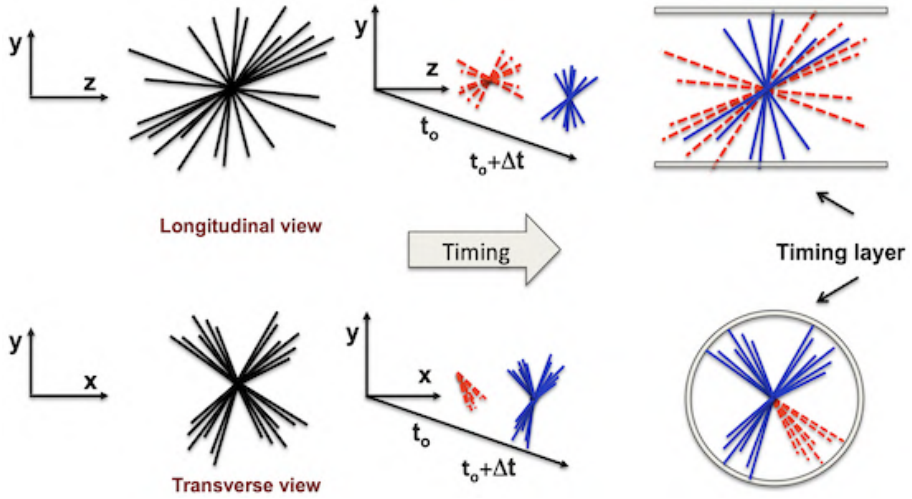

Figure 4.4: Schematic representation of 4D tracking in distinguishing overlapping events [32].

The inclusion of the time information into the 4D tracking is the solution of choice for the CMS Phase-2 upgrade program. In fact, including a time information on a track enables the reconstruction of the time at which the collision vertex occurred. Other tracks originating roughly from the same vertex position but at a different time will therefore be eliminated as they do not contribute to the same collision but they originated from a collision in the same position but at another time within the bunch crossing [32]. Fig. 4.4 explains schematically this process, in particular how the time measurement helps distinguishing between two overlapping events, even if all the tracks originate from the same point and the events overlap in both longitudinal and transverse views [32].

4D tracking in an upgraded CMS Phase-2 detector would also benefit the trigger. In fact, as shown in Fig. 4.5, a time information on the tracks enables the trigger to reject event topologies that look similar without the time information. This significantly reduces the trigger rate by eliminating all fake, time incompatible, events.

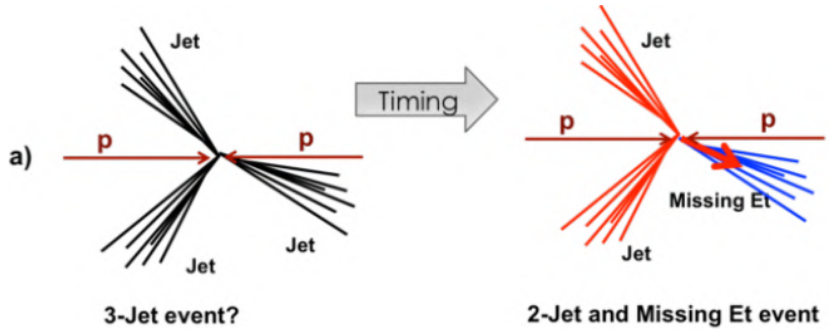

Figure 4.5: Schematic representation of the effect of timing information on trigger [32].

As it was described earlier, in a HL-LHC scenario of approximately 200 collisions per bunch crossing, each 25 ns, the vertices are spread in the time domain with a RMS value of $180-200$ ps and this value is expected to be nearly constant during the fill and almost completely uncorrelated with the vertices spatial distribution. A time information with a resolution of $\sigma_t \simeq 30-40$ ps would allow to figuratively slice the bunch crossing duration into $5-6$, $1\sigma_t$ long, time intervals, each containing $40-60$ collisions. A time resolution of this size would therefore reduce the 'effective multiplicity' of concurrent collisions, thereby recovering the Phase-1 quality of event reconstruction.
In order to recover the current CMS Phase-1 quality of event reconstruction, the upgraded CMS Phase-2 detector is required to provide a timing measurement to the tracks with a time resolution of $\sigma_t \simeq 30-40$ ps.

The $z-t$ map of the simulated and reconstructed vertices in Fig. 4.6 explains and demonstrates the power of the 4D tracking in reconstructing single collisions in a 200 pileup scenario. The spatial overlap is resolved as, according to simulation, the instances of vertex merging are reduced from 15% in 3D to only 1% in 4D. The use of timing information for each track reduces the number of the tracks from pileup which are mistakenly associated with the primary vertex of the hard interaction of interest.
For the worst case of a line density of 1.9 collisions per mm, peak density in the 200 pileup case, the average number of mistakenly associated tracks is reduced to less than its half if 4D tracking is implemented and the peak line density is effectively reduced to about 0.8 mm^{-1} [53], which roughly corresponds to the CMS Phase-1 pileup conditions.

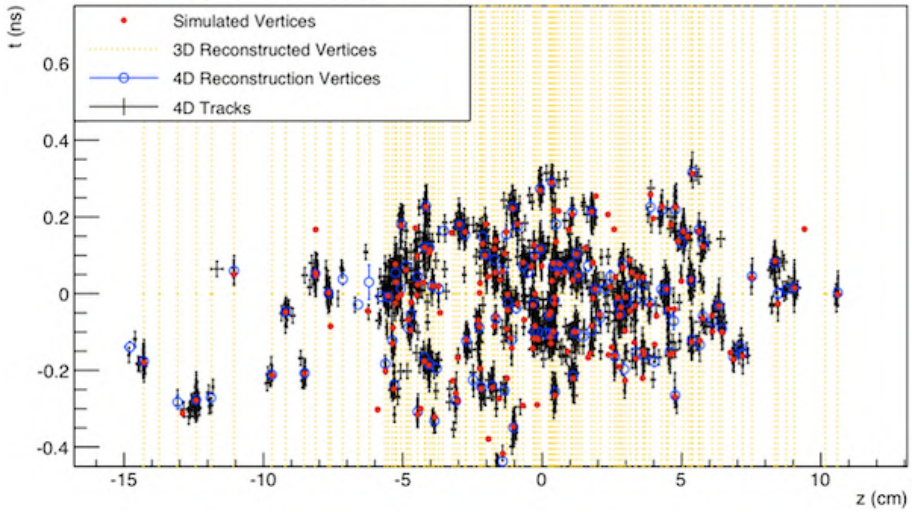

Figure 4.6: Simulated and reconstructed vertices spread over the z position (horizontal axis) and time (vertical axis), the $(0,0)$ point corresponding to the center of the interaction region at the instant when the two bunches completely overlap. The simulated vertices (red dots) refer to a scenario with 200 pileup collisions. The vertical yellow lines are the 3D-reconstructed (i.e. no time information) vertices, the black crosses and blue circles represent tracks and vertices reconstructed with 4D tracking with a $\sigma_t \simeq 30$ ps. Many of the vertices that are overlapped in the spatial dimension are clearly separated when time information is available [53].

In addition, the implementation of 4D tracking significantly reduces the number of tracks which are incorrectly associated to the primary vertex. The removal from the event of pileup tracks greatly improves the reconstruction and the understanding of the final state. As matter of example, having fewer pileup tracks incorrectly associated to the event will result in a lower probability of having them inside the isolation cone of an isolated lepton, hence improving the identification efficiency for signature leptons which are of most importance in many physics processes studied by CMS.

4.2.2 MIP Timing Detector

The goal for the MIP Timing Detector (MTD) of a required time resolution of $\sigma_t = 30 - 40\,\text{ps}$ is challenging but it has been shown to be achievable. However, based on the studies on the candidate detector technologies, it is also expected that the extremely intense radiation exposure will cause the time resolution to degrade approximately linearly with the integrated radiation dose. A fulfilling target would be to reach the end of the HL-LHC operation with a time resolution of $\sigma_t = 50 - 60\,\text{ps}$, with the luminosity-weighted average of $\sigma_t = 40 - 50\,\text{ps}$. In order to be hermetic as possible, the MTD geometry will have a cylindrical geometry and will be composed of a Barrel Timing Detector (BTL) and an Endcap Timing Detector (ETL), hence covering a pseudorapidity range of $|\eta| < 3$. The MTD geometry is constrained from the fact that it needs to fit within the existing CMS detector and minimize its impact on the outer detectors. The performance of the outer detectors is significantly limited by the amount of material in front of them, so a strict material budget constraint has to be taken into account.
Naturally, the new detector must also conform to the same requirements as the other subdetectors inside CMS, such as tolerance to high magnetic fields and a robust mechanical design in order for it to survive for the full duration of the HL-LHC program.

In the barrel region, the MTD will be installed in the space between the last layer of the outer tracker (OT) and the inner extremity of the barrel electromagnetic calorimeter (ECAL). The BTL will therefore cover the pseudorapidity range of $|\eta| < 1.5$. For the endcap region, in the $1.6 < |\eta| < 3$ pseudorapity range, on the other hand, the MTD will occupy the thin gap between the tracker and the Phase-2 High Granularity Calorimeter (HGCal), a utterly new detector that will replace the current endcap calorimeter [54]. The installation of both parts must occur alongside the neighbouring detectors and only the endcap will be accessible during future Technical Stops or Long Shutdowns.
Fig. 4.7 provides a schematic recap on the MTD main characteristics and geometry as it is implemented in CMSSW.

For both the BTL and the ETL, the detector elements, also called sensor segments or cells, should be small enough to keep the detector occupancy lower than a few percent but high enough to limit the total number of channel for the detector to produce a manageable data volume.

The most challenging requirements for the whole MIP Timing Detector, however, regards its radiation hardness. As for all other CMS Phase-2 subdetectors, the MTD is required to operate efficiently throughout the whole HL-LHC era, withstanding a total integrated luminosity of at least $L_{tot} = 3000\,\text{fb}^{-1} = 3\,\text{ab}^{-1}$. The radiation exposure for the different parts of the MTD are predicted using

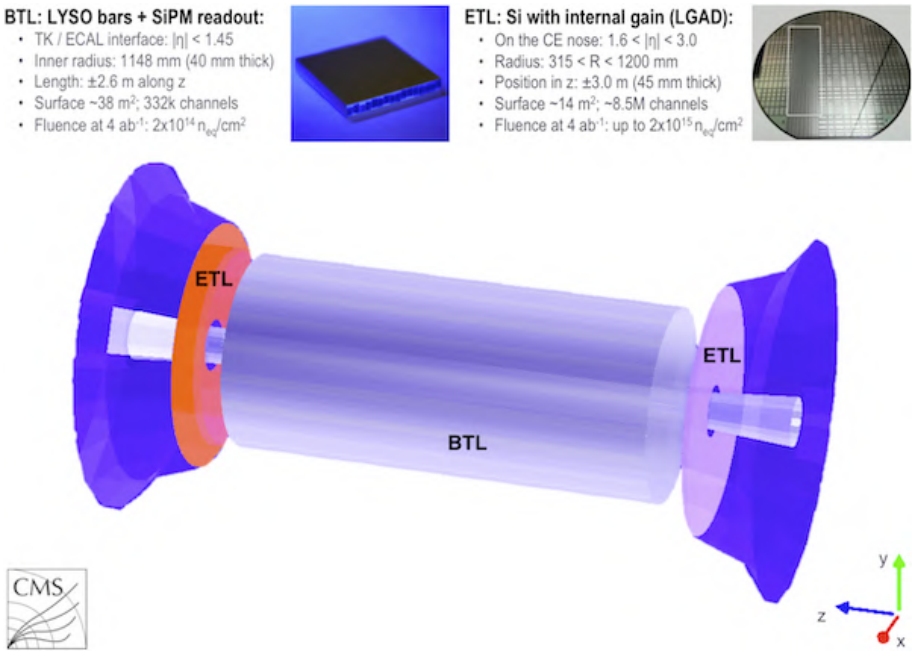

Figure 4.7: A schematic view of the MTD geometry as implemented in CMSSW. It comprises a barrel layer (light blue cylinder), equipped with fast scintillator detectors, and two silicon endcap layers [53].

simulation tools with the currently expected set of parameters. The received radiation dose will vary greatly between the ETL, high pseudorapidity region, and the central region occupied by the BTL. The expected fluence is also calculated in terms of the equivalent number of 1 MeV neutrons in silicon per squared centimetre, $\mathrm{n_{eq}cm^{-2}}$. At an integrated luminosity of 3000 $\mathrm{fb^{-1}}$, the BTL will have received a radiation dose of up to 30 kGy, or rather a fluence up to $1.9 \cdot 10^{14}\,\mathrm{n_{eq}cm^{-2}}$. The most forward (i.e. high-η) rings of the ETL are expected to receive a dose as high as 450 kGy, corresponding to a fluence of $1.6 \cdot 10^{15}\,\mathrm{n_{eq}cm^{-2}}$. Moreover, all the MTD components must be qualified to withstand radiation level at least a safety factor 1.5 higher than the prediction, in order to account for uncertainties in the geometry model, in the *pp* inelastic cross-section, and technological variations between sensors.

The requirements on the MTD are significantly different in the barrel and endcap regions. Besides the very different radiation doses, the smallest ETL rings receiving at factor of 30 higher dose than the most irradiated past of the BTL, the surface areas of the BTL is approximately 2.5 times the surface area of the two endcaps. Moreover, the installation of the ETL is later than the BTL one, requiring the choice for the BTL of a technology that needs relatively little research and development.
After five sensor technologies were investigated, a choice of two different ones the ETL and the BTL was made, based on the considerations on mechanical constraints, performance, radiation tolerance, cost and the upgrade schedule. For the BTL, the best available technology is a crystal scintillator that is read out with SiPMs. For the endcaps, the LGAD technology was selected [53].

The following subsection will give a brief description of the two detectors making up the MTD.

Barrel Timing Detector

The Barrel Timing Layer is a 40 mm thin cylindrical detector whose inner part is 1148 mm from the beam and whose total active length along the z direction is about 5 m. The total active surface results in about 38 m^2.
The material for the scintillating crystals is Lutetium Yttrium Orthosilicate (LYSO:Ce), and the readout is performed with silicon photomultipliers (SiPMs). The detector cell consists of a crystal bar oriented along the ϕ direction for a length of 57 mm and a width of 3 mm along the z direction. The thickness along the r radiation is variable as a function of the barrel length in order for the particles coming from the center of CMS to cross the crystal for the approximately the same path length: the crystal is thicker (3.7 mm in the center ($|\eta| < 0.7$) and gets thinner as the inclination of the tracks increases, 3.0 mm for $0.7 < |\eta| < 1.1$ and 2.4 mm for $1.1 < |\eta| < 1.48$. A SiPM will be coupled to each end of the bar, in order to provide two time measurements in order to eliminate the effect of the time delay of the light traveling along the crystal. The SiPMs will have a length of 3 mm along ϕ and a variable length along r, approximately matching the crystal radial thickness [53].
The TOFHIR (Time-of-flight, High Rate) ASIC[1] is the dedicated chip designed for the readout of 32 SiPMs based on leading edge (LE) discriminators followed by a time-to-digital converter (TDC) [53].
Fig. 4.8 provides a visual explanation of the orientation of the components which constitute the BTL.

Both LYSO based scintillators and SiPMs devices are extremely mature technologies and are proven capable of achieving time resolutions in the order of $\sigma_t \sim 10 - 20$ ps and radiation tolerant up to neutron equivalent fluence of $3 \cdot 10^{14}\, n_{eq} cm^{-2}$, when cooled to $T = -30°C$ [55].

[1] ASIC stands for application-specific integrated circuit

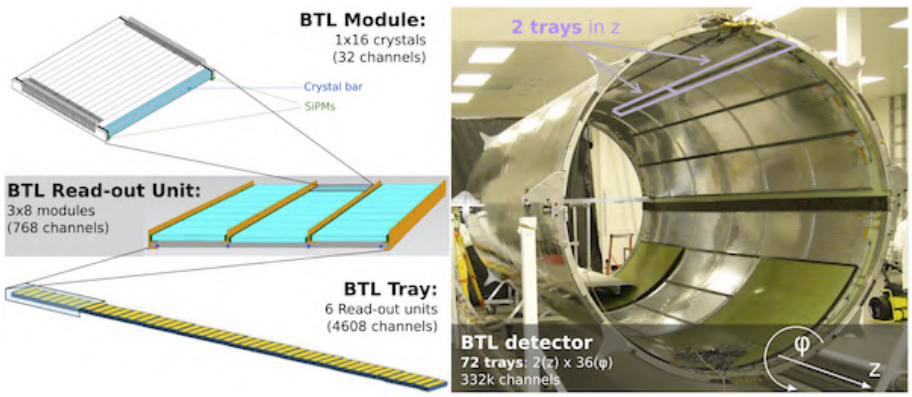

Figure 4.8: Overview of the BTL and the hierarchical arrangement of its components: starting from the top left crystals, modules, readout units, tray and the tray collocation inside of the barrel (right) [53].

Endcap Timing Detector

The ETL is composed of two disks, one on each side of the interaction point at a distance $z \simeq \pm 3\,\text{m}$ and with a radial extension of $315\,\text{mm} < r < 1200\,\text{mm}$. The ETL volume is mechanically and thermally separated from the rest of the CMS detector volume. Unfortunately, the geometry of this cover prevents the ETL from extending to $|\eta| > 3$ ($r < 315\,\text{mm}$), hence preventing it from matching the full acceptance of the upgraded Tracker, which will reach to $|\eta| = 4$.
Each endcap disk is 45 mm thick and contains two layers of silicon devices, hence providing an excellent time resolution thanks to the two hits per track. Each layer is covered by alternating active silicon sensors and service electronics so that the whole area of the disk is covered with active devices for both layers. The total active sensor area is about $14.4\,\text{m}^2$. Fig. 4.9 presents an exploded view of the ETL and its internal structure.

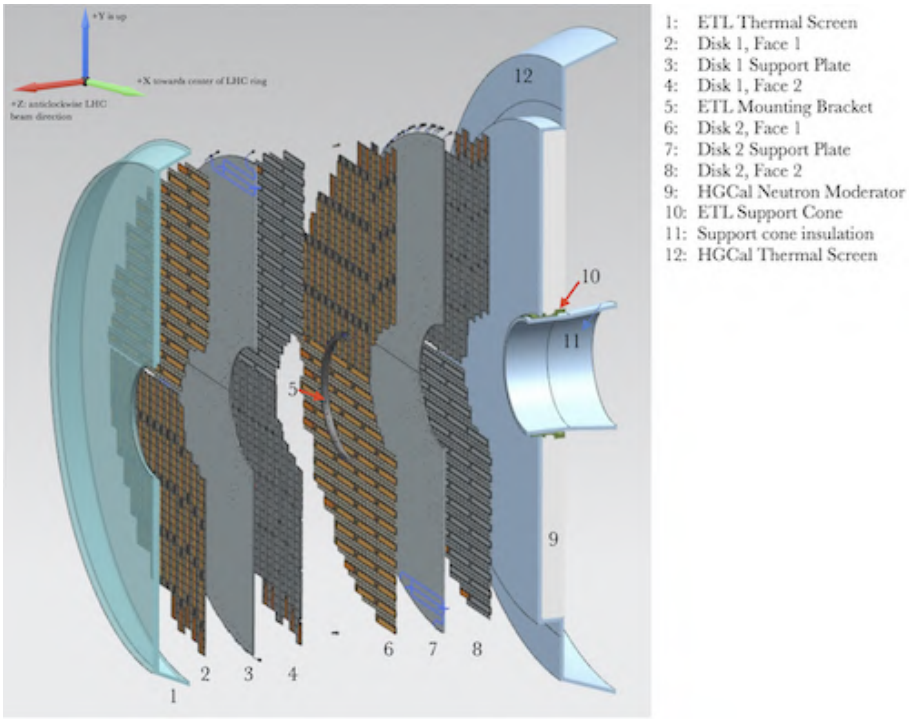

Figure 4.9: Exploded view of the ETL with the interaction point to the left of the image. The grey sections are the active areas of the modules and the orange bars represent the service hybrids. The detector is shielded from back-scattered neutrons from the HGCal and is enclosed in a thermal screen [53].

Although the high cost of such a big area covered by silicon sensors, the SiPM technology could not withstand the radiation levels expected for the most part of the ETL region. Therefore the sensor choice for the ETL was to use Ultra-Fast Silicon Detectors (UFSDs), planar silicon devices based on the Low-Gain Avalanche Detector (LGAD) technology [32]. These devices will be described in further detail in Section 7.2 in Part II of this thesis as I participated in the research and development effort for this detector technology. UFSDs incorpo-

rate a low, controlled charge multiplication in the signal formation mechanism in order to boost the signal amplitude while keeping a low noise level, hence providing an excellent performance in timing measurements. This multiplication results in an intrinsic gain of $10-30$ and the production of low jitter, fast-rising pulses. The research and development on this technology determined that the optimal geometry for this application has an active sensor volume with a thickness of $50\,\mu$m and an area of less than $2\,\mathrm{mm}^2$. Therefore, each ETL disk will comprise $4 \cdot 10^6$ sensor cells (pads), $1.3 \cdot 1.3\,\mathrm{mm}^2$. A ETL module will contain a 16×32 array of LGADs which will be read out by two bump-bonded ASICs, called Endcap Timing Readout Chips (ETROCs). The readout chip contains a leading edge discriminator, amplifiers and circuits to measure the Time-of-Arrival (TOA) of each particle and Time-over-Threshold (TOT) to measure the pulse height for time walk correction. The service hybrid contains two boards, a readout board, a power board and sends the data to the Level-1 trigger and to the rest of the data acquisition chain.
Radiation damage in UFSD has been extensively studied and at this point is reasonably understood and mitigated. It manifests in three main symptoms. It decreases the charge collection efficiency and increases the leakage current, both of these effects are moderate in a $50\,\mu$m thick sensor. The behaviour of UFSD at lower temperatures has been studied [56] so an operation at $\simeq -30°\mathrm{C}$ is possible to keep the leakage current and shot noise at bay. Thirdly, the radiation damage in UFSD reduces the sensor intrinsic gain and an intensive effort is being made to improve the technology. Recent studies on the irradiation of the latest UFSD productions are consistent in demonstrating that these devices maintain a time resolution below 40 ps up to fluences of $1.5 \cdot 10^{15}\,\mathrm{n_{eq}cm^{-2}}$ and the time resolution moderately degrades to $40-60\,\mathrm{ps}$ at a fluence of $3 \cdot 10^{15}\,\mathrm{n_{eq}cm^{-2}}$, which is relative to target integrated luminosity of the whole HL-LHC era, plus the safety factor [53] [57].

Part II

Innovative silicon detector technologies

Designing and building new particle detectors with ever improved performances is of paramount importance as current and next generation colliders are planned to provide very high interaction rates.
During my PhD I joined the TimeSpot project, aimed at studying and characterizing new detectors for the measurement of timing with improved precision. In addition, I worked on the research and development of innovative silicon detectors for the PPS detector of the CMS experiment and other future high energy physics experiments.
Part II of my thesis describes the works that I have performed in these contexts either within CMS and for future experiments. Given that all the systems described in this part are based on silicon detectors, first an introduction to the general features of solid-state particle detectors will be given before moving onto the specific technologies treated during my PhD.

Chapter 5

Principles of Silicon Detectors

Silicon and its properties have characterized the radiation detector technology, because of the immense level of knowledge on its characteristics, but also because it gives a great number of advantages in particle detection when compared to many other materials. First of all, it allows a good intrinsic energy resolution: an electron-hole pair is produced every 3.6 eV released by a particle crossing the material. This is of crucial importance as silicon detectors can be considered as solid state ionisation chambers. While in ionisation chambers the ionisation takes place in a gas, in silicon detectors it takes place in a semiconductor. For the same amount of energy $\simeq 30$ eV needed to ionise a gas molecule in an ionisation chamber, in silicon about 10 times the number of charge carriers are produced. Other important and useful features are its abundance in soil, its low energy band gap, the possibility to alter the gap properties by adding dopant atoms and the existence of a natural oxide SiO_2.
The small energy band gap causes some disadvantages as well: in order to be able to distinguish between the electrical signal produced by the passage of radiation and the thermal noise, the full detector volume must correspond to the depleted region of a *pn* junction whose thickness W increases with the applied reverse bias as $W \propto \sqrt{V}$.
In order to decrease the power consumption, the warm-up and the noise, the bias leakage current, or *dark current* must be as small as possible. This current is dominated by the thermally generated $e-h$ pairs, which cannot recombine in the presence of the electric field and then drift separately to the respective electrodes. Leakage current depends on the quality of the material and on the fabrication technique.

The depletion region can be seen as a parallel plate capacitor with dielectric in it, whose capacitance decreases with the square of the bias voltage until the whole semiconductor volume is depleted $V_{bias} = V_{FD}$, after which it remains constant:

$$C(V) = \begin{cases} \sqrt{\frac{q\varepsilon_{Si}N}{V_{bias}}} & \text{for} \quad V_{bias} \leq V_{FD} \\ \frac{\varepsilon_{Si}}{W} = const & \text{for} \quad V_{bias} > V_{FD} \end{cases} . \tag{5.0.1}$$

The full depletion voltage can be therefore determined by both the capacity curve as a function of the voltage $C(V)$ and its reciprocal squared $1/C^2(V)$. Typical values for a silicon detector capacitance are of the orders of hundreds of femtofarads ($\sim 100\,\mathrm{fF}$) for a single pixel.
In a real detector the electric field resulting from the application of the bias voltage is largely dependent on irregularities on the geometry of the detector and can cause local sensor breakdown. For this reason, the differences between a real detector and the idealised parallel plate capacitor must be taken into account.

5.1 Signal Formation

Radiation, including particles, lose energy via ionising and non-ionising processes when it travels in silicon. The non-ionising energy loss causes radiation damage to the semiconductor crystal, while the ionising one can also create electron-hole pairs and hence an electrical signal.
Silicon has a band gap of $E_{gap} = 1.12\,\mathrm{eV}$, which is one third of the mean energy needed to produce an electron-hole pair. At a temperature of $T = 300\,\mathrm{K}$, minimum ionising particle (MIP) produces approximately 75 electron-hole pairs per micrometer.

5.1.1 Induced current

The signal of a silicon sensor takes the form of a induced current pulse on the electrodes. Even if it is sometimes described as charge collection, signal does not start when the charge is collected, but when the charge begins to move inside the sensor. Consequently, it stops after necessary time for the whole charge to be collected (the so called *charge collection time*).
When an e-h pair is produced inside of the detector active volume two kind of scenarios are possible, according to the initial position of the pair:

1. if its initial position is about in the middle between the electrodes, the charge induced on the two electrodes is approximately the same. The two electrodes are crossed by the same density of field lines;

2. if it is closer to one electrode, field lines will be denser on this electrode; thus the amplitude of the induced signal will be larger.

Figure 5.1 shows the two circumstances.

When a charge moves through the sensor, the induced charge on the electrodes changes. The magnitude of the instant induced current on a single electrode i for a charge q is modelled by the *Shockley-Ramo's* theorem [58][59]:

$$I_i = -q\,\vec{v}(x) \cdot \vec{E}_w(x)\ , \tag{5.1.1}$$

where $v(x)$ is the charge velocity and depends on the applied electric field E and on the charge position x. E_w is called *weighting field* and is defined as the virtual electric field which is determined by applying to the collecting electrode i the $+1$ voltage potential state and 0 to the others. The weighting field depends solely on the detector geometry and it is independent of bias voltage.
With respect to a given electrode i, the currents induced by electrons and holes

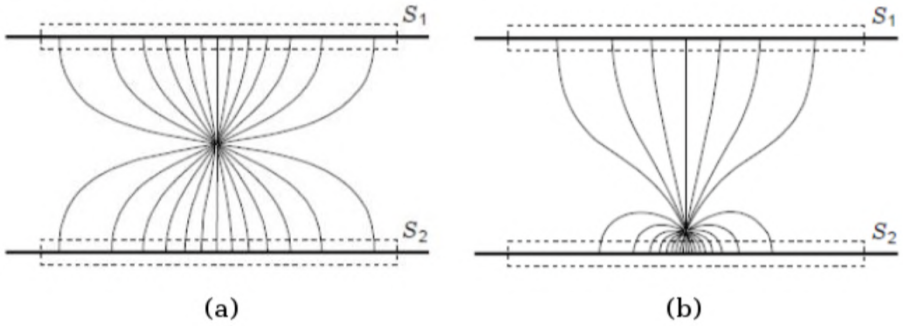

Figure 5.1: Field lines for a charge produced in the middle between two electrodes (a), close to one electrode (b).

add up because carriers of opposite charge sign drift in opposite directions. For a parallel plate geometry, since drift can be expressed in relation to the applied electric field E and the bias voltage V_b as $v = \mu E = \mu V_b/d$, and the electric fields E and E_w are constant until the charge reaches the electrode, the induced current I on the electrode i results:

$$I_i = -evE_w = -e\mu\frac{V_b}{d^2}\ , \tag{5.1.2}$$

where d is the detector thickness and e is the absolute value of the electron charge. The current induced by all moving charges can be expressed as

$$I = -eE_w\left(\sum_i v_{i,electrons} + \sum_j v_{j,holes}\right)\ . \tag{5.1.3}$$

If an electron-hole pair is produced at a given distance x from the anode, the charge collection time is with good approximation:

$$t_e = \frac{x}{v_e} = \frac{xd}{\mu_e V_b} \quad \text{for} \quad \text{electrons,} \tag{5.1.4}$$

$$t_h = \frac{d-x}{v_h} = \frac{(d-x)d}{\mu_h V_b} \quad \text{for holes,} \tag{5.1.5}$$

and the total induced charge by their motion is $Q = \int_0^{t_{e,h}} I(t)dt$, more specifically

$$Q_e = e\mu_e\frac{V_b}{d^2}\frac{xd}{\mu_e V_b} = e\frac{x}{d} \quad \text{for} \quad \text{electrons,} \tag{5.1.6}$$

$$Q_h = e\mu_h\frac{V_b}{d^2}\frac{(d-x)d}{\mu_h V_b} = e\left(1-\frac{x}{d}\right) \quad \text{for} \quad \text{holes.} \tag{5.1.7}$$

Most importantly for physics applications, the total collected charge Q_e+Q_h is proportional to the energy deposited by passage of radiation.

5.1.2 Charge carriers motion

The Shockley-Ramo's theorem shows that the current induced on an electrode by charge carriers moving inside the sensor depends on the drift and weighting

field. The electric field and the corresponding potential can be related to the charge density which gives rise to them. The electric field dependence on charge density ρ is expressed by the divergence

$$\vec{\nabla} \cdot \vec{E} = \frac{\rho}{\varepsilon} \tag{5.1.8}$$

where ε is the permittivity. The electrostatic potential V is defined by

$$\vec{E} = -\vec{\nabla} V \quad . \tag{5.1.9}$$

For the drift potential, charge density is given by $\rho = eN$ where N is the dopant density and e is the electron charge. The potential is related to the charge density by the so-called *Poisson's equation*

$$\nabla^2 V = -\frac{\rho}{\varepsilon} \tag{5.1.10}$$

which, in absence of charge (as for the weighting field), becomes *Laplace's equation*

$$\nabla^2 V = 0 \tag{5.1.11}$$

The drift and weighting field are therefore evaluated by solving the Poisson's and Laplace's equations [60].

As already mentioned, the charge drift is one of the main contributions in carrier motion and the drift velocity depends on the applied electric field when it is not saturated. This electric field is in turn determined by depletion and bias voltage. By setting a bias voltage lower than the depletion voltage the sensor bulk is only partially depleted, causing an inefficient charge collection (figure 5.2).

For bias voltages higher than depletion voltage, the bulk is fully depleted and the overbias $V_b - V_{depl}$ adds a uniform offset to the electric field given by $(V_b - V_{depl})/d$, as shown in figure 5.3).

The drift electric field is not uniform within the bulk: it starts from a minimum value at the backplane and reaches the maximum value at the readout electrode.

When the drift velocity is not saturated, it is much influenced by the applied electric field: charges drifting to a lower electric field region will be subjected to a minor acceleration, while those drifting to a higher field region will accelerate

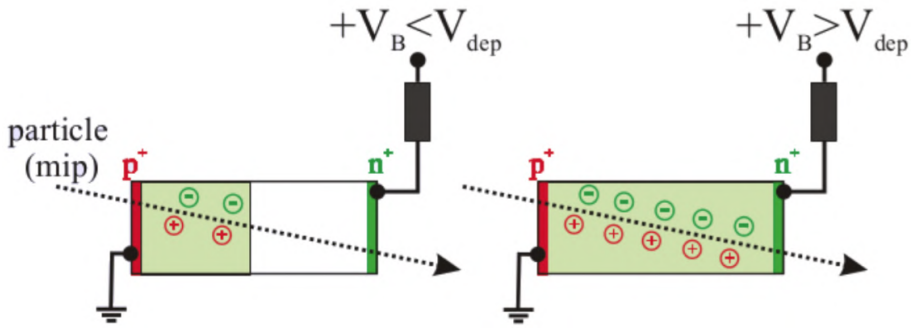

Figure 5.2: Depleted volume (in green) in a sensor for two bias voltage values.

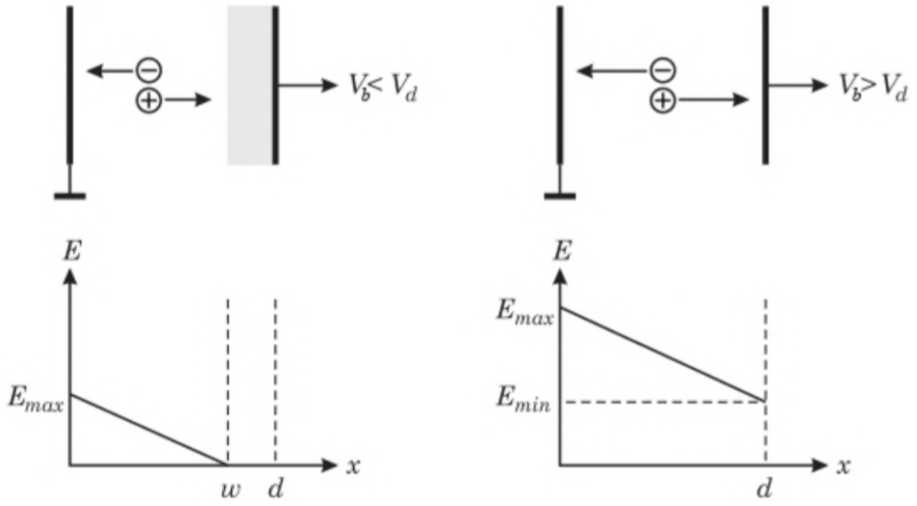

Figure 5.3: Distribution of the electric field for $V_b < V_{depl}$ and $V_b > V_{depl}$

until their velocity reaches the saturation value.
The uniformity of the drift electric field within the bulk, on the other hand, is determined by depletion voltage: if bias and depletion voltage are different, a lower depletion voltage reduces the variation of the electric field across the detector thickness, leading to a more uniform drift velocity. For example, if one considers a sensor with $V_{depl} = 50\,\mathrm{V}$ biased with $V_b = 200\,\mathrm{V}$ and a second sensor with $V_{depl} = 20\,\mathrm{V}$ biased with $V_b = 170\,\mathrm{V}$, even if the overbias $V_b - V_{bias} = 150\,\mathrm{V}$ is the same in both cases, in the second sensor the drift field is more constant within the bulk volume, since the depletion voltage is lower.
In addition, one has to note that the signal in a detector depends on the detector geometry itself: different geometries lead to different electric field shapes hence to different $I(t)$ patterns.

Charge carrier drift is affected by thermal diffusion, causing the spread of the charge distribution, with a resulting root mean square of

$$\sigma_{th} = \sqrt{2Dt} \tag{5.1.12}$$

after a drift time t, where D is the diffusion coefficient in silicon.
The measured signal results therefore in a superposition of Gaussian distributions. Electrons created close to cathode and holes created close to anode are more affected by charge diffusion, due to a longer drift time.

5.1.3 Radiation damage

Tracking devices are often placed in the inner part of high energy physics experiments, as close as possible to the interaction point, so they are designed and tested to operate at high radiation levels.
The instant luminosity expected for HL-LHC of $L \sim 10^{35}\,\mathrm{cm^{-2}s^{-1}}$ will translate into a further increase of the radiation dose afflicting detectors and electronics performances. For this reason, new radiation-hard detectors are being designed to withstand the higher particle fluences.

Radiation may harm the silicon crystal and displace the atoms in the lattice. The entity of the damage greatly varies with the particle energy: lower-energy charged particles create more point-like defects, while higher-energy charged particles and neutral particles (e.g. neutrons) lead to cluster-like damage.
Damage involves either the bulk or the oxide surface:

bulk damage (also known as *displacement damage*) is due to Non-Ionising Energy Loss (NIEL). It often translates into a change of the depletion voltage (higher values are needed to deplete the sensor) due to additional donors settling in the upper half of the band gap and acceptors in the lower, a reduction of charge collection efficiency due to electrons and holes trapping, and an increase of the leakage current, as shown in Figure 5.4.

surface damage is due to Ionising Energy Loss (IEL) which causes the deposit of charges into the oxide structure or at the Si/SiO_2 interface; it leads typically to alterations in noise and breakdown voltage.

Therefore it is possible to conclude that the damage caused by charged particles is mostly on the surface, while neutral ones (especially low-energy ones) damage the bulk. For materials used in current detectors, the damage caused by different particles can be normalised to the 1 MeV *neutron equivalent* NIEL damage n_{eq}: most fluence numbers are given using this normalisation.
If the displacement caused by radiation damage is small, a modest amount of thermal energy ($E \sim k_B T$) may be enough to restore the atom to its original configuration: it is possible then to recover from damage without heating the sensor, just keeping it at room temperature ($T = 300\,\mathrm{K}$). For displacements of more severe entity, the sensors are kept at a certain temperature for a certain time with the process called *thermal annealing*: silicon conditions generally improve with increasing annealing time.
It is to be noted that thermal energy is effective in repairing only the so-called

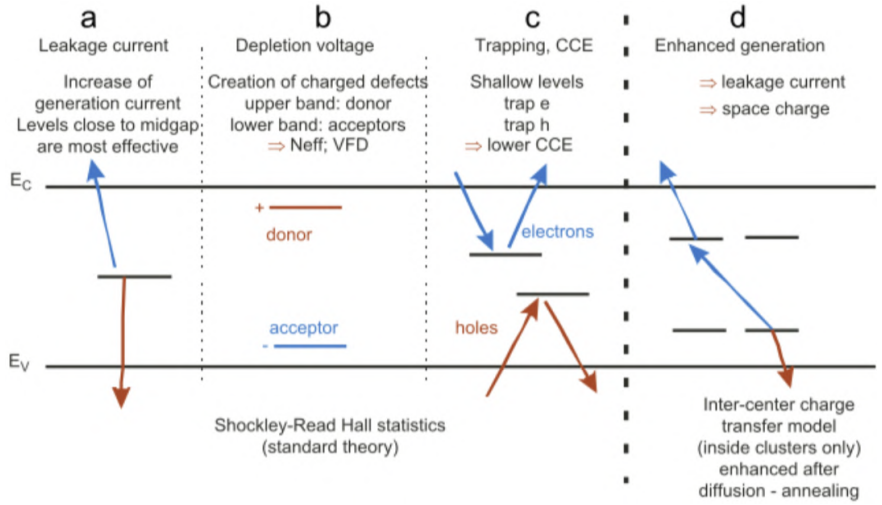

Figure 5.4: Schematic view of the introduced energy levels due to defects caused by radiation.

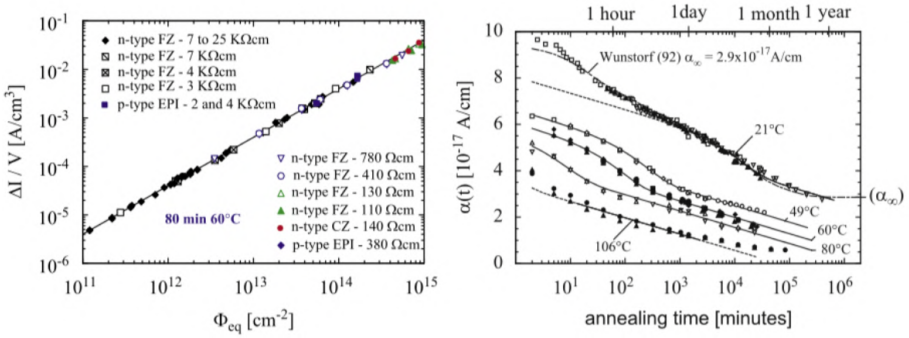

Figure 5.5: Leakage current variation with fluence and annealing time.

shallow level damages, while in case of more severe damage the initial configuration cannot be completely restored [61].
How operating parameters of a sensor change with irradiation will be shortly explained hereunder.

Leakage current

Above fluences of $\Phi_{eq} = 10^{14}\,\mathrm{n_{eq}cm^{-2}}$ the main problem which arises from radiation damage is the increase of the leakage current I. Leakage current varies with particle fluence and time, as depicted in figure 5.5, according to the relation [61]:

$$\frac{\Delta I}{V} = \alpha \Phi_{eq} \tag{5.1.13}$$

where V is the normalisation volume, α is the current-related damage rate. Mid-gap levels are responsible for the current increase, while annealing causes the current to decrease with time.

Depletion voltage

Depletion voltage depends on the effective charge N_{eff}, which evolves with fluence and time and becomes problematic at $\Phi_{eq} \geq 10^{15}\,\mathrm{n_{eq}cm^{-2}}$ [61]. Irradiated sensors have a different number of acceptor and donor levels with respect to not irradiated ones. This variation may lead to an inversion of the material type, typically from n to p but also from p to p^+. Hence, the depletion voltage exhibits an initial drop, after which it starts to rise (Figure 5.6). This behaviour can be parametrised by [61]:

$$N_{eff} = N_{D,0} e^{-c_D \Phi_{eq}} - N_{A,0} e^{-c_A \Phi_{eq}} - b\Phi_{eq} \tag{5.1.14}$$

where $N_{D,0}$ and $N_{A,0}$ are the initial donor and acceptor concentrations, c_D and c_A the donor and acceptor removal rates, $b\Phi_{eq}$ the acceptor creation term.
In addition, N_{eff} is subjected to a temperature dependent diffusion with time:

$$\Delta N_{eff}(\Phi_{eq}, t, T) = N_{C,0}(\Phi_{eq}) + N_A(\Phi_{eq}, t, T) + N_Y(\Phi_{eq}, t, T) \tag{5.1.15}$$

where $N_{C,0}$ is the stable term, N_A and N_Y are the annealing short term and second-order long term respectively.

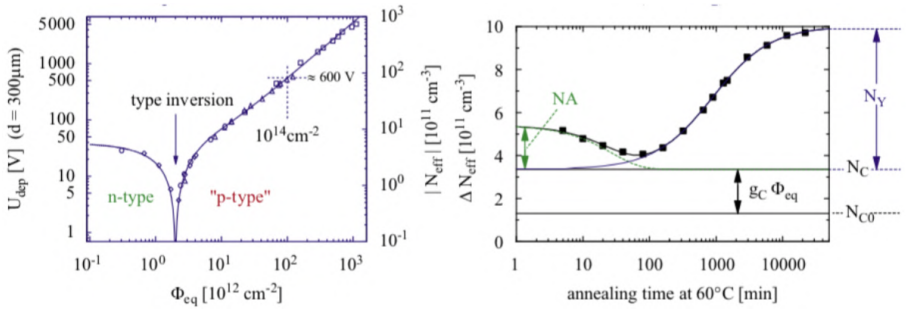

Figure 5.6: Depletion voltage variation with fluence and annealing time.

Charge trapping

Damage by irradiation creates trapping centres inside the silicon: the concentration of these new trapping centres N_i can be approximated by the linear relation [61]

$$N_i = \Phi_{eq} g_i f_i(t) \propto \frac{1}{\tau_{eff}} \tag{5.1.16}$$

where the product $g_i f_i(t)$ describes the evolution of annealing with time. This worsens the Charge Collection Efficiency (CCE), as described by:

$$Q_{eh}(t) = Q_{0_{e,h}} e^{-\frac{t}{\tau_{eff}}} \tag{5.1.17}$$

5.2 Front-end electronics

The front-end electronics amplifies the signal produced by the detector, shapes it and converts it into a digital sequence. Its importance is therefore crucial to the purpose of the experiment as it allows to extract the needed information from the signal produced by a sensor, which is typically a short current pulse. Since the total charge, given by the integral of the signal current $I(t)$, contains the information about the energy deposited by radiation in the sensor, one often needs to integrate the current. This is possible by integrating on a capacitance, by using a charge sensitive amplifier or an integrating ADC (Analog-to-Digital Converter) on an amplified pulse.

When integrating on the input capacitance, the circuit in figure 5.7 has to be considered, where C_{det} is the sensor capacitance, C_i and R_i are the amplifier input capacitance and resistance. If the time constant of the circuit $\tau = R_i(C_{det} + C_i)$ is significantly longer than the charge collection time $\tau \gg t_c$, then the peak voltage at the amplifier input is

$$V_{in} = \frac{Q}{C_{det} + C_i} \tag{5.2.1}$$

and therefore depends on the input and sensor capacitances.
However, the sensor capacitance may be subjected to variations since it depends on the sensor geometry and on the bias voltage, as in the case where the the sensor bulk is not completely depleted. Therefore it is preferable to use systems whose response does not depend on the sensor capacitance, for example by using

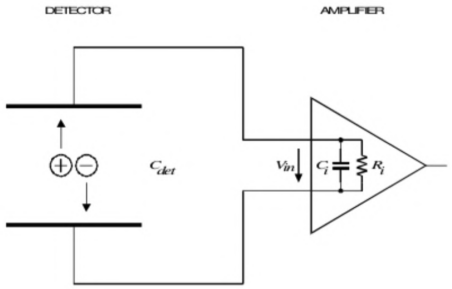

Figure 5.7: Scheme of the read out by integration on input capacitance.

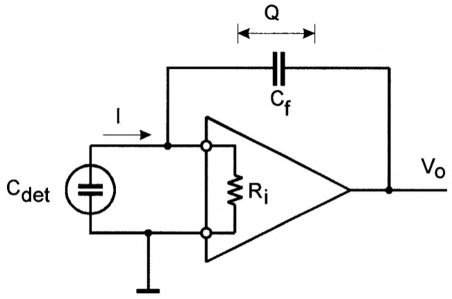

Figure 5.8: Schematic of an ideal charge sensitive amplifier.

a charge sensitive amplifier, where the sensor capacitance is much lower than the amplifier input capacitance $C_{det} \ll C_i$.

5.2.1 Charge sensitive amplifier

The charge sensitive amplifier (CSA) is a transimpedance operational amplifier which converts the current pulse into a voltage signal which can be measured, for example, with an oscilloscope. It is often used as preamplifier stage in a front-end chain. The scheme of a charge sensitive amplifier is shown in Figure 5.8: in the ideal case, it is characterised by a high input impedance $R_i \to \infty$ and by a feedback capacitance C_f, while the feedback resistance (parallel to C_f) is supposed to be infinite and then omitted. The current pulse is integrated on the feedback capacitance C_f and the resulting voltage has the step function shape and does not depend of the capacitance of the detector

$$V_{out} = \frac{Q}{C_f} \qquad . \tag{5.2.2}$$

A more realistic amplifier, instead, responds to a current pulse with a finite speed and then its response affects the pulse shape: the output voltage cannot be a step function but is modulated by a negative exponential and depends on the circuit time constant τ, since the capacitors inside of the amplifier need to charge up before allowing the output voltage to change.
Moreover, the signal also includes the noise on the signal itself and on the baseline (electronic noise). Therefore, measurements of peak amplitude include both signal amplitude and fluctuations due to noise.

5.2.2 Broad-band amplifiers

Broad-band (also called current-mode) amplifiers (BBA) translate the current signal from the sensor into a voltage signal with some gain, so that $V(t) \propto i(t)$, and they require a wide bandwidth to approximately follow the time structure of the current sourced by the sensor.

The read-out of a silicon detector by a BBA can be ideally described as an RC circuit with a current source in parallel to the capacitor [32]. In this approximation the time constant of the circuit is $\tau = R_{in}C_{det}$ where R_in is the read-out input capacitance and C_{det} the detector capacitance. The time constant of the amplifier must be matched with the rising time of the detector signal $\tau \leq t_{rise}$ in order to avoid a reduction of the bandwidth. This constraint strongly link the sensor and electronics designs, as the electronics should be designed such that it does not slow down very fast input signals. Generally, the ideal BBA is characterized by a low input impedance and a high output impedance.

5.2.3 Noise

The noise in a silicon detector system plays an essential role, since the signals are usually small and it affects both the peak signal and the time distribution. The current signal I of a sensor of thickness d, produced by n carriers of charge e moving with a certain velocity v is

$$I = \frac{nev}{d} \quad , \tag{5.2.3}$$

and the total noise can be estimated from the fluctuations of this current, given by the total differential

$$\langle dI \rangle^2 = \left(\frac{ne}{d}\langle dv \rangle\right)^2 + \left(\frac{ev}{d}\langle dn \rangle\right)^2 \quad , \tag{5.2.4}$$

which highlights two statistically uncorrelated contributions: a fluctuation of the carriers velocities, i.e. *thermal noise*, and a fluctuation of the number of the carriers, i.e. *shot noise*.
Both contributions provide a purely random noise and are called *white noise* sources, since their noise power per unit bandwidth is constant.
A good detector should have a high *signal-to-noise* ratio (SNR), obtained from a reasonable compromise between a *large signal*, which implies low ionisation energy, i.e. a reduced band gap, and a *low noise*, which implies a small number of intrinsic charge carriers and a larger band gap. This compromise is optimised by a band gap of $E_{gap} \approx 6\,\text{eV}$. For this reason, the best material would certainly be the diamond, but due to the high cost it is not feasible to use diamonds to build large area detectors.

Considering both the sensor and the read-out electronics, the detector has several noise sources such as sensor leakage current, resistor thermal noise, amplifier noise. Each noise source can be modelled by a function that describes the power generated by the noise source as a function of frequency, the so called *spectral power density* referred to the input. The spectral density functions of capacitors, resistors and of the sensor leakage current do not depend on the specific circuit, while the amplifier has its own specific spectral density function.

The noise sources can be divided into two groups: parallel and series noise sources. The noise due to the detector leakage current, the feedback and biasing resistor thermal noise behave as a current source in parallel with the amplifier input; the resistors thermal noise and the amplifier noise act as voltage sources in series with the amplifier input.
Finally, the actual contribution to the total noise from each source can be calculated as the convolution of the power density function with the amplifier transfer function and therefore depends on the amplifier specific transfer function. Each noise contribution is quoted then as the number of electrons needed at the input to produce the same voltage signal as the noise does, the so-called *equivalent noise charge* (ENC). This is directly applicable to the CSA as it measures the charge collected from the sensor.

In a very general way, one can express the total equivalent noise charge for a CR-RC shaper as the sum of three contributions: series noise, parallel noise and the technology dependent amplifier flicker $1/f$ noise

$$ENC = \sqrt{ENC_{series}^2 + ENC_{parallel}^2 + ENC_{flicker}^2} \tag{5.2.5}$$

The effect of series noise ENC_{series}^2 is directly proportional to the input capacitance; therefore sensors with a small capacitance to the front-end amplifier are preferable, while parallel noise does not depend on the input capacitance.

Since noise is part of the signal, amplifying the signal results in an amplification of the noise as well. In order to avoid this, a threshold in the readout electronics is necessary to distinguish the effective signal from thermal fluctuations: the choice of the threshold value must be made in a way that reduces the effect of noise and avoids efficiency loss at the same time.

Chapter 6

3D pixel detectors

In a traditional planar pixel detector technology, the charge produced by a particle is collected by electrodes which are implanted in the surface of the silicon wafer. In the case of the 3D silicon sensor, on the other hand, the electrodes are etched in a columnar structure which is perpendicular to the surface. Novel 3D geometries are being designed and developed and they will be described in further detail in next Section 7.3.1. However, the description in this Chapter refers to the most widely used 3D column geometry.
Figure 6.1 shows the planar sensor structure and charge drift (Fig. 6.1a) compared to the structure and charge drift in a 3D column sensor (Fig. 6.1b and 6.1c).

The bulk of a 3D sensor is vertically crossed by electrodes of type p and n, which are organised in alternate columns: this allows to reduce the distance between opposite electrodes with respect to present planar sensors, reducing the depth of the depletion zone and subsequently the depletion voltage (between 10 and 30 V instead of 100 V).
As the distance between electrodes does not depend on the substrate thickness even for a fully depleted bulk it is possible to reach higher electric fields between electrodes hence increasing the carriers velocity. Due to a shorter drift distance, passing-through electrodes also accomplish a faster detector signal response and a reduction of trapping centres and defects, resulting in a sensor which is more resistant to radiation damage.

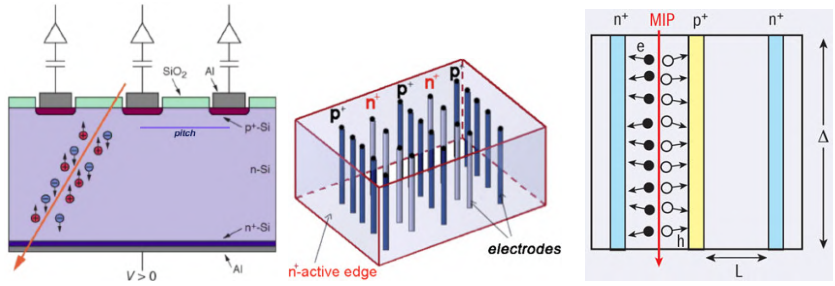

(a) Structure and charge drift in a planar sensor. **(b)** Structure of a 3D sensor. **(c)** Charge drift in a 3D sensor

Figure 6.1: Comparison between planar and 3D sensor geometries.

The main limits of the 3D pixel sensor technology are

- increased pixel capacitance due to the electrode configuration, which may lead to an increased output noise;
- increased production costs with respect to planar technology due to the etching procedure to make deep hole-like electrodes with small diameter, called Deep Reactive Ion Etching;
- low-field zones between same doping type electrodes causing charge collection inefficiency.

As explained in Section 2.2.2, the Precision Proton Spectrometer chose the 3D silicon detector technology as the baseline for its tracker. With the possibility of reducing the dead area at the border of the sensor and its intrinsic high radiation hardness, the 3D silicon sensor technology fits the requirements of the detector. These two characteristics will be described in more detail in the following paragraph.

One of the goals of 3D detectors is to reduce the edge inefficiency or even to remove it by using active edges. In planar detectors the insensitive surface is very wide (about 14% of the surface area for the pixel sensor used in ATLAS at CERN), since edges show a last electrode field bulging, as well as occasional micro-cracks. Moreover, the area reserved to guard rings is significant, compared to sensor overall surface.
To overcome this problem, planar sensors are usually staggered over many layers, to avoid inefficient coverage. This arrangement, however, forces particles to cross additional layers of material. Active edges will allow to avoid this superposition of detector layers, being electrodes themselves.
In order to reduce the inactive region at the edge of a 3D silicon sensor, two main techniques have been developed.
The first solution is to etch trenches around the margin of the device and apply to them the same doping used for the column electrodes. In this way, the edge itself is an electrode and act as the boundary of the active volume and its electric field. However, after this process, the sensor must rely on a support wafer in order to preserve its mechanical integrity and this prevents the creation of a double sided 3D sensor, which is a sensor in which the column electrodes are etched from opposite sides of the wafer.
The other technique allows for a significant reduction of the inactive edge, but not its complete elimination, therefore it is referred as slim edges techniques. In this case, a smooth reduction of the electric field is provided by the creation of a dense fence of ohmic columns extending from the active area towards the margin. By increasing the bias voltage of the sensor, the electric field produced by such column fence will extend towards the edge and the inactive region can be reduced to $\sim 50\,\mu$m.

In a 3D silicon sensor the charges produced by a particle drift for a shorter distance than in a planar sensor before begin collected by the electrode. This makes 3D sensors intrinsically more resistant to radiation damage. The electrode configuration inside the pixel cell can be optimized in order to even increase this resistance. For example, a higher number of columns can go in this direction but it would cause an increase of the pixel capacitance and of the structural fragility.

In the remaining part of this Chapter, I will briefly report on the activities I did during my PhD regarding the PPS pixel detector.

6.1 PPS RPIX operation in LHC Run 2

The data acquisition (DAQ) of any LHC detector is controlled by sophisticated software and this is also true for the PPS tracking detector. All the CMS subdetectors are expected to concur in the data taking efficiently in order to minimize the dead time, which is any moment in which the LHC is providing collisions but the CMS experiment is not able to record the events. For this reason all the CMS detectors are supervised by an appointed person, who has the responsibility for the correct operation of the detector but also can watch online histograms providing snapshots of the CMS data being produced in that very moment.
Figure 6.2 shows the DAQ display window containing all the diagnostic plots and maps necessary to control the detector operation. Four groups of six maps of the hits positions can be seen in the `hits position` frames: each group concerns one tracking station and each map in any of them represents the hits in a tracker plane. As the figure refers to the 2018 data taking, the 4 tracking stations consisted in pixel detectors (see Figure 2.12 pag. 22). From the hit maps it is possible to notice the extreme non uniformity of the detector occupancy as most hits are concentrated in a very small area of the detector.
The Single Event Upset (SEU) is one of the most frequent issues during a tracker operation and generally it is solved by a reset of the readout chip (ROC). The ROC is bump-bonded to the sensor and hence is traversed by the same particles. The charge locally deposited by these particles can alter the state of a transistor which will cause the full circuit to stop working. In the `ROC hits per event` maps, the colour of a horizontal line abruptly turns blue if the correspondent chip stopped working.

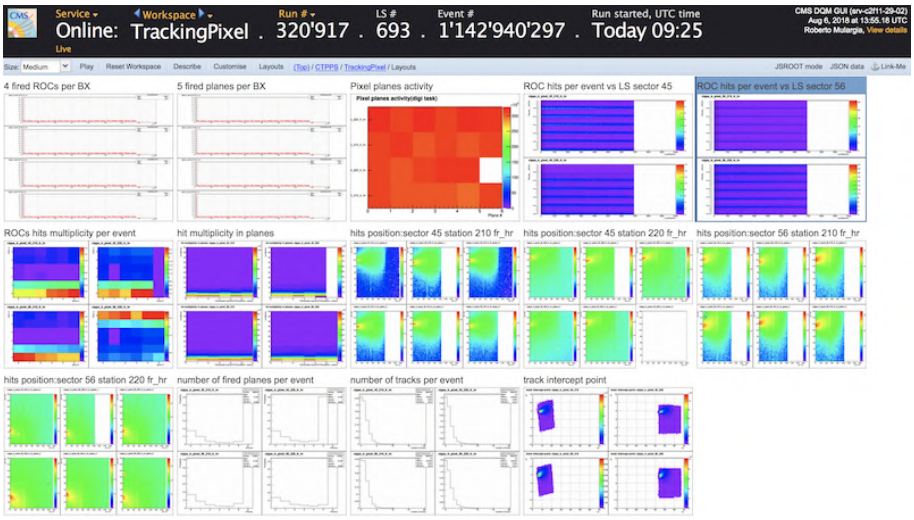

Figure 6.2: A view of the RPIX control screen during an ordinary LHC run.

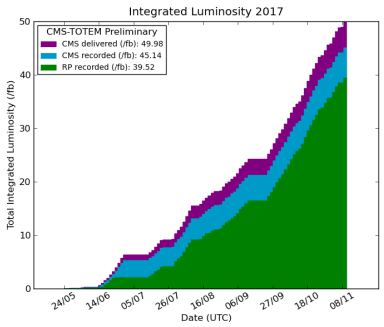

(a) Total integrated luminosity recorded by PPS in 2017 [62].

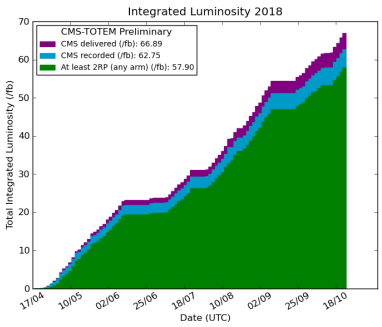

(b) Total integrated luminosity recorded by PPS in 2018 [63].

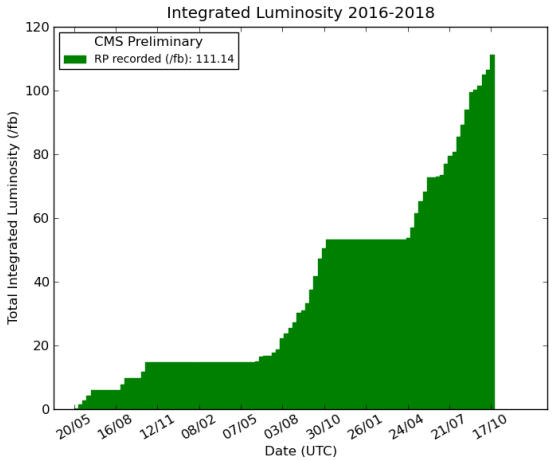

(c) Total integrated luminosity recorded by PPS during Run 2.

Figure 6.3: Integrated luminosities recorded by PPS during Run 2.

Figure 6.3 presents the plots of the integrated luminosity recorded by PPS, with respect to the one delivered and recorded by CMS. The plot in Figure 6.3a refers to the 2017 data taking, while the one in Figure 6.3b refers to 2018. PPS collected approximately 88% of the full statistics recorded by CMS in 2017 and 92% for the 2018, summing up to a total integrated recorded luminosity of $L_{tot} \simeq 111.14\,\mathrm{fb}^{-1}$ for Run 2 (see Figure 6.3c).

The PPS pixel detector suffered heavy damage in its region closest to the beam, consequently to the very high radiation exposure visible in the hit maps in Figure 6.2. The evolution of the efficiency map of that detector region during the 2018 data taking is shown in Figure 6.4. The deterioration of the efficiency caused by the radiation damage is clearly visible as a blue region growing very close to the detector edge. Given the small extent of the damaged area, it was possible to address this problem during the LHC technical stops (TS): the whole detector was shifted by 0.5 mm or 1 mm in order to expose a virgin detector region to the high statistics beam profile and therefore restore the detector efficiency [64].
The RPIX spatial resolution resulted $\sigma_x = \simeq 17\,\mu m$ [63].

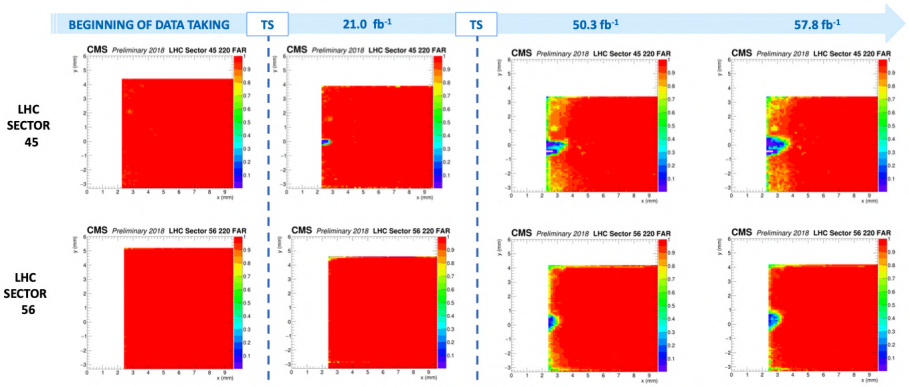

Figure 6.4: Evolution of the efficiency map in the PPS pixel detector region closest to the beam during 2018. During each technical stop (TS), both detectors were shifted 0.5 mm downwards [64].

6.2 PPS RPIX detector in LHC Run 3

PPS will take data during LHC Run 3 starting in 2022. As in Run 2, the detector apparatus will consists of 2 tracking stations and 2 timing stations per arm. Each tracking detector will be equipped with new 3D silicon pixel sensors. The sensor have benn produced by Fondazione Bruno Kessler and are characterized by a 150 μm thickness and single-sided technology. As a difference to the previous runs, all pixel sensors will have the same size and each will be readout by the PROC600 chip, currently used in the first layer of the CMS central pixel detector. Irradiation tests performed on the new ROC chip show a behaviour similar to the old one, the PSI46dig. Instead of relying on a manual shift of the whole detector during a technical stop, to mitigate the effect of radiation on the efficiency every detector package will be equipped with a motor that will make possible finer, remotely controlled, vertical movements. This should allow to better distribute the radiation damage with respect to LHC Run2 and to reduce its impact. In order to allow a smooth and wide movement, the flex hybrid board and the detector packages have been redesigned.
Figure 6.5 shows the updated design of the flex hybrid board (Fig. 6.5a) and the detector package and mechanical structure (Fig. 6.5b): the arrow indicates the motor which will be used to remotely shift the detector.

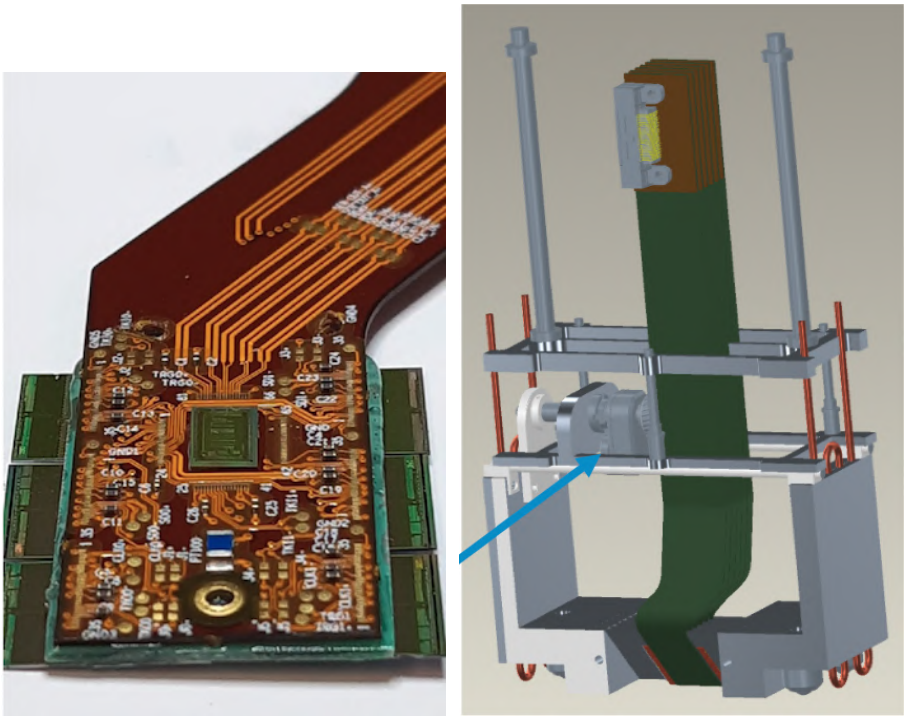

(a) New flex hybrid board design.

(b) New detector package and structure. The arrow indicates the motor which will be used to automatically shift the detector.

Figure 6.5: New design for the PPS pixel tracker detector in Run 3.

Chapter 7

Innovative timing detectors

In the last decades, particle detectors based on silicon sensor technologies have proved to be excellent trackers in high energy physics experiments. The research and development of these technologies enabled an ever more accurate, reliable and efficient measurement process. The development of the front-end electronics has been simultaneous to this process and both followed the the experimental necessities and goals.
In Chapter 4 of Part I of this thesis, the future plans developed for the main particle physics experiments at LHC was discussed and their new necessities were mentioned. The evolution of silicon detectors is expected to follow those needs and, in particular, to fulfill the need for measurement including very accurate timing information.
In this Chapter a brief discussion on the necessities for high accuracy in timing measurement will be presented and, following that, two very innovative technologies for silicon timing detectors will be presented, together with some experimental results obtained during my PhD.

7.1 Technology requirements for timing

A simple schematic setup for the measurement of the time of passage of a particle is shown in Figure 7.1 and it consists of the detector, that produces the current signal; an amplifier, that converts it into voltage; a discriminator, that changes its digital output when the signal meets certain requirements. The time of arrival is set in correspondence of the change of the discriminator output and the following electronics converts the time interval into an array of bits (time-to-digital conversion) or an analog signal with given amplitude (time-to-amplitude conversion).

The discrimination circuit is a crucial element for the timing electronics as its logic defines the time of arrival. For this reason there are several types of implementation in order to well operate with different signal characteristics. These types can be summarised as follows:

Single threshold (or *Leading edge*): the discriminator is a comparator between the input voltage signal V_i and a fixed voltage threshold V_{th} (as in Figure 7.1). Its digital output is set to low when the signal is below the

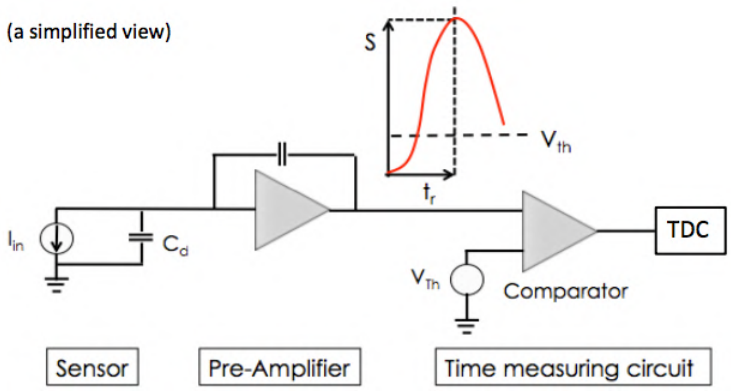

Figure 7.1: Main components of a time-tagging detector

threshold and high otherwise. This is the simplest form of discriminator but it is not reliable when the input signals have a variable amplitude.

Multiple threshold : the input signal is compared to two different threshold voltage values and the time is set when it crosses each of them.

Constant Fraction Discriminator (CFD) : this more elaborate system is very reliable when the signal shape is regular and already known as it measures the peak of the signal and sets the time in correspondence with a given fraction of the measured maximum amplitude. More specifically, the incoming signal is first split into two components: one is inverted, mildly attenuated, the other is delayed by a time t_d smaller than the expected rise time t_r. The two signals are eventually added again and, as shown in Figure 7.2 the resulting signal starts as negative and crosses the zero voltage value at a time which depends on the delay time and the attenuation factor. This very time is put in coincidence with the digital result of the comparison between the original signal and a fixed threshold, giving the final output of the discriminator.

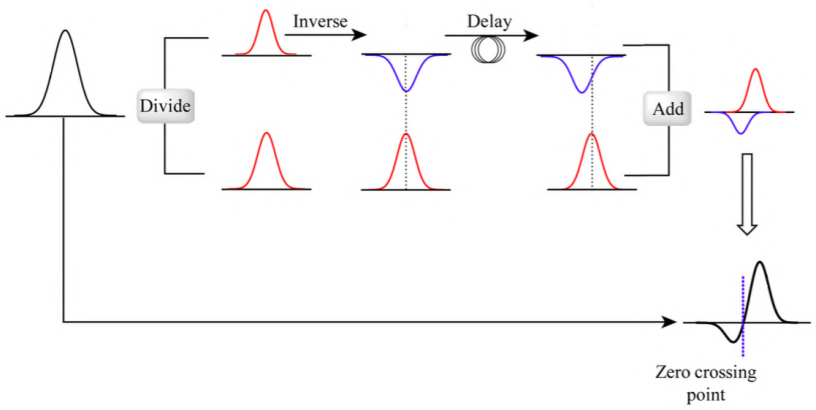

Figure 7.2: Creation of the modified signal in a CFD.

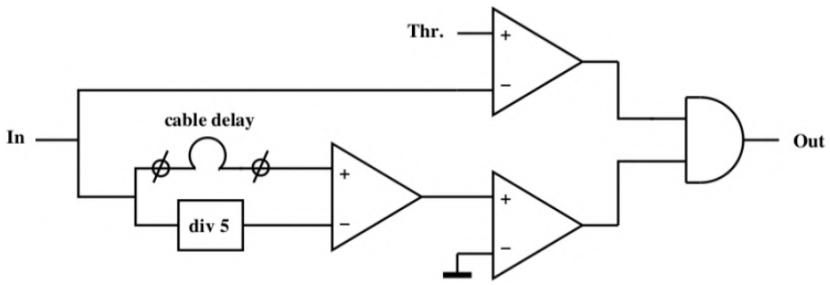

Figure 7.3: Basic functional diagram of a constant fraction discriminator.

Waveform sampling : this method consists in converting the analog input signal into a discrete one thanks to sampling and an analog-to-digital converter (ADC). The time can be set offline applying very accurate requirements and is therefore very precise. A very quick sampling is needed in order to reconstruct fast signals and this limits the acceptable rate of incoming signals as the processing may take several microseconds per event.

7.1.1 Time Resolution

The particle arrival time is always defined as a fixed instant t_0: many effects make this value move either earlier or later and they affect the overall accuracy of the time measurement, quantified as the *time resolution sigma*$_t$. The origins of these effect are diverse, from the physics of the interaction between the particle and the detector material, to the device physics itself, to the amplification electronics and the digital conversion.

It is possible to discern five main contributions to the time resolution:

$$\sigma_t^2 = \sigma_{Jitter}^2 + \sigma_{Landau-timewalk}^2 + \sigma_{Landau-noise}^2 + \sigma_{Distortion}^2 + \sigma_{TDC}^2 \quad (7.1.1)$$

which can be broadly grouped into four categories [32]:

particle-matter interaction: the release of energy by the passage of a particle in a semiconductor is an irregular process. The actual amount of energy released fluctuates: this causes a fluctuation of the number of e-h pairs which are produced and hence important variations of the signal amplitude, which causes the time walk uncertainty $\sigma_{Landau-timewalk}$. In addition, the energy release is highly non uniform through the particle path and this implies an irregularity of the signal shape which is intrinsically linked to the physics process and causes an unavoidable $\sigma_{Landau-noise}$ uncertainty.

device physics: the produced e-h pairs drift under the effect of the electric field inside the device and the velocity of the carriers is not constant if the electric field is not high enough. Differences in the weighting field throughout the sensor volume causes the produced signal shape to depend on the position where the particle hit, and hence a signal distortion which is expressed by $\sigma_{Distortion}$.

electronics: the noise of the readout system adds up to the produced signal and causes the discriminator to mistakenly set the t_0 too early or too late. The concurrent effect of this noise and the amplifier signal steepness is accounted into the σ_{Jitter} term.

digitisation: the TDC introduces a σ_{TDC} uncertainty caused by the intrinsic, yet small, approximation in the digital conversion of an analog signal. More specifically, this uncertainty is fixed and linked to the least significant bit (LSB) equivalent in time ΔT_{LSB}, hence decreasing for TDC with higher time granularity. This contribute can be easily expressed as $\sigma_{TDC} = \Delta T_{LSB}/\sqrt{12}$.

Due to the importance of these effects on the overall timing performance and the requirements they pose on the development of a timing detector, some of them will be discussed in detail hereafter.

Time Walk

This uncertainty is typical of the single threshold discrimination and represents the fact that a small amplitude signal crosses a fixed threshold V_{th} later than a large amplitude one. If not corrected, the time set by the discriminator would depend on the signal amplitude, as shown in Figure 7.4a.
The delay t_d in the time set for a smaller signal is shown in Figure 7.4b (under the approximation of a locally linear signal) where S is the signal amplitude and t_r its rise time. It is possible to deduce a proportional law for the delay time

$$t_d = \frac{t_r V_{th}}{S} \tag{7.1.2}$$

It is possible to evaluate the uncertainty $\sigma_{Landau-timewalk}$ by considering the delay time distribution: this uncertainty is defined as the root mean square

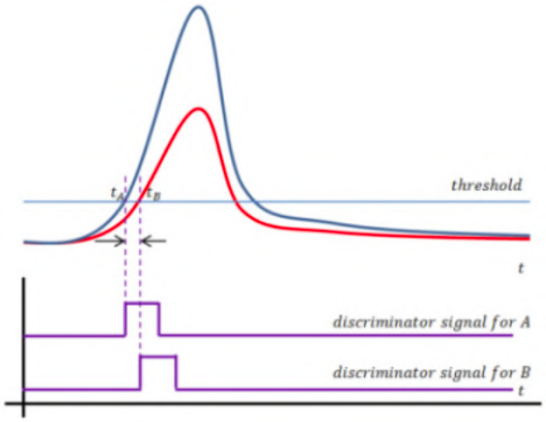

(a) Time walk effect on the discriminator output.

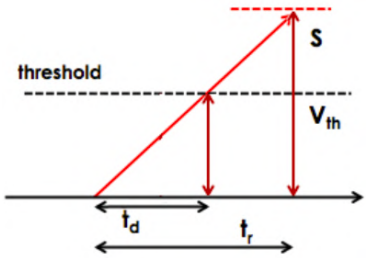

(b) Delay caused by time walk

Figure 7.4: Timing uncertainty due to time walk in a single threshold discriminator.

(RMS) of the delay distribution:

$$\sigma_{Landau-timewalk} = [t_d]_{RMS} = \left[\frac{V_{th}}{\frac{S}{t_r}}\right]_{RMS} . \quad (7.1.3)$$

The time walk effect is certainly minimised by choosing the lowest possible value for the threshold, which is commonly expressed as a multiple of the noise at the output of the preamplifier $V_{th} \propto N$. The $\frac{S}{t_r}$ ratio is the signal steepness, the slew rate $\frac{dV}{dt}$.
The final formula for the uncertainty due to time walk shows how this effect must be minimised by keeping the noise level low and the slew rate as high as possible:

$$\sigma_{Landau-timewalk} \propto \left[\frac{N}{\frac{dV}{dt}}\right]_{RMS} . \quad (7.1.4)$$

When implementing a constant fraction discriminator is not possible, even with a single threshold discriminator this effect may be corrected in case of regularly shaped signals by the measurement of the *time over threshold* (TOT) of the signals. If the signal shape is known, in fact, it is possible to infer the signal amplitude from the TOT measurement and correct for the time walk.

Non uniform Weighting Field

As explained in Sec. 5.1.2, Ramo's theorem states that the induced current signal $i(t)$ is proportional to the generated electric charge q, the drift velocity $\vec{v}$ and the weighting field $\vec{E_w}$ (Eq. 5.1.1, pag.60). If any of these quantities vary throughout the sensor volume, then the produced signal will have a different shape depending on where the particle hit, as schematically shown in Figure 7.5a, spoiling the time resolution by increasing the $\sigma_{Distortion}$ term.

As previously seen, the drift velocity of the carriers saturates for high values of the electric field ($\sim 30\ kV/cm$) which is hence required to be uniform throughout the sensor volume. The weighting field E_w, representing the capacitive coupling of a unitary charge to the read out electrode, must also be constant throughout the sensor volume and this limits the possible geometries for the doping regions. For example, in Figure 7.5b, two doping implants geometries and the produced weighting field are shown: only in the case of an implant as wide as the strip pitch the resulting E_w is sufficiently uniform under the strip, as it get closer to the parallel plate capacitor geometry. The figure also shows how the implant width must be larger than the sensor thickness in order to keep the E_w to acceptable values in the whole depth.

Jitter

The term σ_{jitter} accounts for the time uncertainty caused by a fluctuation on the signal which makes it cross the threshold earlier or later than it would have without noise, as represented in Figure 7.6. The nature of these signal oscillations are for instance thermal and the can be originated inside of the sensor or in the amplification electronics. Jitter is then directly proportional to the noise level N and inversely proportional to the slope of the signal around

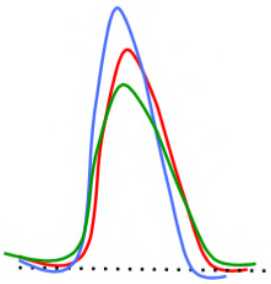

(a) Distorted signals.

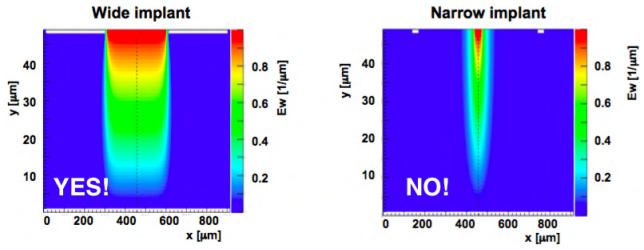

(b) Weighting field generated by two electrode geometries.

Figure 7.5: Effect and cause of irregularities of the weighting field.

the value of the comparator threshold. If again the slope is assumed locally constant $dV/dt = S/t_r$ then the time uncertainty introduced by jitter is

$$\sigma_{jitter} = \frac{N}{dV/dt} = \frac{t_r}{S/N} \quad . \tag{7.1.5}$$

The two requirements of a low noise N and a large slew rate $\frac{dV}{dt}$ are competing with each other as the latter requires a wide bandwidth which in turn increases the noise level. For this reason the compromise chosen for this parameter is at the core of the electronics design optimisation [32].

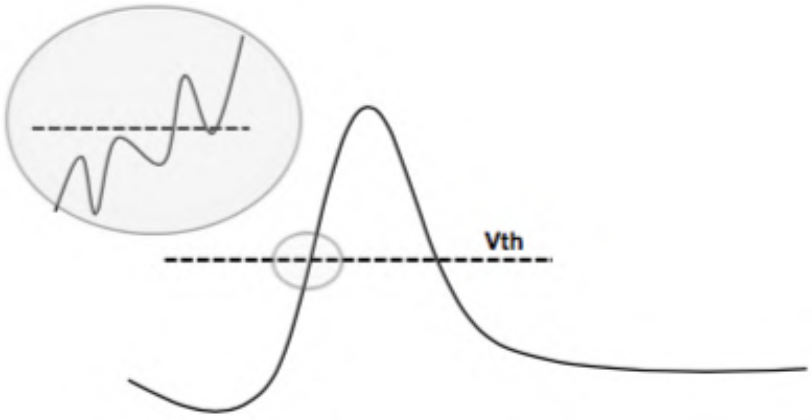

Figure 7.6: Jitter effect on a single threshold discriminator.

7.2 Ultra Fast Silicon Detectors

In order to provide good timing performance, the previous section on the contribution to the time resolution showed that a silicon detector is required to produce fast and large electrical signals. Ultra-Fast Silicon Detector (UFSD) technology proposes to provide these properties by adapting the Low-Gain Avalanche Detectors technology [65] to the design of a thin device with a controlled charge multiplication mechanism. In addition to being short and large,

the signal is also required to be as uniform as possible. This translates into the strict requirement of low noise levels, both in the signal production inside the sensor and in the readout electronics.
These requirements, if met, would guarantee a detector with a very good time resolution which can be combined with existing detectors that afford high precision in locating particles, such as the widely used silicon pixel detectors.
The long-term goal for UFSD is, however, a concurrent space-time measurement, with simultaneous space and time resolution of, respectively, $\sigma_x \sim 10\,\mu$m and $\sigma_t \sim 10\,$ps[32]. In order to do so, a UFSD must also provide high granularity for spatial measurement while measuring the track arrival time with high accuracy. The fine segmentation of a device is only possible when the internal electric fields are mild and the multiplication mechanism is controllable, resulting in the requirement of low gain, which also contributes in keeping the noise low.
Summing up, the underlying idea of the UFSD development is to manufacture thin silicon sensors based on the Low-Gain Avalanche Detectors design that have the lowest gain sufficient to perform accurate single particle time measurements.

7.2.1 Low-Gain Avalanche Detectors (LGAD)

Charge multiplication is based on the avalanche process initiated by a charge moving in large electric fields, leading to impact ionisation with a gain given by the average number of final particles created by one particle.
Differently from the APD and SiPM technologies, UFSD are based on *Low-Gain Avalanche Detectors* (LGAD) with an internal gain of $G \approx 10 - 50$ [32]. LGAD design is based on a modification of the doping profile of a silicon detector based on the $p-n$ junction, where an additional doping layer is introduced close to the junction. As shown in Figure 7.7, in a traditional n-in-p LGAD the substrate is high resistivity p^-, the electrode is n-doped and the additional layer, p^+-doped (Boron or Gallium), is introduced close to the pn junction.

The resulting doping profile is characterised by a large increase in doping concentration in close proximity to the junction, creating in turn a locally large electric field.
The electric field in LGAD is therefore clearly divided into two distinct zones: the drift volume with rather low values of the electric field ($E_{drift} \sim 30\ kV/cm$), and a thin multiplication zone located within a depth of a few micrometers with

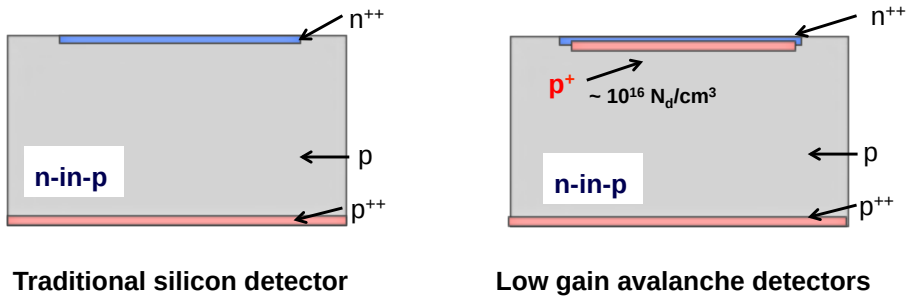

Figure 7.7: Schematic comparison between a traditional pn-junction based detector and a LGAD

very high field ($E_{mult} \sim 300\ kV/cm$).
In this LGAD design, the electrons produced by the passage of the radiation drift toward the n^{++} electrode and initiate the multiplication process when they encounter the highly doped layer. In the p-in-n design, the process is mirrored: multiplication is initiated by the holes drifting toward the p++ electrode.
Since the multiplication mechanism starts for electrons at a lower value of the electric field than what is necessary for holes multiplication, the n-in-p design offers the best control over the multiplication process. In the n-in-p design it is in fact possible to tune the value of the electric field in such a way that only electrons drive the multiplication process, hence allowing a high voltage operation without breakdown, also called avalanche mode.
Under such conditions the gain is not very sensitive to the exact value of the electric field and the LGAD can be operated very reliably; this condition also minimises the noise coming from the multiplication process, the so called excess noise factor (see Section 5.2.3), enhancing the LGAD performances.

Sensor thickness

The choice of the sensor thickness must be made out of a compromise between a short charge collection time, a big signal and a small detector capacitance.
The rise time of a current signal generated by a MIP in a LGAD is as long as the drift time of an electron traversing the entire sensor thickness, which is basically dependent on its saturated drift velocity, as explained in Section 5.1.
As a MIP creates a constant number of pairs per micron $n_{e-h} \approx 73\ \frac{pairs}{\mu m}$, in a thin sensor, an ionising particle creates fewer e-h pairs than in a thicker sensor, for a total produced charge

$$Q = GQ_0 = Gn_{e-h}ed\ ,$$

where $G = Q/Q_0$ is the gain multiplication factor of the detector, e is the elementary charge and d is the detector thickness.
In spite of the expectations, the peak of the current signal is approximately the same for silicon sensors of all thicknesses [32]. In fact, according to Ramo's theorem (Eq. 5.1.1) the induced current is also proportional to the weighting field which is inversely proportional to the detector thickness for the parallel plate geometry: $E_w \propto 1/d$. For a detector with gain G, the current signal peak is therefore

$$I_{max} = QE_w v_{sat} \propto Gn_{e-h}ed\frac{1}{d}v_{sat} = Gn_{e-h}ev_{sat}\ . \tag{7.2.1}$$

Given a fixed gain, employing thinner sensors guarantees shorter signals with same amplitude as shown in Figure 7.8: a steeper rising edge, i.e. a higher *slew rate* $\frac{dV}{dt}$, is one of the main requirements for an improved time resolution. Sensors which are very thin, however, have large values of capacitance and the gain must be high in order to produce a charge big enough to be measured accurately by the read-out electronics. The high capacity and the noise introduced by the multiplication worsens the time resolution.

Eq. 7.2.1 also shows that the peak amplitude is limited by the saturated velocity and proportional to the charge. This fact is at the core of the limited time precision of no-gain silicon detectors: the signal amplitude is limited by the saturation of the velocity and the maximum value of the weighting field, and

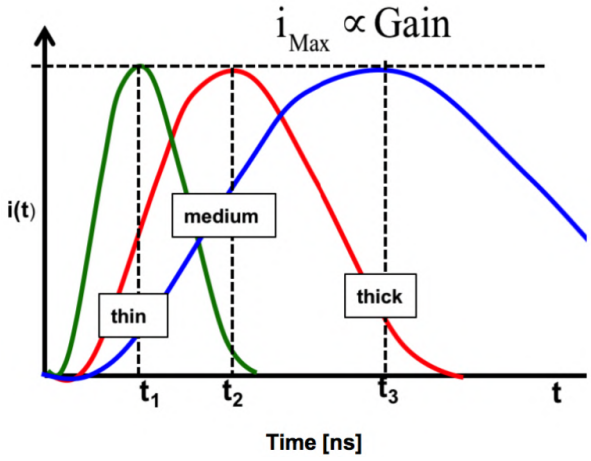

Figure 7.8: Current signals from sensors with same gain and different thickness.

it cannot be increased using thicker sensors. Current amplifiers, exploiting the fast initial burst of current, give therefore similar time resolutions when used with thin and thick sensors for same noise performance, while charge sensitive amplifiers might benefit from thicker sensors as they integrate the charge over a longer period, however at the price of a longer rise time.

7.2.2 UFSD Read out electronic board

Most of the times, the sensor prototypes appear as very small silicon devices, not bigger than few square millimeters, and their sole electrical contacts are even smaller metal pads on their surface whose typical dimensions are of the order of tens, or few hundreds of micrometers. In addition, at this stage, the dedicated integrated circuits is still in development or debugging phase, hence it is not available for its final task. In order to measure the electrical characteristics of the silicon sensor prototype it is therefore necessary a simple and reliable readout board in order to study the sensor signal in as many of its characteristics as possible.
The design and production of a discrete components printed circuit board (PBC) for timing, however, is not an easy task. The readout board is required to accurately amplify very fast electrical signals while keeping the noise level as low as possible. In fact, in order to be able to understand the sensor prototype characteristics, the noise produced by the board should ideally be negligible with respect to that produced by the sensor itself.

I participated in such effort together with the Genova INFN group and the result was the production of a 6-channel, two-stage broad-band amplifier which is depicted in Figure 7.9. The scheme can be described as a Broad Band Amplifier, as the kind described in Section 5.2.2, more specifically an inverting trans-impedance amplifier.
The first amplification stage is performed by an AC-coupled silicon-germanium bipolar transistor (BJT) designed for high bandwidth (up to 5 GHz) and low noise applications, featuring a gain of nearly 30 dB at 2 GHz and an integrated output noise of 260 μV.

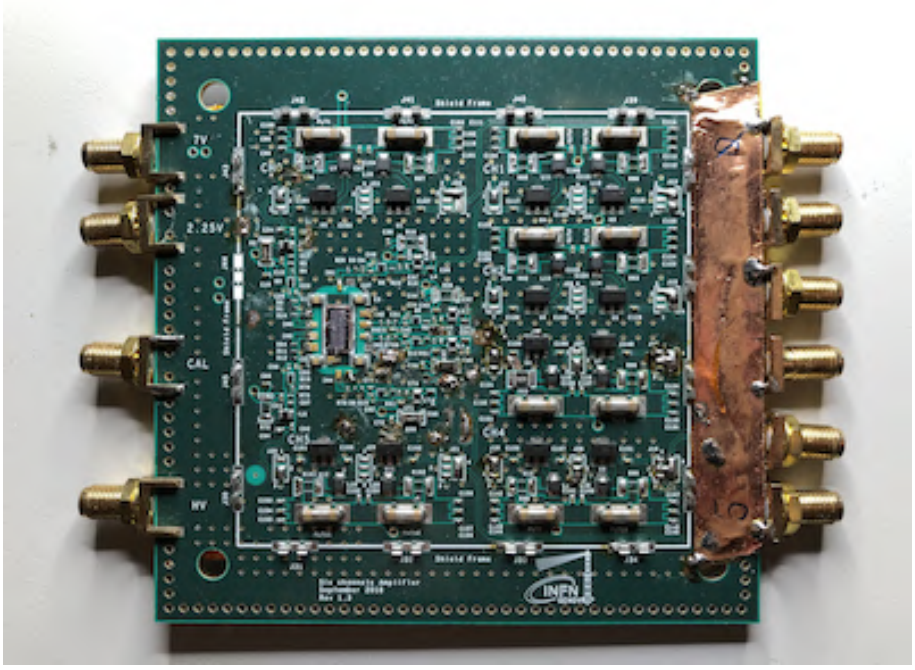

Figure 7.9: The six-channel amplification board developed by the Genova INFN group used as front-end for prototype silicon sensors for timing.

The amplifier design was optimised for sensors with capacitance of the order $\sim$ 10 pF such as UFSD prototypes. It is expected to produce signals with a total charge of $\sim$ 10 fC and a rise time of about 500 ps.
The second stage consists of a current amplifier, designed for fast signals. It is based on a monolithic wide band amplifier, with 2 GHz bandwidth, and provides a 20 dB gain factor.
The PCB design has been optimised for small and fast signals by minimising all parasitic capacitance and inductance sources, choosing very small size surface-mount components, and ground-burying all signal and power lines whenever possible. Protection from external electromagnetic noise is ensured by hermetic metal shields. Some additional metallic shields were added, together with other modifications, in order to correct design flaws and to obtain a good timing performance.

During my PhD, this board version was not used as UFSD readout but it has proved to perform satisfactorily on the signals produced by another silicon sensor technology for timing applications which will be described in next section.

The design and the production of a second generation board was completed in late 2020. The new board design addressed the flaws of the old one and it is expected to feature an even better timing performance.

7.3 Timespot 3D timing detectors

The TIMESPOT Project (TIME and SPace real-time Operating Tracker) [66] is an INFN research and development project which is also proposing a design of a tracking detector able to fulfill the requirements of future experiments at high luminosity colliders.
Future experiments at the High Luminosity LHC [50], for instance, will have to deal with as many as ~ 200 independent proton-proton collisions during a $\sim 150\,\text{ps}$ long bunch crossing. Adding the time information to the recorded tracks, i.e. enabling a *4D tracking*, is expected to restore the tracking efficiency at the level of current LHC conditions [53]. This argument has been described in Chapter 4 in Part I of this thesis.
The solution proposed by the TIMESPOT project involves the optimization of all the steps in track detection, from the sensor level to the readout electronics and the real-time track reconstruction. The project aims at the production of a complete demonstrator of such a device, so to face all the technical problems of a full-size system that can be installed in an actual experiment.
The TIMESPOT detector design addresses the following requirements:

- Radiation hardness, in order to sustain fluences up to $\sim 10^{16}\ \text{n}_{\text{eq}}\text{cm}^{-2}$.
- Space resolution as good as current tracking detectors, hence $\simeq 10\,\mu\text{m}$.
- Time resolution ideally less than 20 ps per pixel.
- More intelligent trigger and reconstruction algorithms characterized by real-time reconstruction of tracks, possibly at the early stages of readout, in order to reduce the DAQ bandwidth down to $1 - 5\,\text{Tb/s}$ (for an exemplifying $\sim 1\,\text{cm}^2$ sensor)

The development of a full detector system able to address all these requirements involves considerable specialised knowledge and effort in various sectors. The activity of the project is hence organized in different branches: sensor development, front-end electronics development, studies on reconstruction algorithms based on pattern recognition techniques.

7.3.1 3D silicon detector for timing

The 3D technology for silicon sensors [24], described in the previous Chapter 6, allows the fabrication of sensors which are characterized by a higher radiation resistance [68] compared to those produced with planar geometry. 3D geometry also allows a complete decoupling of the distance between the collecting electrodes and the bulk thickness, enabling the construction of very close electrodes

Figure 7.10: Geometry and weighting field comparison for 3D column and 3D trench sensor geometries [67].

given a standard wafer thickness, hence enabling a very fast charge collection. As it was also previously discussed in Section 7.1.1, in order to have excellent timing performance, the electric signal produced by the detector is required to be uniformly shaped. This is only possible if the electric field is both intense and uniform throughout the sensitive silicon volume and the charge collection does not depend on where the electrons and holes were produced. Unfortunately the traditional 3D sensors geometry is characterized by column electrodes which produce a highly non uniform electric field and hence poor timing performance. The TIMESPOT project proposed the idea that this limit can be overcome by using an innovative geometry of trench-shaped electrodes which approximately replicates a parallel plate geometry in a 3D sensor (figure 7.10).
Simulation studies show that a 3D trench sensor produces a nearly uniform electric field in its active volume, hence it is expected to produce uniform signal shapes and charge collection times of less than 400 ps. A custom software, named *TCode* [69], has been developed in order to accurately simulate the electrical behaviour of 3D trench silicon sensors and it has proven to be a reliable tool to predict the characteristics of the produced signals (Figure 7.11).
The necessary technology studies have been finalized at Fondazione Bruno Kessler (FBK), Trento and the first production batch (figure 7.12) has been completed in summer 2019. It includes a wide variety of sensor geometries with a 150 μm deep active volume, including a pixel sensor whose pixel size is 55 μm $\times$ 55 μm. A second production has been launched and was completed during 2020 and it will be tested shortly.
The TIMESPOT collaboration has also been developing the readout electronics for this detector. In fact it designed and produced the first prototype of an integrated circuit in 28 nm CMOS technology with size 1.5 mm $\times$ 1.5 mm. The circuit prototype has been conceived mainly for testing purposes and includes a full test readout chain for the 55 μm $\times$ 55 μm $\times$ 150 μm pixel. Three different time-to-digital converters (TDC) technologies are included, in order to compare their performances. The 8 front-end channels consist in a Charge Sensitive Amplifier (CSA) and a leading edge discriminator. All the cells are independently accessible for their full characterization and testing. An updated version has been submitted for production.

This thesis presents preliminary results on TIMESPOT 3D trench sensors obtained with laboratory tests involving both focused laser beams and particle beams. A first estimation of their timing performance will be provided.

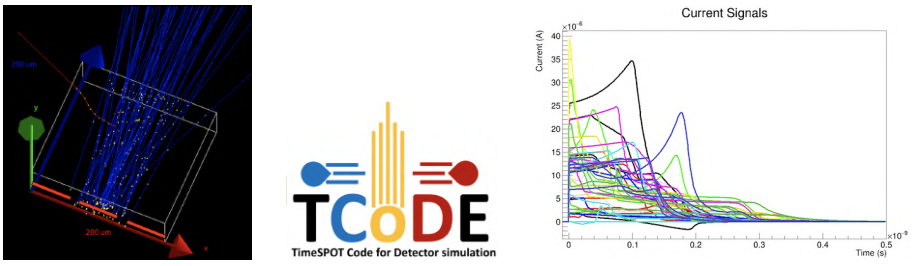

Figure 7.11: Example of TCode simulated current signals for a 3D trench sensor [67].

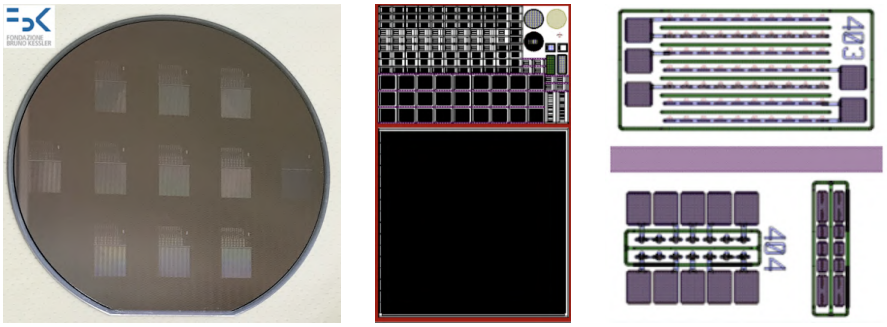

Figure 7.12: 3D silicon sensor production by FBK. From left to right: wafer, repeated pattern using a stepper device, example of individual and strip-pixel readouts.

7.3.2 Electrical tests results

Standard electrical tests have been performed on the newly produced 3D silicon trench sensors. Measurement of sensor current and capacitance versus bias voltage (IV and CV curves) have been performed using a probe station at room temperature. Figure 7.13 shows the results of the electrical tests on the sensors: IV curves show no breakdown for inverse bias voltages as low as $-50\,\mathrm{V}$, whereas CV curves show how the whole volume of the sensor appears as depleted, and hence sensitive to radiation, for reverse bias voltages lower than $-13\,\mathrm{V}$.

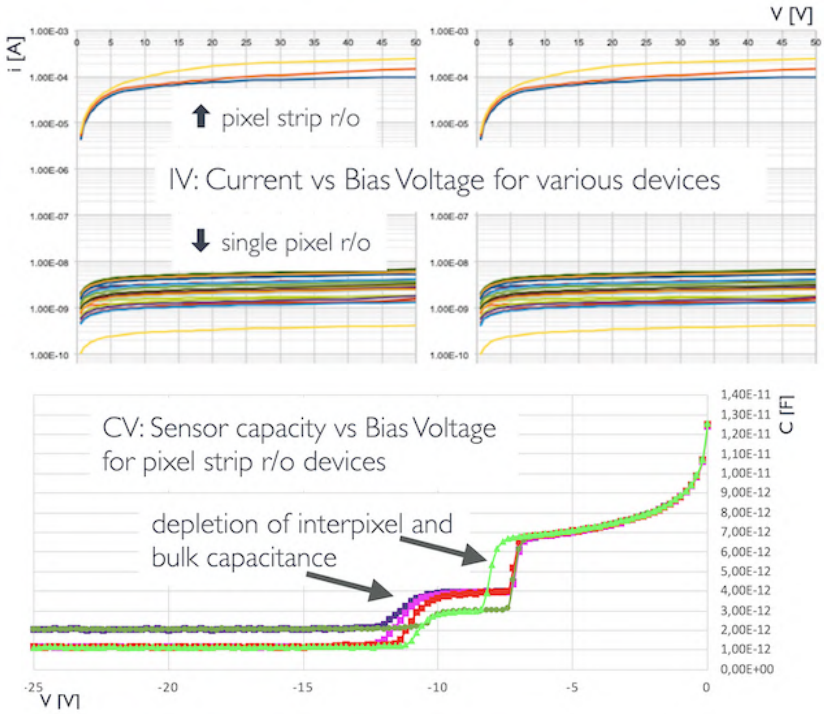

Figure 7.13: IV and CV curves for 3D trench silicon sensors [67].

Laser tests

In order to study the signal formation, sensors have been exposed to infrared laser light ($\lambda_{\text{laser}} \simeq 1064\,\text{nm}$) which is able to penetrate the sensor bulk and simulate the charge creation by a ionizing charged particle crossing it. This measurement is widely known as Transient Current Technique (TCT) and allows a deep investigation of the signal characteristics and timing performances of the sensor. Figure 7.14 illustrates the results of the signal measurements using TCT. In particular, signal amplitude, area and rise time are studied as a function of the bias voltage. All signal characteristics are approximately constant for reverse bias voltage lower than $\simeq -10\,\text{V}$.
It is possible to conclude that any reverse bias voltage lower than $-15\,\text{V}$ can be considered an appropriate working point for the sensor.
Simulation studies predict a saturation of the carrier velocity for $\Delta V_{bias} \leq -40\text{V}$, which can be chosen as working point.

7.3.3 Beam tests at Paul Scherrer Institute (PSI)

In early October 2019 a full beam test of the 3D trench silicon sensors was performed at the Paul Scherrer Institute (PSI) accelerator. The setup and the preliminary results will be briefly described. Measurements focused on the study of "single pixel" performance, the most promising in terms of timing performance. The sensors were wire-bonded to broadband amplifier boards with discrete elements designed in Genova and in Kansas University. The results that will be presented in this thesis are obtained with the Genova amplifier board, described in more detail earlier in Section 7.2.2.
The device under test (DUT) was aligned to two Cherenkov time taggers (Micro Channel Plate, MCP), as schematized in Figure 7.15. The data acquisition system consisted of a high-end oscilloscope.
The laboratory provided a 50 MHz beam clock which was used for absolute time determination. The trigger logic was set as the coincidence of DUT and MCP1 signals, while the combination of MCP1 and MCP2 signals was taken as the time reference. Figure 7.16 shows the signal amplitude distribution is shown. The shape of the distribution clearly resembles the Landau function as the successful fit indicates. The peak of the distribution coincides with the signal amplitude associated to a Minimum Ionizing Particle (MIP) and results in $\Delta V_{\text{MIP}} \simeq 21\,\text{mV}$, which is in agreement with simulation studies.
The following plot in Figure 7.16 shows the distribution of the time difference between the DUT signal and the time tagger (MPC) one. For each signal, the time is set when the signal crosses a threshold which is defined as a fixed ratio of its amplitude, with a technique known as Constant Fraction Discriminator (CFD) (see Section 7.1). The central portion of the distribution of time differences can be described as a Gaussian function whose width is an estimate of the combined time resolutions of the DUT and the MCP. The sigma value of the fitted Gaussian function resulted around 32 ps. In Figure 7.17 the dependence of the time resolution on both the bias voltage and the signal amplitude is shown. The plot on the upper part shows an extremely small change of the time resolution for different values of the bias voltage. The bottom plot shows the expected improvement of the time resolution for bigger signals. It is worth noting that the time resolution for the signal amplitude associated with a MIP

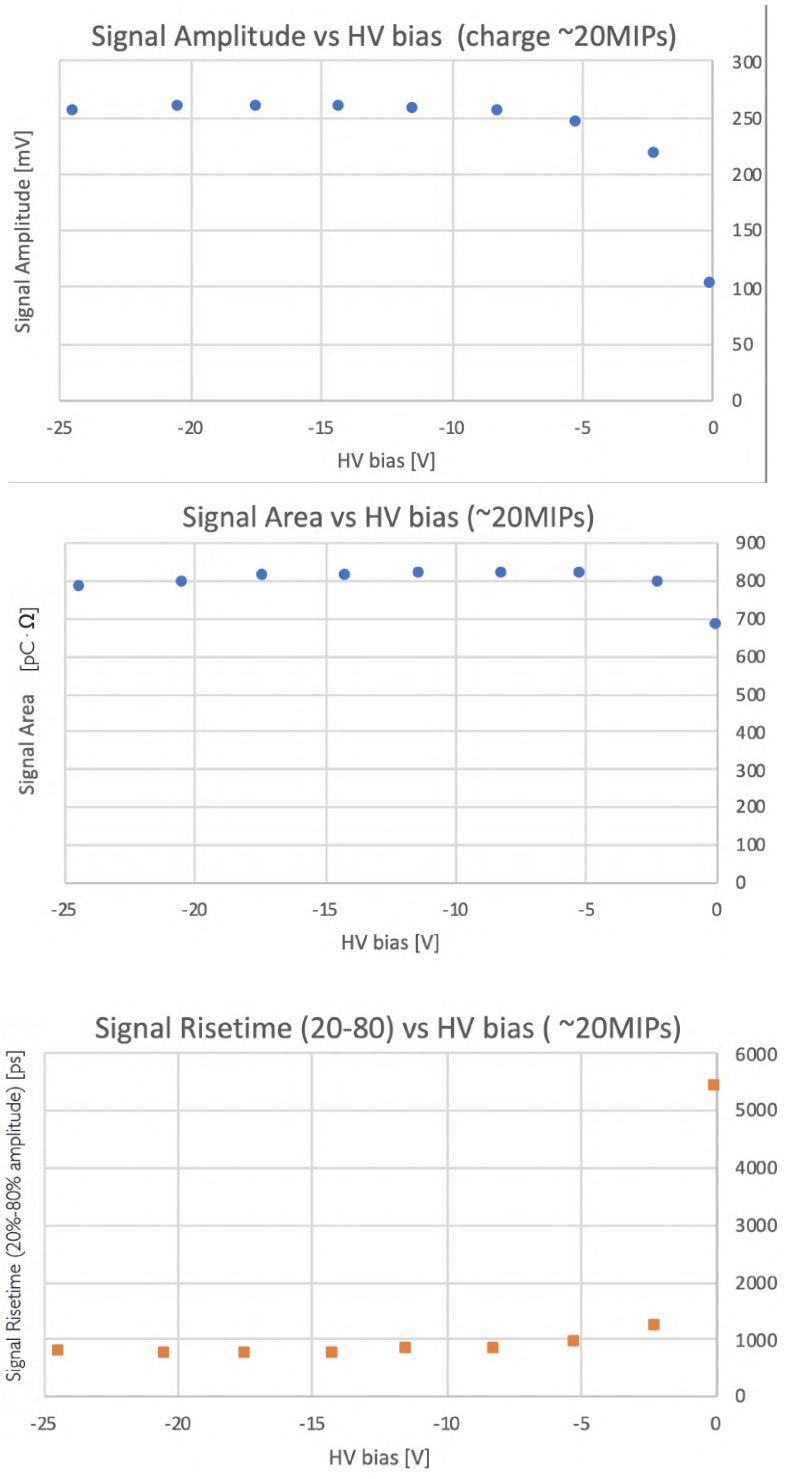

Figure 7.14: TCT tests for 3D trench silicon sensors

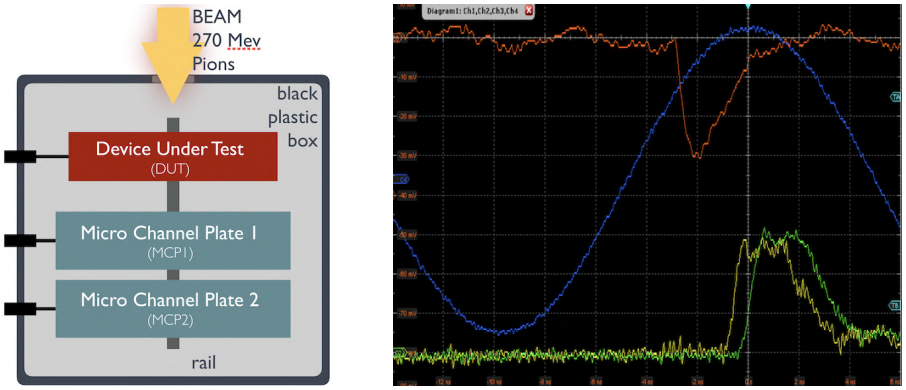

Figure 7.15: Beam test setup and resulting signals (red: DUT, green and yellow: MCP, blue: beam clock)

is around $\sigma_t \simeq 32\,\text{ps}$ which is to be considered an excellent result.
In fact, the measured time resolution has several contributions:

$$\sigma_t^2 = \sigma_{t,\,\text{Jitter}}^2 + \sigma_{t,\,\text{TimeWalk}}^2 + \sigma_{t,\,\text{Landau}}^2 + \sigma_{t,\,\text{MCP}}^2 \quad .$$

In order to extract the DUT jitter which can be interpreted as the time resolution of the 3D silicon sensor itself, it is necessary to analyse the other contributions.
$\sigma_{t,\,\text{TimeWalk}}^2$ can be considered as negligible as a constant fraction discriminator was implemented offline.
$\sigma_{t,\,\text{Landau}}^2$ is very small as 3D sensor geometries are almost immune to fluctuations in charge deposition.
The time resolution of the time tagger was measured to be $\sigma_{t,\,\text{MCP}} \simeq 18.2\,\text{ps}$ and can be easily subtracted.
The resulting measurement for the time resolution is therefore

$$\sigma_{t,\,\text{3D}} \simeq 30\,\text{ps} \quad .$$

This value also includes the noise contribution introduced by the readout electronics, which can be subtracted in order to achieve an even smaller time resolution which can be considered as intrinsic of the 3D silicon sensor with trench geometry [70].

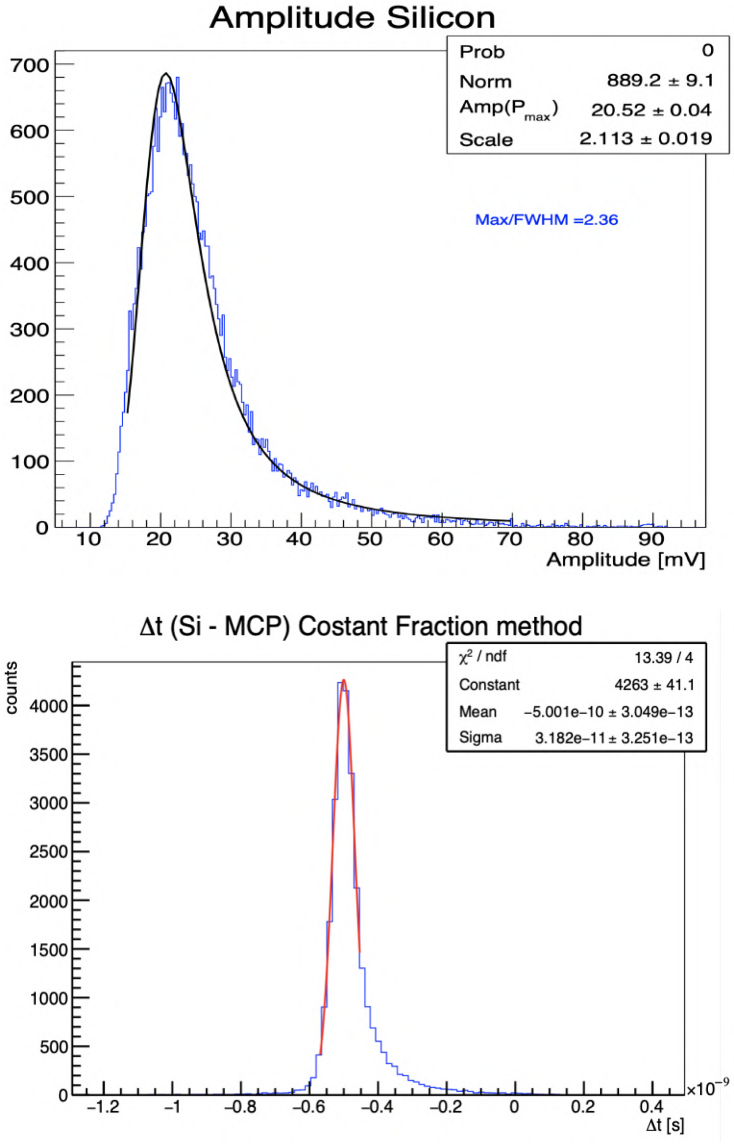

Figure 7.16: Signal amplitude and time difference distribution

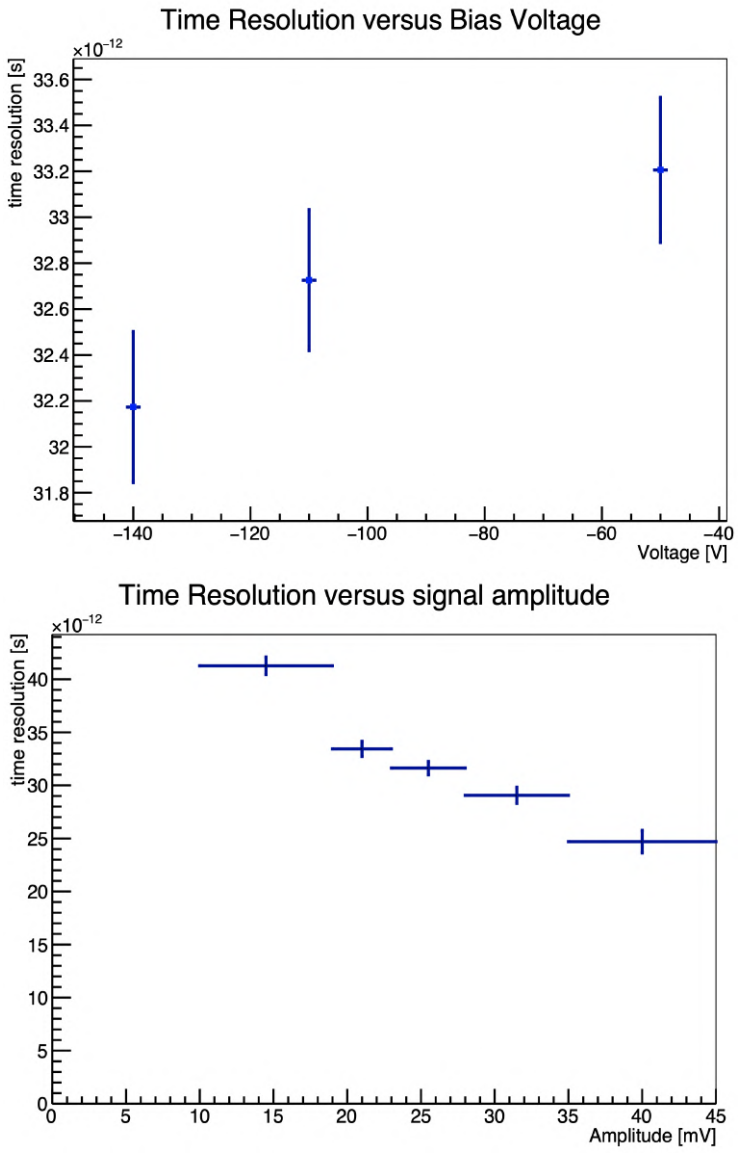

Figure 7.17: Time resolution dependence on bias voltage and signal amplitude

Part III

Central exclusive production of ttbar pairs at CMS

This last part of my thesis is devoted to the description of a data analysis work performed within the CMS collaboration to measure for the first time the cross section of the central exclusive production of top quark-antiquark pairs. Such a measurement heavily relies on the PPS system described in Section 2.2 of Part I of this thesis and represents therefore a natural application of my works on the detector described in Part II.

In central exclusive production processes, the incoming beam protons interact without dissociating. As a result of the interaction, a set of particles ($t\bar{t}$ pairs in the case of my thesis) is produced in the final state, and the protons that interacted lose a fraction of their momentum and are slightly deflected from their original trajectory.
Due to their large mass, top quarks decay almost immediately, before hadronizing, to a W boson and a b quark; the W boson in turn can decay to a charged lepton-neutrino pair or to a pair of quarks: depending on the decays of the two W bosons yielded by a $t\bar{t}$ pair, $t\bar{t}$ pairs can be classified as dileptonic (9% of all $t\bar{t}$ pairs), semileptonic (45 %) or all hadronic (46 %).
In particular here we focus on $t\bar{t}$ pairs decaying semileptonically ($b\ell\nu\bar{b}jj$), where ℓ represents either an electron or a muon and j represents any light jet (i.e. a jet originated by u, d, s or c quarks). Because of their more difficult experimental reconstruction, semileptonic $t\bar{t}$ pairs where the charged lepton is a τ are not considered here.
The $t\bar{t}$ pair production process in central exclusive mode can be represented by the Feynman diagrams shown in Figure 7.18. According to theoretical calculations within the Standard Model, the dominant contribution is via the quantum electro-dynamics (QED) photon-fusion process, which has a cross section of the order of 0.1 fb, while the QCD interaction provides a contribution to the cross section smaller by two orders of magnitudes [71]. Hence, only the QED contribution is considered in the analysis.
In the analysis, the $t\bar{t}$ decay products are measured in the central CMS system, while the outgoing protons are detected by the Precision Proton Spectrometer (PPS). My major role in the data analysis effort has been the set up and optimization of the event selection strategy to suppress the backgrounds while maintaining a good signal efficiency, as will be detailed later.

Part III of my thesis describes the ongoing efforts to measure the cross section for the central exclusive production of $t\bar{t}$ pairs and preliminary (not yet public) results. The text is synchronized with the internal CMS document AN-20-004, under preparation, of which I am co-author.

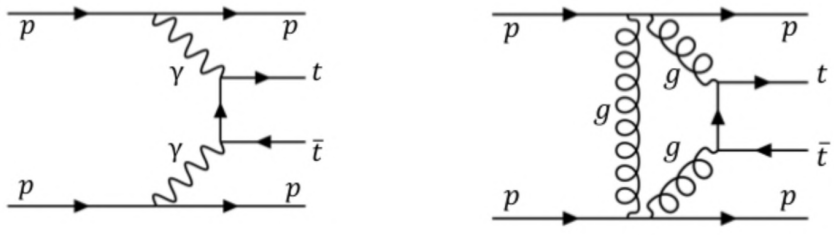

Figure 7.18: $t\bar{t}$ exclusive production via $\gamma\gamma$ fusion (left) or via gg fusion (right).

Chapter 8

Final state proton reconstruction

The CMS Precision Proton Spectrometer (PPS) was already described in the previous Section 2.2 of Part I of this thesis with particular focus on its experimental apparatus. This CMS detector allowed the studies on Central Exclusive Production (CEP) processes in proton-proton collisions in standard LHC running conditions. PPS consists of a tracker which is installed along the beam pipe at approximately 210 m from the CMS interaction point on both sides of the LHC tunnel. A schematic representation of the system layout of one side from CMS is shown in Figure 8.1 .
The PPS detectors evolved during the data taking (see Figure 2.12 at pag. 22). During 2017 PPS used two tracking systems: strips and 3D pixels. During 2018 strips were replaced by 3D pixel detectors. This analysis, as any, must account for this change and the results presented in this thesis only refer to the data produced in 2017, as the newer data sets are yet to be validated.
In this Chapter, the reconstruction of the final state protons will be described.

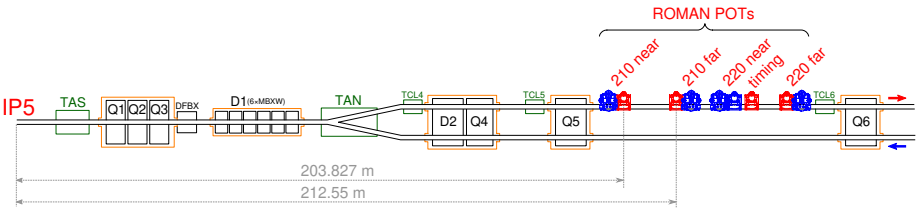

Figure 8.1: A schematic layout of the beamline as seen from above between the interaction point within CMS (IP5) and the location of the Roman Pots (cf. Section 2.2.1). The image also displays the dipole magnets (D1, D2), quadrupoles (Q1-Q6), collimators (TCL4-TCL6), absorbers (TAS, TAN), and quadrupole feedboxes (DFBX). The 210 near and 210 far PPS stations are indicated, along with the timing RPs not used here. The 220 near and 220 far units (not used here) are also shown. The RPs indicated in red are the horizontal PPS ones; those in blue are part of the TOTEM experiment. The red (blue) arrow indicates the outgoing (incoming) beam. In the CMS coordinate system, the z-axis points to the left. The arm in the opposite LHC sector 45 (not shown) is symmetric with respect to the IP [18].

8.1 Proton Kinematics

The PPS tracking detectors are focused on the measurement of the trajectory of the protons which were deflected, but not dissociated, by an interaction at the center of the CMS detector. From the measurement of the proton trajectory deflection from the beam axis, proton momentum loss (commonly denoted as $\xi = \Delta p/p$) and proton energy transfer (denoted as $t = (p_f - p_i)^2$) are obtained. In this analysis PPS used as a tagger for CEP $t\bar{t}$ production processes. In fact, in order to look for exclusive $t\bar{t}$ production processes in IP5, the PPS measurement is necessary to correlate the kinematic quantities of the central $t\bar{t}$ system (measured by the the central CMS detector) with the ones coming from the protons (PPS).

In order to describe the protons kinematic, it is necessary to define the following quantities::

- x^*: x coordinate of the proton when it interacts at IP5;
- y^*: y coordinate of the proton when it interacts at IP5;
- θ_x^*: projection of the polar angle onto the xy plane;
- θ_y^*: projection of the polar angle onto the yz plane;
- $\xi^* = \frac{|\vec{p}_f| - |\vec{p}_i|}{|\vec{p}_i|}$: proton fractional momentum loss, being $\vec{p}_f$ the proton momentum after the interaction and $\vec{p}_i$ the one before the interaction.

We call $x, \theta_x, y, \theta_y, \xi$ the same quantities evaluated in the outer system. We then define $\vec{d^*} = (x^*, \theta_x^*, y^*, \theta_y^*, \xi^*)^T$ and $\vec{d} = (x, \theta_x, y, \theta_y, \xi)^T$. We can write $\vec{d}$ in function of $\vec{d^*}$ using the equation:

$$\vec{d} = T\vec{d^*}$$

Having defined T as:

$$T = \begin{pmatrix} v_x & L_x & m_{13} & m_{14} & D_x \\ \frac{dv_x}{ds} & \frac{dL_x}{ds} & m_{23} & m_{24} & \frac{dD_x}{ds} \\ m_{31} & m_{32} & m_{23} & v_y & D_y \\ m_{41} & m_{42} & \frac{dv_y}{ds} & \frac{dL_y}{ds} & \frac{dD_y}{ds} \\ 0 & 0 & 0 & 0 & 1 \end{pmatrix} \tag{8.1.1}$$

Each element of the matrix is linked to the optical parameters of the machine. PPS measures the values of $x^*, y^*, \theta_x^*, \theta_y^*$. Solving the system associated to the matrix, it is possible finding out the value of ξ. We will call ξ_1 the value obtained from the negative arm and ξ_2 the one obtained by the positive arm. Knowing ξ_1, ξ_2 it can be shown with relativistic kinematic that:

$$M_{t\bar{t}}^2 = s\xi_1\xi_2 \tag{8.1.2}$$

$$y_{t\bar{t}} = \frac{1}{2}\ln\frac{\xi_1}{\xi_2} \tag{8.1.3}$$

Where $M_{t\bar{t}}$ is the $t\bar{t}$ pair invariant mass measured by CMS and $y_{t\bar{t}}$ is its rapidity. s is the square of the invariant mass of the system.
The two above cited relations are fully independent and are the conditions that connect the kinematic of the central system with the one of the outer system. Finding events in which these relations are validated for the reconstructed objects is the scope of this analysis.

8.2 PPS acceptance

The PPS detector is far from hermetic: the small active area of the sensors and the position of its tracking stations limit the acceptance it can reach, in other words the values of the kinematic quantities of the objects it can measure. This limit can be expressed in terms of the measurable range of proton fractional momentum loss ξ. Moreover, equations 8.1.2 and 8.1.3 allow the detector acceptance to be expressed as a range for the mass M_X and the rapidity y_X (or pseudorapidity η_X) of the system X produced in the central CMS detector and measured by it.
This acceptance yields the acceptance region which can be visualized as an area in a plot which has M_X and y_X along its axes. Figure 8.2 shows such acceptance map for the 2018 data. The small light green area corresponds to the M_X and y_X values matching the two protons which can be measured by all the tracking stations in both arms of PPS.
This region extends considerably to the yellow area if one settles for the measurement of only one proton in the final state (such processes are generally referred to as Central *semi*-Exclusive Production ones).
The acceptance map is strongly affected by the LHC optics, expressed by the values of the parameters inside of the T matrix in Equation 8.1.1. During the 2017 data taking, in fact, the LHC machine adopted different optics conditions, varying the crossing angle at the CMS interaction point the β^* value. Therefore two acceptance maps are provided in Figure 8.3. The Figures show that the PPS detector can measure both final state protons in Central Exclusive Production of a central systems with a high mass $381\,\text{GeV} < M_X < 1.924\,\text{TeV}$ and produced in the central rapidity region, approximately $|y| < 1$, or $|\eta| < 1$ as the two quantities are almost identical in LHC conditions.

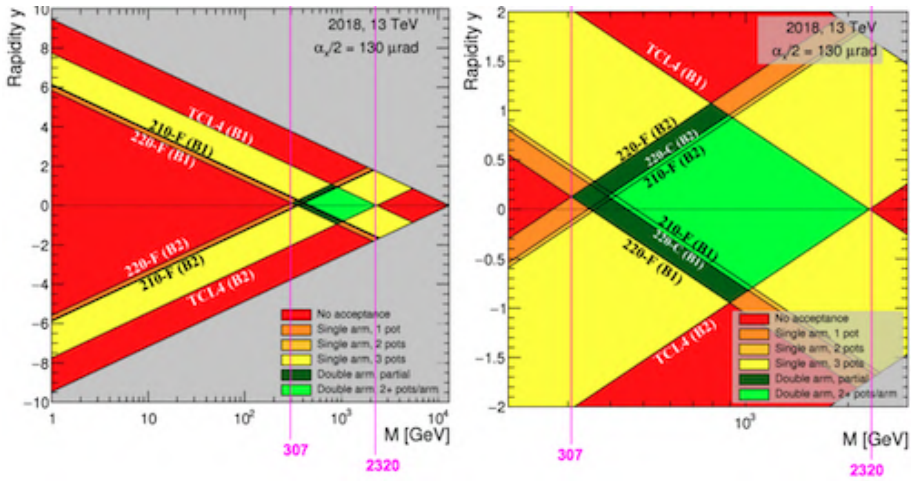

Figure 8.2: Acceptance map for PPS protons in terms of mass and rapidity of the central system for the 2018 dataset [72].

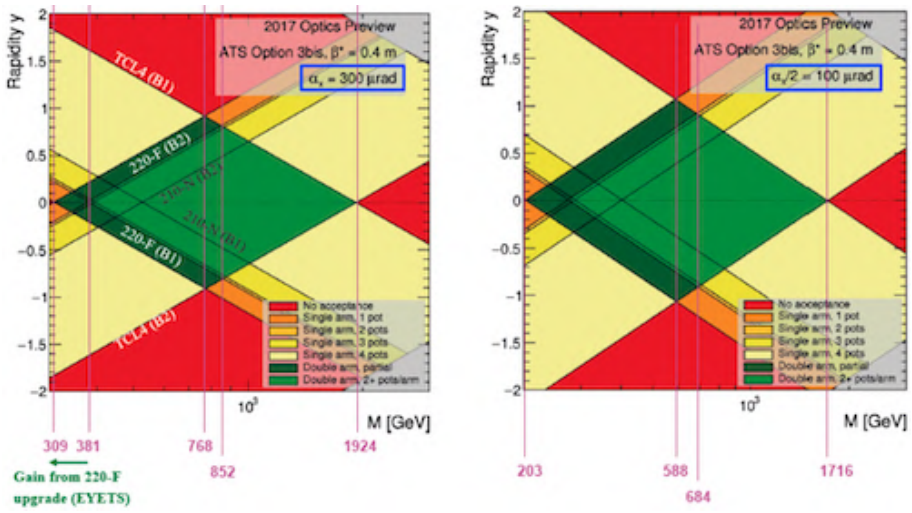

Figure 8.3: Acceptance maps for PPS protons in terms of mass and rapidity of the central system for the 2017 dataset. Each map refers to a different crossing angle in IP5. [72]

Chapter 9

Search for central exclusive production of top quark pairs.

9.1 Data and simulation samples

9.1.1 Data

The analysis is performed using proton-proton collision data at $\sqrt{s} = 13\,\text{TeV}$ collected in 2017 by CMS and PPS. Events were triggered by the single lepton lowest unprescaled triggers in the central detector (CMS). The triggers used in the analysis are listed in Table 9.1: as the names indicate, these triggers select events with isolated muons having transverse momentum (p_T) above 27 GeV, or with electrons having p_T above a given threshold specified in the string name (35, 28, 30 GeV), and eventual additional selections on other variables, such as the absolute value of the pseudorapidity (η) below 2.1, and/or H_T above 150 GeV, where H_T is the scalar sum of the p_T of all reconstructed particles in the event.

The total integrated luminosity collected by PPS and CMS corresponds to $39.5\,\text{fb}^{-1}$ for 2017 and $57.9\,\text{fb}^{-1}$ for 2018 data [73]. Therefore, the analysis will eventually be performed on a total integrated luminosity of $97.4\,\text{fb}^{-1}$. A dedicated json file with the official CMS good data quality criteria is used to select the triggered events. However, as mentioned earlier, the 2017 and 2018 datasets are significantly different because of the different detector configuration. The analysis described in this thesis targets only 2017 data, while the processing

Description	Trigger name
Muon trigger	HLT_IsoMu27_v
Electron trigger	HLT_Ele35_WPTight_Gsf_v
Electron trigger	HLT_Ele28_eta2p1_WPTight_Gsf_HT150_v
Electron trigger	HLT_Ele30_eta2p1_WPTight_Gsf_CentralPFJet35_EleCleaned_v

Table 9.1: List of the CMS triggers used.

of 2018 samples will be performed in next months.

As described in previous Section 8.1, in order to obtain the values of ξ_1, ξ_2, the measurement from the PPS tracking stations is needed. While in 2018 both the stations had pixels, in 2017 the "far" station had pixels, while the other one had strips. Pixel trackers allow multi-tracks reconstruction, while strips do not. This means that with the 2018 data set it will be possible to reconstruct events with more than one proton per side of PPS, while in the 2017 data set this is not possible. Therefore, when considering 2017 data, one will have just the events with exactly one proton per arm of PPS. Of course, this will lead to an efficiency loss, since all signal events with extra pile up protons will be automatically discarded. For 2018, instead, no events will be automatically discarded but there will be, in general, more than two protons in the final state. Therefore, we will have to choose just one pair of them. In particular, we will choose the pair that minimises the quantity $f(\xi_1, \xi_2) = |M_X^2 - s\xi_1\xi_2|$. For these reasons, 2018 analysis will have a bigger efficiency.

9.1.2 Simulated samples

Several Monte Carlo (MC) event generators are used to simulate both signal and background processes. For all processes generated this way, the detector response is simulated, using a detailed description of the CMS detector, based on the GEANT4 package [74].

Table 9.2 includes a list of the background samples used in this thesis, together with their cross section σ. The $t\bar{t}$ samples are generated with the MG5_aMCatNLO event generator [75], with up to 3 jets at NLO.

Signal samples for the $pp \to p \oplus t\bar{t} \oplus p$ has been generated using FPMC [3] generator with Equivalent Photon Approximation (EPA) for photon fluxes [76]. Signal samples were generated for the forward protons with momentum loss in a range of $0.2\% < \xi < 15\%$. Top quark decays were simulated with MadSpin [77], vetoing fully hadronic decays. The cross-section times filter efficiency for signal samples is estimated to be 0.128 fb.

For all processes, the parton showering and hadronization are simulated using PYTHIA 8 [78, 79] with `CP5` tune [80].
The samples from the dataset labelled as *RunIISummer19UL17MiniAOD- - 106X_mc2017_realistic_v6-v2*, according to the CMS internal conventions, are used for 2017 data.

Process	Truncated sample name	σ [pb]
$W + jets$	WJetsToLNu_TuneCP5_13TeV-madgraphMLM-pythia8	61526.7
$t\bar{t}$	TTJets_TuneCP5_13TeV-amcatnloFXFX-pythia8	832
tW	ST_tW_top_5f_NoFullyHadronicDecays_TuneCP5_13TeV	35.85
$\bar{t}W$	ST_tW_antitop_5f_NoFullyHadronicDecays_TuneCP5_13TeV	35.85
$DY + jets$	DYJetsToLL_M-50_TuneCP5_13TeV-madgraphMLM-pythia8	460
WW	WW_TuneCP5_13TeV-pythia8	75.88
WZ	WZ_TuneCP5_13TeV-pythia8	27.57

Table 9.2: Samples and production cross-sections of the considered backgrounds.

9.2 Event selection

The event selection is optimised using simulated samples in order to reduce the number of background events while maintaining a high efficiency on the signal. It comprises several levels that are described in the following, starting from the CMS basic objects up to higher level selections.

9.2.1 CMS Object selection (jets, leptons)

Jets are reconstructed using the anti-k_T algorithm with $R = 0.4$, required to pass $p_T > 25\ GeV$ and $|\eta| < 2.4$. Jets contain b-hadrons were tagged with the deepCSV "medium" working point [81])

Leptons with a kinematic cut at $p_T > 30\ GeV$ are selected, and in addition the requirement $|\eta| < 2.1$ for electrons and $|\eta| < 2.4$ for muons is imposed. Lepton isolation cuts were also applied, imposing that the angular distance ΔR between a jet and a lepton must be at least 0.4.

9.2.2 Event preselection

The event selection can be summarised in this way:

- Events saved by the triggers (Table 9.1)
- At least 4 jets with at least 2 b-tagged jets
- Exactly one accepted lepton.

9.2.3 b-jet assignment algorithm

Since b-jet tagging can't discriminate between a jet from b and a jet from $\bar{b}$, an important problem is the so called "b-Jet assignment", which means understanding which b-jet can be associated with the leptonically decaying top quark. To solve this problem, the following approach is used:

- let's suppose we have in the final state n b-Jets and m light-Jets. Each b-Jet will be called b_i ($i \in \{1, ..., n\}$) and each light jet will be called q_j ($j \in \{1, ..., m\}$);
- the neutrino 4-momentum is extracted from lepton and missing energy by imposing a W-boson mass constrain: $m_{\ell\nu} = m_W$.
- all the possible combinations are tried of b-jet, lepton and the neutrino, $b_i\ell\nu$, and each time the invariant mass m_i of the system is computed.
- We call i^* the value of i such that m_i is closest to the top mass;
- b_{i^*} will be called "leptonic b-Jet" and will be considered as the b-Jet resulting from the top decaying leptonically.

With this procedure, the leptonic side of the decay is defined. Based on MOnte Carlo truth studies using $t\bar{t}$ samples, we found that using this procedure the b-jet is correctly assigned in ≈85% of all cases..

Now of course one has to understand which particles belong to the hadronic side. To do that, we use the following procedure:

- We consider all the possible combinations of $b_i q_j q_k$, being $i \neq i^*, j \neq k$;
- For each combination we calculate the invariant mass of the system;
- The set of light and b-Jets whose invariant mass is closest to the top mass is identified as the hadronic system.

This is a preliminary procedure that allow us to solve the b-Jet assignment problem and to decide which jets belong to the hadronic decay side. At the end of the following chapter we will discuss an improvement to this strategy.

9.2.4 Reconstruction of the proton candidates

Proton candidates can be reconstructed from single RP stations (either pixels or strips), or after a combination of two stations in the same arm (so-called multi-RP reconstruction). The latter is expected to offer a superior resolution, as a consequence of a multi-hit fit of the proton tracks but suffers form lower efficiency due to limited efficiency in silicon strip detectors. Reconstruction efficiency and resolution for different reconstruction algorithms and detectors are shown in Figures 9.1 and 9.2.

One can clearly observe a significant improvement on the final resolution from using the multi-RP reconstruction method. The drawback in the 2017 data-taking period is that the strip detectors are strongly affected by radiation damage. Thus, in our analysis we compare the expected results from using the different methods and decide at the end which one is optimal for our search.

9.3 Background determination

In this section, the background model is described and validated. The main background in this analysis is the inclusive production of SM $t\bar{t}$ pairs with two protons from PU events (combinatorial background). It originates from the random superposition of proton candidates, such as those from pileup collisions, reconstructed in the RPs on both sides. It is impossible to associate the

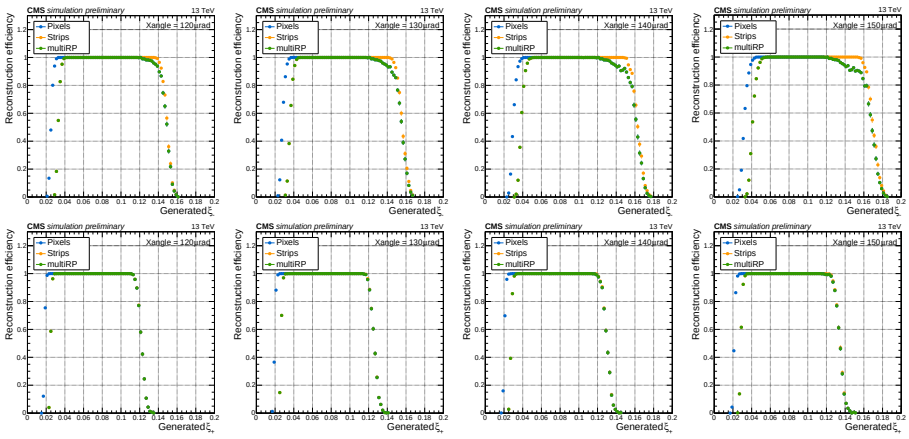

Figure 9.1: Reconstruction Efficiency for positive (top) and negative (bottom) arms as function of proton momentum loss (ξ) for the different beam crossing angles.

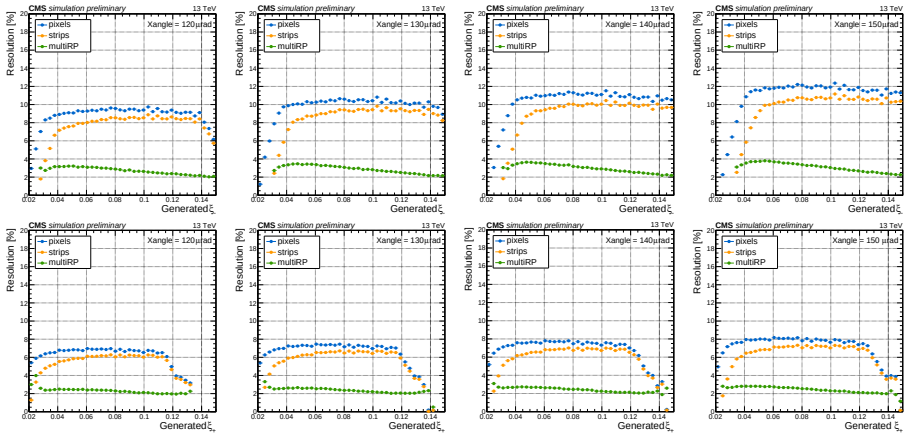

Figure 9.2: Resolution for positive (top) and negative (bottom) arms as function of proton momentum loss (ξ) for the different beam crossing angles.

protons to a specific primary vertex without any experimental information on the proton origin and exact timing at which it is reconstructed (at present, PPS timing detectors still do not have sufficient sensibility). Matching between the kinematic quantities measured by CMS and the ones measured by the forward detectors (PPS) can provide a strong discrimination against the combinatorial background. The kinematic quantities that can be correlated between CMS and PPS are:

$$M_X^2 = s\xi_1\xi_2 \tag{9.3.1}$$

$$Y_X = \frac{1}{2}\log\left(\frac{\xi_1}{\xi_2}\right) \tag{9.3.2}$$

where M_X and Y_X are the invariant mass and the rapidity of $t\bar{t}$ system respectively (measured in the central detector), and ξ_1, ξ_2 are the proton fraction momentum loss of positive/negative arm measured by PPS. Therefore, it is of primary importance having small uncertainties on M_X, ξ_1, ξ_2, so that this relation becomes a strong selection tool to discriminate the combinatorial background.

Due to the unprecedented resolution of the PPS (Section 9.2.4), the main challenge in the analysis is to achieve excellent mass resolution of the central system measured by the CMS detector. The reconstruction resolution can be estimated by evaluating the error:

- Uncertainty on M_X: the standard deviation of $M_{X,rec} - M_{X,gen}$ distribution, being $M_{X,rec}$ the value of $t\bar{t}$ invariant mass calculated starting from reconstructed values of top/anti-top momenta and $M_{X,gen}$ the same quantity evaluated using Monte Carlo truth simulated top/anti-top momenta.

In figure 9.3 the resolution on the $M_{X,rec}$ obtained from reconstructed $t\bar{t}$ events (as discussed in section 9.2.3) and obtained from the PPS is shown.

One can see than the main challenge will be in reconstructing the ttbar system in the central detector. Therefore we used a kinematic fitter to tag and calibrate the measurement of the $t\bar{t}$ system which will be discussed in Section 9.4.

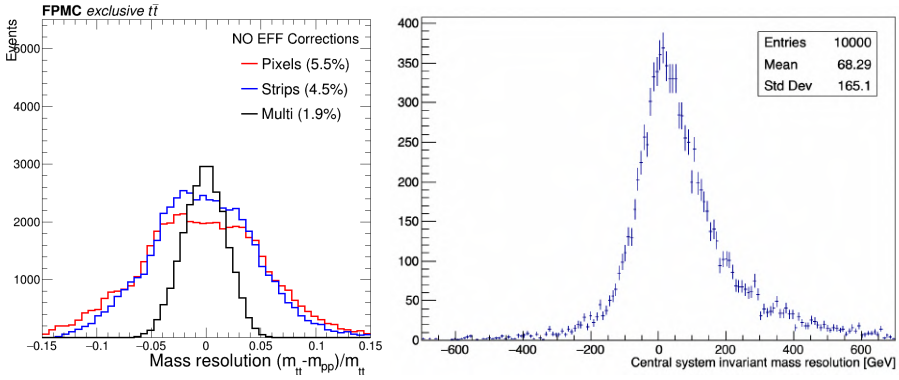

Figure 9.3: Resolution of $t\bar{t}$ mass measured from PPS (left) or central detector (right).

9.3.1 Proton mixing

As said, the dominant background in the analysis is the combinatorial background, originated from a random superposition of intact protons produced by pileup interactions and inclusive SM processes (like $gg \to t\bar{t}$) measured in the central detector. It is not possible to confirm a direct association of the protons with the primary vertex.

The combinatorial background is modeled by enriching the MC sample with pileup protons obtained from a pool of protons in the data.

The proton pool is selected using a selection similar to the signal region, but with inverted jet requirements. The mixing is performed, dividing each control region according to the data-taking period (aka era) in 5 categories corresponding to eras B, C, D, E, or F. Furthermore, the events in each era are sub-categorized according to four beam-crossing angles: 120μrad, 130μrad, 140μrad, and 150μrad.

The proton mixing procedure is done in two steps:

- From the data, we measure the fraction of events corresponding to each of the control regions ($f_{\mathrm{era},\alpha_X}$).
- We loop over all MC event, and select *eta* and crossing angle according to the relative probability proportional from the previous step. Then we assign to MC event run number, crossing angle, and two pileup protons randomly selected from the corresponding proton pool.

The fraction of events with 2 protons is measured as a function of *era* and crossing angle in the data at the early preselection stage (after the trigger requirement), and we assign extra weight to MC events based on these fractions.

In figure 9.4 protons kinematics are shown after mixing procedure was applied on MC. We find a good agreement between mixed sample and the data.

9.3.2 Pileup reweighting

The effects of multiple proton-proton interactions per event are included in the simulations and the distribution of these pileup interactions is reweighted

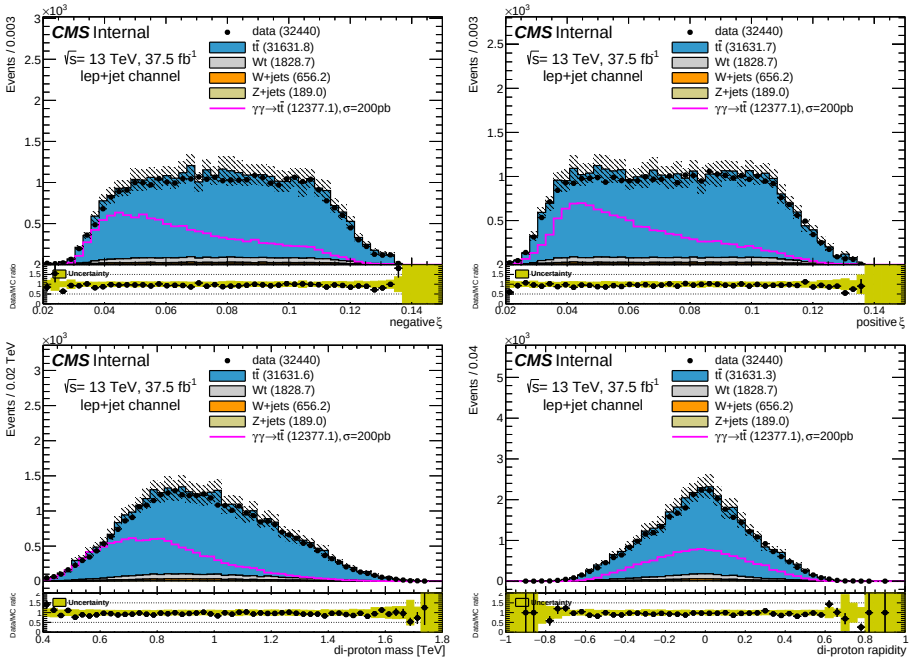

Figure 9.4: Proton variables computed at event preselection level. MC samples are enriched with pileup protons using the procedure described in the text.

to the vertex multiplicity distribution in the data. Since the average number of interactions per bunch crossing strongly depends on the crossing angle, the standard CMS procedure for pileup reweighting is inappropriate. An ad-hoc strategy has been pursued by obtaining new pileup weights using the following procedure: we produce a distribution of an average number of bunch crossing for each signal region. During the assignment of pileup protons, we also assign extra weights to match the distributions of $< n_{\mathrm{VTX}} >$ between the signal regions in data and MC distribution.

The average number of vertices before and after pileup reweighting is shown in Fig. 9.5

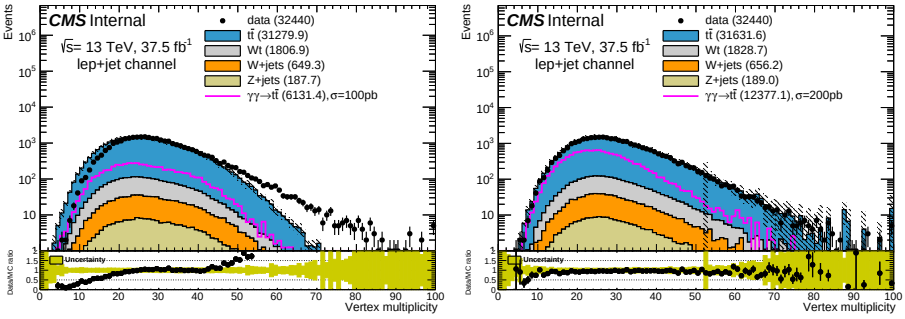

Figure 9.5: Number of reconstructed vertices before (left) and after (right) pileup reweighting procedure.

9.3.3 Control plots using MC simulation mixed with the pileup protons

In this section, we compare the data to the MC simulation of inclusive production of various SM processes mixed with the pileup protons and normalized to the corresponding proton tagging rate factor as described in the previous section.

Proton tagging rate has a significant effect on the acceptance of the signal and background events. Acceptance for signal and main backgrounds (inclusive $t\bar{t}$) is shown in Table 9.3.

Table 9.3: Cut-flow for signal and background events. For background only inclusive $t\bar{t}$ is considered, while for the signal only semi-leptonic exclusive $t\bar{t}$ events normalized to 100 pb are considered.

Selection	Signal	Background
Initial yield	3.75×10^6	31.2×10^6
TopLJets skim	0.64×10^6	3.1×10^6
Event selection	0.1×10^6	1.1×10^6
Proton tag efficiency[1]	17.7×10^3	—
Strip multiple hits veto	6.2×10^3	31.5×10^3

As previously stated, in the case of the simulation, the crossing angle is sampled from the observed crossing angle multiplicity in the proton pool.

We conclude this section with the final validation of the background at preselection level by looking at the different event kinematics.

The following distributions are shown: Fig. 9.6 shows the $t\bar{t}$ related variables, Fig. 9.7–Fig. 9.9 show jets and missing transverse energy related variables, Fig. 9.10 is the lepton kinematics (electron and muons separately), Fig. 9.11 shows kinematic fitter input variables and Fig. 9.12 shows the top quark reconstruction.

In addition to the main shape predicted for the background, a systematic uncertainty band is included. The uncertainty band includes all the systematic uncertainties listed in Section 9.6. Overall a good agreement for all the tested distributions is found.

[1] In the proton tag efficiency calculations, periods where PPS multiRP reconstruction was off due to missing strips, are also incorporated. The overall luminosity count of these runs so is reflected in the lower PPS multi-RP reconstruction efficiency.

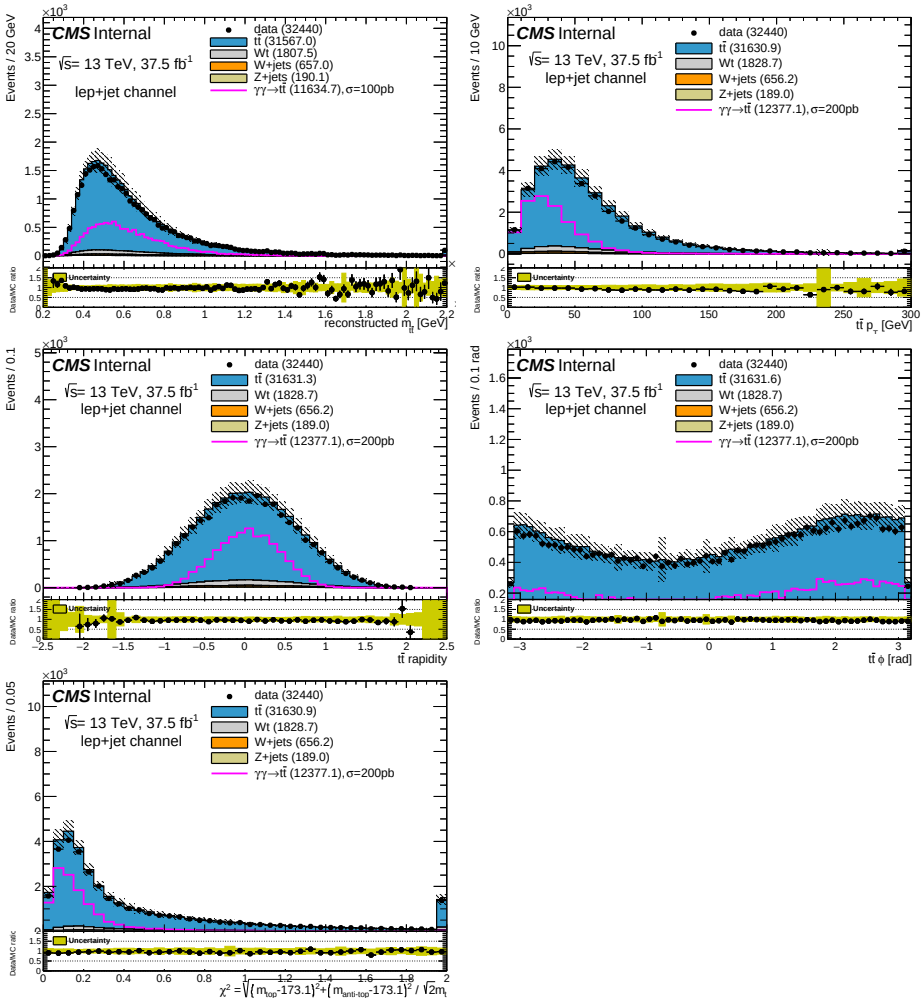

Figure 9.6: Kinematic of the $t\bar{t}$ system

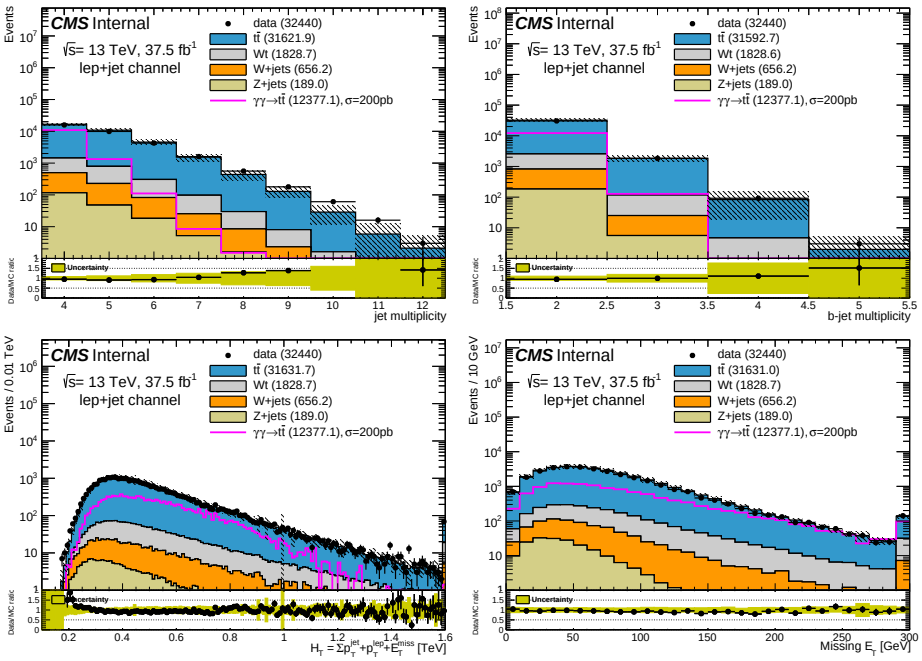

Figure 9.7: Top: number of all jets, and number of b-jets only. Bottom: Sum of transverse momentum of all objects (jets, lepton and missing energy), and transverse missing energy only.

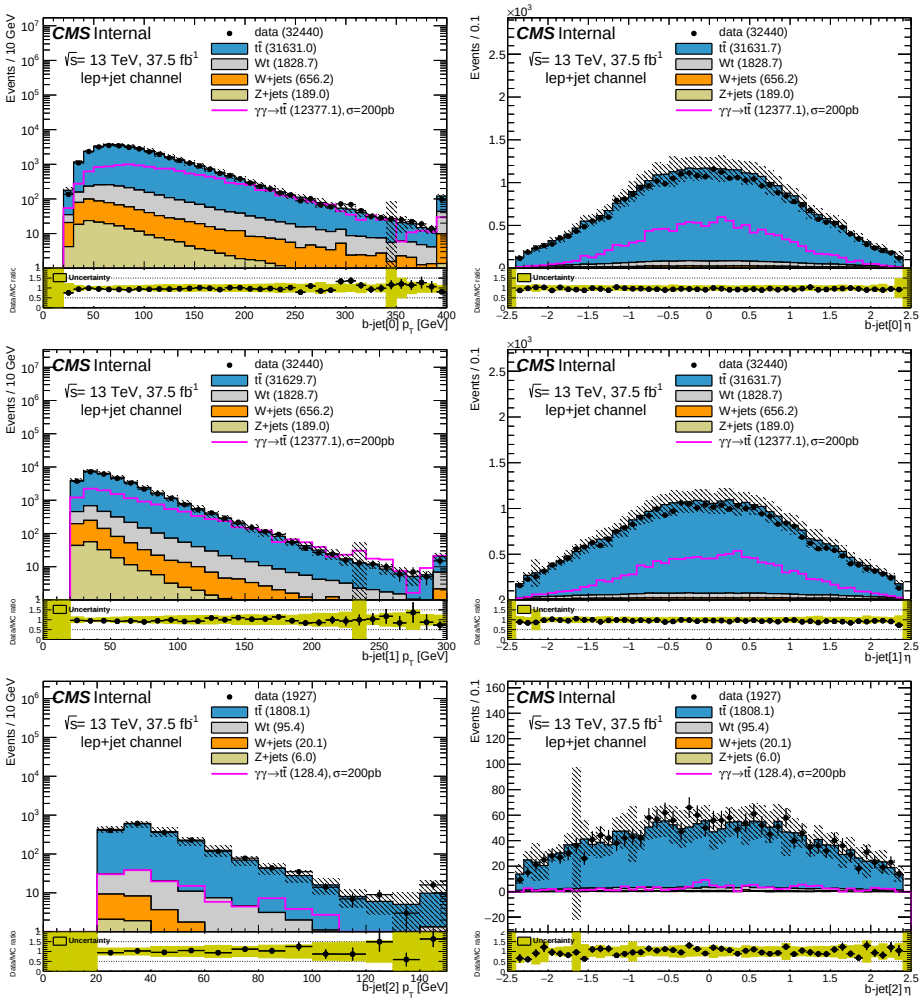

Figure 9.8: Three leading b-jets p_T and η (in case of third jet event yield is reduced due to $n_{b-jet} \geq 2$ cut).

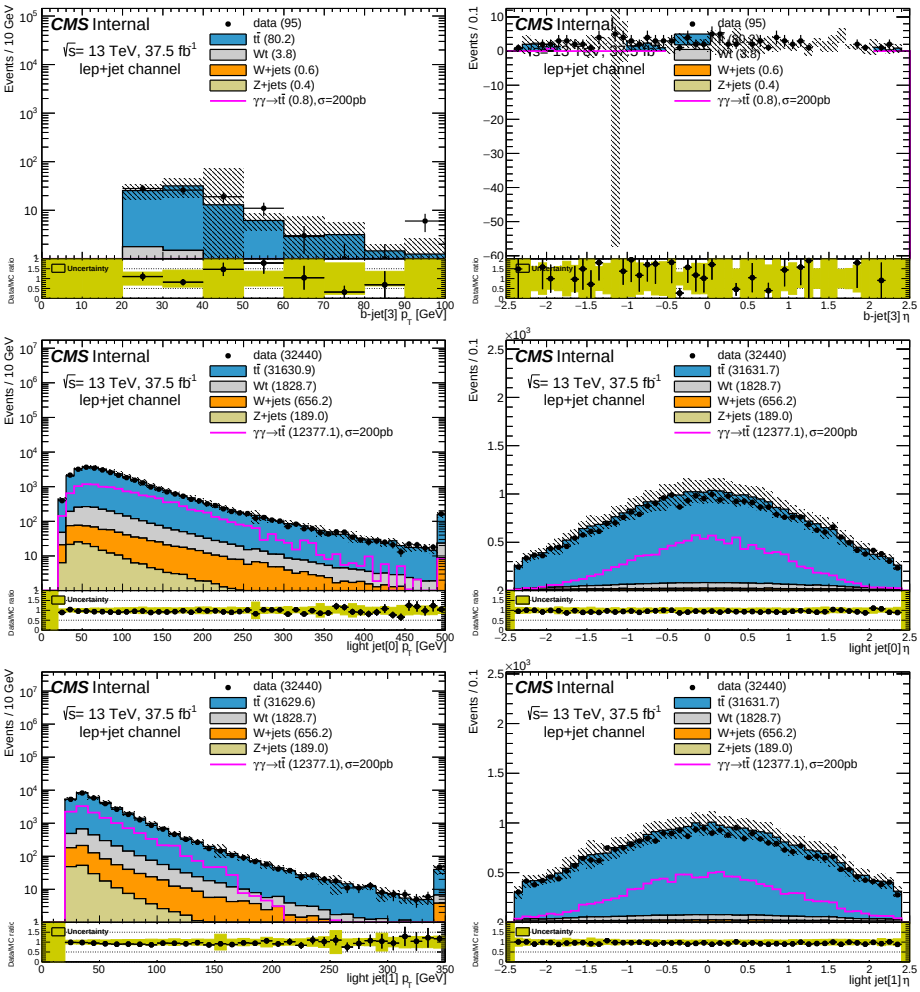

Figure 9.9: fourth b-jet and two light jets

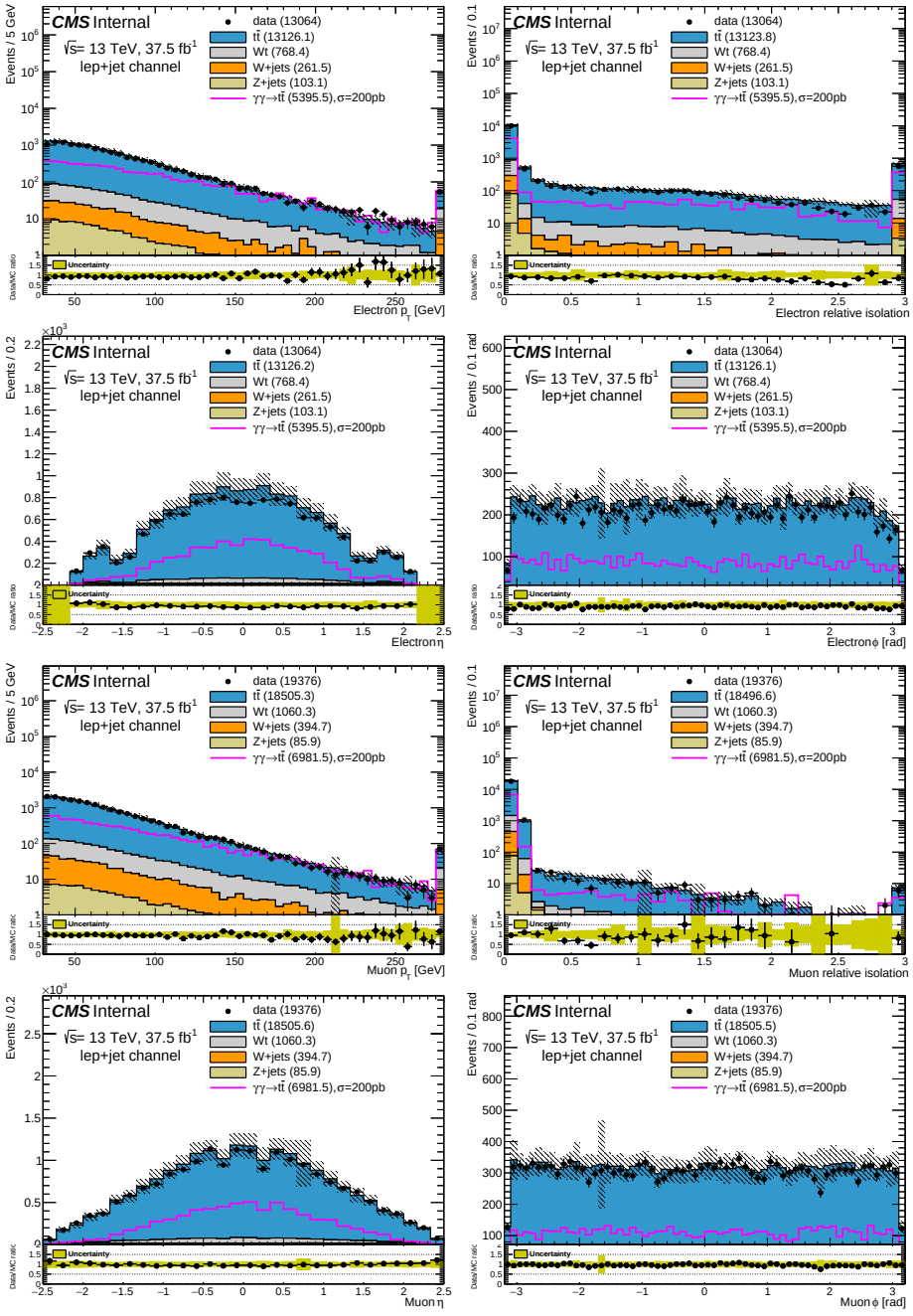

Figure 9.10: Lepton related variables.

Having validated the background determination method, the implementation of high level algorithms to reconstruct the system with top quark pairs will be discussed in the next section.

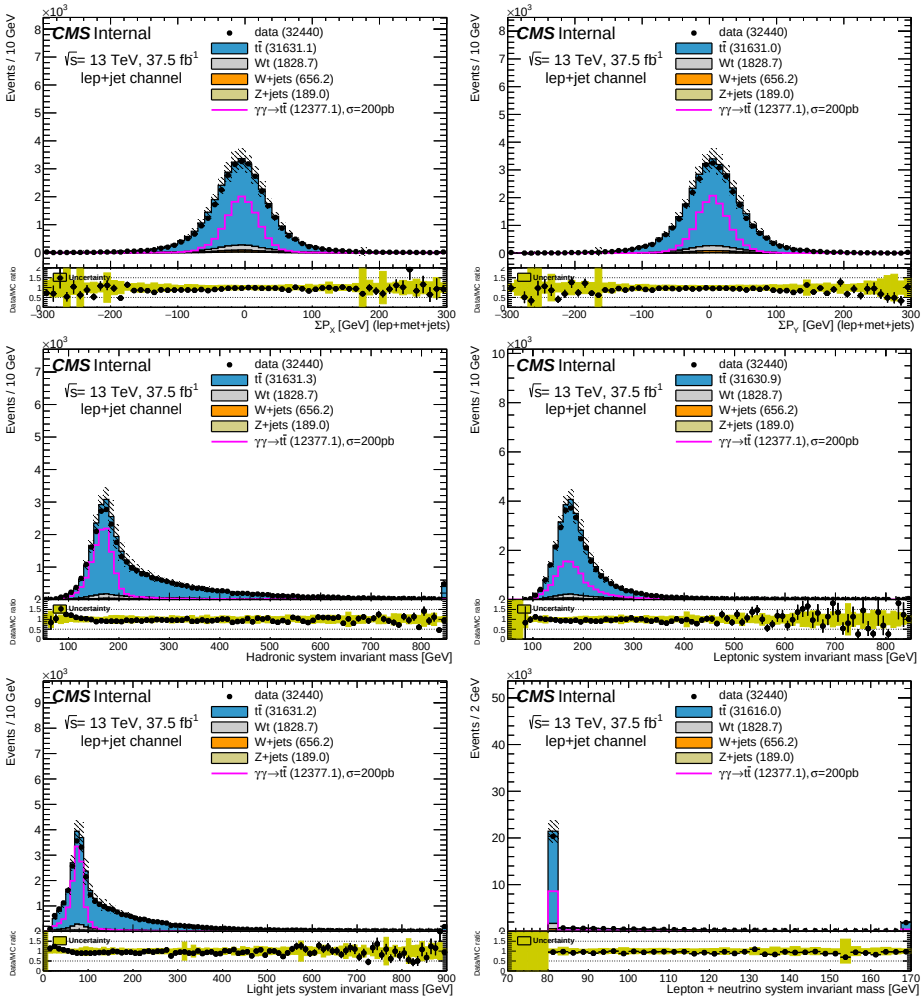

Figure 9.11: Variables used in the kinematic fitter's χ^2 minimization.

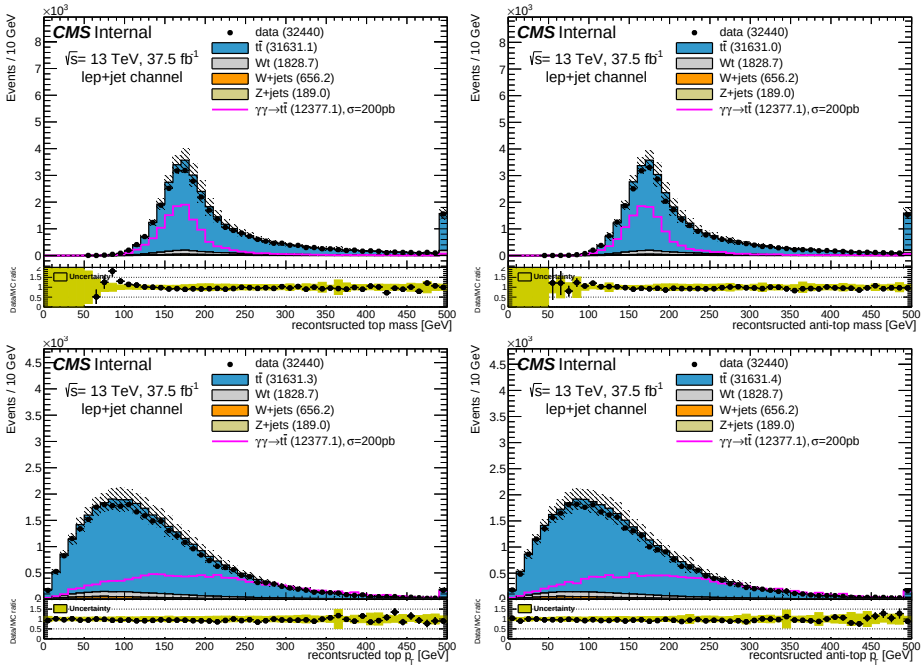

Figure 9.12: Top reconstruction obtained by selecting 2 b-jets and 2 light jets which has minimal χ^2, these set of objects is used in the kinematic fitter. ($\chi^2 = \Delta m_{top1} \oplus \Delta m_{top2}$)

9.4 $t\bar{t}$ tagging with the kinematic fitter

The $t\bar{t}$ mass estimated at preselection has a large standard deviation, bigger than 160 GeV ($\approx$ 32% of the mean $t\bar{t}$ invariant mass $\approx$ 500 GeV). The aim of the kinematic fitter, better discussed in this paragraph, is considering a set of quantities that must be conserved in the top/anti-top decay process (i.e. the invariant mass of the hadronic/leptonic system) and varying the kinematic quantities of the daughter particles inside their error bands in order to satisfy the conservation principles. Ideally, this will help to find the "most correct value" for each kinematic quantity and will thus improve the M_X resolution distribution. In the following paragraphs, we will describe and then optimise the kinematic fitter, focusing only on the main source of background, the $t\bar{t}$ inclusive production, that is $t\bar{t}$ pairs produced via QCD diagrams often together with many additional jets. This is indeed the most worrisome background because its final state looks very similar to our exclusive production signal (where the $t\bar{t}$ pair may be accompanied by additional jets coming from pile up) and has a much larger cross section (more than 800 pb at 13 TeV).

As we will see, a few different approaches will be attempted and their efficiency will be rated, based on the effect against the $t\bar{t}$ inclusive background. Then, the most efficient approach will be chosen and it will be applied to all the existing backgrounds. For this reason, for all the remainder of the paragraph, with the word "background" we will mean only the $t\bar{t}$ inclusive source of background.

The following different approaches are considered:

First approach :
As a first level, a good way to use the kinematic fitter is the following:

- Using the central system kinematic constraints (top and W masses) to move the values of the kinematic quantities within their error bands until one finds the ones that best satisfy the constraints;
- Improving M_X resolution (σ_{M_X});
- Saving only the events such that $|\sqrt{M_X^2} - \sqrt{s\xi_1\xi_2}| < \zeta \cdot \sigma_{M_X}$, where ζ is optimized in section 9.6.
- Of course, the events selected with this criterion won't be only signal events (σ_{M_X}¿0). Therefore, we will need to apply multivariate analysis (MVA) techniques on the selected events to best separate the signal from background.

Second approach :
Another interesting approach, that will be called "second approach", is the following:

- Using the central system kinematic constraints together with the matching condition $M_X^2 - s\xi_1\xi_2 = 0$ to move the values of the kinematic quantities within their error bands until one finds the ones that best satisfy the constraints;
- Calculating the χ^2 distributions both for signal and background samples;

- Using the χ^2 distribution as a discriminating input variable of the MVA tool.

This second approach uses the matching condition as a further constraint and does not cut out any event after applying the fitter. Therefore, the only tool that will help us separating signal from background is the MVA. The key point is that, in this case, among the input variables, we will use the χ^2 distribution, which is expected to be very different for signal and background: in the first case, in fact, we expect that the kinematic quantities are "close" to satisfy the constraints (including the matching condition), while for background these will be hard to satisfy (especially the $M_X^2 - s\xi_1\xi_2 = 0$ condition). Therefore, the χ^2 variable should be bigger for background events than for signal events. We will evaluate both approaches and we will determine which one is the most performing. The implementation of the algorithm is explained below. The kinematic fitter has been mainly developed during the master thesis of a student of the University of Genova [82].

9.4.1 Kinematic fitter: the algorithm

General theoretical background and notation

The $t\bar{t}$ semileptonic decay yields six particles in the final state: $b_1 b_2 q_1 q_2 l\nu$, where b_1 and b_2 are respectively the hadronic and the leptonic b-jets, while the notation for the other particles has already been clarified. In order to understand what follows, let's consider that the $t\bar{t}$ pair decays in two steps:

- First step: $t\bar{t} \rightarrow b_1 W_1 b_2 W_2$;
- Second step: $W_1 \rightarrow q_1 q_2$ and $W_2 \rightarrow l\nu$;
- Final result: $t\bar{t} \rightarrow b_1 b_2 l\nu q_1 q_2$

Furthermore, if one considers a single top or anti-top, its decay process can be written as it follows:

$$t \rightarrow b_1 q_1 q_2$$
$$\bar{t} \rightarrow b_2 l\nu$$

or vice versa. From now on, we will call $b_1 q_1 q_2$ "hadronic system" and $b_2 l\nu$ "leptonic system". We will call $p_{x,i}$ the x-component of the momentum of the particle i (where i can be one of the six final state particles), $p_{y,i}$ the y-component of the momentum of the particle i and $p_{z,i}$ the z-component of the momentum of the particle i. Then, other four quantities are of interest:

- $m_{l\nu}$: the invariant mass of the system lepton + neutrino;
- $m_{q_1 q_2}$: the invariant mass of the light jets system;
- m_{AD}: the invariant mass of the hadronic system;
- m_{LEP}: the invariant mass of the leptonic system.

Using this notation, since the invariant mass must be conserved, looking at step 2 of the $t\bar{t}$ decay mode, we can observe $m_{l\nu} = m_W$ and $m_{q_1 q_2} = m_W$. Furthermore, considering the whole decay process of a t or a $\bar{t}$, one can observe

$m_{AD} = m_t$ and $m_{LEP} = m_t$.
Let's now calculate the analytic form of the invariant mass of the leptonic and hadronic system. Let's start from the leptonic system:

$$m^2_{LEP} = E^2_{LEP} - p^2_{LEP} \approx (|\vec{p}_{b_2}| + |\vec{p}_l| + |\vec{p}_\nu|)^2 - (p_{x,b_2} + p_{x,\nu} + p_{x,l})^2 - (p_{y,b_2} + p_{y,\nu} + p_{y,l})^2$$
$$-(p_{z,b_2} + p_{z,\nu} + p_{z,l})^2 =$$
$$= 2|\vec{p}_{b_2}||\vec{p}_l| + 2|\vec{p}_{b_2}||\vec{p}_\nu| + 2|\vec{p}_l||\vec{p}_\nu| - 2p_{x,b_2}p_{x,l} - 2p_{x,b_2}p_{x,\nu} - 2p_{x,l}p_{x,\nu} - 2p_{y,b_2}p_{y,l} - 2p_{y,b_2}p_{y,\nu}$$
$$-2p_{y,l}p_{y,\nu} - 2p_{z,b_2}p_{z,l} - 2p_{z,b_2}p_{z,\nu} - 2p_{z,l}p_{z,\nu}$$

In the previous calculation we have assumed that the mass of each particle can be neglected. We can now linearise this expression (the importance of the linearisation will be clarified later). In particular, we will call $\bar{p}_{x,i}, \bar{p}_{y,i}, \bar{p}_{z,i}$ the coordinates around which we linearise the expression. The result can be written as follows:

$$m^2_{LEP} \approx 2|\vec{p_{b_2}}||\vec{p_l}| + 2\frac{|\vec{p_l}|}{|\vec{p_{b_2}}|}[\bar{p_{x,b_2}}(p_{x,b_2} - \bar{p_{x,b_2}}) + \bar{p}_{y,b_2}(p_{y,b_2} - \bar{p}_{y,b_2}) + \bar{p}_{z,b_2}(p_{z,b_2} - \bar{p}_{z,b_2})] +$$
$$+2\frac{|\vec{p_{b_2}}|}{|\vec{p_l}|}[\bar{p}_{x,l}(p_{x,l} - \bar{p}_{x,l}) + \bar{p}_{y,l}(p_{y,l} - \bar{p}_{y,l}) + \bar{p}_{z,l}(p_{z,l} - \bar{p}_{z,l})] +$$
$$+2|\vec{p_{b_2}}||\vec{p_\nu}| + 2\frac{|\vec{p_\nu}|}{|\vec{p_{b_2}}|}[\bar{p}_{x,b_2}(p_{x,b_2} - \bar{p}_{x,b_2}) + \bar{p}_{y,b_2}(p_{y,b_2} - \bar{p}_{y,b_2}) + \bar{p}_{z,b_2}(p_{z,b_2} - \bar{p}_{z,b_2})] +$$
$$+2\frac{|\vec{p_{b_2}}|}{|\vec{p_\nu}|}[\bar{p}_{x,\nu}(p_{x,\nu} - \bar{p}_{x,\nu}) + \bar{p}_{y,\nu}(p_{y,\nu} - \bar{p}_{y,\nu}) + \bar{p}_{z,\nu}(p_{z,\nu} - \bar{p}_{z,\nu})] +$$
$$+2|\vec{p_l}||\vec{p_\nu}| + 2\frac{|\vec{p_\nu}|}{|\vec{p_l}|}[\bar{p}_{x,l}(p_{x,l} - \bar{p}_{x,l}) + \bar{p}_{y,l}(p_{y,l} - \bar{p}_{y,l}) + \bar{p}_{z,l}(p_{z,l} - \bar{p}_{z,l})] +$$
$$+2\frac{|\vec{p_l}|}{|\vec{p_\nu}|}[\bar{p}_{x,\nu}(p_{x,\nu} - \bar{p}_{x,\nu}) + \bar{p}_{y,\nu}(p_{y,\nu} - \bar{p}_{y,\nu}) + \bar{p}_{z,\nu}(p_{z,\nu} - \bar{p}_{z,\nu})] +$$
$$-2\bar{p}_{x,b_2}\bar{p}_{x,l} - 2\bar{p}_{x,l}(p_{x,b_2} - \bar{p}_{x,b2}) - 2\bar{p}_{x,b2}(p_{x,l} - \bar{p}_{x,l}) +$$
$$-2\bar{p}_{x,b_2}\bar{p}_{x,\nu} - 2\bar{p}_{x,\nu}(p_{x,b_2} - \bar{p}_{x,b2}) - 2\bar{p}_{x,b2}(p_{x,\nu} - \bar{p}_{x,\nu}) +$$
$$-2\bar{p}_{x,l}\bar{p}_{x,\nu} - 2\bar{p}_{x,\nu}(p_{x,l} - \bar{p}_{x,l}) - 2\bar{p}_{x,l}(p_{x,\nu} - \bar{p}_{x,\nu}) +$$
$$-2\bar{p}_{y,b_2}\bar{p}_{y,l} - 2\bar{p}_{y,l}(p_{y,b_2} - \bar{p}_{y,b2}) - 2\bar{p}_{y,b2}(p_{y,l} - \bar{p}_{y,l}) +$$
$$-2\bar{p}_{y,b_2}\bar{p}_{y,\nu} - 2\bar{p}_{y,\nu}(p_{y,b_2} - \bar{p}_{y,b2}) - 2\bar{p}_{y,b2}(p_{y,\nu} - \bar{p}_{y,\nu}) +$$
$$-2\bar{p}_{y,l}\bar{p}_{y,\nu} - 2\bar{p}_{y,\nu}(p_{y,l} - \bar{p}_{y,l}) - 2\bar{p}_{y,l}(p_{y,\nu} - \bar{p}_{y,\nu}) +$$
$$-2\bar{p}_{z,b_2}\bar{p}_{z,l} - 2\bar{p}_{z,l}(p_{z,b_2} - \bar{p}_{z,b2}) - 2\bar{p}_{z,b2}(p_{z,l} - \bar{p}_{z,l}) +$$
$$-2\bar{p}_{z,b_2}\bar{p}_{z,\nu} - 2\bar{p}_{z,\nu}(p_{z,b_2} - \bar{p}_{z,b2}) - 2\bar{p}_{z,b2}(p_{z,\nu} - \bar{p}_{z,\nu}) +$$
$$-2\bar{p}_{z,l}\bar{p}_{z,\nu} - 2\bar{p}_{z,\nu}(p_{z,l} - \bar{p}_{z,l}) - 2\bar{p}_{z,l}(p_{z,\nu} - \bar{p}_{z,\nu})$$

The same thing can be done considering the hadronic system. The expression obtained is the same, remembering to replace $b_2 \to b_1$, $l \to q_1$ and $\nu \to q_2$.
We will call the linearised invariant masses of the two systems $m_{AD,lin}$ and

$m_{LEP,lin}$.
Let's now calculate the invariant mass of the $l\nu$ pair, neglecting the lepton mass:

$$m_{l\nu} = 2|\vec{p_l}||\vec{p_\nu}| - 2p_{x,l}p_{x,\nu} - 2p_{y,l}p_{y,\nu} - 2p_{z,l}p_{z,\nu}$$

Then, this expression can be linearised:

$$m_{l\nu}^2 \approx 2\frac{|\vec{p_\nu}|}{|\vec{p_l}|}\bar{p}_{x,l}(p_{x,l} - \bar{p}_{x,l}) + 2\frac{|\vec{p_\nu}|}{|\vec{p_l}|}\bar{p}_{y,l}(p_{y,l} - \bar{p}_{y,l}) + 2\frac{|\vec{p_\nu}|}{|\vec{p_l}|}\bar{p}_{z,l}(p_{z,l} - \bar{p}_{z,l}) +$$

$$+2\frac{|\vec{p_l}|}{|\vec{p_\nu}|}\bar{p}_{x,\nu}(p_{x,\nu} - \bar{p}_{x,\nu}) + 2\frac{|\vec{p_\nu}|}{|\vec{p_\nu}|}\bar{p}_{y,\nu}(p_{y,\nu} - \bar{p}_{y,\nu}) + 2\frac{|\vec{p_l}|}{|\vec{p_\nu}|}\bar{p}_{z,\nu}(p_{z,\nu} - \bar{p}_{z,\nu}) +$$

$$+2|\vec{p_l}||\vec{p_\nu}| - 2\bar{p}_{x,l}\bar{p}_{x,\nu} - 2\bar{p}_{y,l}\bar{p}_{y,\nu} - 2\bar{p}_{z,l}\bar{p}_{z,\nu} - 2\bar{p}_{x,l}(p_{x,\nu} - \bar{p}_{x,\nu}) - 2\bar{p}_{x,\nu}(p_{x,l} - \bar{p}_{x,l}) +$$

$$-2\bar{p}_{y,l}(p_{y,\nu} - \bar{p}_{y,\nu}) - 2\bar{p}_{y,\nu}(p_{y,l} - \bar{p}_{y,l}) - 2\bar{p}_{z,l}(p_{z,\nu} - \bar{p}_{z,\nu}) - 2\bar{p}_{z,\nu}(p_{z,l} - \bar{p}_{z,l})$$

The same thing can be done considering the q_1q_2 system, getting the same expression (just substituting $l \to q_1$ and $\nu \to q_2$). We will call the linearised invariant masses of the two systems $m_{l\nu,lin}$ and $m_{q_1q_2,lin}$.
Therefore, in the kinematic fitter, these constraints will be enforced:

- $m_{AD,lin}^2 - m_t^2 = 0$
- $m_{LEP,lin}^2 - m_t^2 = 0$
- $m_{l\nu,lin}^2 - m_W^2 = 0$
- $m_{q_1q_2,lin}^2 - m_W^2 = 0$

Besides, since the momentum must be conserved, we will enforce:

- $\sum_{i=0}^{6} p_{x,i} = 0$;
- $\sum_{i=0}^{6} p_{y,i} = 0$.

These constraints must be enforced both if we are interested in following the first approach and if we are interested in following the second one.
Then, if we are interested in following the first method, no other constraint must be considered. On the other hand, to follow the second one, we will have to impose $M_X^2 - s\xi_1\xi_2 = 0$.
A question that may arise at this point is why we use linearised expressions as constraints and not the correct expressions. As we will see later, the whole algorithm will be implemented using the matrix formalism. In order to do that, we need to have all the constraints expressed as powers of $p_{x,i}, p_{y,i}, p_{z,i}$, that's why we had to consider linearised constraints. Anyway, an iterative method (below discussed) will be implemented to deal with this approximation.
Another good question is which set of $\bar{p}_{x,i}, \bar{p}_{y,i}, \bar{p}_{z,i}$ variables to use as centre of the expansion. The most natural choice is using the pre-fit values. If we look at the values of $\bar{p}_{x,i}$,$\bar{p}_{y,i}$ and $\bar{p}_{z,i}$ contained there, we find out that the previous constraints are not respected. Actually this doesn't mean that the physics conservation principles are not respected by the system, but that's because, since each measure has an uncertainty, it is possible, as mentioned before, that using the central value of each quantity one doesn't fulfil exactly the constraints. Anyway, we expect that, moving the kinematic quantities of each particle around their central value, we can get a combination of them that accomplishes all the constraints.

Algorithm implementation

Let's now explain how the fitter attempts to correct the initial values. We will treat the algorithm of the second-approach-fitter, since the other one is just a simplified version without the matching condition as a constraint. Before explaining the algorithm, let's introduce some vectors and matrices that then will be fully commented:
x =

$$\begin{bmatrix} p_{x,b_1} - \bar{p}_{x,b_1} \\ p_{y,b_1} - \bar{p}_{y,b_1} \\ p_{z,b_1} - \bar{p}_{z,b_1} \\ p_{x,b_2} - \bar{p}_{x,b_2} \\ p_{y,b_2} - \bar{p}_{y,b_2} \\ p_{z,b_2} - \bar{p}_{z,b_2} \\ p_{x,l} - \bar{p}_{x,l} \\ p_{y,l} - \bar{p}_{y,l} \\ p_{z,l} - \bar{p}_{z,l} \\ p_{x,\nu} - \bar{p}_{x,\nu} \\ p_{y,\nu} - \bar{p}_{y,\nu} \\ p_{z,\nu} - \bar{p}_{z,\nu} \\ p_{x,q_1} - \bar{p}_{x,q_1} \\ p_{y,q_1} - \bar{p}_{y,q_1} \\ p_{z,q_1} - \bar{p}_{z,q_1} \\ p_{x,q_2} - \bar{p}_{x,q_2} \\ p_{y,q_2} - \bar{p}_{y,q_2} \\ p_{z,q_2} - \bar{p}_{z,q_2} \\ \xi_1 - \bar{\xi}_1 \\ \xi_2 - \bar{\xi}_2 \\ \lambda_1 \\ \lambda_2 \\ \lambda_3 \\ \lambda_4 \\ \lambda_5 \\ \lambda_6 \\ \lambda_7 \end{bmatrix}$$

C^*=

$$\begin{bmatrix} \mathcal{C}^{-1}_{20\times 20} & 0_{20\times 7} \\ 0_{7\times 20} & 0_{7\times 7} \end{bmatrix}$$

K^*=

$$\begin{bmatrix} 0_{20\times 20} & \mathcal{K}_{20\times 7} \\ \mathcal{K}^T_{7\times 20} & 0_{7\times 7} \end{bmatrix}$$

P^* =

$$\begin{bmatrix} 0_{20\times 20} & \mathcal{P}_{20\times 7} \\ \mathcal{P}^T_{7\times 20} & 0_{7\times 7} \end{bmatrix}$$

$\mathcal{K}_{20\times 7} =$

$$\begin{bmatrix}
1 & 0 & 0 & 0 & 0 & 0 & 0 \\
0 & 1 & 0 & 0 & 0 & 0 & 0 \\
0 & 0 & 0 & 0 & 0 & 0 & 0 \\
1 & 0 & 0 & 0 & 0 & 0 & 0 \\
0 & 1 & 0 & 0 & 0 & 0 & 0 \\
0 & 0 & 0 & 0 & 0 & 0 & 0 \\
1 & 0 & 0 & 0 & 0 & 0 & 0 \\
0 & 1 & 0 & 0 & 0 & 0 & 0 \\
0 & 0 & 0 & 0 & 0 & 0 & 0 \\
1 & 0 & 0 & 0 & 0 & 0 & 0 \\
0 & 1 & 0 & 0 & 0 & 0 & 0 \\
0 & 0 & 0 & 0 & 0 & 0 & 0 \\
1 & 0 & 0 & 0 & 0 & 0 & 0 \\
0 & 1 & 0 & 0 & 0 & 0 & 0 \\
0 & 0 & 0 & 0 & 0 & 0 & 0 \\
1 & 0 & 0 & 0 & 0 & 0 & 0 \\
0 & 1 & 0 & 0 & 0 & 0 & 0 \\
0 & 0 & 0 & 0 & 0 & 0 & 0 \\
0 & 0 & 0 & 0 & 0 & 0 & 0
\end{bmatrix}$$

$f =$

$$\begin{bmatrix}
\bar{p}_{x,b_1} \\
\bar{p}_{y,b_1} \\
\bar{p}_{z,b_1} \\
\bar{p}_{x,b_2} \\
\bar{p}_{y,b_2} \\
\bar{p}_{z,b_2} \\
\bar{p}_{x,l} \\
\bar{p}_{y,l} \\
\bar{p}_{z,l} \\
\bar{p}_{x,\nu} \\
\bar{p}_{y,\nu} \\
\bar{p}_{z,\nu} \\
\bar{p}_{x,q_1} \\
\bar{p}_{y,q_1} \\
\bar{p}_{z,q_1} \\
\bar{p}_{x,q_2} \\
\bar{p}_{y,q_2} \\
\bar{p}_{z,q_2} \\
\bar{\xi}_1 \\
\bar{\xi}_2 \\
0_{7\times 1}
\end{bmatrix}$$

$$Q^* = \begin{bmatrix} 0_{20\times 1} \\ \bar{m}^2_{LEP} - m_t^2 \\ \bar{m}^2_{AD} - m_t^2 \\ \bar{m}^2_{l\nu} - m_W^2 \\ \bar{m}^2_{q_1 q_2} - m_W^2 \\ \bar{m}^2_{t\bar{t}} - s\bar{\xi}_1\bar{\xi}_2 \end{bmatrix}$$

$$\mathcal{P}_{20\times 7} =$$

$$\left[\begin{array}{cccccc}
 & 0 & 2\frac{|\vec{p_{q_1}}|}{|\vec{p_{b_1}}|}\bar{p}_{x,b_1} + 2\frac{|\vec{p_{q_2}}|}{|\vec{p_{b_1}}|}\bar{p}_{x,b_1} - 2\bar{p}_{x,q_1} - 2\bar{p}_{x,q_2} & 0 & 0 & 2(|\vec{p_{b2}}|\frac{\bar{p}_{x,b1}}{|\vec{p_{b1}}|} + |\vec{p_l}|\frac{\bar{p}_{x,b1}}{|\vec{p_{b1}}|} + |\vec{p_\nu}|\frac{\bar{p}_{x,b1}}{|\vec{p_{b1}}|} + |\vec{p_{q1}}|\frac{\bar{p}_{x,b1}}{|\vec{p_{b1}}|} + |\vec{p_{q2}}|\frac{\bar{p}_{x,b1}}{|\vec{p_{b1}}|} - \bar{p}_{x,b2} - \bar{p}_{x,l} - \bar{p}_{x,\nu} - \bar{p}_{x,q1} - \bar{p}_{x,q2}) \\
 & 0 & 2\frac{|\vec{p_{q_1}}|}{|\vec{p_{b_1}}|}\bar{p}_{y,b_1} + 2\frac{|\vec{p_{q_2}}|}{|\vec{p_{b_1}}|}\bar{p}_{y,b_1} - 2\bar{p}_{y,q_1} - 2\bar{p}_{y,q_2} & 0 & 0 & 2(|\vec{p_{b2}}|\frac{\bar{p}_{y,b1}}{|\vec{p_{b1}}|} + |\vec{p_l}|\frac{\bar{p}_{y,b1}}{|\vec{p_{b1}}|} + |\vec{p_\nu}|\frac{\bar{p}_{y,b1}}{|\vec{p_{b1}}|} + |\vec{p_{q1}}|\frac{\bar{p}_{y,b1}}{|\vec{p_{b1}}|} + |\vec{p_{q2}}|\frac{\bar{p}_{y,b1}}{|\vec{p_{b1}}|} - \bar{p}_{y,b2} - \bar{p}_{y,l} - \bar{p}_{y,\nu} - \bar{p}_{y,q1} - \bar{p}_{y,q2}) \\
 & 0 & 2\frac{|\vec{p_{q_1}}|}{|\vec{p_{b_1}}|}\bar{p}_{z,b_1} + 2\frac{|\vec{p_{q_2}}|}{|\vec{p_{b_1}}|}\bar{p}_{z,b_1} - 2\bar{p}_{z,q_1} - 2\bar{p}_{z,q_2} & 0 & 0 & 2(|\vec{p_{b2}}|\frac{\bar{p}_{z,b1}}{|\vec{p_{b1}}|} + |\vec{p_l}|\frac{\bar{p}_{z,b1}}{|\vec{p_{b1}}|} + |\vec{p_\nu}|\frac{\bar{p}_{z,b1}}{|\vec{p_{b1}}|} + |\vec{p_{q1}}|\frac{\bar{p}_{z,b1}}{|\vec{p_{b1}}|} + |\vec{p_{q2}}|\frac{\bar{p}_{z,b1}}{|\vec{p_{b1}}|} - \bar{p}_{z,b2} - \bar{p}_{z,l} - \bar{p}_{z,\nu} - \bar{p}_{z,q1} - \bar{p}_{z,q2}) \\
 & 2\frac{|\vec{p_l}|}{|\vec{p_{b_2}}|}\bar{p}_{x,b_2} + 2\frac{|\vec{p_\nu}|}{|\vec{p_{b_2}}|}\bar{p}_{x,b_2} - 2\bar{p}_{x,l} - 2\bar{p}_{x,\nu} & 0 & 0 & 0 & 2(|\vec{p_{b1}}|\frac{\bar{p}_{x,b2}}{|\vec{p_{b2}}|} + |\vec{p_l}|\frac{\bar{p}_{x,b2}}{|\vec{p_{b2}}|} + |\vec{p_\nu}|\frac{\bar{p}_{x,b2}}{|\vec{p_{b2}}|} + |\vec{p_{q1}}|\frac{\bar{p}_{x,b2}}{|\vec{p_{b2}}|} + |\vec{p_{q2}}|\frac{\bar{p}_{x,b2}}{|\vec{p_{b2}}|} - \bar{p}_{x,b1} - \bar{p}_{x,l} - \bar{p}_{x,\nu} - \bar{p}_{x,q1} - \bar{p}_{x,q2}) \\
 & 2\frac{|\vec{p_l}|}{|\vec{p_{b_2}}|}\bar{p}_{y,b_2} + 2\frac{|\vec{p_\nu}|}{|\vec{p_{b_2}}|}\bar{p}_{y,b_2} - 2\bar{p}_{y,l} - 2\bar{p}_{y,\nu} & 0 & 0 & 0 & 2(|\vec{p_{b1}}|\frac{\bar{p}_{y,b2}}{|\vec{p_{b2}}|} + |\vec{p_l}|\frac{\bar{p}_{y,b2}}{|\vec{p_{b2}}|} + |\vec{p_\nu}|\frac{\bar{p}_{y,b2}}{|\vec{p_{b2}}|} + |\vec{p_{q1}}|\frac{\bar{p}_{y,b2}}{|\vec{p_{b2}}|} + |\vec{p_{q2}}|\frac{\bar{p}_{y,b2}}{|\vec{p_{b2}}|} - \bar{p}_{y,b1} - \bar{p}_{y,l} - \bar{p}_{y,\nu} - \bar{p}_{y,q1} - \bar{p}_{y,q2}) \\
 & 2\frac{|\vec{p_l}|}{|\vec{p_{b_2}}|}\bar{p}_{z,b_2} + 2\frac{|\vec{p_\nu}|}{|\vec{p_{b_2}}|}\bar{p}_{z,b_2} - 2\bar{p}_{z,l} - 2\bar{p}_{z,\nu} & 0 & 0 & 0 & 2(|\vec{p_{b1}}|\frac{\bar{p}_{z,b2}}{|\vec{p_{b2}}|} + |\vec{p_l}|\frac{\bar{p}_{z,b2}}{|\vec{p_{b2}}|} + |\vec{p_\nu}|\frac{\bar{p}_{z,b2}}{|\vec{p_{b2}}|} + |\vec{p_{q1}}|\frac{\bar{p}_{z,b2}}{|\vec{p_{b2}}|} + |\vec{p_{q2}}|\frac{\bar{p}_{z,b2}}{|\vec{p_{b2}}|} - \bar{p}_{z,b1} - \bar{p}_{z,l} - \bar{p}_{z,\nu} - \bar{p}_{z,q1} - \bar{p}_{z,q2}) \\
 & 2\frac{|\vec{p_{b_2}}|}{|\vec{p_l}|}\bar{p}_{x,l} + 2\frac{|\vec{p_\nu}|}{|\vec{p_l}|}\bar{p}_{x,l} - 2\bar{p}_{x,b_2} - 2\bar{p}_{x,\nu} & 0 & 2\frac{|\vec{p_\nu}|}{|\vec{p_l}|}\bar{p}_{x,l} - 2\bar{p}_{x,\nu} & 0 & 2(|\vec{p_{b1}}|\frac{\bar{p}_{x,l}}{|\vec{p_l}|} + |\vec{p_{b2}}|\frac{\bar{p}_{x,l}}{|\vec{p_l}|} + |\vec{p_\nu}|\frac{\bar{p}_{x,l}}{|\vec{p_l}|} + |\vec{p_{q1}}|\frac{\bar{p}_{x,l}}{|\vec{p_l}|} + |\vec{p_{q2}}|\frac{\bar{p}_{x,l}}{|\vec{p_l}|} - \bar{p}_{x,b1} - \bar{p}_{x,b2} - \bar{p}_{x,\nu} - \bar{p}_{x,q1} - \bar{p}_{x,q2}) \\
 & 2\frac{|\vec{p_{b_2}}|}{|\vec{p_l}|}\bar{p}_{y,l} + 2\frac{|\vec{p_\nu}|}{|\vec{p_l}|}\bar{p}_{y,l} - 2\bar{p}_{y,b_2} - 2\bar{p}_{y,\nu} & 0 & 2\frac{|\vec{p_\nu}|}{|\vec{p_l}|}\bar{p}_{y,l} - 2\bar{p}_{y,\nu} & 0 & 2(|\vec{p_{b1}}|\frac{\bar{p}_{y,l}}{|\vec{p_l}|} + |\vec{p_{b2}}|\frac{\bar{p}_{y,l}}{|\vec{p_l}|} + |\vec{p_\nu}|\frac{\bar{p}_{y,l}}{|\vec{p_l}|} + |\vec{p_{q1}}|\frac{\bar{p}_{y,l}}{|\vec{p_l}|} + |\vec{p_{q2}}|\frac{\bar{p}_{y,l}}{|\vec{p_l}|} - \bar{p}_{y,b1} - \bar{p}_{y,b2} - \bar{p}_{y,\nu} - \bar{p}_{y,q1} - \bar{p}_{y,q2}) \\
 & 2\frac{|\vec{p_{b_2}}|}{|\vec{p_l}|}\bar{p}_{z,l} + 2\frac{|\vec{p_\nu}|}{|\vec{p_l}|}\bar{p}_{z,l} - 2\bar{p}_{z,b_2} - 2\bar{p}_{z,\nu} & 0 & 2\frac{|\vec{p_\nu}|}{|\vec{p_l}|}\bar{p}_{z,l} - 2\bar{p}_{z,\nu} & 0 & 2(|\vec{p_{b1}}|\frac{\bar{p}_{z,l}}{|\vec{p_l}|} + |\vec{p_{b2}}|\frac{\bar{p}_{z,l}}{|\vec{p_l}|} + |\vec{p_\nu}|\frac{\bar{p}_{z,l}}{|\vec{p_l}|} + |\vec{p_{q1}}|\frac{\bar{p}_{z,l}}{|\vec{p_l}|} + |\vec{p_{q2}}|\frac{\bar{p}_{z,l}}{|\vec{p_l}|} - \bar{p}_{z,b1} - \bar{p}_{z,b2} - \bar{p}_{z,\nu} - \bar{p}_{z,q1} - \bar{p}_{z,q2}) \\
0_{20x2} & 2\frac{|\vec{p_{b_2}}|}{|\vec{p_\nu}|}\bar{p}_{x,\nu} + 2\frac{|\vec{p_l}|}{|\vec{p_\nu}|}\bar{p}_{x,\nu} - 2\bar{p}_{x,b_2} - 2\bar{p}_{x,l} & 0 & 2\frac{|\vec{p_l}|}{|\vec{p_\nu}|}\bar{p}_{x,\nu} - 2\bar{p}_{x,l} & 0 & 2(|\vec{p_{b1}}|\frac{\bar{p}_{x,\nu}}{|\vec{p_\nu}|} + |\vec{p_{b2}}|\frac{\bar{p}_{x,\nu}}{|\vec{p_\nu}|} + |\vec{p_l}|\frac{\bar{p}_{x,\nu}}{|\vec{p_\nu}|} + |\vec{p_{q1}}|\frac{\bar{p}_{x,\nu}}{|\vec{p_\nu}|} + |\vec{p_{q2}}|\frac{\bar{p}_{x,\nu}}{|\vec{p_\nu}|} - \bar{p}_{x,b1} - \bar{p}_{x,b2} - \bar{p}_{x,l} - \bar{p}_{x,q1} - \bar{p}_{x,q2}) \\
 & 2\frac{|\vec{p_{b_2}}|}{|\vec{p_\nu}|}\bar{p}_{y,\nu} + 2\frac{|\vec{p_l}|}{|\vec{p_\nu}|}\bar{p}_{y,\nu} - 2\bar{p}_{y,b_2} - 2\bar{p}_{y,l} & 0 & 2\frac{|\vec{p_l}|}{|\vec{p_\nu}|}\bar{p}_{y,\nu} - 2\bar{p}_{y,l} & 0 & 2(|\vec{p_{b1}}|\frac{\bar{p}_{y,\nu}}{|\vec{p_\nu}|} + |\vec{p_{b2}}|\frac{\bar{p}_{y,\nu}}{|\vec{p_\nu}|} + |\vec{p_l}|\frac{\bar{p}_{y,\nu}}{|\vec{p_\nu}|} + |\vec{p_{q1}}|\frac{\bar{p}_{y,\nu}}{|\vec{p_\nu}|} + |\vec{p_{q2}}|\frac{\bar{p}_{y,\nu}}{|\vec{p_\nu}|} - \bar{p}_{y,b1} - \bar{p}_{y,b2} - \bar{p}_{y,l} - \bar{p}_{y,q1} - \bar{p}_{y,q2}) \\
 & 2\frac{|\vec{p_{b_2}}|}{|\vec{p_\nu}|}\bar{p}_{z,\nu} + 2\frac{|\vec{p_l}|}{|\vec{p_\nu}|}\bar{p}_{z,\nu} - 2\bar{p}_{z,b_2} - 2\bar{p}_{z,l} & 0 & 2\frac{|\vec{p_l}|}{|\vec{p_\nu}|}\bar{p}_{z,\nu} - 2\bar{p}_{z,l} & 0 & 2(|\vec{p_{b1}}|\frac{\bar{p}_{z,\nu}}{|\vec{p_\nu}|} + |\vec{p_{b2}}|\frac{\bar{p}_{z,\nu}}{|\vec{p_\nu}|} + |\vec{p_l}|\frac{\bar{p}_{z,\nu}}{|\vec{p_\nu}|} + |\vec{p_{q1}}|\frac{\bar{p}_{z,\nu}}{|\vec{p_\nu}|} + |\vec{p_{q2}}|\frac{\bar{p}_{z,\nu}}{|\vec{p_\nu}|} - \bar{p}_{z,b1} - \bar{p}_{z,b2} - \bar{p}_{z,l} - \bar{p}_{z,q1} - \bar{p}_{z,q2}) \\
 & 0 & 2\frac{|\vec{p_{b_1}}|}{|\vec{p_{q_1}}|}\bar{p}_{x,q_1} + 2\frac{|\vec{p_{q_2}}|}{|\vec{p_{q_1}}|}\bar{p}_{x,q_1} - 2\bar{p}_{x,b_1} - 2\bar{p}_{x,q_2} & 0 & 2\frac{|\vec{p_{q_2}}|}{|\vec{p_{q_1}}|}\bar{p}_{x,q_1} - 2\bar{p}_{x,q_2} & 2(|\vec{p_{b2}}|\frac{\bar{p}_{x,q1}}{|\vec{p_{q1}}|} + |\vec{p_l}|\frac{\bar{p}_{x,q1}}{|\vec{p_{q1}}|} + |\vec{p_\nu}|\frac{\bar{p}_{x,q1}}{|\vec{p_{q1}}|} + |\vec{p_{b1}}|\frac{\bar{p}_{x,q1}}{|\vec{p_{q1}}|} + |\vec{p_{q2}}|\frac{\bar{p}_{x,q1}}{|\vec{p_{q1}}|} - \bar{p}_{x,b2} - \bar{p}_{x,l} - \bar{p}_{x,\nu} - \bar{p}_{x,b1} - \bar{p}_{x,q2}) \\
 & 0 & 2\frac{|\vec{p_{b_1}}|}{|\vec{p_{q_1}}|}\bar{p}_{y,q_1} + 2\frac{|\vec{p_{q_2}}|}{|\vec{p_{q_1}}|}\bar{p}_{y,q_1} - 2\bar{p}_{y,b_1} - 2\bar{p}_{y,q_2} & 0 & 2\frac{|\vec{p_{q_2}}|}{|\vec{p_{q_1}}|}\bar{p}_{y,q_1} - 2\bar{p}_{y,q_2} & 2(|\vec{p_{b2}}|\frac{\bar{p}_{y,q1}}{|\vec{p_{q1}}|} + |\vec{p_l}|\frac{\bar{p}_{y,q1}}{|\vec{p_{q1}}|} + |\vec{p_\nu}|\frac{\bar{p}_{y,q1}}{|\vec{p_{q1}}|} + |\vec{p_{b1}}|\frac{\bar{p}_{y,q1}}{|\vec{p_{q1}}|} + |\vec{p_{q2}}|\frac{\bar{p}_{y,q1}}{|\vec{p_{q1}}|} - \bar{p}_{y,b2} - \bar{p}_{y,l} - \bar{p}_{y,\nu} - \bar{p}_{y,b1} - \bar{p}_{y,q2}) \\
 & 0 & 2\frac{|\vec{p_{b_1}}|}{|\vec{p_{q_1}}|}\bar{p}_{z,q_1} + 2\frac{|\vec{p_{q_2}}|}{|\vec{p_{q_1}}|}\bar{p}_{z,q_1} - 2\bar{p}_{z,b_1} - 2\bar{p}_{z,q_2} & 0 & 2\frac{|\vec{p_{q_2}}|}{|\vec{p_{q_1}}|}\bar{p}_{z,q_1} - 2\bar{p}_{z,q_2} & 2(|\vec{p_{b2}}|\frac{\bar{p}_{z,q1}}{|\vec{p_{q1}}|} + |\vec{p_l}|\frac{\bar{p}_{z,q1}}{|\vec{p_{q1}}|} + |\vec{p_\nu}|\frac{\bar{p}_{z,q1}}{|\vec{p_{q1}}|} + |\vec{p_{b1}}|\frac{\bar{p}_{z,q1}}{|\vec{p_{q1}}|} + |\vec{p_{q2}}|\frac{\bar{p}_{z,q1}}{|\vec{p_{q1}}|} - \bar{p}_{z,b2} - \bar{p}_{z,l} - \bar{p}_{z,\nu} - \bar{p}_{z,b1} - \bar{p}_{z,q2}) \\
 & 0 & 2\frac{|\vec{p_{b_1}}|}{|\vec{p_{q_2}}|}\bar{p}_{x,q_2} + 2\frac{|\vec{p_{q_1}}|}{|\vec{p_{q_2}}|}\bar{p}_{x,q_2} - 2\bar{p}_{x,b_1} - 2\bar{p}_{x,q_1} & 0 & 2\frac{|\vec{p_{q_1}}|}{|\vec{p_{q_2}}|}\bar{p}_{x,q_2} - 2\bar{p}_{x,q_1} & 2(|\vec{p_{b2}}|\frac{\bar{p}_{x,q2}}{|\vec{p_{q2}}|} + |\vec{p_l}|\frac{\bar{p}_{x,q2}}{|\vec{p_{q2}}|} + |\vec{p_\nu}|\frac{\bar{p}_{x,q2}}{|\vec{p_{q2}}|} + |\vec{p_{b1}}|\frac{\bar{p}_{x,q2}}{|\vec{p_{q2}}|} + |\vec{p_{q1}}|\frac{\bar{p}_{x,q2}}{|\vec{p_{q2}}|} - \bar{p}_{x,b2} - \bar{p}_{x,l} - \bar{p}_{x,\nu} - \bar{p}_{x,b1} - \bar{p}_{x,q1}) \\
 & 0 & 2\frac{|\vec{p_{b_1}}|}{|\vec{p_{q_2}}|}\bar{p}_{y,q_2} + 2\frac{|\vec{p_{q_1}}|}{|\vec{p_{q_2}}|}\bar{p}_{y,q_2} - 2\bar{p}_{y,b_1} - 2\bar{p}_{y,q_1} & 0 & 2\frac{|\vec{p_{q_1}}|}{|\vec{p_{q_2}}|}\bar{p}_{y,q_2} - 2\bar{p}_{y,q_1} & 2(|\vec{p_{b2}}|\frac{\bar{p}_{y,q2}}{|\vec{p_{q2}}|} + |\vec{p_l}|\frac{\bar{p}_{y,q2}}{|\vec{p_{q2}}|} + |\vec{p_\nu}|\frac{\bar{p}_{y,q2}}{|\vec{p_{q2}}|} + |\vec{p_{b1}}|\frac{\bar{p}_{y,q2}}{|\vec{p_{q2}}|} + |\vec{p_{q1}}|\frac{\bar{p}_{y,q2}}{|\vec{p_{q2}}|} - \bar{p}_{y,b2} - \bar{p}_{y,l} - \bar{p}_{y,\nu} - \bar{p}_{y,b1} - \bar{p}_{y,q1}) \\
 & 0 & 2\frac{|\vec{p_{b_1}}|}{|\vec{p_{q_2}}|}\bar{p}_{z,q_2} + 2\frac{|\vec{p_{q_1}}|}{|\vec{p_{q_2}}|}\bar{p}_{z,q_2} - 2\bar{p}_{z,b_1} - 2\bar{p}_{z,q_1} & 0 & 2\frac{|\vec{p_{q_1}}|}{|\vec{p_{q_2}}|}\bar{p}_{z,q_2} - 2\bar{p}_{z,q_1} & 2(|\vec{p_{b2}}|\frac{\bar{p}_{y,q2}}{|\vec{p_{q2}}|} + |\vec{p_l}|\frac{\bar{p}_{y,q2}}{|\vec{p_{q2}}|} + |\vec{p_\nu}|\frac{\bar{p}_{y,q2}}{|\vec{p_{q2}}|} + |\vec{p_{b1}}|\frac{\bar{p}_{y,q2}}{|\vec{p_{q2}}|} + |\vec{p_{q1}}|\frac{\bar{p}_{y,q2}}{|\vec{p_{q2}}|} - \bar{p}_{y,b2} - \bar{p}_{y,l} - \bar{p}_{y,\nu} - \bar{p}_{y,b1} - \bar{p}_{y,q1}) \\
 & 0 & 0 & 0 & 0 & -s\bar{\xi}_2 \\
 & 0 & 0 & 0 & 0 & -s\bar{\xi}_1
\end{array}\right]$$

In these matrices, with the notation $\bar{p}_{x,i}$, $\bar{p}_{y,i}$, $\bar{p}_{z,i}$ we mean the initial[2] momenta of the particles resulted from the decay. These are values that must be corrected to satisfy the constrains and will be used as initial parameters of the fit. On the other hand, with $p_{x,i}$, $p_{y,i}$, $p_{z,i}$ we mean the particles momenta after the kinematic fit (hopefully the ones that satisfy the kinematic constrains).
Furthermore, $\lambda_1, \lambda_2, \lambda_3, \lambda_4, \lambda_5, \lambda_6, \lambda_7$ are called "Lagrangian multipliers"; we will discuss them later. As to $\mathcal{C}^{-1}_{20\times 20}$, it is the inverse covariance matrix of the quantities $p_{x,i}$, $p_{y,i}$, $p_{z,i}$,ξ_1,ξ_2.
Lastly, the quantities $\bar{m}^2_{LEP}$, $\bar{m}^2_{AD}$ and $\bar{m}_{t\bar{t}}$ are respectively the invariant mass of the leptonic, hadronic and $t\bar{t}$ system calculated using the values $\bar{p}_{x,i}$, $\bar{p}_{y,i}$, $\bar{p}_{z,i}$.
Let's now describe how the kinematic fitter works: we consider a function that we will call chi-square modified (χ^{2*}) defined as:

$$\chi^{2*} = \chi^2 + 2\lambda_1 \sum_{i=0}^{6} p_{x,i} + 2\lambda_2 \sum_{i=0}^{6} p_{y,i} + 2\lambda_3(m^2_{LEP,lin} - m^2_t) + 2\lambda_4(m^2_{AD,lin} - m^2_t) +$$

$$+2\lambda_5(m^2_{l\nu,lin} - m^2_W) + 2\lambda_6(m^2_{q_1q_2,lin} - m^2_W) + 2\lambda_7(M^2_X - s\xi_1\xi_2)$$

where χ^2 is defined as usual $\chi^2 = x^T C^* x$ and it takes in account also the cross-correlation terms (in principle). What one can discover by direct calculations is that in our analysis the quantities of interest are mostly uncorrelated, therefore we will neglect the terms out of the diagonal of the correlation matrix. Furthermore, it can be shown by direct calculation that

$$2\lambda_1 \sum_{i=0}^{6} p_{x,i} + 2\lambda_2 \sum_{i=0}^{6} p_{y,i} = (x+f)^T K^* (x+f)$$

$$2\lambda_3(m^2_{LEP,lin} - m^2_t) + 2\lambda_4(m^2_{AD,lin} - m^2_t) + 2\lambda_5(m^2_{l\nu,lin} - m^2_W)$$
$$+2\lambda_6(m^2_{q_1q_2,lin} - m^2_W) + 2\lambda_7(M^2_X - s\xi_1\xi_2) =$$
$$= x^T P^* x + Q^{*T} x$$

Therefore, we can write:

$$\chi^{2*} = x^T C^* x + (x+f)^T K^* (x+f) + x^T P^* x + Q^{*T} x$$

We note the both C^* and K^* are symmetric matrices (it will be useful in the next steps).
Before going on, it can be useful giving a deeper look to the function χ^{2*}. We introduced this function because we want minimise the function χ^2 on the kinematic constraints cited earlier.
In order to do that, we use the Lagrangian Multipliers Theorem, that guarantees that the values $(p_{x,b1}, p_{x,b2}, ..., p_{z,q1}, p_{z,q2}, \xi_1, \xi_2)$ that minimise χ^2 satisfying the kinematic constrains, are such that:

$$\vec{\nabla}\chi^{2*}(p_{x,b1}, p_{x,b2}, ..., p_{z,q1}, p_{z,q2}, \xi_1, \xi_2, \lambda_1, \lambda_2, \lambda_3, \lambda_4, \lambda_5, \lambda_6, \lambda_7) = 0$$

[2]With "initial" we mean "Before applying the fitter"

As one can see, differently from χ^2, the χ^{2*} depends also on seven extra parameters $\lambda_1, \lambda_2, \lambda_3, \lambda_4, \lambda_5, \lambda_6, \lambda_7$ called Lagrangian Multipliers. They do not have a physical interpretation, they are just a mathematical trick to impose the constraints. In fact, asking:

$$\frac{d\chi^{2*}}{d\lambda_a} = 0, \ a \in \{1, 2, 3, 4, 5, 6\}$$

means imposing the kinematic constrains. For example, asking $\frac{d\chi^{2*}}{d\lambda_1} = 0$ implies $\sum_{i=0}^{6} p_{x,i} = 0$, which is exactly one of the seven kinematic constraints we are looking for. Therefore, considering again:

$$\chi^{2*} = x^T C^* x + (x + f)^T K^* (x + f) + x^T P^* x + Q^{T*} x$$

it can be calculated (remembering that C^* and K^* are symmetric):

$$\vec{\nabla}\chi^{2*} = 2(C^* + K^*)x + 2K^* f + 2P^* x + Q^*$$

Imposing $\vec{\nabla}\chi^{2*} = 0$ it can be obtained:

$$x = -(C^* + K^* + P^*)^{-1} \frac{2K^* f + Q^*}{2}$$

which is the set of parameters that minimises χ^2 satisfying the requested kinematic conditions. Actually we point out that, since the invariant masses are linearised, the solution provided by x is not exact. To avoid this problem, the algorithm is iterated several times. In particular, the (i+1)th iteration has as initial parameters the fitted parameters given by the (i)th iteration. We will discuss this point better below.

9.4.2 Performance

Before checking the kinematic fitter performances, it is mandatory understanding whether the algorithm converges and in how many steps, since it is based on many iterations,.
First of all, let's remind that doing an iteration just means using as input variables of the fitter the "output values" of the previous step. What happens is that, after each iteration, the linearised constraints are always perfectly satisfied (since the minimisation on χ^2 on the constraints is done analytically) but the key point is that, since the bounds enforced are linearised, at each step one gets closer to the constraint that one really wants to satisfy. Therefore, many questions arise:

- Does the algorithm reach convergence or, after some steps, it starts oscillating around a value?
- If it converges, does it converge to a set of variables that reasonably satisfy the constraints?
- If the answer to both questions is positive, in how many steps do the algorithm reach convergence?

Before going on, one must underline that each graph shown in this paragraph refers to the second-approach fitter. The results for the other fitter will be briefly summarised at the end of this paragraph, but actually are pretty similar. To answer this question, let's consider the graph shown in figure 9.13. It shows the value assumed by a kinematic variable (in this case the z-component of a light jet momentum) as a function of the iteration number (having chosen one signal event from MC sample).

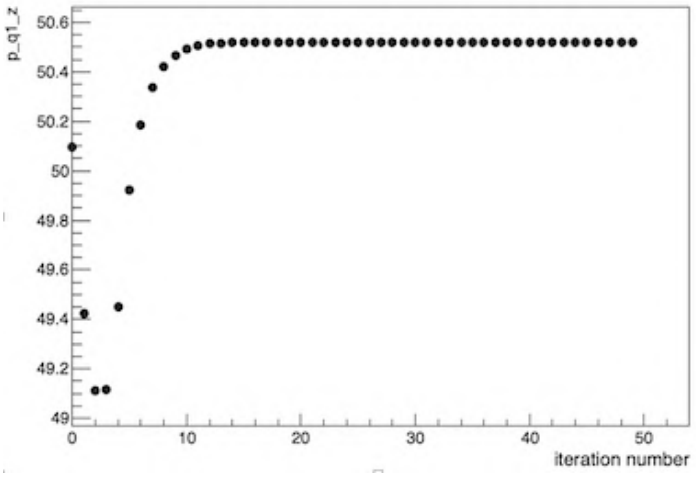

Figure 9.13: z-component of a light jet momentum measured in GeV vs. kinematic fitter iteration number.

It can be clearly seen that after approximately 15 iteration, the variable has reached convergence. Looking at the other variables, one can note the same behaviour, even if the iteration number needed to reach convergence cannot be considered fixed. Another example is given in 9.14.

Looking at the same graphs for all the other 18 kinematic quantities, one can find the same result. Therefore, it can be stated that the algorithm reaches convergence. The number of iterations cannot be fixed (it depends on the variable and on the event chosen), but after 50 iterations in all cases convergence is reached. Therefore, we will choose this number of iterations.
The next step is understanding if after the number of iterations chosen (50), the constraints enforced are satisfied.
Therefore, the kinematic fitter was applied to 10000 signal events. Then, starting from the kinematic quantities obtained after having applied the algorithm, the invariant mass of neutrino+lepton system, of the light jets system, of the hadronic/leptonic systems and the sum of x and y component of the final state particles were calculated. All these values were used to fill different histograms, shown in the following figures (9.15, 9.16, 9.17, 9.18, 9.19, 9.20 and 9.21). The quantities plotted are explained in the caption of each picture.

It can be seen looking at the above mentioned histograms that the kinematic constraints are perfectly satisfied by the fitter. Of course, it is just an obvious check since the theory already guarantees that all the events must satisfy the enforced constraints. To probe that the fitter works properly, what we must do is verifying that the resolution of the kinematic quantities improves after applying

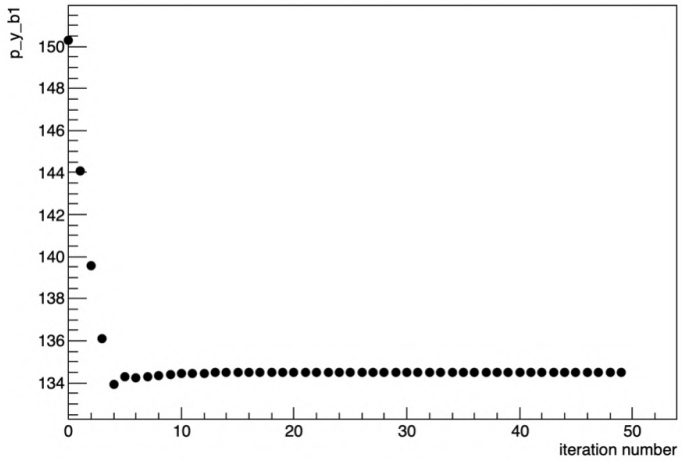

Figure 9.14: y-component of the hadronic b jet momentum measured in GeV vs. kinematic fitter iteration number.

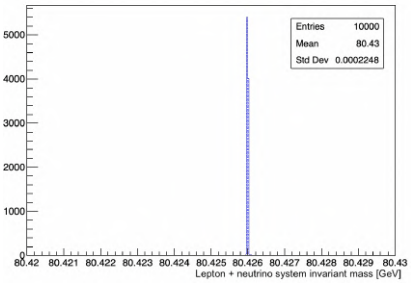

Figure 9.15: Invariant mass neutrino + lepton system.

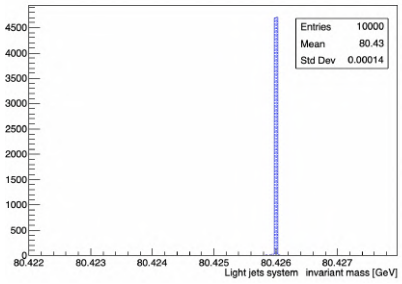

Figure 9.16: Invariant mass light jets system.

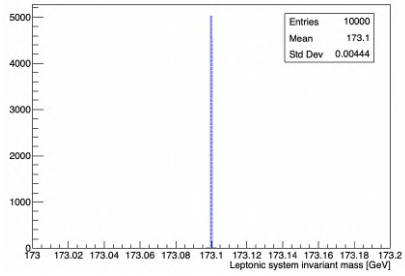

Figure 9.17: Invariant mass leptonic system.

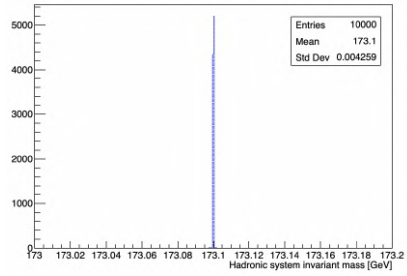

Figure 9.18: Invariant mass hadronic system.

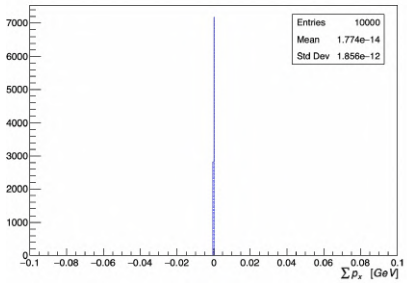

Figure 9.19: Sum of the x-component of the momentum of all the final state particles.

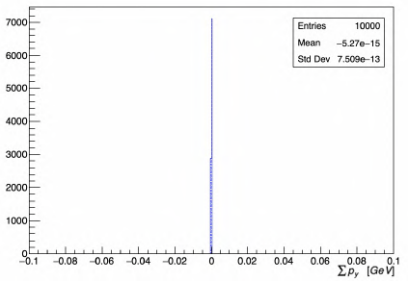

Figure 9.20: Sum of the y-component of the momentum of all the final state particles.

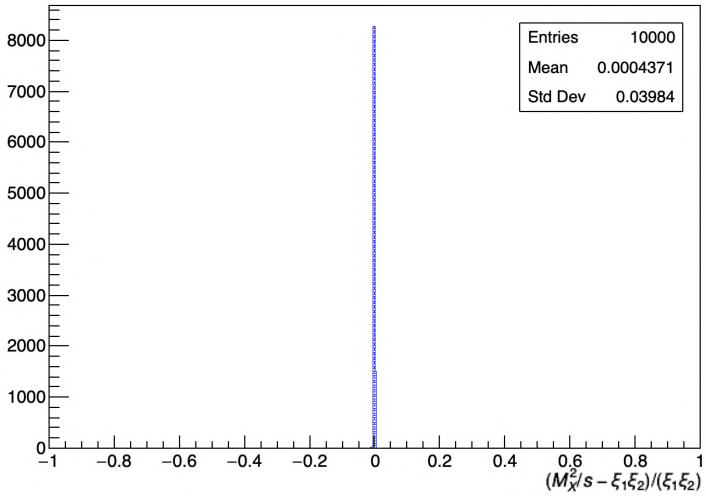

Figure 9.21: Relative violation of the matching condition constraint.

the algorithm: for each fitted kinematic quantity we must consider the Pre Fit and Post Fit resolution. If the fitter works, the resolution should improve. Anyway, it must be remembered that b-jets are assigned to the hadronic/leptonic decay side following the procedure explained at the end of the previous chapter: the efficiency of that procedure can be estimated, using MC truth, to be around 83%. It means that the probability of a mis-assignment is 17%. Therefore, what we want to do is first testing the fitter without being influenced by the b-jet assignment efficiency. Then, when we are sure that the fitter works, we can have a look at what happens without considering the MC truth on the b-jet assignment.
For the sake of clarity, we will show in this chapter as an example only the change in resolution of two of the 20 fitted kinematic quantities. A similar reasoning may be applied to the others. In particular, the variables chosen are the x-component of the hadronic and leptonic b-jets.
Therefore, we plot the $p_{x,b\ had}$ resolution before applying the fitter, considering signal MC samples and using the MC truth to do the b-jet assignment. Than we do the same thing for $p_{x,b\ lep}$. The results are shown respectively in figures 9.22 and 9.23.

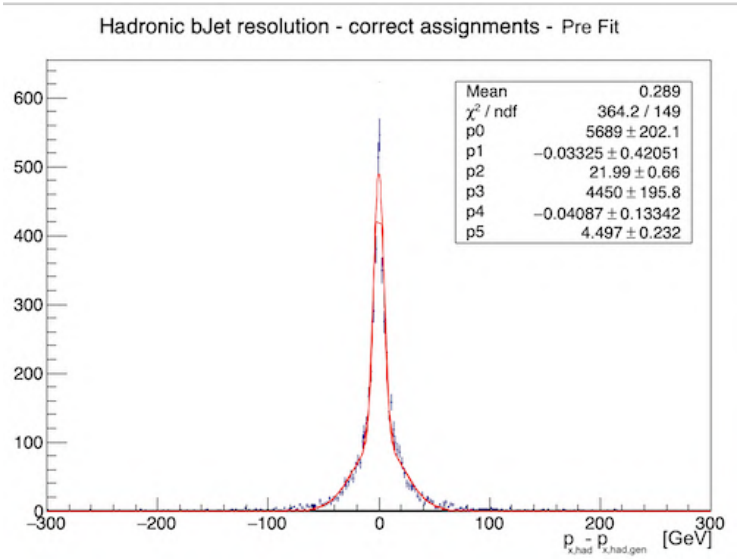

Figure 9.22: Hadronic pre-fit bJet momentum resolution (x-component) in GeV.

In these plots, fits are performed using the sum of two normalised Gaussian functions[3]. Using just one, in fact, the fit cannot converge. The parameters of the first Gaussian distribution are p_0 (Constant), p_1 (Mean) and p_2 (standard deviation). As to the second curve, p_3, p_4 and p_5 are the parameters of interest (with the same meaning). For the sake of clarity, we write the expression used to fit the distributions:

$$f(x) = \frac{p_0}{\sqrt{2\pi}p_2} e^{-\frac{(x-p_1)^2}{2p_2^2}} + \frac{p_3}{\sqrt{2\pi}p_5} e^{-\frac{(x-p_4)^2}{2p_5^2}}$$

[3]From now on, when we say "Gaussian distribution/curve" we mean "normalised Gaussian distribution/curve".

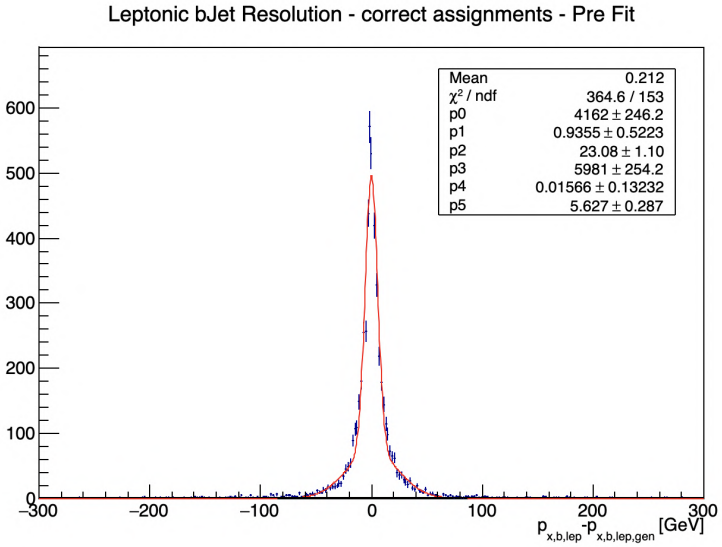

Figure 9.23: Leptonic pre-fit bJet momentum resolution (x-component) in GeV.

A few considerations about the constant term are in order. Let's consider a generic Gaussian distribution:

$$g(x) = \frac{c}{\sqrt{2\pi}\sigma} e^{-\frac{(x-\mu)^2}{2\sigma^2}}$$

One can write:

$$\int_{-\infty}^{+\infty} g(x) = A$$

being A the area under the curve $g(x)$. Furthermore:

$$\int_{-\infty}^{+\infty} g(x) = \int_{-\infty}^{+\infty} \frac{c}{\sqrt{2\pi}\sigma} e^{-\frac{(x-\mu)^2}{2\sigma^2}} = c \int_{-\infty}^{+\infty} \frac{1}{\sqrt{2\pi}\sigma} e^{-\frac{(x-\mu)^2}{2\sigma^2}} = c$$

Therefore, we can state that $c = A$. Since we are fitting histograms, in the reasonable hypothesis of having a lot of thin bins, one can write $A = \sum_{i=1}^{n_{bins}} N_i \Delta x_i$, being N_i the number of events in each bin and Δx_i the width of each bin. Assuming this last one constant for each bin: $A = \Delta x \sum_{i=1}^{n_{bins}} N_i = \Delta x N_{tot}$, being N_{tot} the total number of events hold by the distribution. Summing up, one can write:

$$c = \Delta x N_{tot}$$

Therefore, the constant parameter perfectly reflects the number of events hold by a Gaussian curve. In particular, since each histogram shown has the same bin-width, there is fully correspondence between the constant term and the number of events hold by a curve.
Now, looking at the plots 9.22 and 9.23, in both cases each curve is peaked around zero; then, the constant makes us understand that the events are more or less equally divided in the two distributions.

In order to evaluate if the resolution improves after applying the kinematic fitter, we introduce a quantity that we will call "effective standard deviation", which is defined as follows:

$$\sigma^* = \frac{c_1\sigma_1 + c_2\sigma_2}{c_1 + c_2}$$

where c_1, c_2 are respectively the constant terms of the first and of the second Gaussian distribution, while σ_1, σ_2 are the standard deviations. For the hadronic b-jet pre-fit distribution shown above, we obtain $\sigma^*_{pre-fit,had} \approx 14.3\ GeV$, while for the leptonic bJet pre-fit distribution we get $\sigma^*_{pre-fit,lep} \approx 12.8\ GeV$.
Let's move on to the post fit resolution. In figures 9.24 and 9.25 are shown $p_{x,b\ had}$ and $p_{x,b\ lep}$ resolutions after having applied the algorithm.

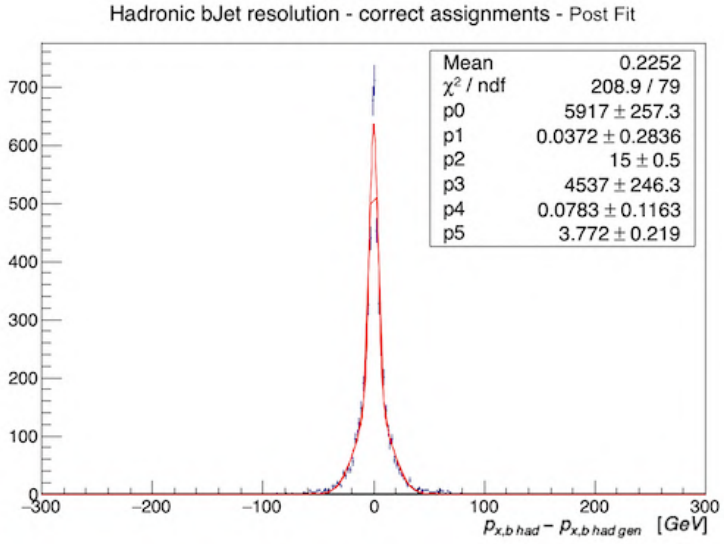

Figure 9.24: Hadronic post-fit bJet resolution (x-component) in GeV.

Even in this case, the resolutions were fitted using two Gaussian distributions (the parameters have the same meaning). First of all, it can be noticed that, even after applying the algorithm, all the distributions are peaked around zero. Let's then evaluate the effective standard deviation in both cases. For the post-fit hadronic b-jet momentum resolution we obtain:

$$\sigma^*_{post-fit,had} \approx 10.1\ GeV < \sigma^*_{pre-fit,had} \approx 14.3\ GeV$$

Looking instead at the post-fit leptonic distribution, we can calculate:

$$\sigma^*_{post-fit,lep} \approx 9.8\ GeV < \sigma^*_{pre-fit,lep} \approx 12.8\ GeV$$

These two results show that the kinematic fitter works properly.
What we are now interested to do is looking at the resolution plots without using the MC truth to do the b-jet assignment. When, in fact, real data are considered, it is important taking in account that the b-jet assignment algorithm introduces a noise, due to errors in establishing which b-jet belongs to the hadronic side and which one to the leptonic side.

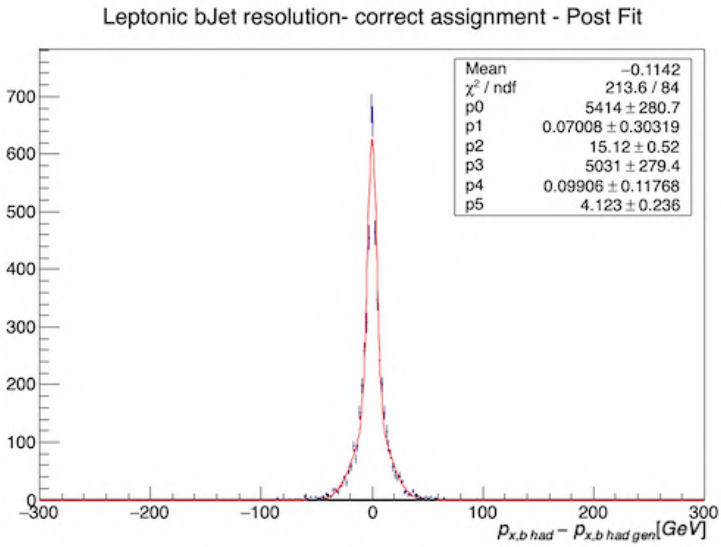

Figure 9.25: Leptonic post-fit bJet resolution (x-component) in GeV.

To do that, we are interested in representing the hadronic and leptonic resolutions of the b-jet pre fit and post fit and checking that also in this case there's an improvement in the resolutions. To do that, it is of great importance modelling the "shape" of the mis-assigned events: as we have recognised the shape of the sum of two Gaussian distributions in the correct assignment sample, we have now to understand what is the shape of the events with incorrect b-jet assignment.
Therefore, first of all we use MC truth to identify the events with incorrect assignment and we plot the resolution of the above cited quantities even in this case. Of course they have a bigger standard deviation then the previous ones. The plot showing these resolutions can be found in figures 9.26, 9.27 (pre-fit), and 9.28, 9.29 (post-fit) .

In this case the distributions can be fitted using just one Gaussian function (and the name of the parameters is self-explaining). Also in this case resolution improves applying the algorithm, but the resolution is by far worse than the case of correct b-jet assignment (as we expected). Even in this case the curves are peaked around zero.
At this point, we are finally ready to evaluate if there is an improvement in the hadronic/leptonic b-jet resolution without using MC truth for b-jet assignment. In fact we now know that correct assignments must be modelled with 2 curves while incorrect ones with just one. It means that when we don't use MC truth assignment, we will obtain a distribution that can be fitted with 3 Gaussian functions, since in this case we don't select just correct or incorrect events, but we have to deal with both. Of course, we expect that the two curves corresponding to the correct assignment would hold much more data than the other one.
Therefore, histograms with x-component hadronic/leptonic bJet momentum resolution were studied. Pre fit plots are shown in figures 9.30 and 9.31, while post fit plots are shown in figures 9.32 and 9.33.

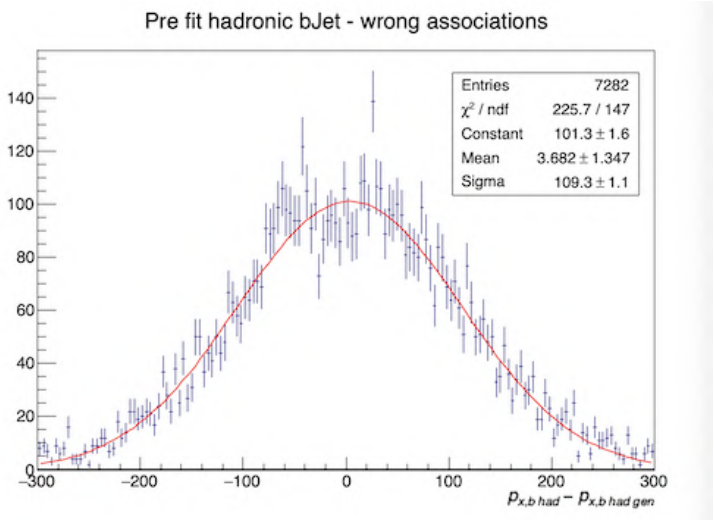

Figure 9.26: Hadronic Pre Fit bJet resolution, wrong assignments.

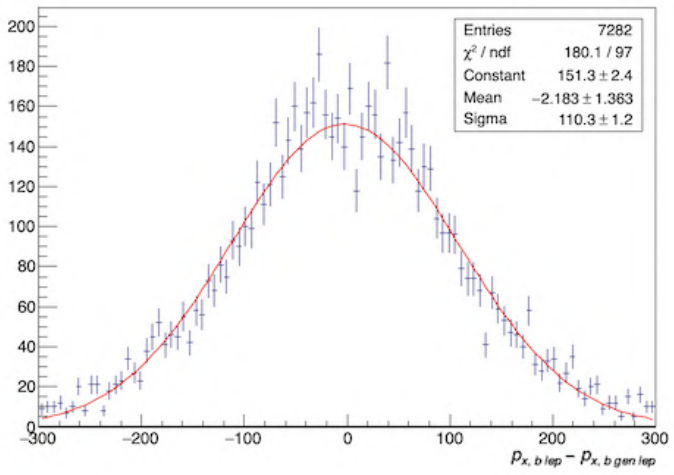

Figure 9.27: Leptonic Pre Fit bJet resolution, wrong assignments.

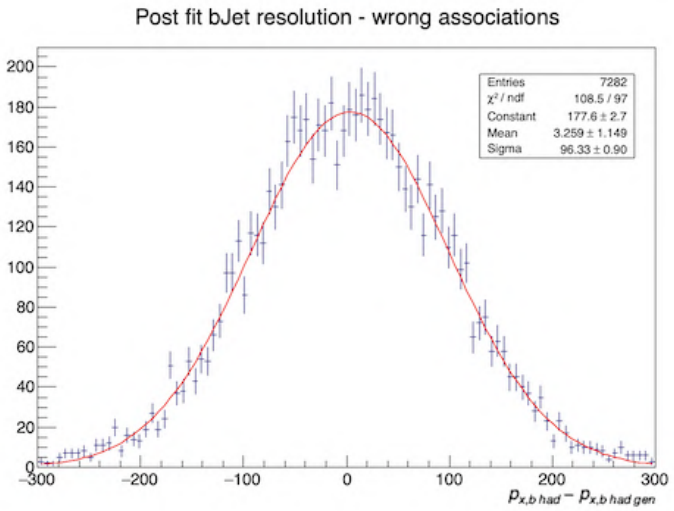

Figure 9.28: Hadronic Post Fit bJet resolution, wrong assignments.

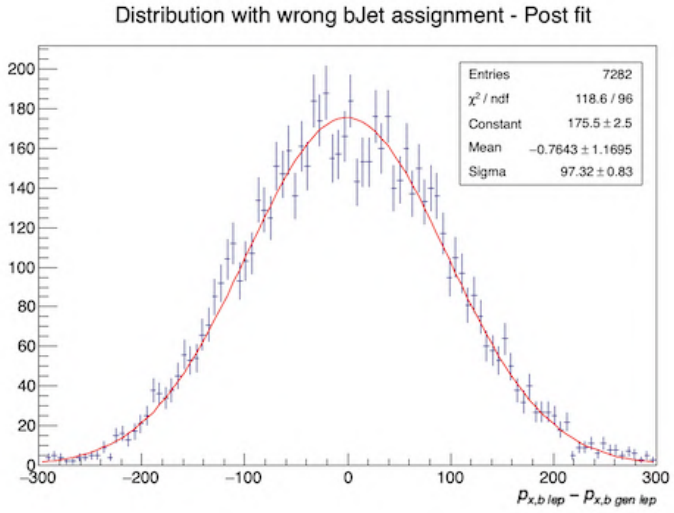

Figure 9.29: Leptonic Post Fit bJet resolution, wrong assignments.

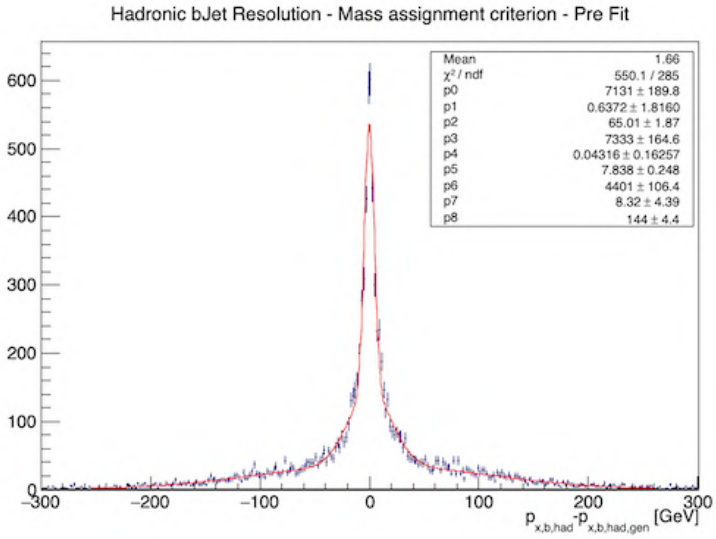

Figure 9.30: Hadronic Pre Fit bJet resolution, without using MC truth for bJet assignment.

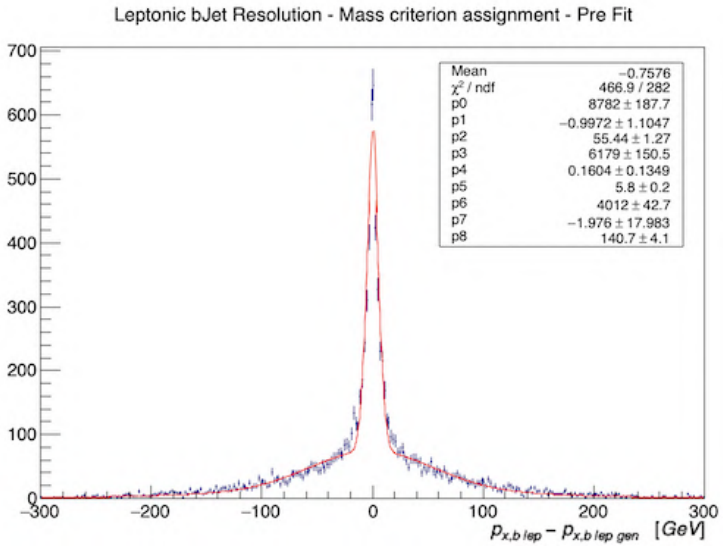

Figure 9.31: Leptonic Pre Fit bJet resolution, without using MC truth for bJet assignment.

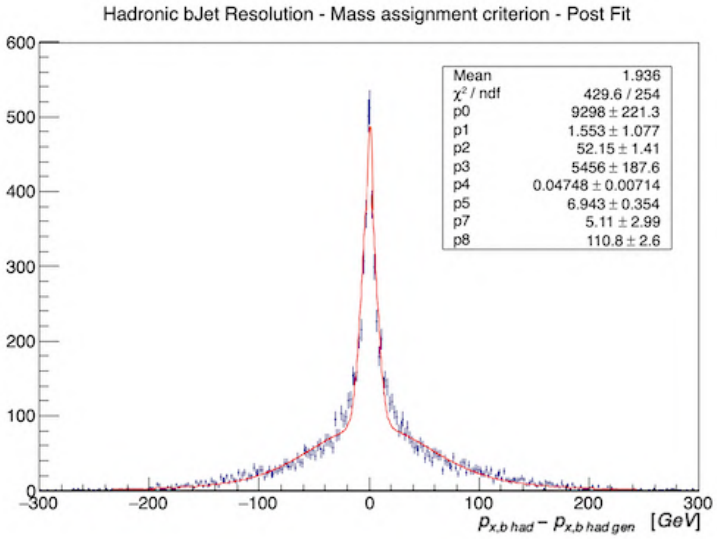

Figure 9.32: Hadronic Post Fit bJet resolution, without using MC truth for bJet assignment.

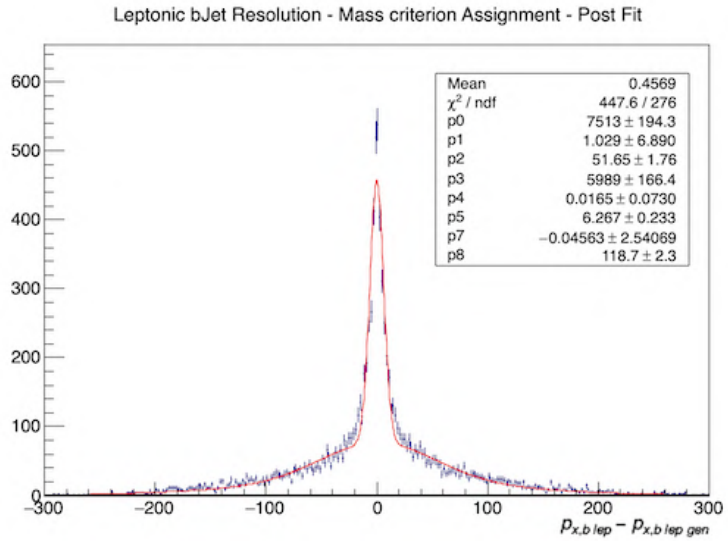

Figure 9.33: Leptonic Post Fit bJet resolution, without using MC truth for bJet assignment.

In this case p_0 (Constant), p_1 (mean) and p_2 (standard deviation) are the parameters that describe the first Gaussian, while the second is described by p_3 (Constant), p_4 (mean) and p_5 (standard deviation) and the third by p_6 (Constant), p_7 (mean) and p_8 (standard deviation).
Let's describe the Pre fit distributions. To fit it with three Gaussian distributions, the values of the standard deviation and of the mean find out using MC truth on b-jet assignment were used as starting values and the parameters were left moving around them. As to the constant term, it was let float freely.
As to post fit distributions, also in this case the initial values for standard deviations and means are the ones obtained with MC b-jet assignment, while the constant term related to b-jet mis-assigned events is fixed to the value obtained in the pre-fit curve (the number of mis-assigned events must be conserved).
Analysing the distributions the following observations can be done:

- All the distributions (pre and post fit) are peaked around zero, as we expect;
- All the standard deviations becomes smaller (or comparable) after applying the kinematic fitter.

All these considerations are consistent with what we expect and are a further proof that the kinematic fitter works properly.
Another check we can do is looking at $m_{t\bar{t}}$ resolution. Let's remind that now we are discussing the second-approach kinematic fitter, therefore in this case it is not of interest obtaining a value for $m_{t\bar{t}}$ resolution. Anyway, what we expect is that after the application of the algorithm, also in this case the resolution should improve.
First of all, it can be of interest considering the figure 9.34, in which it is shown the superimposition of the Pre-Fit $m_{t\bar{t}}$ resolution (in red) and of the Post-Fit $m_{t\bar{t}}$ resolution (in blue), both obtained using MC for correct b-jet assignment.

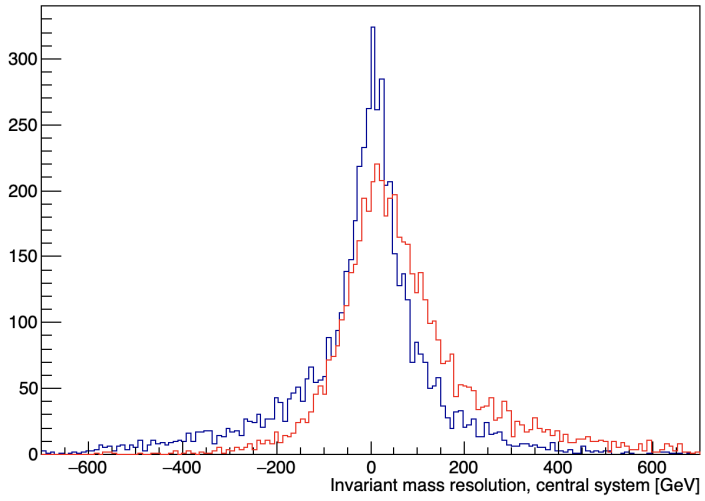

Figure 9.34: Superimposition of the Pre-Fit $m_{t\bar{t}}$ resolution (in red) and of the Post-Fit $m_{t\bar{t}}$ resolution (in blue), both obtained using MC for correct bJet assignment.

It can be noticed that the fitter changes the direction of the tail: before we have a longer tail on the right, then on the left. But the most interesting thing is that the distribution becomes thinner. To make this statement more rigorous, we can proceed as we did for the hadronic/leptonic b-jet momentum resolution. First of all we consider the Pre-Fit $m_{t\bar{t}}$ resolution distributions obtained with MC truth b-jet assignment, shown in figures 9.35 and 9.36.

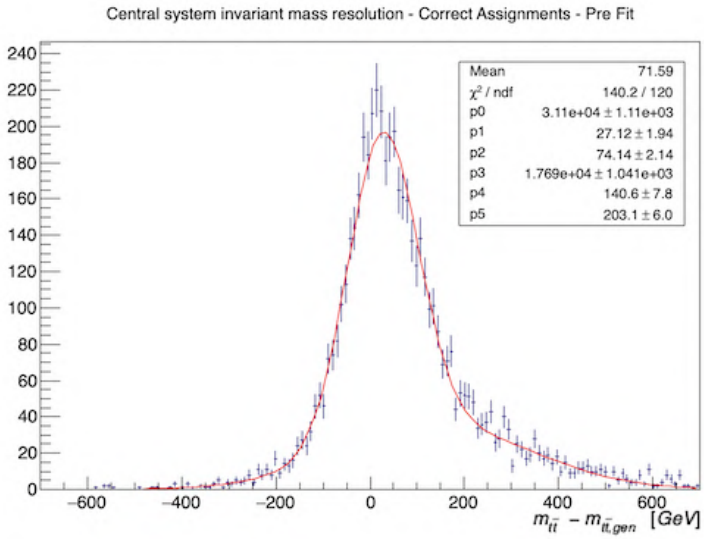

Figure 9.35: $m_{t\bar{t}}$ Pre-Fit resolution, correct assignments done with MC truth.

These plots show that in this case we cannot model the distributions both for signal and for background with just one Gaussian function, but we need two of them. Each normalised Gaussian distribution is defined by three parameters which are respectively p_0 (constant), p_1 (mean), p_2 (standard deviation) and p_3 (constant), p_4 (mean), p_5 (standard deviation).
Then, we can see in figures 9.37 and 9.38 the Post-Fit distributions. Both distributions are fitted with a couple of Gaussian distributions (same meaning of the parameters). If we consider the distributions relative to correct b-jet assignment, we can observe that the standard deviation of the curve holding the greatest number of events reduces after applying the kinematic fitter, while the other get a bit worse. Also in this case, to evaluate the improvement, we consider the equivalent standard deviation:

$$\sigma^*_{post-fit,m_{t\bar{t}}} \approx 116.1\ GeV < \sigma^*_{pre-fit,m_{t\bar{t}}} \approx 120.9\ GeV$$

which shows an improvement in the invariant mass resolution.
On the other hand, considering the events with wrong b-jet assignment, even in this case there is a slight improvement (actually not changing inside the error bands).

Now we don't consider the MC truth information and we process the events assigning the hadronic/leptonic b-jet following the method explained at the end of the previous chapter. In figure 9.39 and 9.40 are represented the Pre-Fit and Post-Fit resolutions.

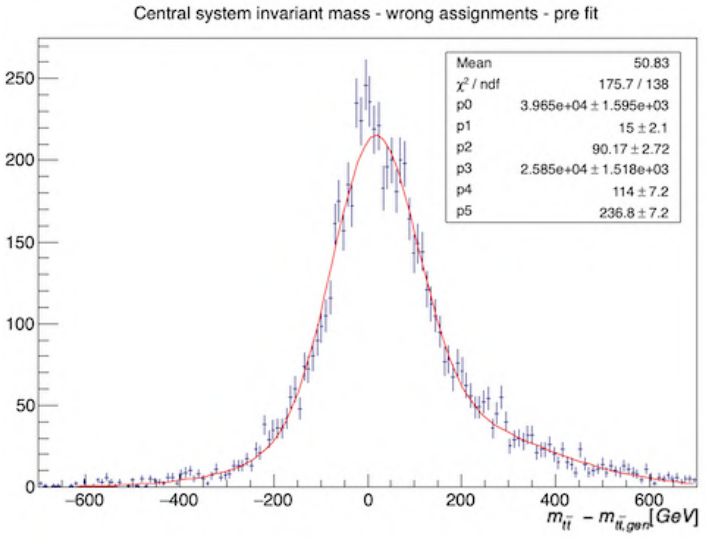

Figure 9.36: $m_{t\bar{t}}$ Pre-Fit resolution, wrong assignments.

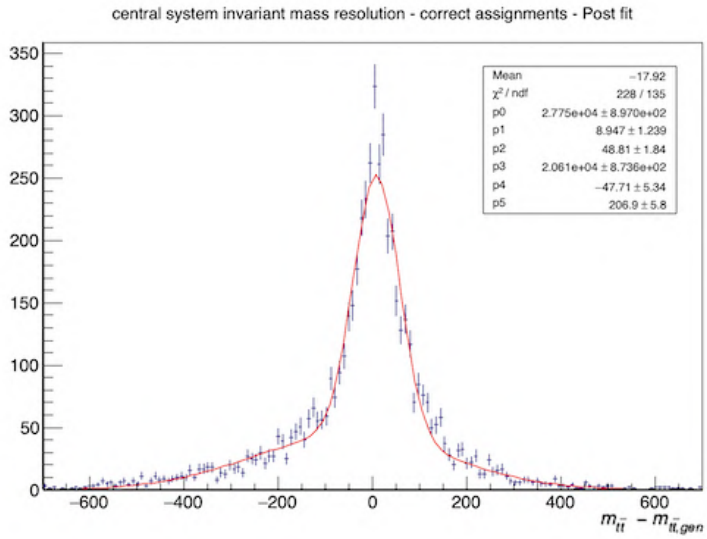

Figure 9.37: $m_{t\bar{t}}$ Post-Fit resolution, correct assignments.

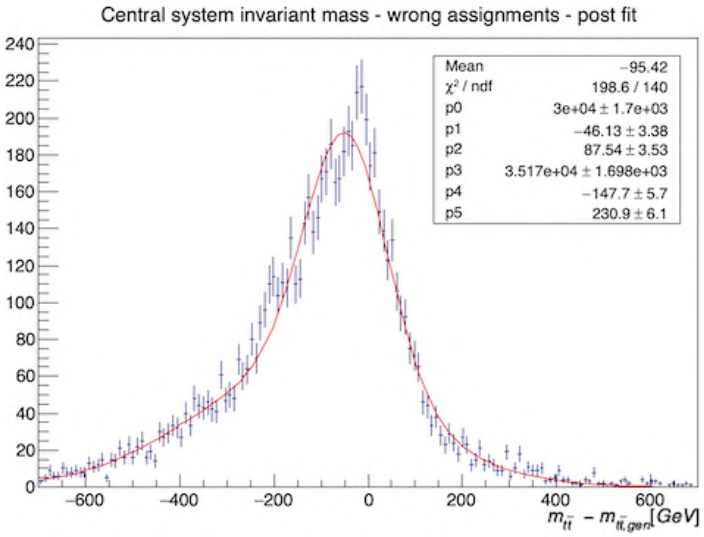

Figure 9.38: $m_{t\bar{t}}$ Post-Fit resolution, wrong assignments.

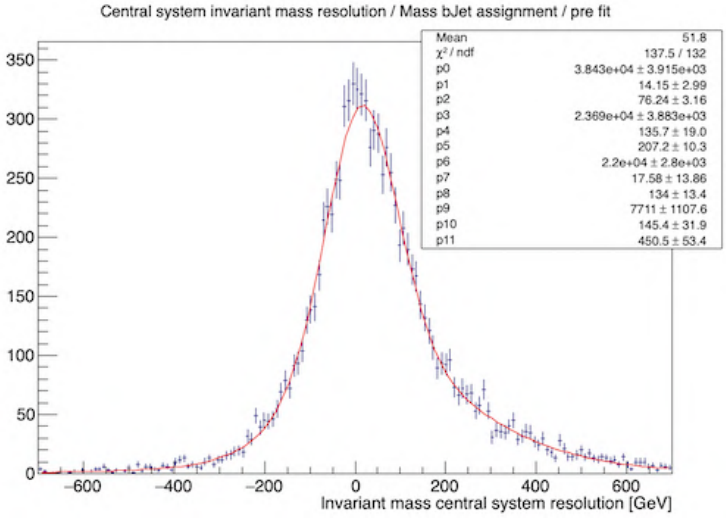

Figure 9.39: $m_{t\bar{t}}$ Pre-Fit Resolution, without using MC truth for bJet assignment.

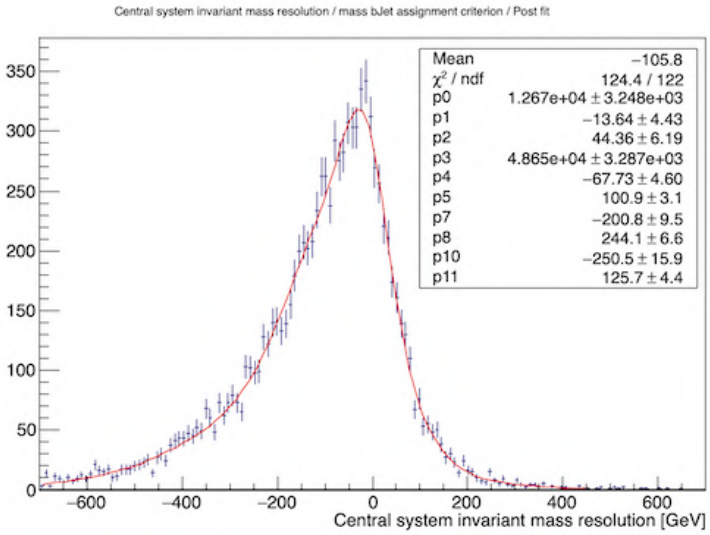

Figure 9.40: $m_{t\bar{t}}$ Post-Fit Resolution, without using MC truth for bJet assignment.

The distributions are fitted with four (normalised) Gaussian distributions (two for correct assignments and two for wrong ones). Each Gaussian is described by three parameters which are p_0 (constant), p_1 (mean), p_2 (standard deviation) for the first one, p_3 (constant), p_4 (mean), p_5 (standard deviation) for the second one, p_6 (constant), p_7 (mean), p_8 (standard deviation) for the third one and p_9 (constant), p_{10} (mean), p_{11} (standard deviation) for the forth one. First and second Gaussian distributions contain the events with correct b-jet assignment, while the other two represents the event with wrong b-jet assignment. As usual, to fit the plot shown in 9.39 we give to mean parameters and to standard deviation parameters the values obtained by MC truth and we leave them free to move around these values. The values obtained for the constants parameters of mis-assigned events in the Pre-Fit graph are fixed in the Post-Fit plot (the number of mis-assigned events must be conserved).
As we expect, the sum of constant terms for wrong assignments curves are by far smaller than the other ones. Furthermore, both the standard deviations of the distributions holding correct assigned events reduce after applying the kinematic fitter.
Even in this case, a good check can be obtained by calculating the equivalent standard deviation. Surely, we will just consider the two distributions holding correct b-jet assignment events in calculating it. Therefore, for Pre-Fit distribution we obtain $\approx 126.1\ GeV$, while for the post fit distribution we get $\approx 88.3\ GeV$, which is a great improvement. All this shows the kinematic fitter is working properly.

Let's now have a look at the χ^2 distribution, calculated using the formula $\chi^2 = x_i^T \mathcal{C}^{-1} x_i$, where x_i is the difference between the set of post-fit (50th iteration) and pre-fit kinematic quantities.
Following the second-approach, the χ^2 distribution is very important, because it will be one of the most discriminating variables in the MVA algorithm, so a

dedicated discussion is mandatory.
First of all, we analyse the χ^2 distribution of signal samples.
If the fitter was "unconstrained", then the χ^2 distribution should be the one shown in 9.41 (the number of degrees of freedom is 20). In our case the situation is different: in fact we don't select each time the minimum of χ^2, but the minimum value such that kinematic constraints are satisfied. For this reason, we expect a longer tail. The distribution of χ^2 obtained after applying the fitter is shown in figure 9.42, and reflects our expectations. Note that the distribution was realised without considering the MC truth on b-jet assignment, therefore the longer tail is justified also by incorrect b-jet assignment.

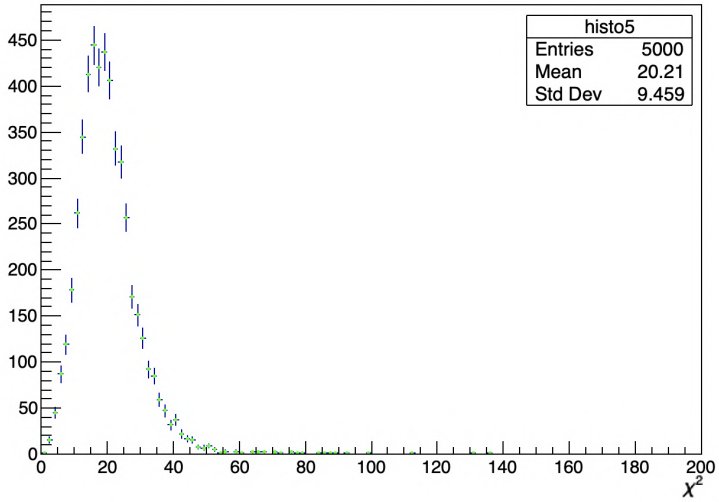

Figure 9.41: χ^2 distribution for a system with 20 degrees of freedom.

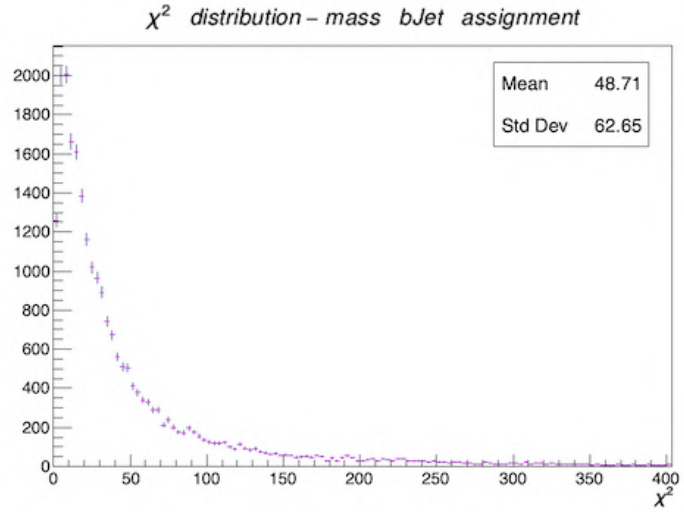

Figure 9.42: Kinematic fitter χ^2 distribution.

It is then important to look at the χ^2 obtained fitting a background sample. In this case the protons kinematic measured thanks to PPS should not be related with the one observed by the central system: the protons detected by the outer system, in fact, are just pile up protons coming from other contemporary diffractive events. Therefore, since following the second-approach we are enforcing the matching constraint $M_X^2 - s\xi_1\xi_2 = 0$, we expect to get a distribution of χ^2 worse than the one obtained for signal (it is actually the key point of the second-approach kinematic fitter). In figure 9.43 we show the superimposition of the χ^2 distributions obtained fitting signal/background MC samples.

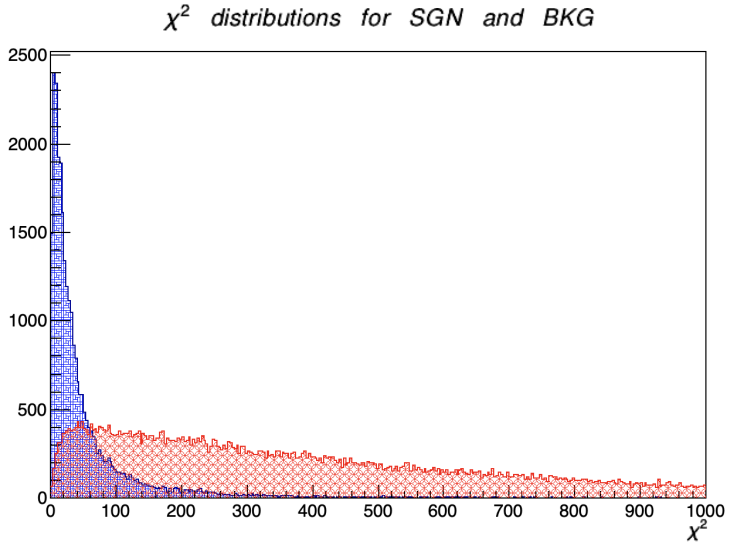

Figure 9.43: Signal (in blue) and Background (in red) χ^2 distributions obtained using the second-approach kinematic fitter.

As we expect, the χ^2 signal distribution is peaked at lower values than the χ^2 background distribution.

Finally, a few comments on the first-approach kinematic fitter are in order. As discussed before, the only difference between the two kinematic fitters is that in this case the matching condition $M_X^2 - s\xi_1\xi_2 = 0$ is not enforced. Considerations about convergence, number of iterations needed to reach convergence are exactly the same discussed above, so we don't add more plots, since it would be very similar. Also the kinematic constraints are perfectly satisfied after the 50th iteration.
The only important thing that we must discuss in this case is the resolution improvement after the algorithm application. In particular, in this case we will show just the Pre-Fit and Post-Fit hadronic b-jet resolution as an example, and then we will discuss the $m_{t\bar{t}}$ resolution improvement. This last point is by far the most important, since following the first approach, all the events that don't satisfy the matching condition within the resolution will be cut out.
One must stress out that in all the plots we are going to show, the same prescriptions described for second-approach kinematic fitter were used to fit the distributions and the parameters name has the same meaning.

So first of all, let's discuss the results obtained with b-jet MC truth. As to Pre-Fit distributions, actually they are already shown in figures 9.22 (correct assignments) and 9.26 (wrong assignments). On the contrary, figure 9.44 shows the Post-Fit b-jet resolution (x-component) obtained with the first-approach kinematic fitter and using MC truth to select only events with correct b-jet assignments.

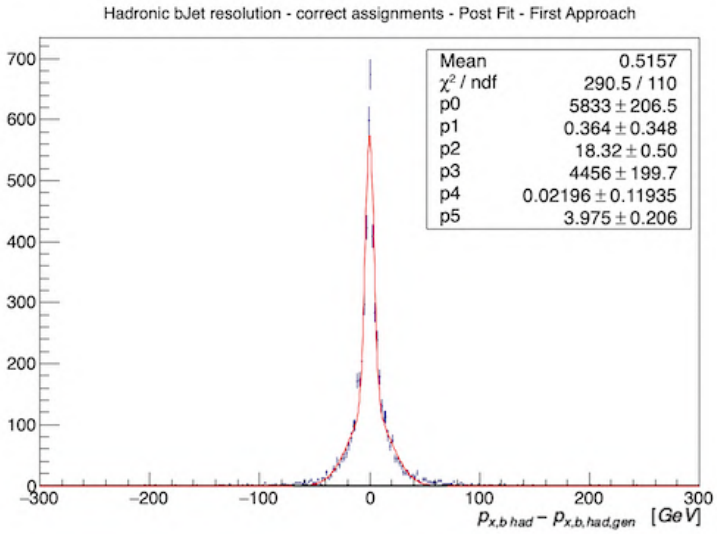

Figure 9.44: Hadronic post-fit bJet momentum resolution (x-component), first-approach fitter.

The results are quite comparable to the one shown in 9.24. Anyway, a slightly improvement can be seen using the second-approach fitter. In any case, let's calculate the effective standard deviation:

$$\sigma^*_{post-fit,had,first-approach} \approx 12.1\ GeV < \sigma^*_{pre-fit,had} \approx 14.3\ GeV$$

That means that we have an improvement in the overall resolution also with the first approach . Also let's note that $\sigma^*_{post-fit,had,first-approach} > \sigma^*_{post-fit,had,(second-approach)} \approx 10.1\ GeV$, which means that the other fitter is more performing in this case.
In figure 9.45 is instead shown the Post-Fit bJet resolution (x-component) using MC truth for selecting just events with wrong b-jet assignment (the Pre-Fit distribution is already shown in 9.26).

The distribution shows that also in this case there is an improvement in the resolution, but it is smaller than the one obtained with the second-approach fitter (see 9.28).
Finally, in figure 9.46 is shown the distribution of b-jet momentum resolution (x-component) without using MC truth for b-jet assignment (to fit the distribution same prescriptions used for second-approach kinematic fitter are used and the parameters have the same meaning).

Even in this case, the resolution of all the curves improves after applying the kinematic fitter (see Pre-Fit distribution in figure 9.30).
Now let's evaluate the post-fit $m_{t\bar{t}}$ resolution, which is by far the most important one following the first approach.

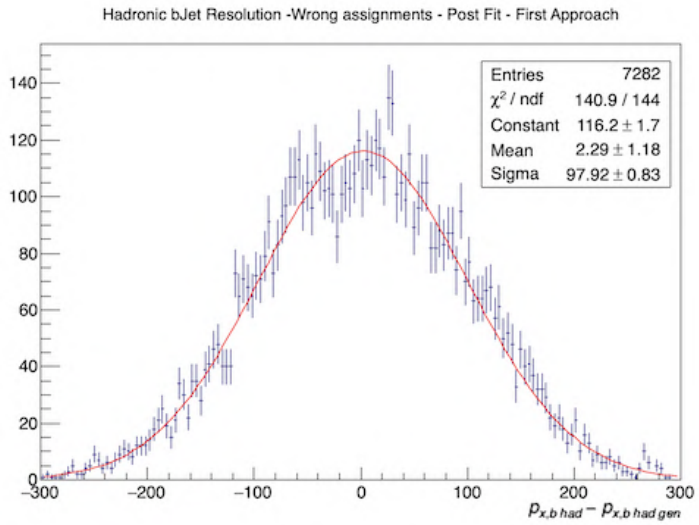

Figure 9.45: Hadronic post-fit bJet momentum resolution (x-component), wrong assignments, first-approach fitter.

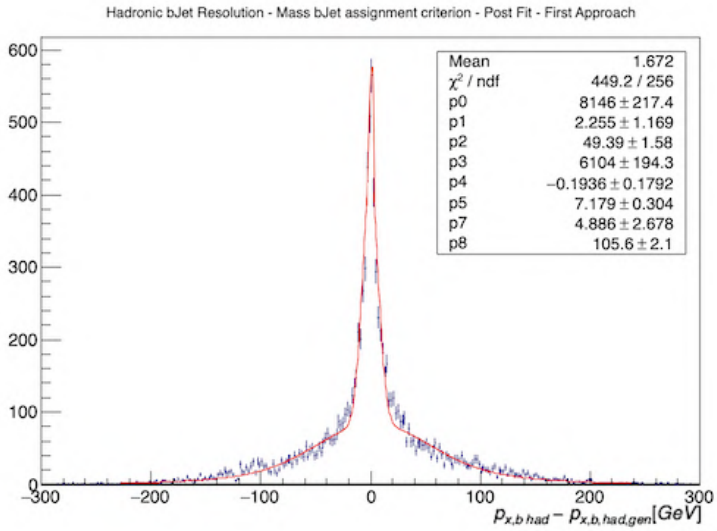

Figure 9.46: Hadronic bJet post-fit momentum resolution (x-component), without using MC truth for bJet assignment, first-approach kinematic fitter.

First of all, we show in figure 9.47 the superimposition of pre-fit and post-fit $m_{t\bar{t}}$ resolution, obtained using MC truth for bJet assignment (post-fit distribution obtained using the first-approach fitter). It is evident that the kinematic fitter

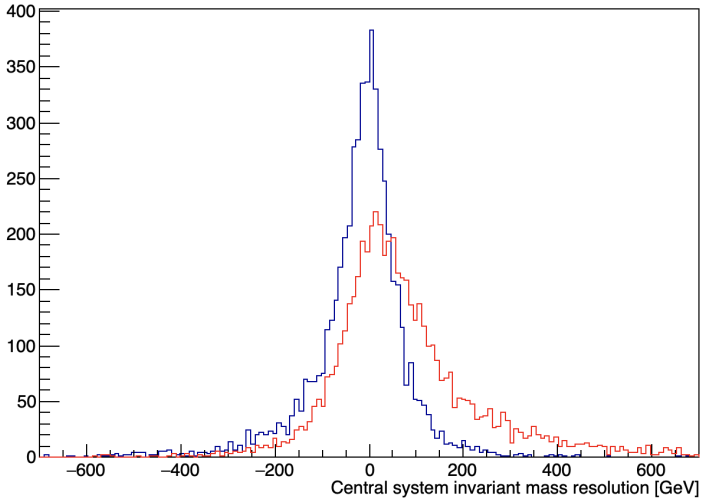

Figure 9.47: Superimposition of pre-fit (in red) and post-fit (in blu) $m_{t\bar{t}}$ resolution, obtained using MC truth for bJet assignment (post-fit distribution obtained using the first-approach fitter).

improves the resolution of this distribution, anyway, estimating a value for the effective standard deviation is mandatory following the first-approach.
Pre fit distributions already have been shown. In particular figure 9.35 shows the distribution obtained for $m_{t\bar{t}}$ resolution, using MC truth to select events with correct b-jet assignment, while 9.36 shows the same resolution for wrong assignments.
Here we show figures 9.48 and 9.49, containing respectively the post-fit $m_{t\bar{t}}$ resolution with correct and incorrect assignments obtained using the first-approach kinematic fitter.

It can be observed that in both cases a fit with two Gaussian distributions is mandatory. The meaning of the parameters is not changed.
Looking at the correct assignments post-fit distribution, we can observe a great improvement in both resolutions. This means that the fitter works properly. In particular for the pre-fit distribution (correct assignments) we had already calculated the equivalent standard deviation obtaining 120.9 GeV, while in this case we obtain ≈ 74.9 GeV
As to the wrong assignments distribution, even in this case both standard deviations have a slightly improvement.
It is interesting looking at the "overall effect", which means evaluating the resolution of the $m_{t\bar{t}}$ distribution obtained without using MC truth for b-jet assignment, which we show in figure 9.50.

Also in this case, the fit is done with four Gaussian distribution (same meaning of the parameters); constant term for b-Jet mis-assignment distributions are fixed to the pre-fit ones for above discussed reasons.
Several remarkable considerations about this last distribution:

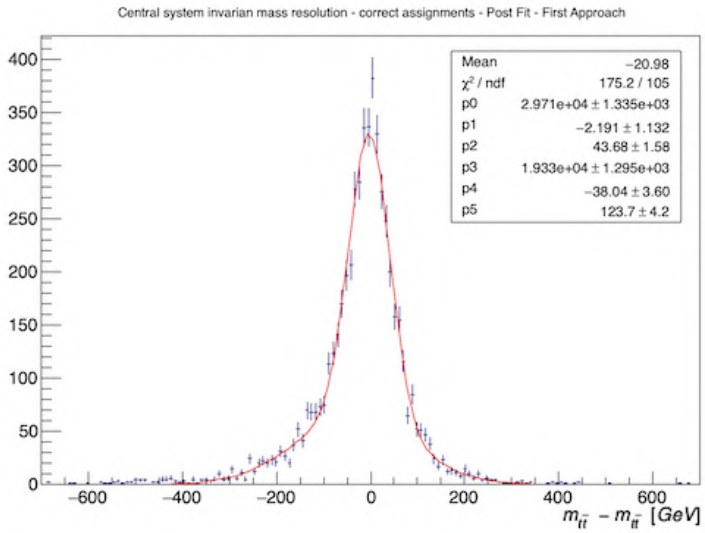

Figure 9.48: Post-Fit $m_{t\bar{t}}$ resolution, correct assignments, first approach.

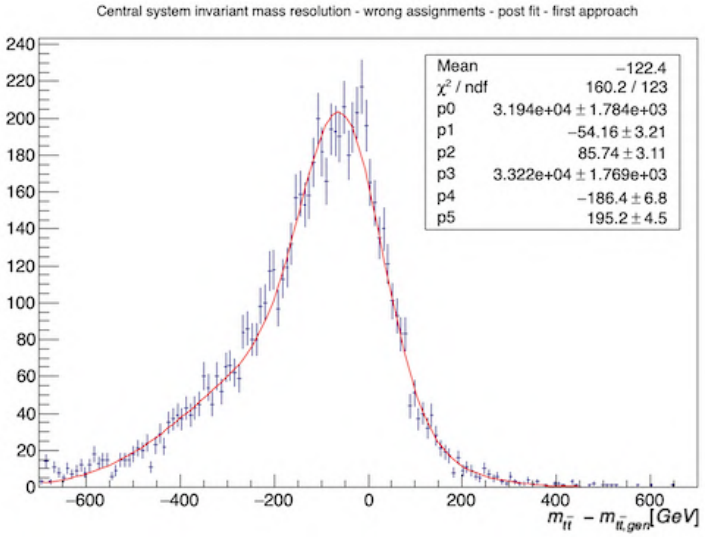

Figure 9.49: Post-Fit $m_{t\bar{t}}$ resolution, incorrect assignments, first approach.

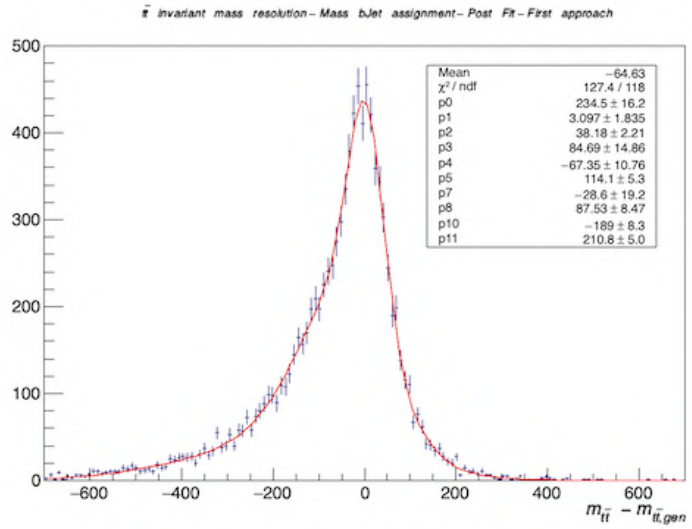

Figure 9.50: $m_{t\bar{t}}$ resolution obtained without using MC truth for bJet assignment

- Comparing this distribution with the post-fit one obtained with the second approach, we find that the "core" correct-assignment-distributions improves more using the first-approach, while the "non-core" distribution obtained using second-approach fitter is thinner. That is the reason why the equivalent standard deviation of the two methods is comparable.
- Comparing this distribution with the one obtained without using MC truth for b-jet assignment and before applying the kinematic fitter, we can observe an improvement in the resolution of both the "core" and the "non-core" correct-assignment-curves.

Finally, let's evaluate the equivalent standard deviation for the post-fit $m_{t\bar{t}}$ resolution distribution obtained with the first approach and without using MC truth for b-jet assignment (9.50). Even in this case, we consider just the distributions holding correct bJet assigned events, obtaining:

$$\sigma^* = 89.2\ GeV$$

. This value will be of capital importance because it will be the one used (in the first approach) to select signal events from background: $M_X^2 - s\xi_1\xi_2 < \sigma^{*2}$ Efficiencies of both methods will be discussed in next chapter. Lastly, let's remark that this value of equivalent standard deviation is by far better than the pre-fit one ($\approx 126.1\ GeV$).

9.4.3 b-jet assignment using the kinematic fitter: an alternative way

Since the b-jet assignment method described in Section 9.2.3 has just the 83% efficiency, maybe we can try another approach. In particular, after fixing an event, we consider all the different combinations of leptonic and hadronic systems. For each combination we calculate the χ^2 and the ones that corresponds

to the lower value of χ^2 is accepted.
We tested this approach using the MC truth and we found out that the efficiency of this method is $\approx 84\%$, therefore slightly better than the previous one. Anyway, the computing time needed to process the same number of events is more than ten times greater, therefore, since the improvement is minimal, we decide to keep the version of the b-jet assigner described earlier.

9.5 Multivariate analysis

While the main aim of the kinematic fitter is improving the $M_{t\bar{t}}$ resolution, we developed a multivariate analysis to further discriminate between inclusive and exclusive $t\bar{t}$ production processes. Even in this case we will optimise the algorithm basing just on the main source of background ($t\bar{t}$ + jets inclusive production). Then, after its optimisation, we will apply it to all the background samples, as shown in the next chapter.

In TMVA (the ROOT framework we used to perform MVA), several classifiers (like fisher discriminant, likelihood, SVM, BDT, MLP, ...) are implemented. A full description of them, including how batches are organised, how many epochs are used on training samples, how do the classifiers work and what is the form of the function f for each classifier, can be found in the TMVA guide (Ref. [83]). In our analysis, the number of events in each batch and the number of epochs is the default value. We tried to change them but there was not a significantly change in the results. The MVA has been mainly set up during a master's degree thesis [82].

9.5.1 The input variables.

The input variables play a central role in multivariate analysis tools. Clearly, choosing variables which are enough different for signal and background is the first golden rule, but one must also pay attention to avoid including too correlated variables. Actually, correlated variables bring "redundant information" which does not help the MVA algorithm to separate signal from background. This aspect implies in turn that we must avoid to include too many variables. Starting from this consideration, we decided to include in our MVA algorithm the following variables, which will be then fully commented:

- Jet total mass: the sum of the invariant mass of all jets (including pile up ones);
- Total light jet energy (including pile up ones);
- Mean angular distance between light jets: we calculated the value of ΔR for each couple of light jets, we summed up these values and divided the sum by the total number of couples;
- Extra energy: the energy of pile up jets;
- Number of light jets;
- Number of b jets;

- Lepton momentum;
- Lepton isolation.
- Rapidity matching: the rapidity of the central system is connected to the fraction of momentum lost by the protons by this relation: $Y_X = 0\frac{1}{2}\ln\frac{\xi_1}{\xi_2}$. For this reason, an interesting variable to consider is $Y_X - \frac{1}{2}\ln\frac{\xi_1}{\xi_2}$, which we expect to be peaked at zero only for the signal.

These variables are the ones used as input when using the first approach of the kinematic fitting procedure. Following the second approach, the same variables are used, together with the χ^2 distribution obtained by the kinematic fitter.

The distribution of the input variables for exclusive $t\bar{t}$ (signal) and inclusive $t\bar{t}$ (background) are shown in Figure 9.51.

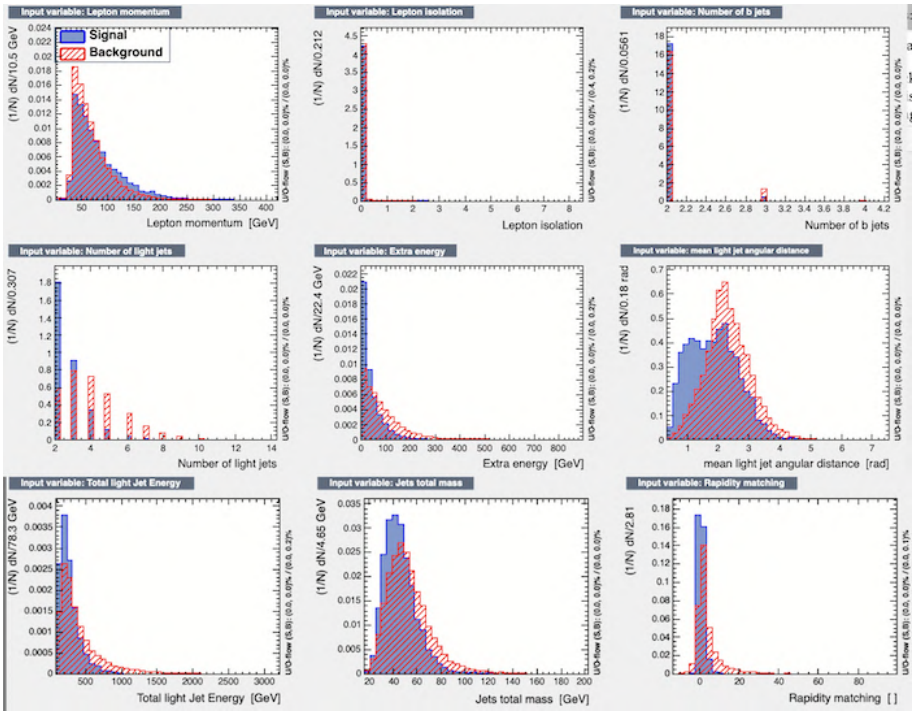

Figure 9.51: Signal/Background training samples variables.

The $t\bar{t}$ + jets source of background is hard to be rejected from signal due to pile up: actually it is difficult understanding when the "extra jets" derive from the interaction in itself (inclusive $t\bar{t}$ production) or when they are just coming from pile up (a thing that may happen for the exclusive production). Hence, signal and background $t\bar{t}$ production processes may look similar having a $t\bar{t}$ pair and additional jets. However, we expect to have more jets in the background case (and effectively the number of jets is the most discriminating variable). Furthermore, also the energetic aspect is quite important: in a central exclusive production, the particles in the final state are not going to have a lot of energy (it derives from protons interaction, and they are just slightly deflected) while,

for the background, protons dissociate, therefore a bigger amount of energy is available (actually all the fraction carried by the interacting quarks). For this reason we added several variables related with energy, having care of checking the correlation matrix to avoid to introduce redundant information. The χ^2 distribution is quite discriminant, since in the fitter, the exclusivity constrain ($p_T^{t\bar{t}} \approx 0$) is considered, resulting in higher values of χ^2 for inclusive production ($t\bar{t}$ + jets.

Independently for the approach used, the variables given as input to TMVA are the ones obtained after the kinematic fitter. Correlation matrix for signal and background samples of the chosen variables is shown in Figure 9.52.

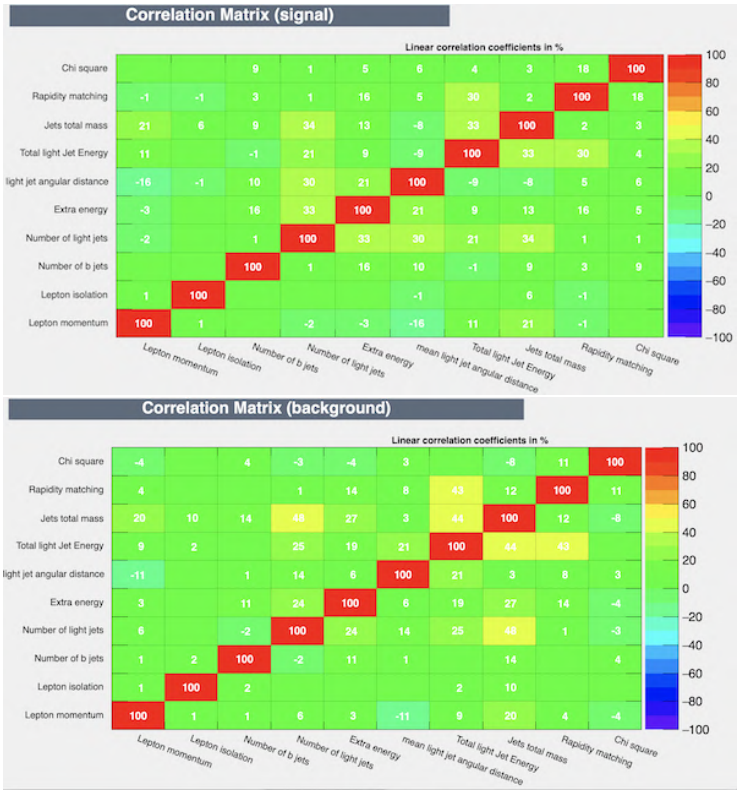

Figure 9.52: Signal (up) and background (down) correlation matrix.

These pictures show clearly that both in signal and background samples there is almost no correlation. Only the "Jet total mass" has a slightly bigger correlation with the extra energy and the number of light jets, but actually it is under the 50%.

9.5.2 TMVA performances and working point choice.

Two sets of input variables were used depending on the analysis strategy that was chosen (the *first approach* or the *second approach*, see Section 9.4 for more details). The performance for the two approaches was tested and will be discussed in the following sub-sections.

9.5.3 The efficiency of the first approach

The training strategy was the following:

- 50000 events from signal and background samples were used in this study.
- Events satisfying correlation cuts between central detector and PPS are kept ($|M_X^2 - s\xi_1\xi_2| < \sigma^{*2}$, being $\sigma^* = 89.2\ GeV$).
- Several classifiers (BDT, BDTD, MLP, Fisher discriminant and likelihood) are trained, and a working point for the best classifier (procedure described below) is chosen.

The procedure described above introduces several efficiencies, one for every step, separately for signal and background. First, we will call $\epsilon_{s,1}$ and $\epsilon_{b,1}$ the efficiencies to pass the correlation cut ($|M_X^2 - s\xi_1\xi_2| < \sigma^{*2}$) for signal and background respectively.

Using the above mentioned signal and background samples, we evaluate these efficiencies to be:

$$\epsilon_{s,1} \approx 71\%$$

$$\epsilon_{b,1} \approx 8.5\%$$

This result is not what we would ideally expect: this approach, in fact, can be considered a strong tool just if $\epsilon_s \approx 100\%$ and $\epsilon_r \approx 0\%$. The values obtained do not fully satisfy this requirement. For this reason, we slightly changed the "first approach": we decided not to do a cut on $|M_X^2 - s\xi_1\xi_2| < \sigma^{*2}$, but we just train a MVA algorithm using as inputs all the above introduced variables together with the quantity $M_X - \sqrt{s\xi_1\xi_2}$, that we expect to be peaked at zero only for the signal. The distributions of the correlation variable ($M_X - \sqrt{s\xi_1\xi_2}$) both for signal and background is shown in Figure 9.53.

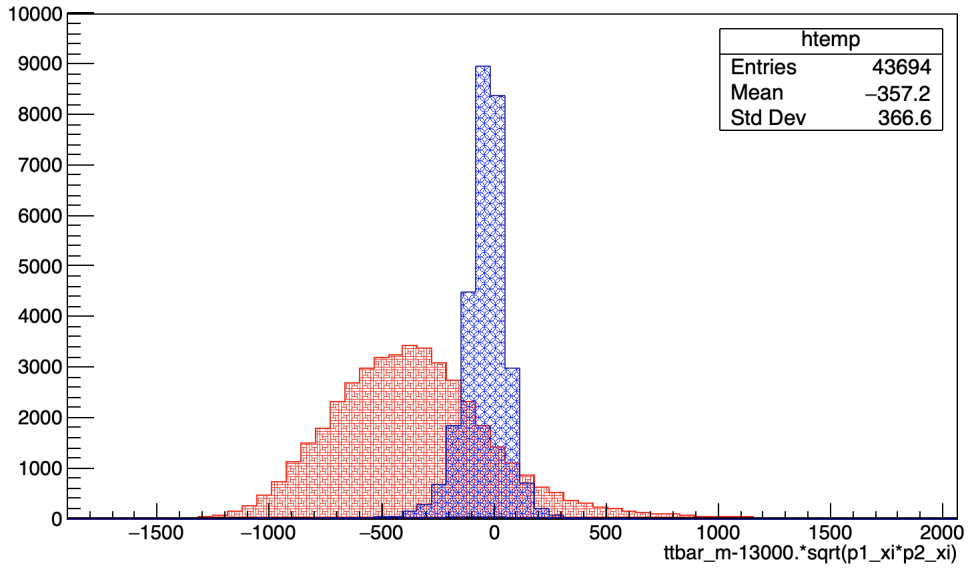

Figure 9.53: Signal (in blue) and background (in red) $M_X - \sqrt{s\xi_1\xi_2}$ distributions.

Now, let's check the performances of the TMVA algorithm. As input variables we use the ones mentioned in the previous paragraph together with the $M_X - \sqrt{s\xi_1\xi_2}$ distribution. The default parameters for batches and epoch number were left, since no significant difference was found when changing them. BDT, BDTD, MLP, Fisher discriminant and likelihood are used as classifiers and the Receiver Operating Characteristic (ROC) curve obtained is the one shown in figure 9.54.

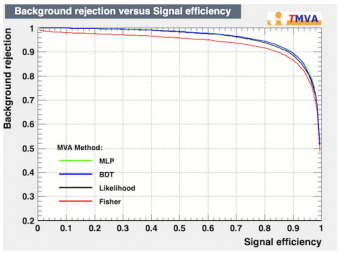

Figure 9.54: ROC curve obtained following the first approach.

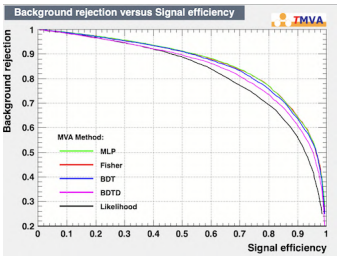

Figure 9.55: ROC curve obtained using pre-fit variables.

That curve is obtained using as input values the post-fit quantities. An improvement can be noticed with respect to the curve shown in figure 9.55, in which it is represented the ROC curve obtained using the same input variables but considering pre-fit values (before kinematic fit). Therefore, this shows that the fitting procedure introduces an improvement in the overall performance of the MVA algorithm. The working point on the curve is chosen by maximising the value of the significance, defined as:

$$\mathcal{S}(\epsilon_s) = \frac{S(\epsilon_s)}{\sqrt{S(\epsilon_s) + B(r_b)}}$$

Where:

- $S(\epsilon_s)$ is the number of signal events saved, which depends on the signal efficiency ϵ_s;
- $B(r_b)$ is the number of background events not rejected which depends on the rejection efficiency r_b.

Since $r_b = 1 - \epsilon_b$ depends on ϵ_s as shown by the ROC curve, the whole expression of $\mathcal{S}$ depends just on ϵ_s.

The working point will be defined as the point (ϵ_s, r_b) that maximises the significance.

Therefore, what we do is considering the best classifier (in our case BDT) and we plot in the same graph the significance, the signal efficiency and the background rejection in function of the cut we do on the classifier output. The result is shown in figure 9.56.

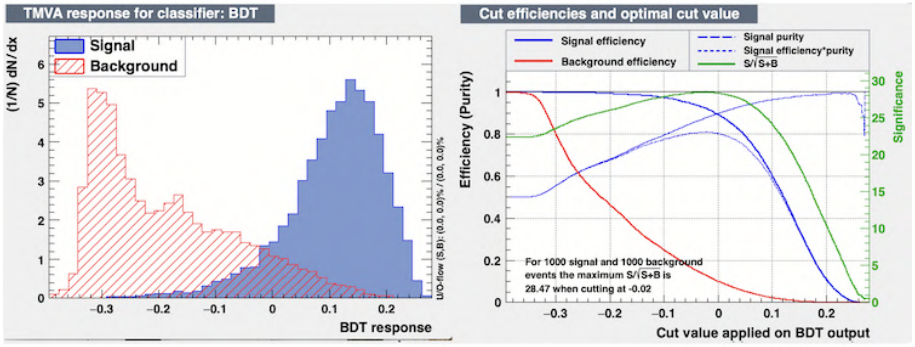

Figure 9.56: Significance, signal efficiency and background rejection in function of BDT output cut (right) and BDT output distributions for signal and background (left), for the first approach.

To estimate a more realistic significance, we may write the significance as:

$$\mathcal{S} = \frac{\epsilon_s N_s}{\sqrt{\epsilon_s N_s + \epsilon_b N_b}}$$

Then we can write $N_b = kN_S$, being k a real number. Therefore:

$$\mathcal{S} = \frac{\epsilon_s N_s}{\sqrt{\epsilon_s N_s + k\epsilon_b N_s}} = \sqrt{N_s}\frac{\epsilon_s}{\sqrt{\epsilon_s + k\epsilon_b}}$$

Since $\sqrt{N_s}$ is a fixed number, then maximising $\mathcal{S}$ means maximising $\mathcal{S}^* = \frac{\epsilon_s}{\sqrt{\epsilon_s + k\epsilon_b}}$. In our case, since $\sigma_{BKG} \approx 800\ pb$ and $\sigma_{SGN} \approx 0.1\ fb$, we expect $k \approx 8 \cdot 10^6$.
It can be shown that the value of $\mathcal{S}^*$ is maximised when the cut on BDT output is done at 0.1, corresponding to $\mathcal{S}^*(\epsilon_s) = 2.3 \cdot 10^{-3}$. For this cut, the signal efficiency is:

$$\epsilon_s \approx 65\%$$

and the background rejection is:

$$r_b \approx 98\%$$

These are the final values that can be obtained for efficiencies using the first approach.

9.5.4 The efficiency of the second approach

In this approach all the discriminating power is given to the MVA algorithm: no previous cut is done and the efficiencies may be evaluated just looking at

the TMVA output. The MVA algorithm was trained using as input variables the ones mentioned in section 9.5.1 (including the χ^2 distribution). The ROC curve obtained is the one shown in figure 9.57 using prefit variables and after the kinematic fitter. Also here one can notice that kinematic fitter improves the results of the MVA algorithm and the effect will be quantified soon.

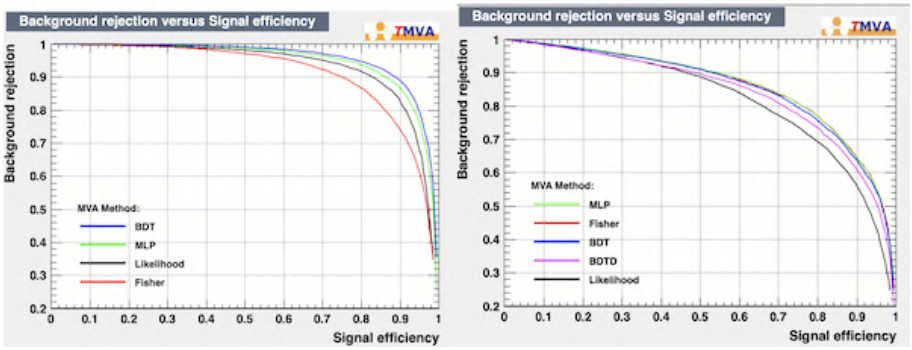

Figure 9.57: ROC curve obtained using post-fit (left) and pre-fit (right) variables and following the second approach.

For the working point selection we are interested in maximising the value of the significance and, even in this case, the working point will be defined as the point (ϵ_s, r_b) that maximises this value.
Therefore, what we do is considering the best classifier (in our case BDT) and we plot in the same graph the significance, the signal efficiency and the background rejection in function of the cut we do on the classifier output. The result is shown in figure 9.58.

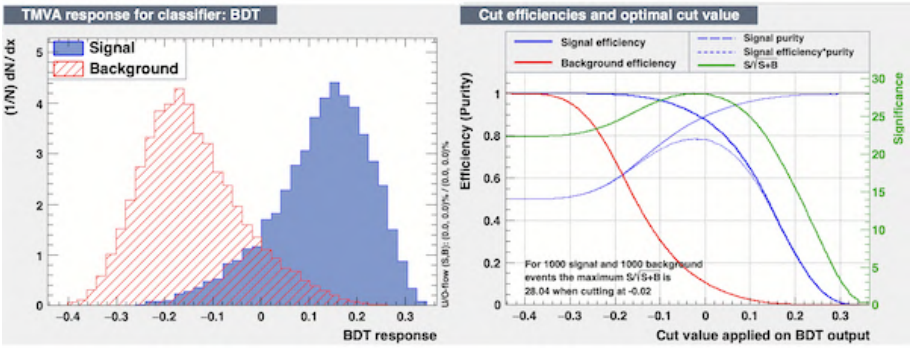

Figure 9.58: Significance, signal efficiency and background rejection in function of BDT output cut (right) and BDT output distributions for signal and background (left) for the second approach.

Even in this case TMVA evaluates cuts efficiencies basing on samples formed by the same number of events, so that we must apply the same reasoning explained in the previous chapter and considering the quantity $\mathcal{S}^*$.
The value of $\mathcal{S}^*$ is maximised when the cut on BDT output is done at 0.15, corresponding to $\mathcal{S}^*(\epsilon_s) = 2.4 \cdot 10^{-3}$. For this cut, the signal efficiency is:

$$\epsilon_s \approx 45\%$$

and the background rejection is:

$$r_b \approx 99.1\%$$

. These two values are the final efficiency results obtained using the second approach. Note that for a working point using the ROC curve obtained using pre-fit quantities, the final efficiencies would be $\epsilon_s \approx 37.5\%$ (by far less performing), and the background rejection would be $r_b \approx 93\%$. In this case the value of $\mathcal{S}^*$ is just $5 \cdot 10^{-4}$.

The second approach is better than the first one, therefore it is the one we will consider. After applying the kinematic fitter followed by the MVA tool, we obtain better signal to background separation (like the one shown on the left of figure 9.58).

9.6 Statistical analysis

9.6.1 Event yields

Proton acceptance depends on different LHC running conditions, such as beam crossing-angle, and the PPS configuration, such as the detector alignment. These conditions evolved during the 2017 data-taking period. Therefore the signal region is combined from 20 orthogonal signal regions (SR) depending on the era (B-F) and beam crossing angle (120,130, 140, and 150 μrad). The total number of events for all different signal regions is shown in Figure 9.59 and summarized in Table 9.4.

The MC samples are normalized to the expected pileup proton tag rate, measured in the dedicated control region (Section 9.3.1). The normalization factors are measured separately in each one of the SR bins. The agreement between the data and MC is expected to be within a few %, depending on the signal region.

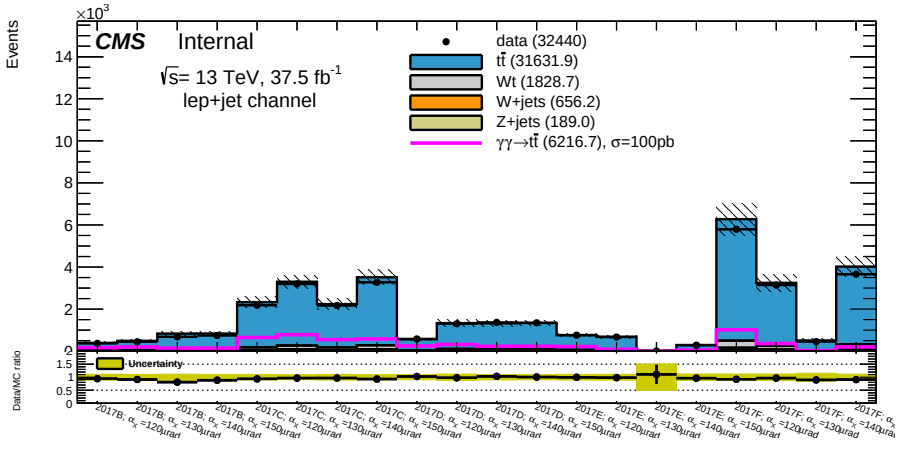

Figure 9.59: The distribution of events in different selection regions. Background normalization is extracted from a dedicated control region (defined by inverting the N_{bjet} requirement, section 9.3.1), and it is found to be within its systematic uncertainties.

Statistical model

Using the signal and background BDT distributions computed in the signal regions, we perform a statistical analysis to search for the central exclusive $t\bar{t}$ production in the data. The analysis is based on RooStats [84] and the combination tool developed by the CMS Higgs-boson analysis working group [85]. A fit to the BDT spectrum is performed, where the observed yields are compared to the expected yields using Poisson statistics.

In the analysis, we are using 20 signal regions. In each signal region, we produce BDT distribution in 11 bins in the range between -0.3 and 0.25. These numbers were not optimized. Systematic uncertainties affecting the background rate (through normalization uncertainties) or the shape of the BDT discriminant (through shape variations) are included in the fit as nuisance parameters, which are also profiled. Next, we discuss the systematic uncertainties affecting the statistical analysis.

Systematic uncertainties

The main uncertainties considered in this analysis pertain to the shapes of the signal and backgrounds. The following uncertainties are considered.

Pileup proton rates. The combinatorial backgrounds are estimated by mixing the MC sample with pileup protons obtained from the dedicated control region a discussed in Section 9.3.1. Later on, the MC is normalized according to the pileup proton rate measured in validation region defined as $N_{bjet} = 1$ which is orthogonal to the signal region but is closer than the original control region ($N_{bjet} \leq 2$). The difference in the expected tagged proton rate between the control region and the tighter control region is systematic uncertainty.

PPS efficiency. This source of uncertainty is due to the radiation damage inefficiency in the strip detectors. The efficiency itself is taken into account by weighting the signal-simulation.

Proton reconstruction. Proton reconstruction is based on a MC simulation, and it is tuned to reproduce zero-bias data events. Due to non-perfect conditions (such as alignment, optics, etc.), reconstructed proton momentum loss in MC might differ from the reconstruction in the data. Thus an additional systematic uncertainty needs to be taken into account.

Jet energy scale. The uncertainty in energy estimation for jets is strongly affected by the reconstruction of the kinematic variables used to calculate the discriminants. Therefore, the jet energy calibration uncertainty

Process	Combined	period B				period C				period D				period E				period F			
		120	130	140	150	120	130	140	150	120	130	140	150	120	130	140	150	120	130	140	150
MC Backgrounds																					
$t\bar{t}$	31631.60	361.54	450.62	770.12	772.02	2147.70	3042.11	2063.48	3242.58	522.90	1230.48	1220.39	1237.62	704.19	630.27	7.40	269.76	5782.41	2999.09	468.22	3708.69
Wt	1828.69	21.41	26.28	44.23	45.08	126.10	177.19	119.63	186.45	30.70	71.37	71.26	70.90	40.88	36.67	0.57	15.80	333.58	170.70	26.81	213.07
$W + jets$	656.17	7.50	9.73	16.90	15.82	42.97	64.15	41.93	65.48	10.18	24.56	26.32	23.83	15.01	13.16	0.08	6.15	123.84	60.52	10.99	77.06
$Z + jets$	189.01	2.19	2.84	4.51	4.93	14.13	18.18	12.56	19.03	3.04	7.33	7.53	7.25	4.31	3.77	0.06	1.50	34.75	17.48	2.54	21.08
Total background	34305.5	392.6	489.5	835.8	837.9	2330.9	3301.6	2237.6	3513.5	566.8	1333.7	1325.5	1339.6	764.4	683.9	8.1	293.2	6274.6	3247.8	508.6	4019.9
MC signal $\sigma = 1pb$																					
$\gamma\gamma \to t\bar{t}$	62.17	1.69	1.97	1.46	1.47	6.51	7.80	5.50	5.80	2.46	3.16	2.34	2.36	2.18	0.89	0.06	0.52	10.13	3.63	0.23	2.00
Data																					
total	32193	368	445	675	738	2167	3171	2156	3251	577	1293	1357	1332	756	664	8	281	5761	3119	452	3622

Table 9.4: Event yields in the SR bins after all selection cuts are applied. The table shows only pre-fitted values.

Table 9.5: Impact of systematic uncertainties (improvement in %) on the expected 95% CL limit on $\sigma(\gamma\gamma \to t\bar{t})$. The impact is obtained by comparing the expected limit with the expected limit when a certain group of systematic uncertainties is removed in the limit-setting procedure. The last two rows shows the total impact of statistical and systematic uncertainties.

Systematic variation	impact on the limit
Experimental	
Jet energy resolution	1.4%
Jet energy calibration	1.0%
Pileup proton rates	0.9%
B-tag efficiency SF	0.1%
Luminosity	0.5%
Modeling	
Initial state radiation	1.0%
Background cross-section uncertainty	1.0%
Remove all systematics	6.6%
Remove all MC stat. errors	2.8%

affects both the expected event yields and the final shapes. The JEC uncertainty effect is studied by rescaling up and down the reconstructed jet energy by p_T- and η-dependent scale factors determined with dedicated studies within CMS, as detailed in [86] and [46], considering each group of uncertainty sources from the full independent set of 29 sources separately.

Jet energy resolution. The jet energy resolution in simulation is typically "smeared" to match the data in bins of jet η. This uncertainty has a larger impact on the analysis since jet energy is used to calculate the discriminants.

Lepton trigger and selection efficiencies. Uncertainties in the efficiency corrections based on control samples in data for the lepton trigger and offline selections are included. The total uncertainty is between 2-3% depending on the lepton p_T and η. These uncertainties are provided by corresponding CMS groups and have a negligible impact on the analysis.

Integrated luminosity. An additional 2.3% uncertainty is assigned on the signal normalization.

Cross-section uncertainty. A systematic uncertainty on the background cross-section of 5% for top-quark backgrounds and 30% for EWK backgrounds was applied.

Limited statistics in the shapes. The Beeston-Barlow method [87] is applied to take into account the limited statistics in the shapes (either from MC or data).

Table 9.5 summarizes the typical values of the systematic uncertainty variations of the signal and background. For shape uncertainties, being the statistical fit made to binned distributions, we quote the overall variation on the normalization.

9.6.2 Treatment of the systematic variations

An important issue in dealing with the systematic variations in the fit model is that in some cases, the corresponding upwards or downwards varied shapes may be dominated by statistical noise. Inserting such noise into the fit causes instabilities and other undesirable behavior. Therefore the following procedure is applied to the shape systematic uncertainties to ensure stable fit results:

Shape significance test The Kolmogorov-Smirnov test[4] between the upwards and the downwards shape variations concerning the nominal is performed. The shape systematic is retained if the Kolmogorov-Smirnov test results are less than 95%, for either of the upwards or downwards fluctuated shape. Otherwise, the shape variation is not significant for the given background sample, and the shape NP is not used in the fit (the corresponding normalization uncertainty is still kept, however).

Pruning of non-significant variations All normalization uncertainties below 0.1% were omitted.

Smoothing of shape variations When shape variations result from limited statistics in the alternative sample, the following two-step sequence is applied to disregard the effect.

Step 1: For every bin, alternative variation (upward – u_i or downward – d_i, where i is the bin index) is shifted depending to its statistical uncertainty (σ_{u_i} or σ_{d_i}) from the nominal value (n_i) as follows:

$$u_i = \max\{n_i, u_i - 0.5 \cdot \sigma_{u_i}\}$$

$$d_i = \min\{n_i, d_i + 0.5 \cdot \sigma_{d_i}\}$$

Step 2: The ratio of variation to nominal (separately for upwards and downwards variations) is smoothed, using the TH1::Smooth(1) method. The smoothed varied shape is then obtained by multiplying the nominal with the smoothed ratio.

Symmetrizing Shape variations within the same direction (either both up or both down) were symmetrized around its nominal shape.

Figure 9.60 shows the combined shape variations for the dominant systematic uncertainties before and after shape correction for statistically limited background source (W+jets) and Figure 9.61 shows corrected shape variations for the dominant systematic uncertainties for the $t\bar{t}$ background.

9.6.3 Validation of the statistical analysis (expected post-fit)

A consistency check of the statistical analysis implementation is made by running the fit on an Asimov dataset [88] and inspecting the post-fit constraints for a signal+background fit. We have tested this using each of the SR bins separately and in the combined fit.

[4]Implemented in TH1::KolmogorovTest() ROOT standard function

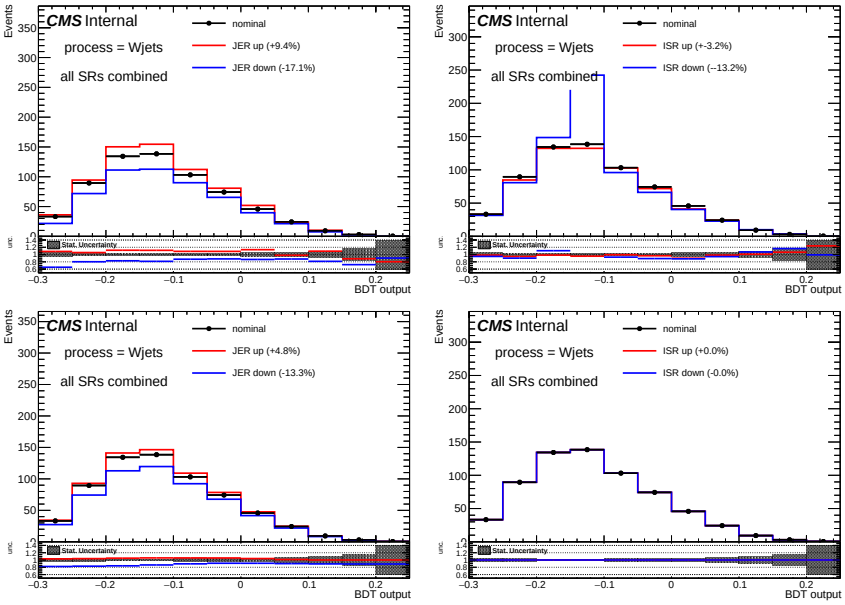

Figure 9.60: Shape variation for JER (left) and ISR (right) uncertainties before (top) and after (bottom) shape correction procedure is applied.

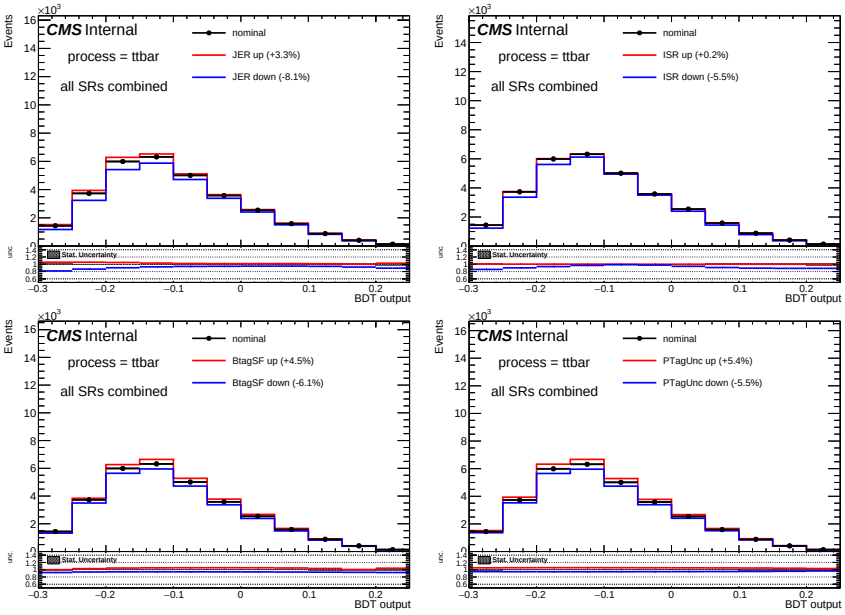

Figure 9.61: Shape variation for the $t\bar{t}$ process of the dominant systematic sources: JER (top left), ISR (top right), b-tagging efficiency (bottom left) and proton tag rate (bottom right).

The post-fit constraints for each nuisance and their corresponding correlation coefficient with the signal strength for the combined fit are shown in Fig. 9.62, and the correlation matrix between different sources of systematic uncertainties is shown in Figure 9.63.

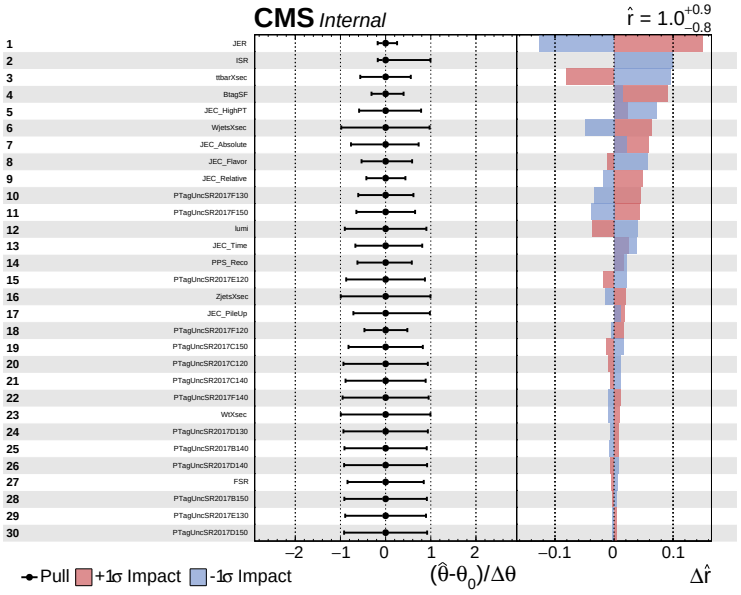

Figure 9.62: Post-fit nuisances in signal+background fit using an Asimov Dataset in the combined fit. In each figure the left panel displays the post-fit value and uncertainty of each nuisance, and the right panel displays the correlation with the signal strength.

The majority of these nuisances are not constrained. The only exceptions are Jet energy resolution and the uncertainty due to the modeling of initial state radiation, which was found to be larger than the statistical uncertainty in the signal region.

Fig. 9.64, shows post-fit constraints for each of the signal region separately.

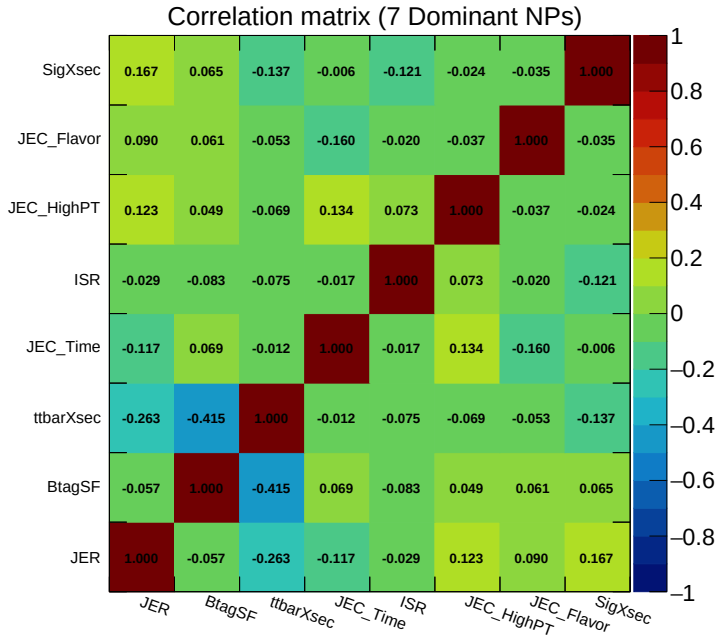

Figure 9.63: Correlation matrix between all NP implemented in the fit model. The fit is performed on the Asimov dataset

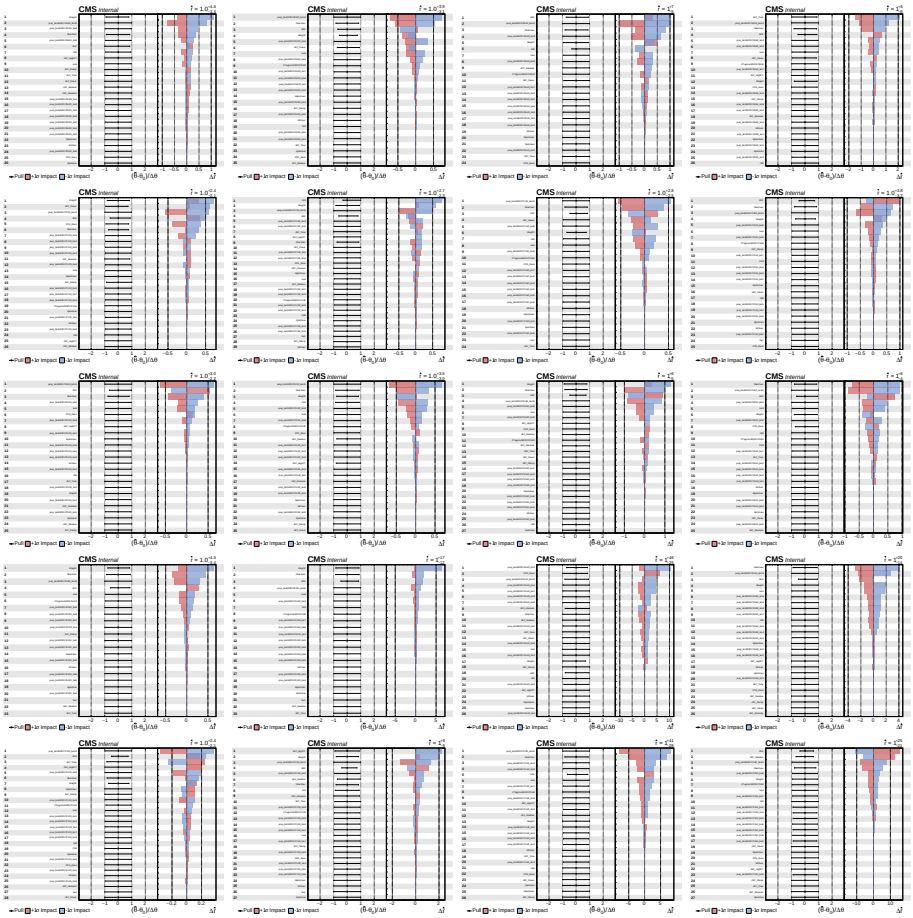

Figure 9.64: Post-fit nuisances in signal+background fit using an Asimov Dataset. In each figure the left panel displays the post-fit value and uncertainty of each nuisance, and the right panel displays the correlation with the signal strength.

9.7 Preliminary results and prospects

In order for authors not to be biased by looking at the data at a too early stage, a so-called "blind" analysis approach is undertaken: the analysis is set up and optimised only using simulations or data in regions other than the signal region, and anyway without exploiting the full information on the selected events in the signal region in the data. Only after a rigorous scrutiny of the methodology by CMS expert members not part of the analysis team, analysts will be allowed to finally have a full look at the data in the signal region to determine the observed number of signal events, if any, and an upper limit on the cross section. This analysis is currently still in the blinded phase: the methodology has been finalized and frozen and has been handed to the collaboration for scrutiny, so the results which are presented in this section are preliminary and not publicly available yet.
The (expected) distribution of the BDT variable is shown in Fig. 9.65, combining the simulated samples for all contributing processes, each rescaled to the data integrated luminosity using the known cross sections. While here we only show the figure for all signal regions combined, we of course produce also one such plot for every signal region separately. To compute the limits on the cross section, we follow the method described in [85]: in this approach, the calculation of the limits is based on an asymptotic approximation of the distributions of the test statistics, which in turn is based on the profile likelihood ratio, under given hypotheses for the signal and the background. In our implementation of the method, we then perform the statistical analysis on the BDT distributions to infer, from the expected number of events, the expected limits on the signal cross section that can be obtained, including the effects of the uncertainties.

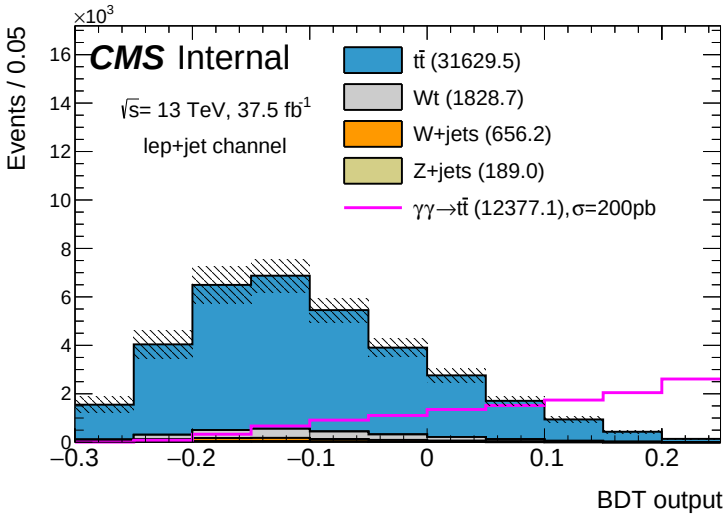

Figure 9.65: Distribution of the BDT score obtained in the signal region used in the statistical analysis, on simulated samples. In this plot, all signal regions were combined. The hatched areas represent the total uncertainty in each bin. To better see the signal, its contribution is drawn assuming a cross section of 200 pb.

The expected cross-section limits for the analysis, optimized as described

in the previous section, are shown in Fig. 9.66. The limits are computed for a cross-section of 1 pb, as an example case. Hence the parameter of interest here represents the limit on the cross-section in picobarn. The figure shows each signal region's sensitivity as well as the combined sensitivity of the analysis. The effects of all uncertainties are included, and yield the bands at the 68 and 95 % confidence levels around the median point. Once the analysis will be "unblinded", that is the full analysis chain can be performed on the data without the aforementioned restrictions, the observed limits on the data will be determined and compared to the expected limits derived in this way: a verification of the standard model expectations on the cross section can then be performed.

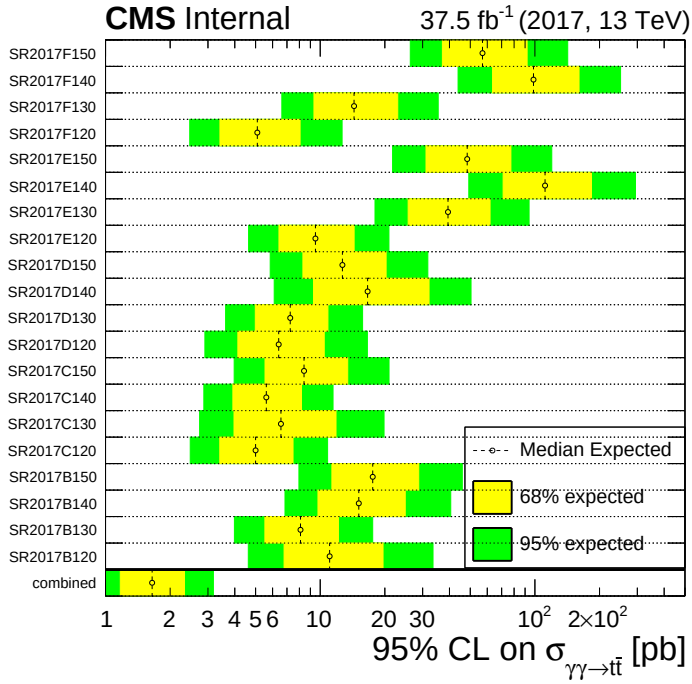

Figure 9.66: Asymptotic 95% CL upper limit on the signal cross-section for the combined result and for each one of the SR separately.

A final remark is in order. While in this analysis we only focused on the semileptonic decay channel of the $t\bar{t}$ pairs, a parallel effort is ongoing within CMS to measure the cross section for the central exclusive production of $t\bar{t}$ pairs using the dileptonic decay channel. The all-hadronic decay channel, on the contrary, based on preliminary studies, would not yield any significant contribution, because of a smaller selection efficiency and a larger background, and thus it is not under consideration at this stage. Initial discussions to combine the results of the semileptonic and dileptonic analyses in a single publication are ongoing. Also, the inclusion of the data taken in 2018 is planned for a future development of the analysis.

Conclusions

The CMS experiment at the CERN LHC is exploiting the huge amount of excellent-quality data produced by the LHC beam collisions to perform wide tests of the standard model of particle physics and broad searches for signatures of new physics models beyond the standard model.

In my PhD thesis, I have been involved in one of such efforts, the first measurement of the central exclusive production of $t\bar{t}$ pairs. At the LHC, $t\bar{t}$ pairs are mainly produced via QCD diagrams and several measurements of inclusive and differential cross sections have been performed. Recently, with the installation of a new system, the proton precision spectrometer (PPS), the possibility arose to study the $t\bar{t}$ pairs production via the gamma-gamma fusion process, in events of the form $pp \to pt\bar{t}p$, where the beam protons interact, losing a fraction of their 4-momentum, continue their path and are detected by PPS. The cross section for this process has never been measured before, and even precise theoretical calculations are not available. In general, theoretical calculations within the standard model predict a cross section below 1 fb, making the process hard to observe in the currently available data sample. However, even in absence of an observation, an upper limit on the cross section is useful to cross check the theoretical calculations and to verify whether any new physics scenario may enhance the cross section to values that make the process already observable. In my thesis I reported the details of the data analysis set up to measure the cross section for $pp \to pt\bar{t}p$ in the semi-leptonic decay channel of the $t\bar{t}$ pairs. The analysis has been finalized and optimized using Monte Carlo simulations and then applied on proton-proton collision data to verify the expected performances of the event selection. Preliminary estimates of the expected limits on the cross section have been obtained. The measured cross section for the $t\bar{t}$ exclusive production signal is not publicly available yet. The data analysis is currently under scrutiny by the collaboration in view of public release and presentation to the upcoming conferences.

In light of the continuous efforts of the LHC accelerator personnel to provide an increased luminosity of beam collisions at higher center-of-mass energies, and the need to keep up with the changing of the operating conditions and maintain excellent conditions of the experimental system, the detectors used to measure and identify the particles produced by the beam collisions undergo constant upgrades, that exploit the new technological advancements in the field. I participated in several efforts in this context. On one side, I participated in the construction and commissioning of the new silicon pixel detectors for PPS and, on the other side, I joined the TimeSpot collaboration to study and propose new precision timing detectors based on silicon p-n junctions in a novel configuration. The results of my studies within TimeSpot have been beyond expectations and

very encouraging. An unprecedented timing resolution below 30 pico-seconds has been achieved, that will be highly valuable for future experiments operating at very high interaction rates and fluences to maintain excellent reconstruction performances. The results of my study have been presented at international conferences and published in scientific journals.

Bibliography

[1] G. Aad *et al.*, "Observation of a new particle in the search for the Standard Model Higgs boson with the ATLAS detector at the LHC," *Phys. Lett. B*, vol. 716, pp. 1–29, 2012.

[2] S. Chatrchyan *et al.*, "Observation of a New Boson at a Mass of 125 GeV with the CMS Experiment at the LHC," *Phys. Lett. B*, vol. 716, pp. 30–61, 2012.

[3] M. Boonekamp, A. Dechambre, V. Juranek, O. Kepka, M. Rangel, C. Royon, and R. Staszewski, "FPMC: A Generator for forward physics," 2 2011.

[4] J. Alwall, M. Herquet, F. Maltoni, O. Mattelaer, and T. Stelzer, "MadGraph 5 : Going Beyond," *JHEP*, vol. 06, p. 128, 2011.

[5] ALICE Collaboration, F. Carminati, P. Foka, P. Giubellino, A. Morsch, G. Paic, J. Revol, K. Safar k, and Y. Schutz, "ALICE: physics performance report, volume i," *Journal of Physics G: Nuclear and Particle Physics*, vol. 30, no. 11, pp. 1517–1763, 2004.

[6] ATLAS Collaboration, G. Aad, J. Butterworth, J. Thion, U. Bratzler, P. Ratoff, R. Nickerson, J. Seixas, I. Grabowska-Bold, F. Meisel, S. Lokwitz *et al.*, "The ATLAS experiment at the CERN large hadron collider," *Jinst*, vol. 3, p. S08003, 2008.

[7] CMS Collaboration, S. Chatrchyan, G. Hmayakyan, V. Khachatryan, A. Sirunyan, W. Adam, T. Bauer, T. Bergauer, H. Bergauer, M. Dragicevic *et al.*, "The CMS experiment at the CERN LHC," 2008.

[8] LHCb Collaboration, A. A. Alves Jr, L. Andrade Filho, A. Barbosa, I. Bediaga, G. Cernicchiaro, G. Guerrer, H. Lima Jr, A. Machado, J. Magnin, F. Marujo *et al.*, "The LHCb detector at the LHC," *Jinst*, vol. 3, no. 08, p. S08005, 2008.

[9] E. Mobs, "The CERN accelerator complex," Aug 2018, general Photo. [Online]. Available: https://cds.cern.ch/record/2636343

[10] CMS Collaboration, "CMS public luminosity results." [Online]. Available: https://twiki.cern.ch/twiki/bin/view/CMSPublic/LumiPublicResults

[11] N. Izaak, "CMS conventional coordinate system with LHC and other detectors." [Online]. Available: https://wiki.physik.uzh.ch/cms/latex:example_spherical_coordinates

[12] A. Dominguez and CMS Collaboration, "CMS Technical Design Report for the Pixel Detector Upgrade," Tech. Rep. CERN-LHCC-2012-016. CMS-TDR-11, Sep 2012. [Online]. Available: http://cds.cern.ch/record/1481838

[13] CMS Collaboration, "CMS tracker detector performance results." [Online]. Available: https://twiki.cern.ch/twiki/bin/view/CMSPublic/DPGResultsTRK

[14] CMS Collaboration, "The CMS electromagnetic calorimeter project: Technical Design Report," Tech. Rep., 1997. [Online]. Available: https://cds.cern.ch/record/349375

[15] CMS collaboration, "HCAL Energy Reconstruction Performance," Tech. Rep., Nov 2016. [Online]. Available: http://cds.cern.ch/record/2235509

[16] J. G. Layter, *The CMS muon project: Technical Design Report*, ser. Technical Design Report CMS. Geneva: CERN, 1997. [Online]. Available: http://cds.cern.ch/record/343814

[17] A. Sirunyan, A. Tumasyan, W. Adam, F. Ambrogi, E. Asilar, T. Bergauer, J. Brandstetter, E. Brondolin, M. Dragicevic, J. Erö, and et al., "Performance of the CMS muon detector and muon reconstruction with proton-proton collisions at $\sqrt{s} = 13\,\text{TeV}$," *Journal of Instrumentation*, vol. 13, no. 06, p. P06015–P06015, Jun 2018. [Online]. Available: http://dx.doi.org/10.1088/1748-0221/13/06/P06015

[18] M. Albrow, M. Arneodo, V. Avati, J. Baechler, N. Cartiglia, M. Deile, M. Gallinaro, J. Hollar, M. Lo Vetere, K. Oesterberg, N. Turini, J. Varela, D. Wright, and C. CMS-TOTEM, "CMS-TOTEM Precision Proton Spectrometer," Tech. Rep. CERN-LHCC-2014-021. TOTEM-TDR-003. CMS-TDR-13, Sep 2014. [Online]. Available: https://cds.cern.ch/record/1753795

[19] V. Berardi, M. G. Catanesi, E. Radicioni, R. Herzog, R. Rudischer, E. Wobst, M. Deile, K. Eggert, F. Haug, P. Jarron, D. Macina, H. Niewiadomski, E. Noschis, M. Oriunno, A. L. Perrot, G. Ruggiero, W. Snoeys, A. Verdier, V. Boccone, M. Bozzo, A. Buzzo, F. Capurro, S. Cuneo, F. Ferro, M. Macri, S. Minutoli, A. Morelli, P. Musico, M. Negri, A. Santroni, G. Sette, A. Sobol, V. Avati, E. Goussev, M. Järvinen, J. Kalliopuska, K. Kurvinen, R. Lauhakangas, F. Oljemark, R. Orava, K. Österberg, V. G. Palmieri, H. Saarikko, A. Toppinen, V. Kundrát, M. Lokajícek, C. Da Via, J. Hasi, A. Kok, and S. Watts, *Total cross-section, elastic scattering and diffraction dissociation at the Large Hadron Collider at CERN: TOTEM Technical Design Report*, ser. Technical Design Report TOTEM. Geneva: CERN, 2004. [Online]. Available: http://cds.cern.ch/record/704349

[20] M. Gallinaro, "[talk] overall status of the CT-PPS project." [Online]. Available: https://indico.cern.ch/event/705748/timetable/#8-overall-status-of-the-ct-pps

[21] U. Amaldi, R. Biancastelli, C. Bosio, G. Matthiae, J. Allaby, W. Bartel, G. Cocconi, A. Diddens, R. Dobinson, and A. Wetherell,

"The energy dependence of the proton-proton total cross-section for centre-of-mass energies between 23 and 53 GeV," *Physics Letters B*, vol. 44, no. 1, pp. 112 – 118, 1973. [Online]. Available: http://www.sciencedirect.com/science/article/pii/0370269373903158

[22] G. G. Ruggiero, V. Avati, G. Antchev, M. Deile, K. Eggert, V. Eremin, J. Kaspar, H. Niewiadomski, J. Petäjäjärvi, E. Radicioni, F. Ravotti, E. Radermacher, W. Snoeys, W. Spearman, and J. Wu, "Characteristics of edgeless silicon detectors for the Roman Pots of the TOTEM experiment at the LHC," *Nucl. Instrum. Methods Phys. Res., A*, vol. 604, no. 1-2, pp. 242–245, 2009. [Online]. Available: https://cds.cern.ch/record/1274024

[23] M. Berretti, "Measurement of the forward charged particle pseudorapidity density in pp collisions at $\sqrt{s} = 7$ TeV with the TOTEM experiment." Ph.D. dissertation, Sep 2012, presented 27 Nov 2012. [Online]. Available: https://cds.cern.ch/record/1508392

[24] S. Parker, C. Kenney, and J. Segal, "3d — a proposed new architecture for solid-state radiation detectors," *Nuclear Instruments and Methods in Physics Research Section A: Accelerators, Spectrometers, Detectors and Associated Equipment*, vol. 395, no. 3, pp. 328 – 343, 1997, proceedings of the Third International Workshop on Semiconductor Pixel Detectors for Particles and X-rays. [Online]. Available: http://www.sciencedirect.com/science/article/pii/S0168900297006943

[25] C. Da Via, M. Boscardin, G.-F. Dalla Betta, G. Darbo, C. Fleta, C. Gemme, P. Grenier, S. Grinstein, T.-E. Hansen, J. Hasi, C. Kenney, A. Kok, S. Parker, G. Pellegrini, E. Vianello, and N. Zorzi, "3d silicon sensors: Design, large area production and quality assurance for the ATLAS IBL pixel detector upgrade," *Nuclear Instruments and Methods in Physics Research Section A: Accelerators, Spectrometers, Detectors and Associated Equipment*, vol. 694, pp. 321 – 330, 2012. [Online]. Available: http://www.sciencedirect.com/science/article/pii/S0168900212008509

[26] F. Ravera, "3D silicon pixel detectors for the CT-PPS tracking system," Ph.D. dissertation, 2017, presented 16 Jun 2017. [Online]. Available: https://cds.cern.ch/record/2682003

[27] J. Troska, S. Detraz, S. S. E. Nasr-Storey, P. Stejskal, C. Sigaud, C. Soos, and F. Vasey, "Prototype pixel optohybrid for the CMS phase 1 upgraded pixel detector," *Journal of Instrumentation*, vol. 7, no. 01, pp. C01 113–C01 113, jan 2012. [Online]. Available: https://iopscience.iop.org/article/10.1088/1748-0221/7/01/C01113

[28] E. Bossini, "Development of a Time Of Flight diamond detector and readout system for the TOTEM experiment at CERN," Ph.D. dissertation, Jun 2016, presented 18 Jul 2016. [Online]. Available: https://cds.cern.ch/record/2227688

[29] F. Anghinolfi, P. Jarron, A. N. Martemyanov, E. Usenko, H. Wenninger, M. C. S. Williams, and A. Zichichi, "NINO: An ultra-fast and low-power front-end amplifier/discriminator ASIC designed for the multigap resistive

plate chamber," *Nucl. Instrum. Methods Phys. Res., A*, vol. 533, pp. 183–187, 2004. [Online]. Available: https://cds.cern.ch/record/818554

[30] J. Christiansen, "HPTDC High Performance Time to Digital Converter," CERN, Geneva, Tech. Rep., 2004, version 2.2 for HPTDC version 1.3. [Online]. Available: https://cds.cern.ch/record/1067476

[31] C. Bostedt, R. Coffee, A. Fry, N. Hartmann, J. May, D. Nicholson, S. Schorb, S. Smith *et al.*, "Status of the LCLS experiment timing system," SLAC National Accelerator Lab., Menlo Park, CA (United States), Tech. Rep., 2012.

[32] H. F.-W. Sadrozinski, A. Seiden, and N. Cartiglia, "4-Dimensional Tracking with Ultra-Fast Silicon Detectors," *Reports on Progress in Physics*, no. AIDA-2020-PUB-2017-010, Apr 2017. [Online]. Available: https://cds.cern.ch/record/2667268

[33] V. Khachatryan, A. Sirunyan, A. Tumasyan, W. Adam, E. Asilar, T. Bergauer, J. Brandstetter, E. Brondolin, M. Dragicevic, J. Erö, and et al., "The cms trigger system," *Journal of Instrumentation*, vol. 12, no. 01, p. P01020–P01020, Jan 2017. [Online]. Available: http://dx.doi.org/10.1088/1748-0221/12/01/P01020

[34] G. L. Bayatyan, M. Della Negra, L. Foa, A. Hervé, and A. Petrilli, *CMS computing: Technical Design Report*, ser. Technical Design Report CMS. Geneva: CERN, 2005, submitted on 31 May 2005. [Online]. Available: http://cds.cern.ch/record/838359

[35] R. Brun and F. Rademakers, "ROOT: An object oriented data analysis framework," *Nucl. Instrum. Meth. A*, vol. 389, pp. 81–86, 1997.

[36] CMS Collaboration, "Particle-flow reconstruction and global event description with the CMS detector. Particle-flow reconstruction and global event description with the CMS detector," *JINST*, vol. 12, no. CMS-PRF-14-001. CMS-PRF-14-001-004. 10, p. P10003. 82 p, Jun 2017. [Online]. Available: http://cds.cern.ch/record/2270046

[37] V. Khachatryan and others, "Description and performance of track and primary-vertex reconstruction with the CMS tracker," *JINST*, vol. 9, no. CMS-TRK-11-001. CERN-PH-EP-2014-070. CMS-TRK-11-001, p. P10009. 80 p, May 2014. [Online]. Available: https://cds.cern.ch/record/1704291

[38] CMS Collaboration, "Muon Identification and Isolation efficiency on full 2016 dataset," Tech. Rep., Mar 2017. [Online]. Available: http://cds.cern.ch/record/2257968

[39] CMS collaboration, "Electron and photon performance in CMS with the full 2016 data sample," Tech. Rep., Mar 2017. [Online]. Available: http://cds.cern.ch/record/2255497

[40] S. Catani, Y. L. Dokshitzer, M. H. Seymour, and B. R. Webber, "Longitudinally-invariant kt-clustering algorithms for hadron-hadron collisions," *Nuclear Physics B*, vol. 406, no. 1-2, pp. 187–224, 1993.

[41] M. Cacciari, G. P. Salam, and G. Soyez, "The anti-ktjet clustering algorithm," *Journal of High Energy Physics*, vol. 2008, no. 04, p. 063–063, Apr 2008. [Online]. Available: http://dx.doi.org/10.1088/1126-6708/2008/04/063

[42] CMS Collaboration, "A Cambridge-Aachen (C-A) based Jet Algorithm for boosted top-jet tagging," CERN, Geneva, Tech. Rep. CMS-PAS-JME-09-001, Jul 2009. [Online]. Available: http://cds.cern.ch/record/1194489

[43] M. Cacciari, G. P. Salam, and G. Soyez, "FastJet user manual," *Eur. Phys. J. C*, vol. 72, no. CERN-PH-TH-2011-297. CERN-PH-TH-2011-297, p. 1896. 69 p, Nov 2011, comments: 69 pages. FastJet 3 is available from http://fastjet.fr/. [Online]. Available: http://cds.cern.ch/record/1402449

[44] T. Sjöstrand, S. Mrenna, and P. Skands, "PYTHIA 6.4 physics and manual," *Journal of High Energy Physics*, vol. 2006, no. 05, p. 026–026, May 2006. [Online]. Available: http://dx.doi.org/10.1088/1126-6708/2006/05/026

[45] M. Bähr, S. Gieseke, M. A. Gigg, D. Grellscheid, K. Hamilton, O. Latunde-Dada, S. Plätzer, P. Richardson, M. H. Seymour, A. Sherstnev, and et al., "Herwig++ physics and manual," *The European Physical Journal C*, vol. 58, no. 4, p. 639–707, Nov 2008. [Online]. Available: http://dx.doi.org/10.1140/epjc/s10052-008-0798-9

[46] CMS Collaboration, "Jet energy scale and resolution performance with 13 TeV data collected by CMS in 2016-2018," Apr 2020. [Online]. Available: http://cds.cern.ch/record/2715872

[47] V. Khachatryan and others, "Identification of heavy-flavour jets with the CMS detector in *pp* collisions at 13 TeV." *JINST*, vol. 13, no. CMS-BTV-16-002. CMS-BTV-16-002-004. 05, p. P05011. 114 p, Dec 2017. [Online]. Available: http://cds.cern.ch/record/2298594

[48] D. Guest, J. Collado, P. Baldi, S.-C. Hsu, G. Urban, and D. Whiteson, "Jet flavor classification in high-energy physics with deep neural networks," *Physical Review D*, vol. 94, no. 11, Dec 2016. [Online]. Available: http://dx.doi.org/10.1103/PhysRevD.94.112002

[49] A.M. Sirunyan and others, "Performance of missing transverse momentum reconstruction in proton-proton collisions at $\sqrt{s} = 13$ TeV using the CMS detector," *JINST*, vol. 14, no. arXiv:1903.06078. CMS-JME-17-001-003. 07, p. P07004. 55 p, Mar 2019. [Online]. Available: http://cds.cern.ch/record/2666972

[50] I. Béjar Alonso, O. Brüning, P. Fessia, M. Lamont, L. Rossi, L. Tavian, and M. Zerlauth, "High-luminosity large hadron collider (HL-LHC): Technical design report," CERN, Tech. Rep., 2020. [Online]. Available: http://doi.org/10.23731/CYRM-2020-0010

[51] L. Rossi, "LHC Upgrade Plans: Options and Strategy," no. CERN-ATS-2011-257, p. 6 p, Dec 2011. [Online]. Available: https://cds.cern.ch/record/1407911

[52] D. Contardo, M. Klute, J. Mans, L. Silvestris, and J. Butler, "Technical Proposal for the Phase-II Upgrade of the CMS Detector," 2015. [Online]. Available: https://cds.cern.ch/record/2020886

[53] A.M. Sirunyan and others, "A MIP Timing Detector for the CMS Phase-2 Upgrade," CERN, Geneva, Tech. Rep. CERN-LHCC-2019-003. CMS-TDR-020, Mar 2019. [Online]. Available: http://cds.cern.ch/record/2667167

[54] "The Phase-2 Upgrade of the CMS Endcap Calorimeter," CERN, Geneva, Tech. Rep. CERN-LHCC-2017-023. CMS-TDR-019, Nov 2017. [Online]. Available: https://cds.cern.ch/record/2293646

[55] A. Benaglia, S. Gundacker, P. Lecoq, M. Lucchini, A. Para, K. Pauwels, and E. Auffray, "Detection of high energy muons with sub-20ps timing resolution using l(y)so crystals and sipm readout," *Nuclear Instruments and Methods in Physics Research Section A: Accelerators, Spectrometers, Detectors and Associated Equipment*, vol. 830, no. Supplement C, pp. 30 – 35, 2016. [Online]. Available: http://www.sciencedirect.com/science/article/pii/S016890021630393X

[56] R. Mulargia, R. Arcidiacono, A. Bellora, M. Boscardin, N. Cartiglia, F. Cenna, R. Cirio, G. Dalla Betta, S. Durando, A. Fadavi *et al.*, "Temperature dependence of the response of ultra fast silicon detectors," *Journal of Instrumentation*, vol. 11, no. 12, p. C12013, 2016. [Online]. Available: https://doi.org/10.1088/1748-0221/11/12/c12013

[57] S. Mazza, E. Estrada, Z. Galloway, C. Gee, A. Goto, Z. Luce, F. McKinney-Martinez, R. Rodriguez, H. Sadrozinski, A. Seiden, B. Smithers, Y. Zhao, V. Cindro, G. Kramberger, I. Mandić, M. Mikuž, M. Zavrtanik, R. Arcidiacono, N. Cartiglia, M. Ferrero, M. Mandurrino, V. Sola, A. Staiano, M. Boscardin, G. Della Betta, F. Ficorella, L. Pancheri, and G. Paternoster, "Proprieties of FBK UFSDs after neutron and proton irradiation up to $6 * 10^{15}$ neq/cm^2," Tech. Rep. arXiv:1804.05449. 04, Apr 2018. [Online]. Available: https://cds.cern.ch/record/2637855

[58] S. Ramo, "Currents induced by electron motion," *Proceedings of the IRE*, vol. 27, no. 9, pp. 584–585, 1939.

[59] W. Shockley, "Currents to conductors induced by a moving point charge," *Journal of applied physics*, vol. 9, no. 10, pp. 635–636, 1938.

[60] F. Cenna, "Signal formation in innovative silicon detectors," Master's thesis, University of Turin, Italy, 2014.

[61] F. Hartmann, "Silicon tracking detectors in high-energy physics," *Nuclear Instruments and Methods in Physics Research Section A: Accelerators, Spectrometers, Detectors and Associated Equipment*, vol. 666, pp. 25–46, 2012.

[62] "CTPPS Performance Plots: Detector Commissioning in 2017," Dec 2018.

[63] "CTPPS Performance Plots: Detector Commissioning in 2018," Dec 2017.

[64] "Efficiency of the Pixel sensors used in the Precision Proton Spectrometer: radiation damage," Oct 2019. [Online]. Available: https://cds.cern.ch/record/2697291

[65] "Technology developments and first measurements of Low Gain Avalanche Detectors (LGAD) for high energy physics applications," *Nuclear Instruments and Methods in Physics Research Section A: Accelerators, Spectrometers, Detectors and Associated Equipment*, vol. 765, pp. 12 – 16, 2014.

[66] (2017) The TIMESPOT project. [Online]. Available: https://web.infn.it/timespot/index.php

[67] R. Mulargia, "Preliminary beam test results for the TIMESPOT project," *Journal of Instrumentation*, vol. 15, no. 11, pp. C11 004–C11 004, nov 2020. [Online]. Available: https://doi.org/10.1088/1748-0221/15/11/c11004

[68] J. Lange, G. Giannini, S. Grinstein, M. Manna, G. Pellegrini, D. Quirion, S. Terzo, and D. Vázquez Furelos, "Radiation hardness of small-pitch 3D pixel sensors up to a fluence of 3×10^{16} n_{eq}/cm^2," *JINST*, vol. 13, no. arXiv:1805.10208. 09, p. P09009. 21 p, May 2018, 21 pages. [Online]. Available: https://cds.cern.ch/record/2633861

[69] A. Loi, G. F. D. Betta, A. Lai, R. Mendicino, and S. Vecchi, "Design and simulation of 3d-silicon sensors for future vertex detectors," pp. 1–3, 2018. [Online]. Available: https://ieeexplore.ieee.org/abstract/document/8824738

[70] R. Mulargia, L. Anderlini, M. Aresti, A. Bizzeti, M. Boscardin, A. Cardini, G.-F. D. Betta, M. Ferrero, G. Forcolin, M. Garau, A. Lai, and et al., "Intrinsic time resolution of 3d-trench silicon pixels for charged particle detection," *Journal of Instrumentation*, vol. 15, no. 09, p. P09029–P09029, Sep 2020. [Online]. Available: http://dx.doi.org/10.1088/1748-0221/15/09/P09029

[71] V. Gonçalves, D. Martins, M. Rangel, and M. Tasevsky, "Top quark pair production in the exclusive processes at LHC," *Phys. Rev. D*, vol. 102, no. arXiv:2007.04565, p. 074014. 10 p, Jul 2020. [Online]. Available: https://cds.cern.ch/record/2725583

[72] A. Solano, "[talk] The PPS detector: status and performance." [Online]. Available: https://indico.cern.ch/event/713101/contributions/3102240/

[73] J. Hollar *et al.*, "PPS datasets in 2017," 2017. [Online]. Available: https://twiki.cern.ch/twiki/bin/viewauth/CMS/CTPPSDatasets2017

[74] S. Agostinelli *et al.*, "GEANT4: A simulation toolkit," *Nucl. Instrum. Meth.*, vol. A506, p. 250, 2003.

[75] J. Alwall, R. Frederix, S. Frixione, V. Hirschi, F. Maltoni, O. Mattelaer, H. S. Shao, T. Stelzer, P. Torrielli, and M. Zaro, "The automated computation of tree-level and next-to-leading order differential cross sections, and their matching to parton shower simulations," *JHEP*, vol. 07, p. 079, 2014.

[76] V. M. Budnev, I. F. Ginzburg, G. V. Meledin, and V. G. Serbo, "The Two photon particle production mechanism. Physical problems. Applications. Equivalent photon approximation," *Physics Reports*, vol. 15, no. 4, pp. 181 – 282, 1975. [Online]. Available: http://www.sciencedirect.com/science/article/pii/0370157375900095

[77] P. Artoisenet, R. Frederix, O. Mattelaer, and R. Rietkerk, "Automatic spin-entangled decays of heavy resonances in Monte Carlo simulations," *JHEP*, vol. 03, p. 015, 2013.

[78] T. Sjöstrand, S. Mrenna, and P. Skands, "PYTHIA 6.4 physics and manual," *JHEP*, vol. 05, p. 026, 2006.

[79] T. Sjöstrand *et al.*, "An introduction to PYTHIA 8.2," *Comput. Phys. Commun.*, vol. 191, pp. 159–177, 2015.

[80] A. M. Sirunyan *et al.*, "Extraction and validation of a new set of CMS PYTHIA8 tunes from underlying-event measurements," *Eur. Phys. J. C*, vol. 80, p. 4, 2019.

[81] Sirunyan, A. M. and others, "Identification of heavy-flavour jets with the CMS detector in pp collisions at 13 TeV," *JINST*, vol. 13, no. 05, p. P05011, 2018.

[82] M. Pisano, "Study of central exclusive production of top quark-antiquark pairs at the LHC," Master's thesis, University of Genova, 2020.

[83] A. Hoecker, P. Speckmayer, J. Stelzer, J. Therhaag, E. von Toerne, and H. Voss, "TMVA: Toolkit for Multivariate Data Analysis," *PoS*, vol. ACAT, p. 040, 2007.

[84] L. Moneta, K. Belasco, K. S. Cranmer, S. Kreiss, A. Lazzaro, D. Piparo, G. Schott, W. Verkerke, and M. Wolf, "The RooStats Project," *PoS*, vol. ACAT2010, p. 057, 2010.

[85] Higgs PAG, "HiggsAnalysis: CombinedLimit," 2018. [Online]. Available: https://github.com/cms-analysis/HiggsAnalysis-CombinedLimit

[86] CMS Collaboration, "Jet energy scale and resolution in the CMS experiment in pp collisions at 8 TeV," *J. Instrum.*, vol. 12, 2017.

[87] R. J. Barlow and C. Beeston, "Fitting using finite Monte Carlo samples," *Comput. Phys. Commun.*, vol. 77, pp. 219–228, 1993.

[88] E. G. G. Cowan, K. Cranmer and O. Vitells, "Asymptotic formulae for likelihood-based tests of new physics," *Eur. Phys. J. C*, vol. 71, p. 1554, 2011.